Université de Montréal
et
Université Montpellier 2

Étude de l'influence de la perte de masse sur l'évolution d'étoiles de plusieurs types

par
Mathieu Vick

Thèse effectuée en cotutelle
au
Département de physique
Faculté des arts et des sciences
Université de Montréal
et au
GRAAL - Groupe de Recherche en Astronomie et Astrophysique du Languedoc
Université Montpellier 2

Thèse présentée à la Faculté des études supérieures de l'Université de Montréal
en vue de l'obtention du grade de Philosophiæ Doctor (Ph.D.)
en physique, option astrophysique
et à
l'I2S: Information, Structures, Systèmes de l'Université Montpellier 2 en vue de
l'obtention du grade de Docteur de l'Université Montpellier II

Octobre, 2010

Université de Montréal
Faculté des études supérieures
et
Université Montpellier 2
I2S: Information, Structures, Systèmes

Cette thèse intitulée:

Étude de l'influence de la perte de masse sur l'évolution d'étoiles de plusieurs types

présentée et soutenue à l'Université de Montréal par:

Mathieu Vick

a été évaluée par un jury composé des personnes suivantes:

Pr CHARBONNEAU Paul,	Président et examinateur, Université de Montréal
Pr MICHAUD Georges,	Directeur de recherche, Université de Montréal
Dr JASNIEWICZ Gérard,	Directeur de recherche, Université Montpellier 2
Dr RICHARD Olivier,	Codirecteur de recherche, Université Montpellier 2
Dr LEBRE Agnès,	Examinateur, Université Montpellier 2
Pr CHARBONNEL Corinne,	Rapporteur externe, Université de Genève
Pr LANDSTREET John,	Rapporteur externe, University of Western Ontario
Pr MAHEU Louis,	Représentant du doyen, Université de Montréal

Thèse soutenue le 15 octobre 2010

RÉSUMÉ

La perte de masse est introduite dans des modèles évolutifs qui traitent en détail le transport microscopique induit par la diffusion atomique et les accélérations radiatives pour 28 espèces y inclus tous les isotopes de la base de données OPAL. Les propriétés physiques des solutions sont analysées en détail. Lorsque l'amplitude de la vitesse advective causée par la perte de masse est plus grande que la vitesse de triage dirigée vers le centre de l'étoile, le flux local d'un élément est déterminé par des variations du flux qui se déroulent profondément dans l'étoile. Par contre, l'abondance locale dépend aussi des variations locales des accélérations radiatives. Dans ces étoiles, la séparation chimique causée par la diffusion atomique affecte 30% du rayon externe de l'étoile.

Les modèles sont aussi comparés à plusieurs observations d'étoiles AmFm, HAeBe et de Population II dans le but de caractériser le rôle que pourrait jouer la perte de masse en tant que processus qui inhibe la diffusion atomique dans les zones stables de ces étoiles. Les anomalies d'abondances observées à la surface de ces étoiles sont reproduites par des modèles évolutifs qui incluent la diffusion atomique et la perte de masse non-séparée. Les taux de perte de masse considérés ne sont contraints que par les abondances en surface puisque leurs amplitudes sont probablement trop petites pour être observées directement. Quant aux étoiles AmFm et HAeBe, les observations d'abondances sont compatibles avec des taux de perte de masse qui sont au maximum 5 fois plus élevés que le taux de perte de masse solaire, alors que les taux requis pour reproduire les observations d'étoiles de Population II sont jusqu'à $50-100$ fois plus élevés que le taux solaire. Des taux de perte de masse $\leq 10^{-14}\,\mathrm{M}_{\odot}\mathrm{yr}^{-1}$, qui permettent l'apparition d'une zone convective due aux éléments du pic du fer, mènent à des abondances en surface qui ne sont pas compatibles avec les observations. Les abondances en surface d'étoiles AmFm et de Population II sont régies par la séparation chimique qui se déroule profondément

dans l'étoile ($\log \Delta M/M_* \sim -5$ à -6), alors que la séparation se produit plus près de la surface ($\log \Delta M/M_* \sim -7$) dans les étoiles HAeBe.

Par rapport aux modèles avec mélange turbulent, la perte de masse mène à une distribution interne des éléments très différente. Le mélange turbulent conduit à des solutions pour lesquelles les abondances sont homogènes depuis la surface jusque profondément dans l'étoile (solution diffusive), alors que la perte de masse permet la séparation chimique dès le bas de la zone convective de surface (solution advective). Ce résultat pourrait peut-être permettre à l'astérosismologie de déterminer l'importance relative de ces deux processus dans l'intérieur de ces étoiles.

Mots-clés : étoiles, évolution, diffusion atomique, abondances, perte de masse.

ABSTRACT

Mass loss has been introduced in a stellar evolution code which takes into account all the effects of atomic diffusion and radiative accelerations for the 28 species included in the OPAL opacity database. The physical properties of the solutions are analyzed in detail. When the advective velocity induced by mass loss dominates the inward settling velocity, the local flux for a given element is determined by flux variations which occur deep within the star. However, local abundances are modulated by local variations in radiative accelerations. Atomic diffusion affects the outer 30% of the stellar radius of these stars.

The computed models are also compared to observations of AmFm, HAeBe and Population II stars in order to determine to what extent mass loss competes with atomic diffusion in the stable regions of these stars. Mass loss rates are solely constrained via surface abundances, since the mass loss rate amplitudes are likely too small to be observed directly.

It is shown that most chemical anomalies observed at the surface of these stars can be reproduced by models with unseparated mass loss. While AmFm and HAeBe abundance determinations are compatible with mass loss rates which are, at most, 5 times larger than the solar mass loss rate, Population II stars require much larger rates (50 to 100 times the solar rate). Mass loss rates ($\leq 10^{-14}\,\mathrm{M_\odot yr^{-1}}$) which lead to an iron peak convection zone are not compatible with surface abundance observations. Surface abundances in AmFm and Population II stars are shown to be the result of chemical separation occurring deep within the star ($\log \Delta M/M_* \sim -5$ to -6); however, in HAeBe stars, for which anomalies appear during the pre–main-sequence, the separation occurs nearer the surface ($\log \Delta M/M_* \sim -7$).

With respect to turbulent mixing, mass loss leads to very different internal abundance distributions. Whereas turbulent mixing homogenizes abundances from the surface down to depths well within the radiative zone (diffusive solution), mass

loss allows for chemical stratification up to the bottom of the surface convection zone (advective solution). This could potentially allow for asteroseismic tests which could elucidate the relative importance of both types of processes in these stars.

Keywords: stars, evolution, atomic diffusion, abundances, mass loss.

TABLE DES MATIÈRES

RÉSUMÉ . . . . . **iii**

ABSTRACT . . . . . **v**

TABLE DES MATIÈRES . . . . . **vii**

LISTE DES FIGURES . . . . . **x**

LISTE DES ANNEXES . . . . . **xiv**

CHAPITRE 1 :INTRODUCTION **1**

1.1 Quelques principes de la diffusion atomique 3

1.2 Propriétés des étoiles chimiquement particulières et apparentées . . 6

1.2.1 Les étoiles CP non-magnétiques 8

1.2.2 Les étoiles CP magnétiques 9

1.2.3 Étoiles de la branche horizontale 10

1.2.4 Étoiles de Population II 10

1.2.5 Les étoiles CP des amas et du champ : des observations aux modèles 13

1.3 Quelques modèles d'étoiles CP 14

1.3.1 Modèles AmFm avec perte de masse 15

1.3.2 Modèles d'étoiles de Population II avec perte de masse . . . 20

1.3.3 Modèles d'étoiles riches en He et roAp avec perte de masse . 21

1.4 Les processus d'accélérations de la perte de masse 22

1.4.1 Vents radiatifs 23

1.4.2 Vents coronaux 26

1.5 Techniques observationnelles directes 26

1.5.1 Asymétries dans les raies en absorption 27

1.5.2 Raies en émission 28
1.5.3 Émission continue 28
1.5.4 Technique indirecte pour vents du type solaire 29
1.6 Vents stellaires observés 30
1.6.1 Survol de la thèse 32
1.6.2 Contribution aux articles 32

CHAPITRE 2 :ÉTOILES AmFm ET LA BRÈCHE DU LITHIUM 34

2.1 Astrophysical context 35
2.2 Calculations 39
2.3 Radiative accelerations 41
2.3.1 Radiative accelerations for Li, Be and B 42
2.4 Mass loss 47
2.4.1 Treatment of mass loss 47
2.4.2 Stellar winds of A and F stars 51
2.4.3 Unseparated vs. separated mass loss 54
2.5 Evolutionary models 56
2.5.1 Radiative accelerations, internal abundance variations and structure 58
2.5.2 Discussion: Internal variations 64
2.5.3 Surface abundance variations 70
2.6 Comparison to turbulence models 84
2.7 Comparison to observations 87
2.7.1 Field stars 88
2.7.2 Open cluster stars 90
2.8 General discussion and conclusion 99
2.8.1 Summary of results 99
2.8.2 Further implications 102

CHAPITRE 3: ANOMALIES D'ABONDANCES DANS LES ÉTOILES DE LA PRÉ-SÉQUENCE PRINCIPALE 106

3.1 Astrophysical context 107

3.2 Calculations 109

3.3 Evolutionary models 110

3.3.1 Radiative accelerations, internal abundances and structure . 111

3.3.2 Surface abundances 113

3.4 Comparison to observations 116

3.5 General discussion and conclusions 119

3.6 Acknowledgments 122

CHAPITRE 4 :LES ÉTOILES DE POPULATION II ET LE PLATEAU DE SPITE 128

4.1 Astrophysical context 129

4.2 Calculations 132

4.3 Evolutionary models 133

4.3.1 Radiative accelerations and internal abundance variations . . 135

4.3.2 Surface abundance variations 141

4.4 Comparison to previous models with mass loss 145

4.5 Comparison to models with turbulence 147

4.6 Conclusion 148

CHAPITRE 5 :CONCLUSION 153

BIBLIOGRAPHIE 158

ANNEXES 173

LISTE DES FIGURES

1.1 Comparaison de l'intérieur d'un modèle avec perte de masse avec celui d'un modèle avec mélange turbulent. 2

1.2 Illustration des processus dans la zone radiative d'une étoile CP. . . 5

1.3 Diagramme H–R des étoiles CP tirée de Vauclair & Vauclair (1982). 7

1.4 Abondances de Li dans les étoiles de faible métallicité du halo galactique : le plateau de Spite. 11

1.5 Détections de ^{6}Li dans les étoiles de faible métallicité (Asplund et al., 2006) ?. 12

1.6 Explorations antérieures de l'effet de la perte de masse sur les anomalies d'abondances en surface d'étoiles AmFm (Michaud et al., 1983). 18

1.7 Explorations antérieures de l'effet de la perte de masse sur l'abondance en surface du lithium dans les Hyades (Swenson & Faulkner, 1992). 19

1.8 Explorations antérieures de l'effet de la perte de masse sur l'abondance en surface du lithium dans les étoiles de Population II (Vauclair & Charbonnel, 1995). 21

1.9 Illustration du processus d'accélération de vents radiatifs. 24

1.10 Illustration de la formation d'un profil P Cygni. 27

2.1 H-R diagram for all the models shown in Fig. 2.4. 40

2.2 Opacity spectra for Li, Fe as well as the total opacity in $\mathrm{cm^2 g^{-1}}$ at a depth where $\log T = 5.3$ and $\log \rho = -4.6$. 44

2.3 Variation of radiative accelerations with temperature for Li and Be. 45

2.4 Evolution of $T_{\rm eff}$, $\log g$, luminosity, temperature and mass at the bottom of the surface convection zone, as well as the surface Fe abundance for selected masses that span the range of AmFm stars. . 57

2.5 Radiative accelerations, local gravity and internal abundances for a few selected elements in a 1.5 $M_\odot$ model. 58
2.6 Radiative accelerations, local gravity and internal abundances for a few selected elements in a 2.5 $M_\odot$ model. 61
2.7 Comparison of the normalized local flux with radiative accelerations and internal abundances for a 2.5 $M_\odot$ model with a mass loss rate of $10^{-13}\,M_\odot yr^{-1}$. 62
2.8 Internal abundances (Fe, Ni), radiative accelerations (Fe, Ni), Rosseland opacity, the difference between the radiative and adiabatic temperature gradients as well as the mean molecular weight per nucleus for three 1.5 $M_\odot$ models with different mass loss rates. 66
2.9 Same as Fig. 2.8, but for 2.5 $M_\odot$ models. 68
2.10 Wind velocities and diffusion velocities of a few selected elements in two 2.50 $M_\odot$ models at 300 Myr. 69
2.11 Surface abundance variations for five 1.50 $M_\odot$ models, as well as three 2.50 $M_\odot$ models with $Z_0 = 0.02$ and varying amounts of mass loss. 71
2.12 Evolution of Ca surface abundances for 1.5 $M_\odot$ models with different mass loss rates. 74
2.13 Effect of varying initial metallicity on the evolution of abundance anomalies at the surface of a 2.0 $M_\odot$ star with a mass loss rate of $10^{-13}\,M_\odot yr^{-1}$. 75
2.14 Evolution of surface abundance anomalies for a 2.50 $M_\odot$ star with a mass loss rate of $10^{-13}\,M_\odot yr^{-1}$. 77
2.15 Effect of stellar mass on surface abundance anomalies. 78
2.16 Evolution of ^{7}Li surface abundances for models with masses ranging from 1.37 $M_\odot$ to 1.48 $M_\odot$ with no mass loss and $Z_0 = 0.02$. 79
2.17 The $T_{\rm eff}$-$X_{\rm Li}$ relation at different ages for the models shown in Fig. 2.16. 81

2.18 Surface abundance evolution for selected elements of 1.40 $M_\odot$ models with different types of wind solutions, including separated winds). . 82
2.19 Internal concentrations of two 2.50 $M_\odot$ models at 500 Myr. 85
2.20 Confronting observations of the surface abundances of Sirius A to various models. 89
2.21 Confronting observations of the surface abundances of *o* Leonis to various models. 91
2.22 Confronting observations of the surface abundances of 68 Tau to various models. 93
2.23 Confronting observations of the surface abundances of HD 73045 to various models. 94
2.24 Confronting observations of the surface abundances of HD 108486 to various models. 95
2.25 Lithium, beryllium, iron and calcium abundances for models with and without mass loss at 625 Myr, the approximate age of the Hyades open cluster. 105

3.1 PMS evolution in the HR diagram for four models with a mass loss rate of $5 \times 10^{-14}\,M_\odot yr^{-1}$. 123
3.2 Internal variation of $\nabla_r - \nabla_{ad}$ for three models with a mass loss rate of $5 \times 10^{-14}\,M_\odot yr^{-1}$ at the onset of the ZAMS. 124
3.3 Comparison of the normalized local flux with radiative accelerations and internal abundances of ^{7}Li, O, Ca and Fe at 3 different ages for the 2.50W5E-14 model. 125
3.4 Wind velocities and diffusion velocities of a few selected elements in a 1.90 $M_\odot$ model near the ZAMS. 126
3.5 Surface abundance variations for models of 1.9 $M_\odot$ with different mass loss rates. 126

3.6 Surface abundances for models representing the components of the binary star V380 Ori. 127

4.1 The position in the Hertzprung-Russell diagram and the evolution of $T_{\rm eff}$, $\log g$, $T_{\rm BSCZ}$, $M_{\rm BSCZ}$ and $X_{\rm c}$ for stars of $0.6 - 0.8\,{\rm M}_{\odot}$ with $Z_0 = 0.00017$ and $\dot{M} = 10^{-12}\,{\rm M}_{\odot}{\rm yr}^{-1}$. 134

4.2 The impact of mass loss rate on the evolution of $T_{\rm BSCZ}$, $M_{\rm BSCZ}$ and $T_{\rm eff}$ for $0.8\,{\rm M}_{\odot}$ models. 135

4.3 Radiative accelerations and gravity at four different ages for a $0.8\,{\rm M}_{\odot}$ model with $\dot{M} = 10^{-12}\,{\rm M}_{\odot}{\rm yr}^{-1}$. 136

4.4 Internal abundance variations for the same model and ages seen in Fig. 4.3. 138

4.5 The impact of mass loss rate on internal abundance profiles for $0.80\,{\rm M}_{\odot}$ models. 139

4.6 Wind velocity and diffusion velocities in the 0.80W1E-12 model at two different ages. 141

4.7 Evolution of surface abundance anomalies for selected stellar masses with a mass loss rate of $10^{-12}\,{\rm M}_{\odot}{\rm yr}^{-1}$. 142

4.8 Comparison of the surface abundance anomalies for $0.8\,{\rm M}_{\odot}$ models with and without mass loss as well as with the T6.09 turbulent parametrization. 143

4.9 Lithium and iron surface abundance isochrones at 12 Gyr and 13.5 Gyr for models with and without mass loss as well as the T6.09 models from Richard et al. (2002b). 151

4.10 Internal lithium profiles for $0.75\,{\rm M}_{\odot}$ models with and without mass loss, as well as a comparison of diffusion and wind velocities for the $0.75\,{\rm M}_{\odot}$ models. 152

LISTE DES ANNEXES

Annexe A : Composition chimique des étoiles A et F des Hyades 1

Annexe B : Les effets de la perte de masse sur l'évolution des abondances chimiques dans les étoiles Fm 26

Annexe C : Modèles évolutifs avec perte de masse et turbulence 33

Annexe D : Diffusion atomique, perte de masse et anomalies d'abondances dans les étoiles Fm 40

À mes parents et à ma soeur.

REMERCIEMENTS

Tout d'abord, je tiens à remercier mes directeurs de recherche, Georges Michaud et Olivier Richard, qui ont toujours été disponibles, souriants et très généreux. En plus d'avoir encadré mon travail pendant quatre ans, ils m'ont permis de participer à plusieurs conférences et à visiter un bon nombre de pays ! Un gros merci à Georges pour sa patience, ses blagues et tout ce temps passé à lire (et à relire) ce manuscrit et une foule d'autres textes qui ont été rédigés au cours de mes 6 années de doctorat et de maîtrise. Sans son intuition et sa mémoire parfois étonnante c'est certain qu'il m'en aurait fallu encore une ou deux encore :) Et à Olivier, un gros merci pour la bonne humeur, la cueillette infinie de signatures et pour avoir rendu mon séjour à Montpellier si agréable. Merci aussi à Jacques Richer sans qui aucun calcul de cette thèse auraient pu être réalisés. Peu importe l'heure ou la journée de la semaine, il a toujours trouvé du temps pour me dépanner :)

À toute l'équipe du GRAAL, merci pour l'accueil si chaleureux. Un petit clin d'oeil aussi à Ana, Marwan, Patrick, Sylvain, Emelyne, Éric, Rana et Michèle pour tous ces beaux moments en France et ailleurs.

Je remercie tous les membres du jury pour l'attention qu'ils ont porté à mon travail et pour tous leurs conseils et remarques, particulièrement à Paul Charbonneau qui a non seulement été le directeur de mon jury de thèse, mais aussi membre de mon comité de prédoc et de maîtrise.

Merci aussi à Francis LeBlanc qui m'a guidé vers l'astronomie dès mes années de baccalauréat à l'Université de Moncton.

Merci à tout le monde au B-416, particulièrement à Antoine de la Chevrotière, qui pendant 6 ans a été mon second au bureau, au hockey, au gym, aux rencontres de l'OMM, en réalisation de film, au pub, etc, ainsi que décorateur d'intérieur du bureau. Tu es le meilleur :p.

Finalement, merci infiniment à mes parents, à ma soeur et à Jessie qui, de près

et de loin, m'ont appuyé tout au long de mon parcours. Leurs encouragements m'ont fourni l'énergie qu'il fallait tous ces matins où le réveil était plus difficile et toutes ces nuits où j'aurais préféré être ailleurs qu'au bureau :)

CHAPITRE 1

INTRODUCTION

Depuis plus d'un siècle, nous observons dans le spectre de radiation de plusieurs étoiles de la séquence principale (MS) des raies atomiques très fortes (ou faibles) par rapport aux raies que nous retrouvons dans le spectre d'étoiles de $T_{\rm eff}$ similaire dites *normales* (Maury 1897; Cannon 1901). Cela indique que dans ces étoiles, les éléments auteurs de ces raies sont surabondants (ou sousabondants) par rapport à leur abondance en surface d'étoiles *normales*. Ces étoiles sont désignées comme *chimiquement particulières* (CP) et sont subdivisées en plusieurs sous-groupes parmi lesquels figurent les étoiles ApBp, HgMn, AmFm et les étoiles à l'hélium (Preston, 1974). Des étoiles de Population II et des étoiles plus évoluées de la branche horizontale (HB) ont aussi des anomalies reliées à celles des étoiles CP.

Mais quelle est l'origine de ces anomalies ? L'analyse d'un échantillon important d'étoiles de Adelman (1973) a permis d'établir qu'il y a vraisemblablement un lien entre l'apparition d'anomalies en surface et la profondeur de la zone convective superficielle (SCZ). Dans les amas ouverts, certaines étoiles chaudes (types B, A et F chaudes) montrent des écarts significatifs d'abondances par rapport à la composition quasi-homogène des étoiles froides (types G et F froides). Puisque les étoiles d'amas émanent du même nuage moléculaire originel, ces différences d'abondances semblent causées par un ou plusieurs processus internes qui affectent davantage certaines étoiles chaudes ayant des SCZ moins profondes.

Suite aux échecs des explications liées à la nucléosynthèse (Fowler et al. 1965; Brancazio & Cameron 1967), Michaud (1970) offre la première interprétation satisfaisante des anomalies d'abondance observées en surface des étoiles CP. Il suggère à partir de principes premiers que la diffusion atomique, régie par la compétition entre les forces radiatives et la gravité, permettrait d'expliquer les anomalies en

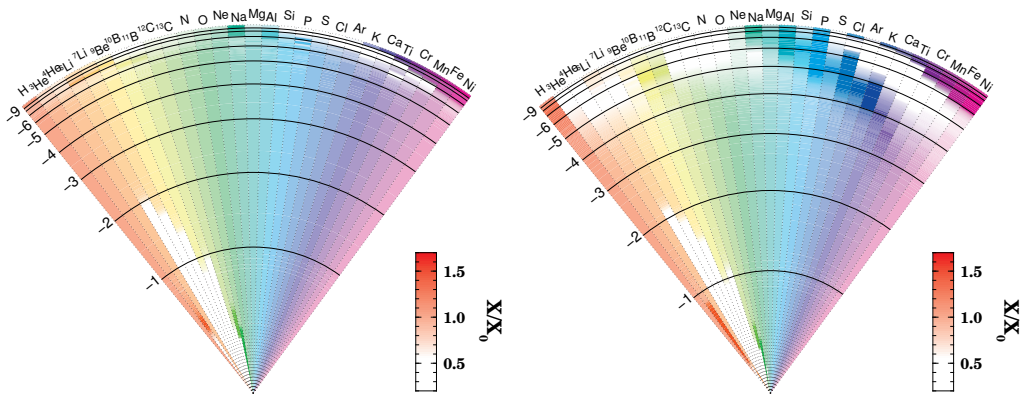

FIG. 1.1 – Concentration relative de plusieurs espèces chimiques dans l'intérieur d'un modèle de 2.5 $M_\odot$ avec diffusion atomique et perte de masse à 10 Myr (gauche) et à 500 Myr (droite). Comme l'échelle est linéaire par rapport au rayon de l'étoile, nous remarquons que la stratification des éléments affecte 25–30% du rayon.

surface des étoiles Ap. La migration des éléments dépend de la compétition entre la gravité, g, qui tend à faire migrer les éléments plus lourds que H vers le centre de l'étoile, et l'accélération radiative, $g_{\rm rad}$, qui tend à pousser certains éléments vers la surface. Étant donné que chaque élément — ou plus précisément, chaque ion — a une section efficace d'absorption différente, chacun réagit différement à la radiation incidente ; certains ions sont accélérés par le flux radiatif alors que d'autres ne le sont pas. Ceci mène à une stratification radiale des éléments dans les régions convectivement stables (zones radiatives) de l'étoile (voir Fig. 1.1).

La diffusion atomique est un processus naturel et fondamental qui agit dans *toutes* les étoiles. Bien qu'elle soit davantage importante dans les régions où l'énergie est transportée par la radiation, elle agit aussi dans les zones convectivement instables[1]. La présence ou non des effets de la diffusion atomique dépend donc de l'épaisseur des zones radiatives et de la présence de processus à grande échelle qui peuvent inhiber la diffusion ou bien réduire, voire effacer, ses effets non seulement

[1]Pour un simple argument intuitif qui illustre cette constatation, nous pouvons penser à l'interface d'une zone radiative et d'une CZ ; puisqu'elle n'est pas étanche, cette "interface" serait mieux représentée par un gradient que par une discontinuité du coefficient de transport turbulent.

à la surface, mais également à l'intérieur de l'étoile. Il est donc primordial de bien cerner l'importance de la diffusion atomique et de ces processus en compétition si nous voulons bien comprendre la physique interne des étoiles. D'autre part, les effets de la diffusion atomique ne sont pas limités aux abondances en surface des étoiles ; connaître ses effets peut aussi s'avérer crucial dans les cas suivants : évaluer l'âge des amas globulaires (GC), calibrer les modèles d'atmosphères stellaires, suivre l'évolution des zones convectives, relier la composition d'étoiles du halo à la composition originelle de l'Univers, etc. Bref, pour bien comprendre plusieurs phénomènes stellaires, il est essentiel de bien cerner les effets la diffusion atomique.

1.1 Quelques principes de la diffusion atomique

La direction de la dérive d'un élément sera approximativement déterminée par la résultante entre la force gravitationnelle, orientée vers le centre de l'étoile, et la force due aux accélérations radiatives, orientée vers la surface. Naturellement, lorsque la gravité domine les accélérations radiatives, l'élément migre vers l'intérieur de l'étoile alors que dans le cas contraire, l'élément se dirige vers l'extérieur de l'étoile. Afin de déterminer la force et la direction de diffusion d'un ion, il est d'abord nécessaire de calculer avec exactitude son accélération radiative (g_{rad}). En première approximation, l'accélération radiative pour un atome A est donnée par (Richer et al. 1998) :

$$g_{\rm rad}(A) = \frac{1}{4\pi r^2}\frac{L_r^{\rm rad}}{c}\frac{\kappa_R}{X_A}\int_0^\infty \frac{\kappa_u(A)}{\kappa_u(total)}\mathcal{P}(u)du, \tag{1.1}$$

où $\mathcal{P}(u)$ est la distribution de flux normalisé d'un corps noir qui s'écrit :

$$\mathcal{P}(u) \equiv \frac{15}{4\pi^4}\frac{u^4 e^u}{(e^u-1)^2}. \tag{1.2}$$

La luminosité radiative au rayon r est $L_r^{\rm rad}$, c est la vitesse de la lumière, X_A est la fraction de masse de l'élément A, κ_R est l'opacité de Rosseland, κ_u(total) et $\kappa_u(A)$ sont respectivement l'opacité totale et la contribution de A à l'opacité totale à la fréquence u définie comme étant :

$$u \equiv h\nu/kT. \tag{1.3}$$

Tel qu'évaluée, l'Éq. [1.1] contient une contribution au g_{rad} due à la photoionisation, mais qui doit être corrigée pour la partie de la quantité de mouvement qui est transférée à l'électron éjecté (Gonzalez et al. 1995; LeBlanc et al. 2000). Nous voyons que cette équation dépend non seulement de l'abondance de l'espèce en question, mais aussi de l'abondance des autres espèces — via le terme $\frac{\kappa_u(A)}{\kappa_u(total)}$ — puisque les atomes d'autres espèces chimiques peuvent être en compétition pour les mêmes photons. Ce calcul nécessite donc des données atomiques (pour le calcul des opacités) très précises et exhaustives pour plusieurs ions et ce, à plusieurs énergies. Quelques détails sur l'approche numérique utilisée seront abordés dans la Sect. 2.3.

Ayant intégré l'Eq. [1.1] nous pouvons ensuite passer au calcul de la vitesse de diffusion. Dans les modèles évolutifs présentés dans les chapitres ultérieurs, cette vitesse est obtenue en solutionnant un réseau complexe d'équations (Burgers 1969, voir aussi Profitt & Michaud 1991). Pour permettre d'interpréter plus facilement les termes importants pour la vitesse de diffusion, nous pouvons considérer l'approximation suivante, qui donne la vitesse de diffusion de l'ion i de l'élément trace A (Aller & Chapman 1960) :

$$v_D \approx D_{ip}\left[-\frac{\partial \ln c_i}{\partial r} + \frac{A_i m_p}{kT}(g_{{\rm rad},i} - g) + \frac{Z_i m_p g}{2kT} + k_T \frac{\partial \ln T}{\partial r}\right] \tag{1.4}$$

où D_{ip} est le coefficient de diffusion de l'ion dans un gaz de protons, c est sa concentration, A_i et Z_i son nombre atomique et sa charge, k la constante de Boltzmann,

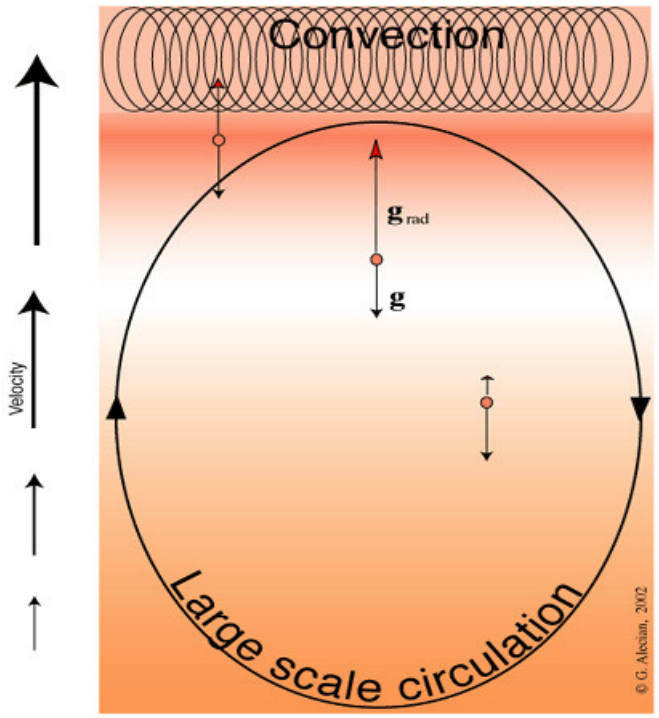

FIG. 1.2 – Illustration de l'intérieur d'une étoile CP. L'abondance en surface sera régie par l'abondance en-dessous de la SCZ qui, de son côté, est déterminée par la compétition entre g et $g_{\rm rad}$. Tel que discuté plus tard dans le texte, le transport peut être affecté par d'autres processus à grande échelle telles la circulation méridienne ou l'advection due à la perte de masse. Cette figure fut produite par G. Alecian.

T la température locale et k_T un coefficient de diffusion thermique. Notez que le premier terme de l'équation est relié à la diffusion *pure* induite par le gradient d'abondance, alors que les trois autres sont respectivement liés aux effets des accélérations radiatives et gravitationnelles, du champ électrique et, finalement, de la diffusion thermique. Nous pouvons aussi rajouter un terme lié à l'accrétion, à la perte de masse et/ou à la turbulence, ce qui sera discuté dans le Chapitre 2.

Pour une espèce donnée, la détermination des points où cette équation s'annule permet de prédire à quel endroit il y aura accumulation de l'espèce. Comme les temps caractéristiques de diffusion sont beaucoup plus longs que les temps caractéristiques de convection, les abondances sont supposées homogènes dans une zone

convective. Par conséquent, l'abondance en surface d'un certain élément dépend des positions relatives des accumulations/déficiences locales et du bas de la SCZ (voir Fig. 1.2).

1.2 Propriétés des étoiles chimiquement particulières et apparentées

Maintenant que nous avons exposé les principes généraux de la diffusion atomique, regardons de plus près certaines étoiles dans lesquelles ses effets se manifestent. Les étoiles avec anomalies d'abondances peuplent une grande partie du diagramme Hertzsprung-Russel (H–R, voir Fig. 1.3). Parmi les étoiles de Population I, les étoiles CP les plus froides ($T_{\rm eff} \sim 7000\,{\rm K}$) se situent là où la masse de la SCZ devient suffisamment petite ($\log \Delta M_{\rm BSCZ}/M_* \lesssim -5$ sur la MS) pour que les effets de la diffusion atomique deviennent assez grands pour être observables en surface. Dès $T_{\rm eff} \geq 10,000\,{\rm K}$, l'hydrogène en surface s'ionise et, en l'absence de processus de mélange telle la rotation, la SCZ peut disparaître si l'abondance d'He diminue suffisamment. Dans cette région, la diffusion atomique est très efficace puisque les temps caractéristiques de diffusion sont très courts.

Dans cette section, nous aborderons les caractéristiques principales de quatre groupes d'étoiles : les étoiles CP non magnétiques (Am, HgMn, He–PGa), les étoiles CP magnétiques (ApBp, He–Si et He–SrTi, riches en He), les étoiles de Population II et les étoiles bleues de la branche horizontale (BHB). Les naines blanches (DA, DB, DC et DO) ont quant à elles de très fortes anomalies d'abondances causées par l'effet du triage gravitationnel sur les abondances laissées par les réactions nucléaires lors de l'évolution stellaire. Mais, nous n'en discuterons pas davantage dans cette thèse.

Outre le fait que le bas de la SCZ mélange en surface de la matière arrivant de régions où la diffusion atomique est efficace[2], la principale propriété qui semble

[2]Le temps typique requis pour qu'il y ait des effets observables en surface (de l'ordre de 0.1 dex) peut varier de 1−1000 Myr pour les étoiles de Population I de la MS dont la masse varie de

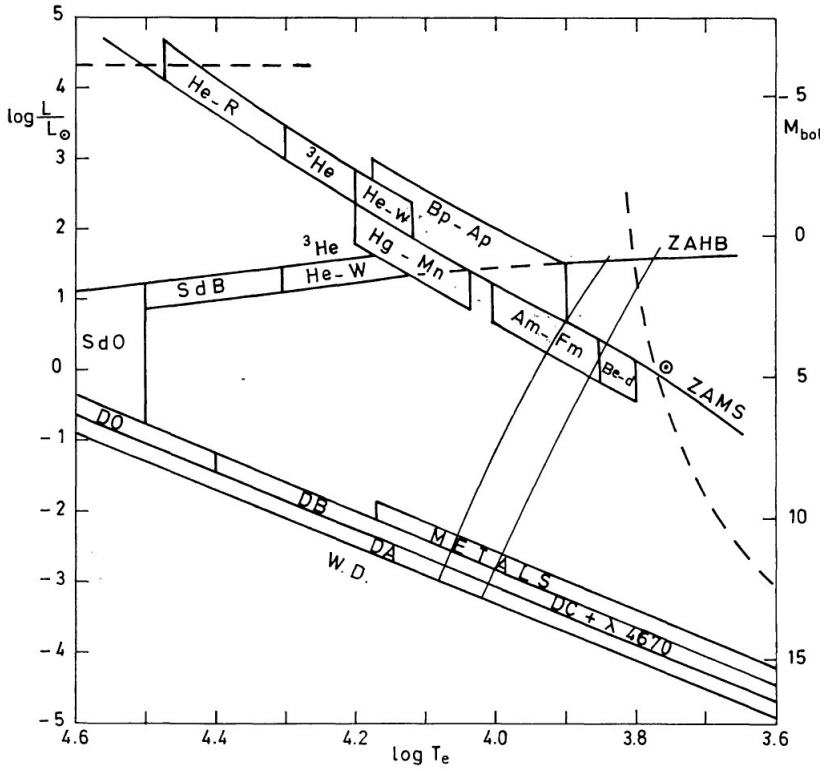

FIG. 1.3 – Diagramme H–R des étoiles CP tiré de Vauclair & Vauclair (1982). Certaines nomenclatures moins courantes : Be-d (étoiles F déficientes en Be et en Li), He-w (déficientes en He), ^{3}He (déficientes en He, mais avec un rapport isotopique ^{3}He/^{4}He élevé) et He-R (riches en He). La ligne hachurée à $M_{bol} = -6$ indique la limite supérieure au-dessus de laquelle les effets de la diffusion atomique sont effacés par de la perte de masse très forte. La bande d'instabilité traverse la ZAMS (δScuti) et la ZAHB (RR Lyrae). La ligne hachurée à la droite du diagramme indique la limite inférieure au-delà de laquelle la diffusion atomique devient moins importante.

lier toutes ces étoiles est la rotation lente ($v \sin i \lesssim 120\,\mathrm{km/s}$). Selon Abt (2000), la rotation serait le seul critère qui détermine si une étoile de type B, A ou F chaude deviendra chimiquement anormale ou non. Lorsque la rotation est lente, le mélange induit à l'intérieur de l'étoile ne permettrait pas d'effacer les effets de la diffusion atomique (Charbonneau & Michaud 1991).

$\sim$3 à 1.4 $M_\odot$, alors que 10–13 Gyr peuvent s'écouler avant que les anomalies se matérialisent en surface des étoiles de Population II.

1.2.1 Les étoiles CP non-magnétiques

Les étoiles AmFm (7000 K$< T_{\rm eff} <$ 10 000 K, Preston 1974) sont caractérisées par des surabondances d'éléments du pic du Fe qui s'élèvent à des facteurs 2-3, ainsi que des surabondances des terres rares de facteurs 5-10 (par rapport aux abondances d'étoiles de même $T_{\rm eff}$ dites normales). L'hélium, les éléments légers (LiBeB) et CNO sont généralement sousabondants de facteurs 2−3 alors que le Ca et le Sc peuvent être sousabondants de facteurs allant jusqu'à 10 (Cayrel et al. 1991). Ces caractéristiques apparaissent dans une grande majorité sinon l'ensemble des étoiles A et F de la MS ayant de faibles vitesses de rotation ($v \sin i < 100$ km/s, Abt & Morrell 1995). En général, ces étoiles se retrouvent dans des systèmes binaires à courte période de rotation (plus petite que ∼100 jours, Abt & Levy 1985). Selon Abt (2000), les faibles vitesses de rotation seraient justement expliquées par les forces de marée. Ces étoiles sont particulièrement intéressantes au point de vue théorique puisqu'elles sont relativement simples à modéliser : rotation faible et aucun champ magnétique observé (Landstreet 1982). À la limite froide des étoiles AmFm, il y a aussi les étoiles F déficientes en Li et Be (identifiées Be-d dans la Fig 1.3), dont l'exemple le plus connu est la brèche du lithium dans les Hyades (Boesgaard & Tripicco 1986).

Les étoiles HgMn (10 000 K$< T_{\rm eff} <$ 15 000 K) sont identifiées par leurs surabondances de Mn et de Hg qui, selon certaines analyses, peuvent s'élever jusqu'à 4 et 6 dex respectivement (Takada-Hidai 1991). L'hélium est généralement sousabondant alors que les éléments terres rares sont surabondants. Il y a par ailleurs des anomalies isotopiques (White et al. 1976). L'atmosphère de ces étoiles est suffisamment stable pour qu'il y ait séparation chimique (Hui-Bon-Hoa et al. 2000; Thiam et al. 2010), d'où la difficulté de construire des modèles évolutifs qui calculent la diffusion atomique pour toute l'étoile.

Les étoiles déficientes en He (He-w) de type He–PGa (14 000 K$< T_{\rm eff} <$ 20 000 K,

Norris 1971) sont marquées par de fortes surabondances de P et de Ga de 2 et 5 dex respectivement, ainsi que de fortes sousabondances de He (jusqu'à un facteur 15). Ces étoiles semblent aussi avoir une atmosphère radialement séparée (Sigut et al. 2000).

1.2.2 Les étoiles CP magnétiques

Les étoiles ApBp (7000 K$< T_{\rm eff} <$ 15 000 K) ont de forts champs magnétiques (jusqu'à 10 kG, Babcock 1958) ayant des géométries souvent complexes (Landstreet et al. 1989). Elles sont caractérisées par des sousabondances de He et d'énormes surabondances des terres rares (jusqu'à 5 dex). À l'intérieur de ce groupe, il y a aussi deux sous-ensembles (voir Ryabchikova 1991; Cowley 1993) : les étoiles Ap–Si (10 000 K$< T_{\rm eff} <$ 15 000 K) ayant de fortes surabondances de Si (jusqu'à un facteur 100) et les étoiles Ap–SrCrEu (7000 K$< T_{\rm eff} <$ 10 000 K) pour lesquelles le Si est 10 fois moins surabondant. Plusieurs observations suggèrent qu'il y a stratification dans l'atmosphère de ces étoiles (Babel 1994; Wade et al. 2001). Par ailleurs, le champ magnétique affecte certainement le transport (Alecian et al. 2007), d'où la présence de fortes *taches* d'abondances en surface (Kochukhov & Wade 2010). On questionne à la fois l'origine du champ magnétique dans ces étoiles, ainsi que le mécanisme via lequel la rotation diminue (contrairement aux Am, il y a une fraction importante des Ap qui ne sont pas binaires). L'observation de fortes anomalies d'abondance en surface d'étoiles HAeBe, les analogues PMS des ApBp, pourrait offrir des éléments de réponse et sera discuté dans le Chapitre 3.

Tout comme les étoiles He–Si et He–SrTi (14 000 K$< T_{\rm eff} <$ 20 000 K, Norris 1971), qui ont de fortes sousabondances de He accompagnées de surabondances de Si et de SrTi, les étoiles enrichies en He (He-R) sont aussi magnétiques (20 000 K$< T_{\rm eff} <$ 25 000 K). Ces dernières sont marquées par un rapport X(He)/X(H) qui varie entre 0.3 et 10.

1.2.3 Étoiles de la branche horizontale

Les étoiles de la branche horizontale (HB) plus chaudes que $T_{\rm eff} \sim 11\,000\,{\rm K}$ ont de fortes anomalies d'abondances incluant des surabondances d'un facteur 10-3000 des éléments du pic du fer, ainsi que de fortes sousabondances de He (Behr, 2003). Cette température marque aussi la transition entre les étoiles qui tournent rapidement et celles qui tournent plus lentement (Grundahl et al. 1999), ce qui les relie aux étoiles CP discutées dans les sections précédentes. Récemment, Khalack et al. (2007, 2008) ont déterminé que l'atmosphère de plusieurs étoiles BHB serait chimiquement stratifiée. Les étoiles sdB, les analogues du champ des BHB, ont aussi des anomalies d'abondances importantes en surface (Heber 2009), bien qu'il y ait plus d'incertitude puisque nous ne connaissons pas leurs abondances initiales ou leur passé évolutif.

1.2.4 Étoiles de Population II

Contrairement aux étoiles CP, les étoiles de Population II toujours présentes dans notre galaxie ont des SCZ relativement profondes ($\log \Delta M/M_* \gtrsim -4.5$). Par contre, puisque leur évolution sur la MS est plus longue (10–13 Gyr), la séparation chimique qui se déroule sous la SCZ a le temps de se développer. Le bénéfice principal d'étudier ces étoiles vieilles est de faire le lien avec l'abondance primordiale de lithium. D'autant plus que la précision des nouvelles mesures du CMB (*Cosmic Microwave Background*) a renouvelé l'intérêt pour l'étude de ces vieilles étoiles. L'analyse des observations de *WMAP* de l'anisotropie du rayonnement fossile a d'ailleurs contraint l'abondance primordiale du Li à $A(^7{\rm Li}) = 2.65 \pm 0.05$ (Cyburt et al. 2003; Steigman 2007). Par contre, Cyburt et al. (2008) ont récemment révisé cette valeur à la hausse en suggérant une abondance primordiale de $A(^7{\rm Li}) = 2.72 \pm 0.05$.

Le problème, c'est que l'abondance moyenne du Li observée dans les vieilles

étoiles de faible métallicité du halo galactique ($5500 \leq T_{\rm eff} \leq 6200\,{\rm K}$, $[{\rm Fe/H}] \leq -1.5$) est 3 fois plus petite que cette valeur (Ryan et al. 1999). De plus, cette abondance moyenne semble indépendante de la $T_{\rm eff}$ (Fig. 1.4). Ce phénomène, communément appelé le *plateau Spite*, pose une contrainte importante à la solution proposée.

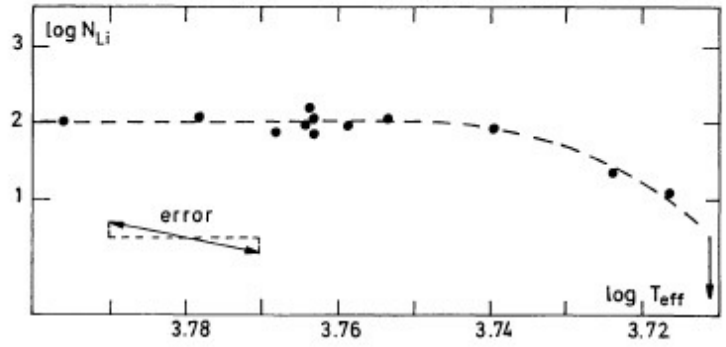

FIG. 1.4 – Figure de Spite & Spite (1982) montrant le *plateau* du ^{7}Li pour les étoiles naines du halo galactique.

Le problème serait, potentiellement, davantage compliqué si les résultats de Asplund et al. (2006) étaient confirmés. Ces derniers croient avoir déterminé une abondance inattendue de ^{6}Li dans 24 naines du halo — bien que ces observations poussent les limites de la signification d'une détection (majoritairement à 2σ ou moins). Néanmoins, plusieurs résultats concordent bien avec les détections préalables (Smith et al. 1998; Cayrel et al. 1999; Nissen et al. 2000) et ils suggèrent même la présence d'un plateau similaire à celui du ^{7}Li (voir Fig. 1.5). Contrairement au cas de l'isotope plus lourd, le plateau de ^{6}Li indique une abondance nettement plus élevée — quelques ordres de grandeur — que 10^{-5}, soit la valeur primordiale prédite par les modèles de nucléosynthèse du Big Bang. Malheureusement, la synthèse du ^{6}Li via les réactions de spallation par des rayons cosmiques et les réactions de fusion $\alpha + \alpha$ dans le milieu interstellaire du jeune Univers ne sont pas suffisantes

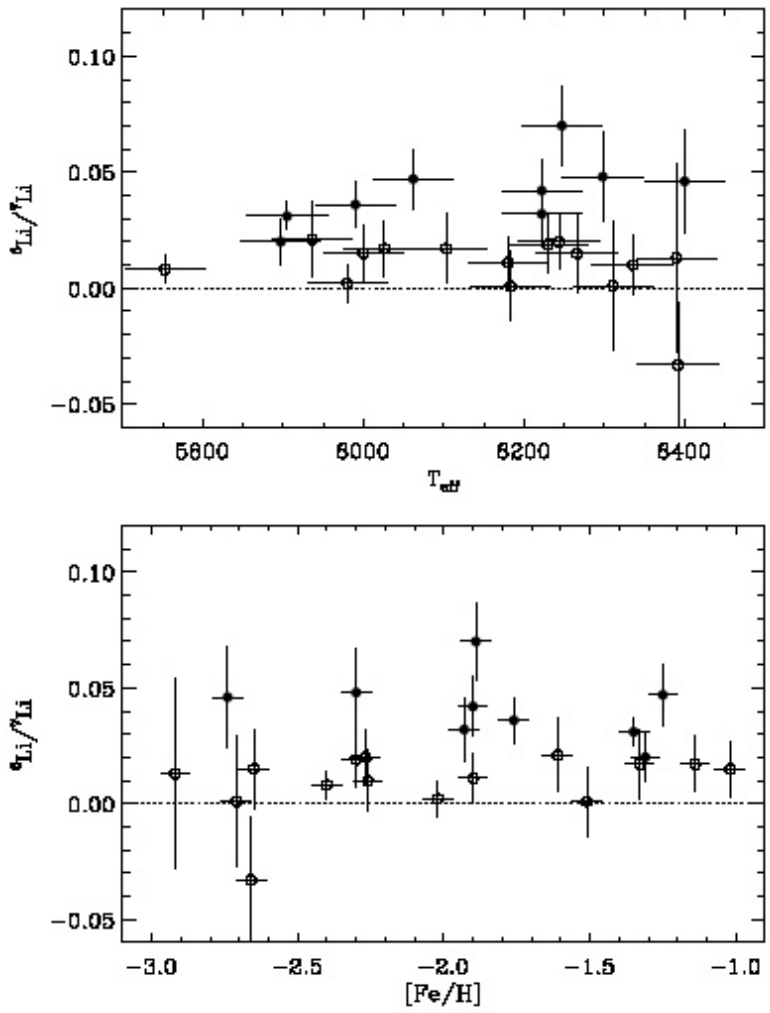

FIG. 1.5 – Ratio ^{6}Li/^{7}Li dérivé par Asplund et al. (2006) par rapport à $T_{\rm eff}$ (en haut) et [Fe/H] (en bas). Les détections à un niveau supérieur à 2σ sont représentées par des cercles remplis et les non-détections par des cercles ouverts.

pour expliquer cet écart (voir Asplund et al. 2006). L'origine du ^{6}Li demeure donc inconnue, et sa présence en surface des étoiles de Population II apporterait une contrainte importante sur les solutions envisagées pour expliquer l'abondance du ^{7}Li, puisque la section efficace de destruction par réactions thermonucléaires du ^{6}Li est 60 fois plus grande que celle du ^{7}Li. Par conséquent, les scénarios proposés doivent peu mélanger la surface aux régions chaudes de l'enveloppe où le Li est dé-

truit (ce qui diluerait considérablement la quantité de ^{6}Li détectée en surface). Cela étant dit, ces observations de ^{6}Li sont très incertaines, voire même complètement remises en question (Cayrel et al. 2007).

1.2.5 Les étoiles CP des amas et du champ : des observations aux modèles

La confrontation des observations aux prédictions des modèles évolutifs n'est pas triviale. Il faut d'ailleurs connaître plusieurs paramètres tels la masse et la composition chimique initiale avant de pouvoir faire la comparaison. Or, la détermination de l'âge, de la masse et de la composition chimique est parfois difficile. En général, l'âge d'une étoile est déterminée à partir de sa position dans le diagramme H–R.

Les étoiles d'amas sont idéales puisque même si nous ne connaissons pas très bien la distance de l'amas, nous pouvons tout de même construire un diagramme H–R à partir du flux de plusieurs centaines d'étoiles, permettant ainsi de déterminer leur âge à partir des étoiles dans lesquels l'hydrogène vient de s'épuiser dans le coeur (les étoiles du *turnoff*). Cela nous donne aussi une bonne idée de la masse des étoiles. Finalement, nous pouvons déterminer leur composition chimique initiale à partir des étoiles de type G de l'amas (voir aussi Sect. 2.7)[3].

Quant aux étoiles multiples, les modulations du spectre de lumière intégré reliées à la rotation de systèmes binaires nous donnent des informations sur la masse individuelle des deux objets et parfois même leur masse exacte (voir Chapitre 7, Carroll & Ostlie 1996). Aussi, puisque les étoiles de systèmes multiples ont, habituellement, le même âge et la même composition initiale, la comparaison de leur composition chimique peut donner des informations sur les processus internes (voir Sects. 2.7.1 et 3.4). Par ailleurs, la masse peut être bien contrainte à partir des

[3]Cela n'est toutefois pas le cas pour tous les éléments. Pour LiBeB, la destruction nucléaire est plus grande dans les étoiles G froides que dans les étoiles F et A.

effets de la rotation autour du centre de masse sur le spectre de lumière intégré, tel le cas de Sirius A et *o*Leonis.

Le grand avantage des étoiles du champ est qu'il en existe habituellement de bien plus brillantes que les étoiles semblables d'amas, ce qui permet d'obtenir des observations plus précises. Par contre, les étoiles individuelles du champ ne sont pas idéales puisque nous ne connaissons ni l'âge, ni les abondances initiales[4]. Malgré cela, pour le lithium dans les étoiles à faible métallicité, dont l'abondance initiale ne dépend pas de l'abondance des autres métaux, mais plutôt de la production du Big Bang, des observations de bonne qualité telles celles d'étoiles du halo galactique sont tout de même contraignantes (voir Sect. 4.1). Par ailleurs, pour cet élément — ainsi que tout autre élément peu abondant — l'abondance est trop petite pour conduire à des effets de saturation dans les raies ; la connaissance de l'abondance initiale n'est donc pas importante pour le calcul de la diffusion atomique (i.e. la non-linéarité du problème est réduite) et l'abondance initiale peut être ajustée sans trop affecter la solution. Cela n'est toutefois pas l'idéal puisque nous ne connaissons pas très bien les abondances initiales des autres éléments, tels Fe et He, qui peuvent conduire à des effets évolutifs qui, à leur tour, affectent l'abondance en surface du Li.

1.3 Quelques modèles d'étoiles CP

Tel qu'expliqué préalablement, la séparation chimique via la diffusion atomique joue un rôle déterminant dans l'explication du phénomène CP. Néanmoins, pour les AmFm et les étoiles de Population II en particulier, les modèles qui n'incluent que la diffusion atomique mènent à des anomalies d'abondances en surface qui surpassent, parfois considérablement, les anomalies observées (voir Turcotte et al. 1998a pour les AmFm et Richard et al. 2002b pour les étoiles de Population II). Il s'ensuit alors

[4]Parfois, le voisinage d'une étoile peut nous donner une idée de la composition initiale (e.g. le voisinage solaire).

qu'au moins un processus macroscopique à grande échelle réduit les effets de la séparation chimique. Les processus considérés incluent la rotation — qui peut être modélisée sous forme de circulation méridienne en 2 ou 3D (Tassoul & Tassoul 1982; Charbonneau & Michaud 1988, 1991; Théado & Vauclair 2003; Quievy et al. 2009) ou d'une diffusion turbulente en 1D (Pinsonneault et al. 1989; Zahn 1992; Talon & Charbonnel 1998; Palacios et al. 2003; Talon et al. 2006)— l'accrétion (Turcotte & Charbonneau 1993), les ondes de gravité (Talon & Charbonnel 2003, 2004, 2005; Charbonnel & Talon 2005) et la perte de masse (voir prochaines sections).

Les modèles avec turbulence du groupe de Montréal permettent d'expliquer non seulement les étoiles AmFm (Richer et al. 2000; Richard et al. 2001), mais aussi les étoiles de Population II (Richard et al. 2002a,b, 2005) et les étoiles BHB (Michaud et al. 2007, 2008). Or, à l'aide d'un seul paramètre effectif pour chaque type d'étoile, ce modèle avec diffusion atomique explique des étoiles un peu partout dans le diagramme H–R. L'origine de ce mélange turbulent n'est pas spécifié bien qu'il pourrait, par exemple, s'apparenter aux effets de la rotation ou des ondes de gravité (voir Talon et al. 2006).

Jusqu'à présent, les modèles d'étoiles CP avec perte de masse se sont surtout limités à des cas statiques ou bien à des cas où les effets des accélérations radiatives n'étaient pas considérés. Puisqu'il s'agit du principal intérêt de ce projet de recherche, regardons de plus près les modèles avec perte de masse d'étoiles AmFm et de Population II.

1.3.1 Modèles AmFm avec perte de masse

Pour une étoile de masse M_*, la conservation de la masse implique que l'effet net d'une perte de masse $\dot{M}$ ayant une symétrie sphérique est l'introduction d'un terme advectif v_w dirigé radialement vers l'extérieur, de la forme :

$$v_w(r) = -\frac{\dot{M}}{4\pi r^2 \rho}\frac{m_r}{M_*} \tag{1.5}$$

où ρ est la densité locale du plasma et m_r est la masse à l'intérieur de la coquille sphérique de rayon r. Un élément trace qui diffuse en présence de perte de masse doit donc satisfaire l'équation de conservation :

$$N_H \frac{\partial c}{\partial t} = -\nabla \cdot [c N_H (\mathbf{v}_w + \mathbf{v}_D)] \tag{1.6}$$

où N_H est la somme des densités de protons et d'hydrogène neutre, c est l'abondance par rapport à l'abondance de nucléons et $\mathbf{v}_D$ est la vitesse de diffusion (obtenue en solutionnant les équations de Burgers). À partir de cette équation, nous constatons que l'effet de la perte de masse sur les abondances dépend de la relation entre $\mathbf{v}_D$ et $\mathbf{v}_w$.

Pour les éléments qui diffusent naturellement vers l'intérieur ($g_{rad} < g$), l'abondance en surface sera déterminée par la relation entre la vitesse de triage (ou de *settling*) v_{sett} et v_w. Puisque v_{sett} varie comme $\rho^{-1}T^{1.5}$ (dépendance thermique du coefficient de diffusion) et que la vitesse du vent varie comme ρ^{-1}, le rapport v_{sett}/v_w augmente vers l'intérieur de l'étoile. Ainsi, plus la perte de masse est importante, plus le point où $v_{sett} = v_w$ est profond dans l'étoile. Il s'ensuit alors que l'augmentation du taux de perte de masse mène à une diminution des anomalies causées par le triage gravitationnel puisque v_{sett} devient plus faible à mesure que l'on s'enfonce dans l'étoile.

Pour les éléments naturellement supportés par le flux radiatif ($g_{rad} > g$ jusqu'à la base de la SCZ), la perte de masse expulsera par la surface de l'étoile les éléments accumulés dans la SCZ, réduisant ainsi les surabondances. Pour illustrer ce mécanisme d'évacuation des surabondances, prenons un modèle analytique très simplifié qui considère l'abondance dans la zone convective d'un élément qui s'y accumule. Pour simplifier, nous supposons que la convection s'étend jusqu'en surface et que la masse évacuée a la même composition que la SCZ. Par conséquent,

lorsque l'équilibre est atteint, la conservation de la masse permet d'écrire :

$$X_{\rm SCZ}\,\rho_{\rm SCZ}\,v_{w,\,\rm SCZ} = X_{\rm BSCZ}\,\rho_{\rm BSCZ}(v_{D,\,\rm BSCZ} + v_{w\,,\,\rm BSCZ}) \tag{1.7}$$

où $X_{\rm SCZ}$ est la fraction de masse dans la SCZ, $X_{\rm BSCZ}$ est la fraction de masse immédiatement en dessous (au *bas*) de la SCZ et ρ est la densité. Alors si nous comparons des modèles avec des taux de perte de masse différents, mais ayant les conditions initiales identiques (i.e. densité, abondances et vitesse de diffusion), la solution pour $X_{\rm SCZ}$ se réduit à étudier le comportement d'une simple fonction de la forme $(1{+}x)/x$; plus grande est la vitesse du vent plus petites seront les anomalies. Évidemment, il s'agit d'un cas limite qui suppose l'équilibre, mais l'essentiel est de comprendre que l'augmentation de la perte de masse diminue les surabondances en surface. Le tout sera expliqué davantage dans les chapitres ultérieurs.

Plusieurs modèles statiques avec perte de masse ont exploré ses effets pour un nombre restreint d'espèces (Michaud et al., 1983; Michaud & Charland, 1986; Alecian, 1996; LeBlanc & Alecian, 2008). Michaud et al. (1983) a montré qu'une perte de masse de $\dot{M} = 10^{-15}\,{\rm M}_\odot{\rm yr}^{-1}$ permet de réduire les surabondances prédites par un modèle de diffusion atomique pure de facteurs $10^3 - 10^4$ à des facteurs d'environ 30 et qu'un taux de perte de masse $\dot{M} = 10^{-13}\,{\rm M}_\odot{\rm yr}^{-1}$ diminue trop les surabondances par rapport aux niveaux observés (voir Fig. 1.6). Par ailleurs, les sousabondances de Ca sont réduites à des niveaux conformes aux observations à partir d'un taux de perte de masse de $2 \times 10^{-14}\,{\rm M}_\odot{\rm yr}^{-1}$, ce qui concorde avec les résultats de Alecian (1996). Cependant, ces modèles d'enveloppe statiques ne tiennent pas compte des effets de la diffusion atomique sur la structure et on y utilise des formules approximatives pour calculer les accélérations radiatives au bas de la SCZ.

D'autres modèles avec perte de masse ont aussi été etudiés pour expliquer les abondances de lithium dans les Hyades. Schramm et al. (1990) ont avancé que des

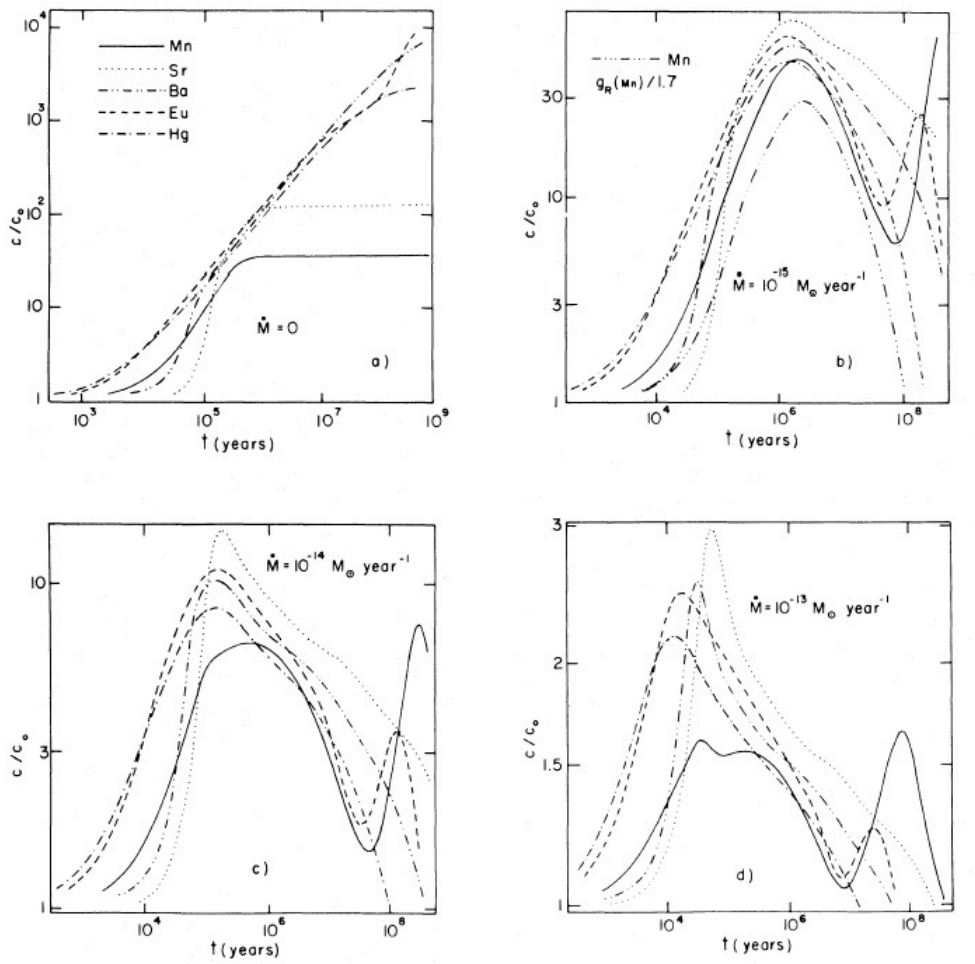

FIG. 1.6 – La variation temporelle des abondances en surface d'étoiles Am calculée pour différents taux de perte de masse. L'abondance c_0 est l'abondance initiale de l'étoile. (Michaud et al. 1983)

taux de perte de masse $\sim 10^{-10}\,\mathrm{M_\odot yr^{-1}}$ — plus de 1000 fois supérieur au taux de perte de masse solaire — générés par les pulsations dans la bande de variabilité δScuti pourraient expliquer la brèche du lithium (les étoiles ayant une $T_{\rm eff} \geq 6300\,\mathrm{K}$ dans la Fig. 1.7). Cependant, Swenson & Faulkner (1992) ont démontré que des modèles avec ces mêmes taux de perte de masse, et sans diffusion atomique, ne pouvaient pas reproduire les étoiles G des Hyades (Fig. 1.7). Ni l'un ni l'autre de ces deux modèles ne traite les effets de la diffusion atomique.

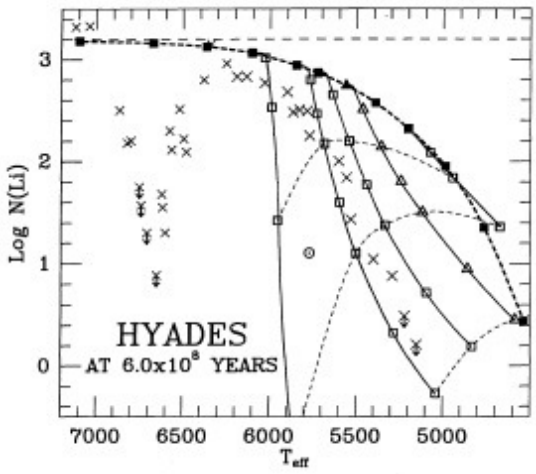

FIG. 1.7 – Les symboles pleins représentent des modèles sans perte de masse alors que les symboles vides représentent des modèles avec perte de masse. Les lignes continues lient les modèles de même masse (1.2, 1.1, 1.05, 1.0 et 0.9 $M_\odot$ de gauche à droite) alors que les lignes pointillées lient des modèles ayant la même perte de masse (1, 2 et 4×10^{-10} $M_\odot yr^{-1}$ du haut vers le bas). Pour expliquer les observations, toutes les étoiles G des Hyades auraient eu une masse initiale similaire ($\sim 1.08\,M_\odot$) tout en ayant des taux de perte de masse différents, ce qui est peu probable. La figure est tirée de Swenson & Faulkner (1992).

Il est donc clair que des modèles plus détaillés sont nécessaires pour mieux comprendre les effets de la perte de masse. En effet, les abondances en surface dépendent d'un réseau compliqué d'équations de transport des éléments qui tout en subissant les effets d'une structure en évolution doit en tout temps obéir aux lois de conservation. De plus, les accélérations radiatives et, par conséquent, la diffusion atomique varient non-linéairement avec les abondances. En somme, le problème devient des plus complexe et requiert une quantité importante de données atomiques précises (forces d'oscillateurs et niveaux d'énergie de tous les états d'ionisation).

Ce genre de modélisation détaillée est maintenant possible grâce aux banques de données atomiques OPACITY (Seaton et al. 1994) et OPAL (Iglesias & Rogers 1996) qui fournissent des données pour plusieurs éléments à de très hautes énergies. Dans le Chapitre 2, ce type de modèle sera présenté et comparé aux observations

récentes d'étoiles AmFm. Dans le Chapitre 3, ces mêmes modèles, sans champ magnétique, seront comparés aux observations d'étoiles binaires HAeBe. Bien qu'il existe des modèles simples explorant l'interaction entre le champ magnétique et la perte de masse (Babel 1994, 1995; Théado et al. 2005), aller plus loin exigerait des modèles impliquant plusieurs paramètres. Pour s'assurer de bien cerner les effets liés à la perte de masse, nous nous limiterons au cas sans champ magnétique.

1.3.2 Modèles d'étoiles de Population II avec perte de masse

Puisque la perte de masse permettrait d'expliquer le phénomène AmFm dans les étoiles de Population I, il est raisonnable de penser qu'elle puisse également agir en surface des étoiles de Population II. Le seul modèle de Population II ayant considéré les effets de la perte de masse est celui de Vauclair & Charbonnel (1995). L'un des avantages de la perte de masse est qu'elle ne lie pas nécessairement la surface à la région où il y a brûlage du lithium. D'ailleurs, selon leurs calculs, les effets de la destruction du lithium n'apparaissent en surface que pour des taux de perte de masse $\geq 10^{-12}\,\mathrm{M_\odot yr^{-1}}$. Des taux de perte de masse entre $10^{-12}\,\mathrm{M_\odot yr^{-1}}$ et $3 \times 10^{-13}\,\mathrm{M_\odot yr^{-1}}$ permettent de réduire les effets de la diffusion atomique suffisamment pour reproduire l'invariabilité observée du lithium dans le plateau de Spite (voir Fig. 1.8). La légère dispersion des valeurs de Li à l'intérieur du plateau serait quant à elle expliquée par de petites différences intrinsèques des taux de perte de masse entre étoiles. Les auteurs trouvent par contre que l'abondance primordiale du Li serait de $A(^7\mathrm{Li}) = 2.5 \pm 0.10$, ce qui est encore 0.15 dex en deçà de l'abondance obtenue par *WMAP*. Il serait donc intéressant de reprendre ces calculs avec des modèles évolutifs plus complets, notamment au niveau des forces radiatives. Ce sera justement l'objet du Chapitre 4.

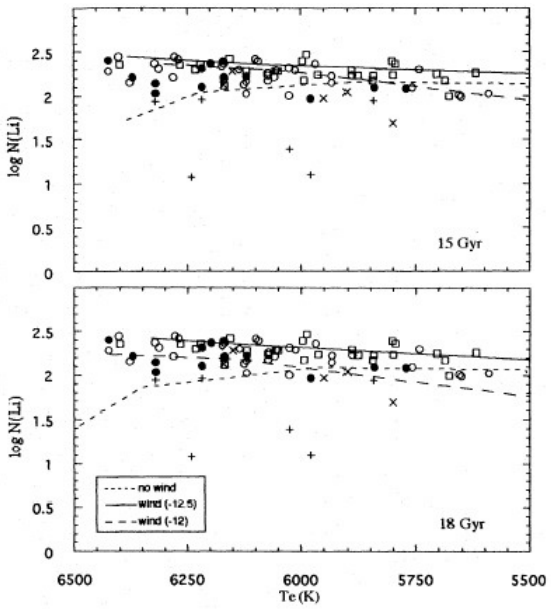

FIG. 1.8 – L'abondance de lithium par rapport à la $T_{\rm eff}$. La ligne pointillée montre l'évolution d'un modèle sans perte de masse alors que la ligne continue et la ligne cassée représentent des modèles ayant de taux de perte de masse de $10^{-12}\,{\rm M}_{\odot}{\rm yr}^{-1}$ et $10^{-12.5}\,{\rm M}_{\odot}{\rm yr}^{-1}$ respectivement. Les prédictions sont montrées pour deux âges. Les observations sont montrés pour plusieurs métallicités identifiées par des symboles différents. Les (+) représentent des limites supérieures et les (×) représentent des binaires.

1.3.3 Modèles d'étoiles riches en He et roAp avec perte de masse

Vauclair (1975) suggère que le triage gravitationnel de l'hélium couplé à une perte de masse de l'ordre de $10^{-12}\,{\rm M}_{\odot}{\rm yr}^{-1}$ permettrait d'expliquer l'enrichissement d'He en surface de certaines étoiles magnétiques B (He-R dans la Fig. 1.3). Le flux interne dû à la perte de masse permettrait de traîner l'hélium ionisé jusque dans des régions superficielles où il est neutre. Il ne s'échapperait pas de l'étoile puisque les collisions (qui provoquent l'entraînement) sont 50 fois moins efficaces lorsque l'hélium est neutre.

Les observations de Kurtz (1982), menant à la découverte des étoiles roAp (*rapidly oscillating* Ap), ont permis de contraindre davantage ce modèle dans la

mesure où les roAp seraient les analogues plus froides des étoiles B enrichies en hélium ; le réservoir d'hélium neutre causé par la perte de masse serait simplement trop profond pour l'observation directe, bien qu'il serait tout de même à l'origine des pulsations. Vauclair et al. (1991) et Balmforth et al. (2001) ont avancé des modèles similaires, où l'interaction entre le champ magnétique fort et la perte de masse expliquerait les inhomogénéités importantes de l'abondance d'hélium superficielle entre les pôles (sousabondant de facteurs $\sim 2-3$) et l'équateur (à peu près normal). Les taux de perte de masse impliqués seraient à peu près 10 fois supérieurs au taux de perte de masse solaire. Dans ces calculs, seule la diffusion de l'hélium est considérée.

En utilisant l'émission en X de l'étoile IQ Aur (A0p) comme contrainte, les modèles de vent de Babel & Montmerle (1997) suggèrent que cette étoile A chaude devait avoir un taux de perte de masse de l'ordre de $5 \times 10^{-11}\,\mathrm{M_{\odot}yr^{-1}}$ qui serait généré par le flux radiatif et qui, en plus, serait confiné par le fort champ magnétique. Townsend & Owocki (2005) ont élaboré un modèle de vent radiatif similaire pour ce même type d'étoiles. Ce modèle, dans lequel le matériel ejecté est confiné par le champ magnétique et est conséquemment pris dans un puits de potentiel en rotation rigide autour de l'étoile, permettrait d'expliquer les phases rotationnelles des courbes de lumière des étoiles Bp chaudes telles σOri E.

Récemment, Unglaub (2008) s'est intéressé aux vents en surface d'étoiles sdB et des naines blanches chaudes.

1.4 Les processus d'accélérations de la perte de masse

Pour bien interpréter les résultats des modèles avec perte de masse, il faudrait d'abord arriver à connaître la nature des vents que nous tentons de modéliser. Malheureusement, les étoiles A et F se situent dans une région du diagramme H–R pour laquelle la perte de masse n'est pas bien comprise. C'est aussi le cas pour les

étoiles de Population II qui ont des $T_{\rm eff}$ comparables aux étoiles F froides. Bref, les étoiles pour lesquelles la séparation chimique peut jouer le plus se retrouvent entre deux groupes pour lesquels les processus d'accélération des vents sont probablement identifiés. Plus précisément, les observateurs et les théoriciens s'entendent pour dire que les étoiles chaudes (O et B) ont des vents accélérés par la pression de radiation et que les étoiles plus froides (G et K) ont des vents accélérés thermiquement. Il reste donc quelques questions : Est-ce que les vents en surface d'étoiles A et F (et de Population II) sont accélérés par les mêmes processus ? Si oui, où exactement, en terme de la $T_{\rm eff}$, se trouve la délimitation entre vents radiatifs et thermiques ? Si non, quel est le processus responsable ? Les sections qui suivent tenteront d'évaluer l'état de ces interrogations. Nous aborderons en particulier les caractéristiques des vents radiatifs et des vents thermiques (aussi désignés vents coronaux) pour ensuite faire le pont avec les observations.

1.4.1 Vents radiatifs

La théorie des vents accélérés par la radiation remonte à Castor et al. (1975). Cette théorie, dénommée CAK, est axée sur le fait que les étoiles chaudes émettent majoritairement dans l'ultraviolet, là où les couches externes des étoiles possèdent énormément de raies. Or, l'absorption via les raies est significativement plus importante que l'absorption dans le continu. Par exemple, l'opacité de la raie de résonance du C IV est 10^6 fois plus grande que l'opacité due à la diffusion (*scattering*) des électrons (Lamers & Cassinelli 1999). Mais, l'effet Doppler joue aussi un role important dans la génération de vents stellaires radiatifs. Sans lui, la radiation émise par la photosphère serait vite atténuée par les raies très opaques du bas de l'atmosphère. D'ailleurs, le flux radiatif dans la photosphère, réduit aux fréquences de résonance au repos des raies fortes, ne serait pas suffisant pour contrer le potentiel gravitationnel.

En effet, lorsque les couches au-dessus de la photosphère sont en expansion,

les ions dans ces couches voient la radiation émanant de la photosphère comme étant décalée vers le rouge et, pour une raie donnée, absorbent des photons plus énergétiques — qui ne sont pas atténués par les raies des couches statiques sous-jacentes. Dans le cas simplifié d'une raie parfaitement opaque centrée à ν_0, tous les photons ayant une fréquence entre ν_0 et $\nu_0(1 + v_\infty/c)$ seraient absorbés (voir Fig. 1.9), où v_∞ est la vitesse terminale du vent. Puisque pour les étoiles chaudes le

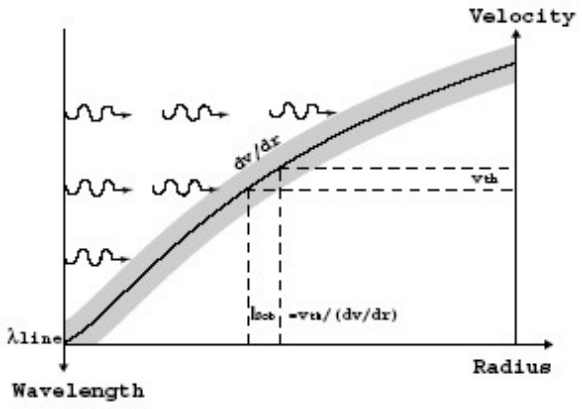

FIG. 1.9 – Cette figure illustre l'absorption de photons par une seule raie se déplaçant à la vitesse du vent. La zone grise montre la largeur de la raie (élargissement thermique). Les photons plus énergétiques que la raie au repos peuvent voyager librement jusqu'à ce qu'ils soient suffisamment décalés pour être absorbés. La figure est tirée de Owocki & Murdin (2000).

pic du spectre de corps noir se produit dans l'UV, là où se trouvent plusieurs raies métalliques fortes, une quantité très importante de flux est absorbée ; la quantité de mouvement transférée par les photons vers les ions est donc suffisante pour expulser ces derniers de l'étoile. Ainsi, nous constatons pourquoi ce mécanisme est si efficace en tant que générateur de vents stellaires dans les étoiles chaudes.

Dans le modèle CAK, le transfert de quantité de mouvement ne se limite pas aux ions absorbants. En effet, le ralentissement via le couplage de Coulomb assure le partage de la quantité de mouvement entre les ions lourds et les principaux constituants du vent : les protons, les électrons et les ions de He. Ce couplage est

simplement lié à l'interaction coulombienne entre particules chargées. Ce processus mène à des vents non-séparés —ayant les mêmes abondances que la photosphère — voyageant uniformément. Une condition importante pour que le couplage de Coulomb soit efficace est que le temps caractéristique de ralentissement t_s soit inférieur au temps nécessaire pour que les ions absorbants atteignent une vitesse importante par rapport au milieu ambiant. Le temps t_d est défini comme étant le temps requis pour que l'accélération radiative entraîne l'ion à une vitesse égale à la vitesse thermique v_{th} des particules ambiantes :

$$t_d = \frac{v_{th}}{g_i} \tag{1.8}$$

où g_i est l'accélération de l'ion absorbant. La condition $t_s < t_d$ est satisfaite pour les étoiles O et B précoces. Cependant pour les étoiles plus froides telles les étoiles A, ce n'est pas nécessairement le cas. D'ailleurs, Babel (1995) montre que le vent en surface d'une étoile A de $T_{\rm eff} = 10\,000\,\mathrm{K}$ serait complètement séparé puisque le couplage de Coulomb ne serait pas suffisamment efficace pour entraîner les espèces les plus abondantes (H et He en particulier). Selon ses calculs, puisque :

$$g^{tot}_{rad,max} < g < g^{Z}_{rad,max} \tag{1.9}$$

où $g^{tot}_{rad,max}$ est l'accélération radiative maximale sur tous les éléments à la fois, alors que $g^{Z}_{rad,max}$ est la valeur maximale pour un élément donné Z, certains métaux sont expulsés par une pression radiative supérieure à la gravité, bien que l'accélération radiative intégrée ne permet pas de contrer la gravité pour l'ensemble des espèces. Nous reprendrons cette discussion dans la Sect. 2.4.2.

Les observations de ce type de vent donnent les valeurs typiques : $1000 \leq v_\infty \leq 3000\,\mathrm{km/s}$ et $10^{-8} \leq \dot{M} \leq 10^{-4}\,\mathrm{M_\odot yr^{-1}}$, où la perte de masse la plus forte est associée aux étoiles Wolf-Rayet (Lamers & Cassinelli 1999).

1.4.2 Vents coronaux

Un vent coronal est accéléré par la pression thermique dans le gaz extrêmement chaud (10^6 K) de la couronne (Parker 1958). Évidemment, la présence d'une couronne est essentielle au fonctionnement de ce mécanisme. Les grandes températures retrouvées dans la couronne sont engendrées par la dissipation d'énergie mécanique ou la reconnection de lignes magnétiques émanant de la zone convective d'étoiles non-dégénérées d'environ 6500 K et moins. La signature par excellence du réchauffement de la couronne est l'émission en X. Bien que des rayons X émanant de plusieurs étoiles froides (F et G par exemple) ont été observés, un seul taux de perte de masse de ce type a été mesuré, soit le taux solaire ($\sim 2 \times 10^{-14}\,\mathrm{M_\odot yr^{-1}}$, Feldman et al. 1977) — ce qui est nettement inférieur aux taux mesurés associés aux vents radiatifs.

Puisqu'on observe des chromosphères en surface d'étoiles de type A7 (Neff & Simon 2008), il n'est pas inconcevable que des étoiles de type A n'ayant que de petites SCZ puissent générer des vents de types coronaux.

1.5 Techniques observationnelles directes

Pourquoi les mesures directes de perte de masse reliée aux étoiles de types A et F et de Population II sont-elles quasi-inexistantes ? Cela ne reflète pas un manque d'intérêt de la part des observateurs, mais démontre plutôt les difficultés rencontrées lors de la détection de ces vents qui, selon les modèles théoriques, seraient relativement faibles et presque impossibles à mesurer. Néanmoins, il existe plusieurs méthodes aptes à identifier la présence de vents stellaires.

Les méthodes par lesquelles on mesure des vents stellaires varient beaucoup selon la nature du vent. Certaines reposent sur la mesure d'asymétries dans les raies spectrales, alors que d'autres s'attachent au flux du continu. Les raies formées dans le vent sont discernables par rapport aux raies émanant de la photosphère

en raison du décalage Doppler provoqué par le mouvement advectif du gaz dans le vent. Cependant, cette identification n'est pas toujours évidente étant donné la myriade de facteurs qui peuvent affecter ces raies (effet Stark, mouvements turbulents, absorption/émission dans la photosphère, etc). Les raies du vent peuvent apparaître en absorption, en émission ou parfois dans une combinaison des deux. Voici quelques méthodes qui pourraient permettre de mesurer les vents en surface d'étoiles A, F et de Population II.

1.5.1 Asymétries dans les raies en absorption

Les raies de résonance d'ions abondants pourraient permettre de détecter la présence de vents stellaires faibles. Pour les étoiles de type A, les raies de résonance

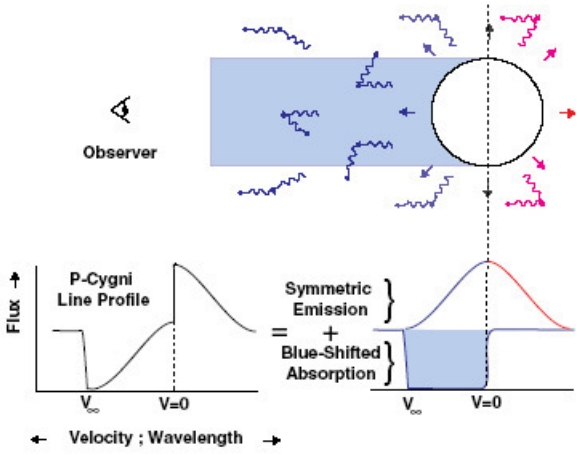

FIG. 1.10 – Illustration de la formation d'un profil P Cygni. La partie du vent dans la ligne de visée absorbe la radiation décalée vers le bleu alors que de la radiation diffusée par les autres parties du vent est réémise dans toutes les directions. La figure est tirée de Owocki & Murdin (2000).

typiques utilisées sont celles de C II, de Mg II et de Fe II dans la région UV du spectre de radiation (Lamers & Cassinelli 1999). S'il y a un vent en surface de l'étoile observée, ces raies auront un profil particulier désigné P Cygni (voir Fig. 1.10). Le

flux radiatif à la longueur d'onde d'une raie forte quelconque est premièrement réduit dans la photosphère. La partie du vent qui se déplace vers l'observateur absorbe ensuite la radiation un peu plus énergétique puisque la radiation sortant de l'atmosphère est décalée dans le référentiel du vent. Cela explique le profil en absorption décalé vers le bleu. Par contre, il y a aussi de la diffusion dans les parties à l'extérieur de la ligne de visée. La radiation y est diffusée dans toutes les directions et par conséquent dans la ligne de visée de l'observateur. Ceci produit une raie en émission centrée à la vitesse de repos de l'étoile avec un décalage entre -v_∞ et v_∞. Le profil net résultant est donc asymétrique avec une partie en absorption décalée vers le bleu et une partie en émission décalée vers le rouge. La longueur d'onde associée à la limite bleue du profil donne une bonne indication de la vitesse terminale du vent.

1.5.2 Raies en émission

Les raies en émission sont aussi un bon indicateur de la présence d'un vent stellaire, notamment pour les pertes de masses fortes de l'ordre de $10^{-5} - 10^{-6}\,\mathrm{M_\odot yr^{-1}}$. L'exemple le plus connu d'une raie en émission est la raie Hα ($\lambda = 6562\,$Å). Ces raies sont formées suite à la recombinaison d'ions avec des électrons, par la désexcitation de l'ion résultant. La forme du vent peut être étudiée avec ces raies parce que l'émissivité est proportionnelle au carré de la densité ; les raies émaneront principalement des couches plus denses du vent (près de la surface de l'étoile). L'avantage de cette raie en particulier est qu'elle peut être observée à partir du sol.

1.5.3 Émission continue

Un excès de radiation dans le proche IR et le domaine radio est émis par les vents stellaires ionisés. Cet excès est mesuré relativement au continu de la photosphère. Cette radiation est causée par l'émission libre-libre (Bremsstrahlung), c'est-à-dire la décélération d'un ion par *collision* avec un autre ion ou un électron. Cette radiation

est surtout observée dans les vents très chauds. Cette mesure à elle seule ne peut pas fournir de l'information au niveau de la vitesse du vent puisque l'analyse Doppler ne peut être effectuée. Elle peut tout de même permettre de construire la structure du vent en terme de la densité et de la température.

1.5.4 Technique indirecte pour vents du type solaire

Récemment, une nouvelle méthode indirecte a été développée dans le but de détecter des taux de perte de masse de l'ordre du taux solaire. À partir du *Hubble Space Telescope* (HST), Wood et al. (2002, 2005) ont utilisé des spectres à haute résolution des raies H I Lyα d'étoiles proches pour tenter de cerner les propriétés de ce qu'ils dénomment l'*astrosphère*. Cette astrosphère décrit l'interaction d'un vent totalement ionisé avec la matière interstellaire locale (LISM) partiellement ionisée, qui résulte en un *mur* d'hydrogène neutre dense et chaud ($T_{\rm eff} \sim 30\,000\,{\rm K}$) comparativement au LISM plutôt froid ($T_{\rm eff} \sim 8000\,{\rm K}$). Par conséquent, une composante d'absorption apparaît dans la partie bleue de la raie H I Lyα. À l'aide d'une relation entre la densité du *mur* d'hydrogène et du taux de perte de masse, qui est calibrée à partir de l'héliosphère, ils obtiennent des taux de perte de masse de 0.15 à 100 fois le taux solaire pour des étoiles de types G et K de la MS. L'incertitude demeure tout de même très grande due, entre autres, à l'incertitude des modèles hydrodynamiques du vent solaire et de l'héliosphère (Cranmer 2008). Le calcul de modèles de vents coronaux nécessite une meilleure compréhension des processus impliqués dans le réchauffement de la chromosphère et de la couronne. Les processus favorisés incluent la dissipation d'ondes sonores et la dissipation d'ondes magnétohydrodynamiques.

1.6 Vents stellaires observés

Malgré les nombreuses techniques par lesquelles les vents stellaires peuvent être en principe mesurés, le cas des étoiles de type A, F et de Population II est particulièrement problématique. Premièrement, les techniques sont plutôt efficaces pour des vents stellaires forts provenant d'étoiles brillantes ayant des flux énergétiques importants. Par ailleurs, la physique des vents n'est pas bien connue. Est-ce que le vent est neutre ? Est-ce que le vent est ionisé ? Est-ce que l'on cherche des vents coronaux (où il y aurait de l'émission dans le X) ou des vents radiatifs ? Il est difficile de choisir la technique la plus appropriée. Voici la (courte) liste des principaux auteurs ayant "observé" des vents en surface de ces étoiles.

Brown et al. (1990) ont observé 17 étoiles A et F à partir du VLA. Ils se sont intéressés à l'émission libre-libre dans le domaine radio. Malheureusement, aucune détection n'a été obtenue. Ils ont pu toutefois établir une limite supérieure au taux de perte de masse, soit $\dot{M} < 3 \times 10^{-10}\,\mathrm{M_{\odot}yr^{-1}}$. Ils stipulent aussi que l'hydrogène dans les vents de ces étoiles serait au moins partiellement ionisé.

Lanz & Catala (1992) de leur côté se sont plutôt concentrés sur la raie d'émission Hα. Ayant obtenu des rapports signal sur bruit élevés pour 5 étoiles de type A, les auteurs espéraient déduire la perte de masse à partir des asymétries dans le profil de la raie. Par contre, puisque l'asymétrie intrinsèque due à l'effet Doppler était tellement petite (de l'ordre de 0.1 %), il était difficile d'éliminer complètement les autres contributions à l'asymétrie. Leur méthode n'a donc pas pu produire de détections, bien qu'ils aient tout de même pu établir une limite supérieure qui est $\dot{M} < 2 \times 10^{-10}\,\mathrm{M_{\odot}yr^{-1}}$. Nous notons que ces deux derniers groupes ont indépendamment obtenu des valeurs supérieures de la perte masse sensiblement égales, ce qui suggère qu'obtenir des taux plus petits à partir de l'émission semble impossible à partir de l'instrumentation de l'époque.

Les deux techniques axées sur l'émission n'ont pas été capables de produire

une détection. Pour sa part, la recherche de profils P Cygni est une technique très efficace pour les étoiles ayant de très fort vents, mais elle est *a priori* peu pratique pour les vents plus faibles étant donné les limitations instrumentales. D'ailleurs, avant l'arrivée de l'instrument *Goddard High Resolution Spectrograph* (GHRS) monté sur le HST, l'analyse du spectre UV de ces objets n'était pas utile puisque les instruments de l'époque (tel par exemple le satellite IUE) avaient une limite de détection bien au-dessus du taux prédit pour les étoiles A et F (les spectres mesurés à partir du IUE avaient une limite de détection d'à peu près $10^{-9}\,\mathrm{M_{\odot}yr^{-1}}$).

Mais avec le GHRS, Bertin et al. (1995) ont obtenu des mesures de haute qualité des raies de résonance du Mg II et du H I pour l'étoile Sirius A (80σ dans le cas de Mg II). Leur analyse du décalage Doppler dans les raies d'absorption de Mg II et de H I a permis d'inférer un taux de perte de masse entre 2×10^{-13}et $1.5 \times 10^{-12}\,\mathrm{M_{\odot}yr^{-1}}$. Ces deux valeurs proviennent de deux modèles différents ayant des méthodes distinctes pour calculer l'équilibre d'ionisation.

Dans ce même article, les auteurs affirment que cette valeur du taux de perte de masse démontre que le vent en surface de Sirius A serait probablement accéléré par la radiation puisqu'elle concorde avec la valeur prédite par le modèle (de vent radiativement accéléré) de Kudritzki et al. (1989) qui est de $1 \times 10^{-12}\,\mathrm{M_{\odot}yr^{-1}}$. Ils avancent par ailleurs que ce vent serait aussi homogène puisque, selon eux, le ralentissement via l'interaction de Coulomb dans le vent assure un partage de la quantité de mouvement. Leur explication s'appuie sur l'existence même des fortes raies en absorption du Mg II ; si ces ions, qui sont aussi accélérés dans le vent, n'étaient pas ralentis par l'interaction de Coulomb, ils seraient tellement accélérés que la profondeur optique de cette raie diminuerait considérablement, ce qui n'est pas le cas puisque la raie a été mesurée.

Aucune autre détection de vent en surface d'étoiles A ou F n'a été trouvée dans la littérature.

Pour les étoiles de Population II, nous savons qu'il y a de la perte de masse sur

la branche des géantes (Boyer et al. 2006). Mais sur la MS, les mêmes limitations se posent ; aucune détection n'a été trouvée dans la littérature.

1.6.1 Survol de la thèse

Dans les chapitres qui suivent, nous explorerons une région du diagramme H–R coincée entre la région où les taux de perte de masse ne permettent aucune séparation chimique (Maeder 1997), et celle où ils n'affectent pratiquement pas la diffusion atomique. Nous présenterons et analyserons des modèles évolutifs avec perte de masse que nous comparerons ensuite aux observations d'étoiles AmFm (Chapitre 2), HAeBe (Chapitre 3) et de Population II (Chapitre 4). En plus de reproduire les observations, l'objectif est de bien cerner les effets de la perte de masse dans la mesure où ils peuvent être différenciés de ceux liés à la turbulence telle que présentée dans Richer et al. (2000). Puisque les contraintes observationnelles sur les taux de perte de masse appropriés pour les étoiles étudiées sont minimes, voire même inexistantes, nous tenterons simplement de contraindre les taux par les anomalies d'abondance. Nous ne tenterons pas, non plus, d'expliquer le processus responsable de la perte de masse, ce qui exigerait des modèles détaillés du vent. Tout au long de l'argumentation, nous nous limiterons aux cas relativement simples afin de nous assurer que nous comprenons bien toute la physique impliquée par le processus étudié, soit la perte de masse.

1.6.2 Contribution aux articles

Pour l'ensemble des trois articles (Chapitres 2, 3 et 4) et les comptes rendus en annexe dont je suis le premier auteur, ma contribution inclut la rédaction complète de la première version (sauf une partie de la Sect. 2.4.1.1), la préparation de toutes les figures et le calcul des modèles. Avec les suggestions de mes superviseurs, Georges Michaud (GM) et Olivier Richard (OR), j'ai aussi analysé toutes les données. Les révisions subséquentes des textes ont été rédigées avec la collaboration

étroite de GM tout en tenant compte des suggestions d'OR et de Jacques Richer (JR). Finalement, pour ce qui est des modèles, j'ai implémenté la perte de masse dans un code évolutif déjà existant, dont les principaux experts sont JR et OR. Ils m'ont d'ailleurs appuyé lors de problèmes avec le code. Certaines figures ont aussi été préparées avec des scripts antérieurement conçus par JR ou OR. Pour l'article Gebran et al. (en annexe, accepté par A&A), j'ai rédigé la Sect. 5, pour laquelle j'ai analysé les données et préparé la Fig. 13. Finalement, pour le compte rendu Braithwaite et al. (2010) (pas inclu dans cette thèse), j'ai préparé la Fig. 6 et j'ai participé à l'analyse qui y est associée.

Une partie importante du travail a été consacrée à des tests numériques pour vérifier la stabilité et la validité des solutions obtenues avec perte de masse. Bien sûr une première étape fut d'implémenter la perte de masse dans le code évolutif, ce qui a demandé plusieurs changements et ajouts dans plusieurs routines différentes. Ensuite, avec des outils de visualisation que j'ai moi-même développés ou bien qui avaient été développés par JR ou OR, j'ai analysé les solutions et j'ai modifié certains algorithmes de convergence, notamment au niveau du maillage, afin de faire évoluer des modèles numériquement et physiquement corrects jusqu'aux âges nécessaires. Une analyse approfondie de l'intérieur des solutions a été effectuée afin de s'assurer que l'on comprenne bien toutes les variations obtenues en terme de principes physiques. D'ailleurs, toute l'analyse de la conservation du flux, qui parsème les descriptions des solutions internes avec perte de masse dans les chapitres ultérieurs, découle d'un test effectué pour vérifier que les solutions satisfaisaient aux équations régissant le transport des éléments dans le contexte de la perte de masse.

CHAPITRE 2

ÉTOILES AmFm ET LA BRÈCHE DU LITHIUM

AmFm and lithium gap stars
Stellar evolution models with mass loss

Mathieu Vick[ac], Georges Michaud[b], Jacques Richer[c], Olivier Richard[a],

Accepted in: *Astronomy & Astrophysics*, 12 June 2010

Abstract

A thorough study of the effects of mass loss on internal and surface abundances of A and F stars is carried out in order to constrain mass loss rates for these stars, as well as further elucidate some of the processes which compete with atomic diffusion.

Self-consistent stellar evolution models of 1.3 to 2.5 $M_\odot$ stars including atomic diffusion and radiative accelerations for all species within the OPAL opacity database were computed with mass loss and compared to observations as well as previous calculations with turbulent mixing.

Models with unseparated mass loss rates between 5×10^{-14} and $10^{-13}\,M_\odot yr^{-1}$ reproduce observations for many cluster AmFm stars as well as Sirius A and *o* Leonis. These models also explain cool Fm stars, but not the Hyades lithium gap. Like turbulent mixing, these mass loss rates reduce surface abundance anomalies; however,

[a]GRAAL UMR5024, Université Montpellier II, CC072, Place E. Bataillon, 34095 Montpellier Cedex 05, France

[b]LUTH, Observatoire de Paris, CNRS, Université Paris Diderot, 5 Place Jules Janssen, 92190 Meudon, France

[c]Département de physique, Université de Montréal, C.P. 6128 Succ. Centre-Ville, Montréal, QC, H3C 3J7, Canada

their effects are very different with respect to internal abundances. For most of the main–sequence lifetime of an A or F star, surface abundances in the presence of such mass loss depend on separation which takes place between $\log \Delta M/M_* = -6$ and -5.

The current observational constraints do not allow us to conclude that mass loss is to be preferred over turbulent mixing (induced by rotation or otherwise) in order to explain the AmFm phenomenon. Internal concentration variations which could be detectable through asteroseismic tests should provide further information. If atomic diffusion coupled with mass loss are to explain the Hyades Li gap, the wind would need to be separated.

Subject headings: Diffusion — stars: chemically peculiar — stars: mass-loss — stars: evolution — stars: abundances — galaxy: open clusters and associations: individual: Hyades

2.1 Astrophysical context

As instruments become more sophisticated and precise observations are readily made available for a growing number of chemical elements, additional constraints are steering the evolution of stellar models. The inclusion of atomic diffusion and radiative accelerations into the standard stellar evolution model resulted in some early success in describing abundance patterns for AmFm stars (Turcotte et al., 1998a). In these models, particle transport within the radiative zone was calculated from all physics known through first principles. However, the calculated surface anomalies were greater than the observed anomalies, and it was determined that additional transport processes were flattening the surface abundance patterns. With the addition of turbulent mixing, the Montreal group's stellar evolution code (Richer et al., 2000; Richard et al., 2001; Michaud et al., 2004, 2005; Talon et al., 2006) was able to explain and reproduce the particular abundances of many cluster

and field stars with a single tunable parameter: the mixed mass. Nonetheless, other studies have suggested that mass loss could also reduce the predicted anomalies to observed levels (Michaud et al., 1983; Michaud & Charland, 1986; Alecian, 1996). Since these studies considered static stellar models incorporating a limited number of species, a rigorous investigation of the effects of mass loss on stellar chemical evolution is warranted. Previously, Vauclair & Charbonnel (1995) have introduced mass loss to reduce the effect of Li settling in Pop II evolutionary models.

AmFm stars ($7000 \leq T_{\rm eff} \leq 10\,000$ K) are slowly rotating ($v_{\rm rot} < 100\,{\rm km\,s^{-1}}$, Abt 2000), non-magnetic stars of the main–sequence (MS). They are interesting candidates for testing evolutionary models because they lie within the temperature range for which the depth of the surface convection zone varies quite rapidly. Chemical separation within the stable radiative zones of these stars generates surface abundance anomalies within timescales that depend strongly on the depth of the surface convection zone, although the exact depth at which the separation occurs is still debated. The original explanation for these chemically peculiar stars stipulated that the separation occurred immediately below the surface H convection zone (Watson, 1971; Alecian, 1986, 1996); however, with the inclusion of turbulent mixing, more recent models (Richer et al., 2000) have suggested that separation occurs much deeper in the star ($T > 200\,000$ K). Though the second scenario has had success not only with AmFm stars, but also with Pop II (Richard et al., 2005; Korn et al., 2006) and Horizontal Branch (HB) stars (Michaud et al., 2007, 2008), it is still premature to accept turbulence as the sought-after macrospopic process since all models with turbulence necessarily involve at least one adjustable parameter. Turbulence models often implicitly assume a link between turbulence and rotation; however, even the most slowly rotating AmFm stars have anomalies which are significantly smaller than those obtained with atomic diffusion only models. This suggests the presence of a competing process even in non rotating stars.

Typical anomalies on the surface of AmFm stars include overabundances of

iron peak elements, as well as underabundances of Ca and/or Sc (see Cayrel et al. 1991 for a more complete description). Recent studies have obtained abundance determinations for numerous A and F stars of open clusters for a number of chemical species (Burkhart & Coupry, 2000; Hui-Bon-Hoa, 2000; Monier, 2005; Fossati et al., 2007; Gebran et al., 2008; Gebran & Monier, 2008) in an effort to confront relatively well constrained stars to current evolutionary models. The advantage of observing cluster stars is that they generally have the same age and initial metallicity, which greatly facilitates a comparison with models.

At the cool end of the Fm star domain, the well documented Li dip, first observed in the Hyades open cluster (Boesgaard & Tripicco, 1986), has challenged theoretical astronomers for decades (Michaud, 1986; Vauclair, 1988; Michaud & Charbonneau, 1991; Talon & Charbonnel, 2005). The lithium abundance has also been observed in many other open clusters (e.g. Balachandran 1995; Burkhart & Coupry 2000; Anthony-Twarog et al. 2009). The Be abundances in these stars (Boesgaard & King, 2002; Boesgaard et al., 2004; Randich et al., 2007) provide additional constraints on particle transport. Recently, Talon & Charbonnel (2003, 2005) have modeled shear turbulence induced by differential rotation and mixing induced by internal gravity waves in order to describe both the hot and cold side of the dip. Other models have also explored the effects of horizontal μ-gradients on rotationally induced mixing in these stars (Palacios et al. 2003). However, the potential effects of atomic diffusion, more specifically of radiative accelerations, in competition with mass loss, were not fully investigated.

At some level, mass loss is present in all stars, and it is important to quantify its effects on observed abundances. Unfortunately, for A and F stars in particular, the mass loss rates are not known. In O and B stars, the radiatively driven winds produce mass loss rates as important as $10^{-4}\,M_{\odot}yr^{-1}$(Lamers & Cassinelli 1999). In colder stars of types G and K, winds are driven by active coronas. The best known example is the solar wind which has a mass loss rate of

$2 \times 10^{-14}\,M_\odot yr^{-1}$ (Feldman et al. 1977). For intermediate stars, our understanding is at best nebulous. Abbott (1982) suggests that radiative accelerations are too small in stars with $T_{\rm eff} \leq 10\,000\,K$ for radiatively driven mass loss to be significant. On the other hand, the thinning of the surface convection zone in F and particularly in A stars might be too important for solar type winds to exist (Parker 1960). Are winds of A and F stars driven by radiation, coronal heating, both or neither? What are the expected mass loss rates? Both of these questions remain unanswered, and answering one could shed light on the other.

Observational constraints on A and F star mass loss rates are limited. Lanz & Catala (1992) as well as Brown et al. (1990) gave an upper limit of $10^{-10}\,M_\odot yr^{-1}$for main sequence A stars. Asymmetries in Mg II spectral lines of Sirius A led Bertin et al. (1995) to conclude that mass loss is present with a rate between $10^{-13}\,M_\odot yr^{-1}$ and $10^{-12}\,M_\odot yr^{-1}$. On the theoretical side, the radiatively driven wind model of Babel (1995) suggests a mass loss rate of $10^{-16}\,M_\odot yr^{-1}$ for A stars. However, according to his results, only heavier elements are evacuated by the radiative field. Similarly, Michaud et al. (1983, see also Michaud & Charland 1986) suggested that mass loss rates between $10^{-14}\,M_\odot yr^{-1}$ and $10^{-15}\,M_\odot yr^{-1}$ could satisfy observational constraints from CP star surface anomalies. Given the large disparity in values, the mass loss rates used in this study will be constrained strictly by surface abundance variations (see also Sect. 2.4.2).

In this paper, we consider mass loss in *non rotating stars*. In these stars, mass loss is arguably the only macroscopic process competing with atomic diffusion within the radiative zones. We will start with a brief description of our stellar evolution code in Sect. 2.2 after which we will discuss the method for calculating radiative accelerations for lithium, beryllium and boron (Sect. 2.3). In Sect. 2.4 we will describe the treatment of mass loss. In Sect. 5 we will discuss its effect on internal structure and surface abundances as the models move along the main–sequence and the subgiant branch. In Sects. 6 and 7 we will compare our models

to turbulence models and observations respectively. In Sect. 2.8, a brief overview of the main results will be followed by a discussion on how asteroseismology could help decipher the effects of advective processes including meridional circulation from those incurred through turbulent processes caused by differential rotation.

2.2 Calculations

This paper is part of the Montreal stellar model development project (Richard et al. 2001, Turcotte et al. 1998b and references therein). The models were evolved from the initially chemically homogeneous pre–main–sequence (see Fig. 2.1) with the solar abundance mix listed in Table 1 of Turcotte et al. (1998b). The transport of chemical elements in 1-D (one dimension) is solved within the basic framework established by Burgers (1969). The chemical transport equation considers all effects of radiative accelerations and atomic diffusion, and it is solved for 28 chemical elements and isotopes at every mesh point (the number of points varies from 800 to about 2800) for each time step. Atomic diffusion is allowed to operate as soon as a radiative zone appears. The radiative accelerations ($g_{\rm rad}$) and the Rosseland mean opacity are continuously updated; the treatment of chemical transport is thereby fully self-consistent. The atomic diffusion coefficients were taken from Paquette et al. (1986, see also Michaud & Proffitt 1993). The Krishna Swamy T–τ relation (Krishna-Swamy, 1966) was imposed as the boundary condition in the atmosphere (this choice was motivated by results presented in VandenBerg et al. 2008). Semiconvection was included as described in Richard et al. (2001), following Kato (1966), Langer et al. (1985), and Maeder (1997).

The chosen values of the mixing length parameter and initial He fraction are respectively $\alpha = 2.096$ and $Y_0 = 0.27769$ (see Model H of Turcotte et al. 1998b), which are calibrated by fitting the current solar radius and luminosity. We chose $Z_0 = 0.01999$ as the initial mass fraction of metals[1] . Some models were also

[1]Asplund et al. (2005, 2009) have proposed a downward revision of the solar abundances of

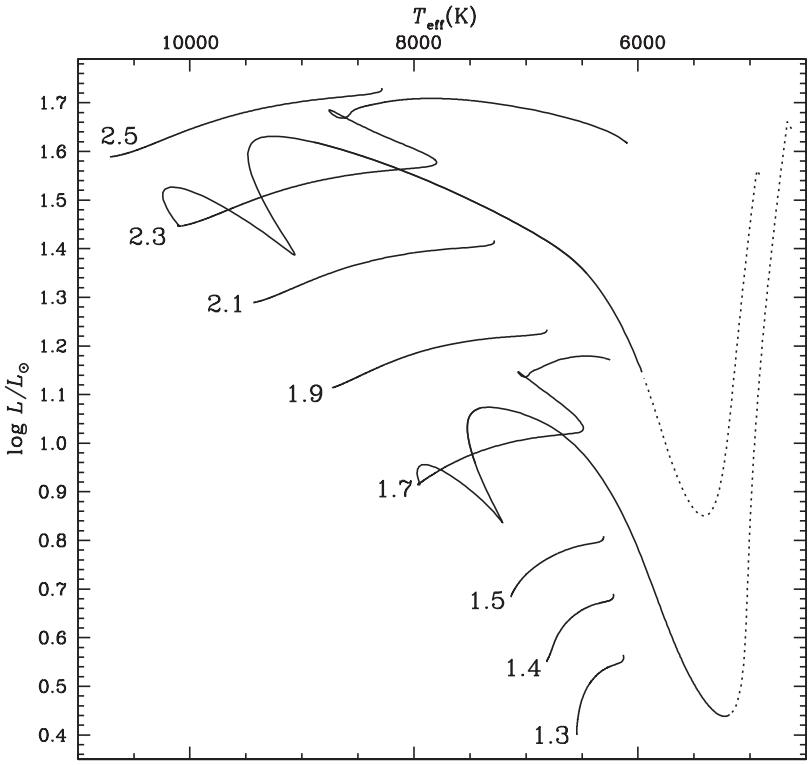

Figure 2.1: H-R diagram for all the models shown in Fig. 2.4. Though all models were calculated from the PMS to the bottom of the subgiant branch, the complete tracks are only shown for the 1.7 and 2.3 $M_\odot$ models. All other models are shown only on the main–sequence, which, for the purpose of this plot, is considered to span from the time at which 1% of core H is burned to the time at which 95% is burned. The dotted line represents evolution on the PMS until diffusion starts (i.e. until a radiative zone appears).

calculated for $Z_0 = 0.01$ and $Z_0 = 0.03$.

These are the first fully self-consistent stellar models which include mass loss. Models were calculated from 1.30 $M_\odot$ to 2.50 $M_\odot$. The mass loss rates considered vary from $1 \times 10^{-16}\,M_\odot yr^{-1}$ to $1 \times 10^{-12}\,M_\odot yr^{-1}$. Our treatment of mass loss will be further discussed in Sect. 2.4.1.

some metals; however we have chosen to keep the previous abundances until their determinations are reconciled with helioseismology (Delahaye & Pinsonneault 2006; Basu et al. 2007 and references therein). The abundance of O, the third most abundant element, is particularly uncertain (Caffau et al., 2008; Delahaye et al., 2010).

2.3 Radiative accelerations

Rosseland opacities as well as radiative accelerations are continuously computed for all 28 species as the relative concentration of each species varies with time. For all elements included in the OPAL database (Iglesias & Rogers, 1996), the radiative acceleration calculations are carried out using direct summations over the actual spectrum (i.e. *opacity sampling*, see Richer et al. 1998). At large optical depths (where the diffusion approximation is valid), the radiative acceleration, $g_{\rm rad}(A)$, of an element A at a radius r in a star may be approximated by:

$$g_{\rm rad}(A) = \frac{1}{4\pi r^2}\frac{L_r^{\rm rad}}{c}\frac{\kappa_R}{X_A}\int_0^\infty \frac{\kappa_u(A)}{\kappa_u(total)}\mathcal{P}(u)du, \tag{2.1}$$

where $\mathcal{P}(u)$, the normalized black body flux distribution, is given by:

$$\mathcal{P}(u) \equiv \frac{15}{4\pi^4}\frac{u^4 e^u}{(e^u-1)^2}. \tag{2.2}$$

The radiative luminosity at a radius r is $L_r^{\rm rad}$, X_A is the mass fraction of A, κ_R is the Rosseland opacity, κ_u(total) and $\kappa_u(A)$ are respectively the total opacity and the contribution of A to the total opacity at the frequency u defined by:

$$u \equiv h\nu/kT. \tag{2.3}$$

Since the competition for photons between element A and all other elements present in the plasma determines the value of $g_{\rm rad}(A)$, atomic data is required for all species in order to compute $g_{\rm rad}$ for any given element.

The corrections for redistribution of momentum are from Gonzalez et al. (1995) and LeBlanc et al. (2000).

2.3.1 Radiative accelerations for Li, Be and B

2.3.1.1 Methods

Li, Be, and B are not included in OPAL since they are not significant in the calculation of Rosseland mean opacity[2]. We have nonetheless computed the radiative accelerations in a manner which is consistent with OPAL spectra. The various corrections determined by Richer et al. (1997) are also included. The atomic data required for LiBeB are taken from Wiese et al. (1966). Since these elements are not sufficiently abundant for pressure broadening to be important (the lines are never saturated), only oscillator strengths are required to compute opacities.

The calculation of $g_{\rm rad}$ for these elements is delicate because of two factors which can lead to large fluctuations: (1) non optimal frequency sampling and (2) random background changes. Both problems arise from the fact that LiBeB not only have very few lines contributing to their $g_{\rm rad}$, but these lines are also very narrow.

(1) The fluctuations due to sampling not being sufficiently refined has an effect on Li as well as on the background (see Fig. 2.2). The Doppler width of a ^{7}Li line is given by:

$$\frac{\Delta u}{u} = \left[\frac{2\,kT}{Mc^2}\right]^{0.5} = 5.1 \times 10^{-5} T_5^{0.5} \tag{2.4}$$

where u is the adimensional energy difference between the upper and lower levels of the transition, M is the mass of the element, T is the local temperature and $T_5 = T/10^5\,{\rm K}$. In this case, one typically has $u \simeq 5$ around the most important temperature range, $\log T \simeq 5.3$, so that

$$\Delta u_{\rm Doppler} = \Delta u_D \simeq 7 \times 10^{-5} \tag{2.5}$$

[2]In Turcotte et al. (1998b) and Turcotte et al. (1998a), $g_{\rm rad}$(Li) and $g_{\rm rad}$(Be) were approximated using formulae derived previously by Richer & Michaud (1993). These are however less accurate than $g_{\rm rad}$ calculated using direct summations over the spectrum throughout stellar evolution (using Eq. [2.1]), which are described here and were used in Richer et al. (2000) and Richard et al. (2001).

which is to be compared to the frequency grid interval, $\Delta u_G = 20/10^4 = 2 \times 10^{-3}$, of the OPAL spectra. Using opacity sampling for Li would imply that the line center would sometimes occur *within* Δu_D of a grid point and sometimes up to $15\Delta u_D$ away. If the sampling point occurs in the far tail of an important Li line, the $g_{\rm rad}$(Li) value would be much smaller than if it occurs in its center.

Likewise, the sampling is not refined enough to reproduce all features of the background spectra (see Fig. 3 of Richer et al. 1998). Variations can therefore result from overlooking an important background line which occurs near a lithium line.

(2) The frequency sampling grid is a function of u and not of ν. Therefore, when one considers an adjacent grid point of different T, the background, as a function of u, changes, and the consequent random variation in background affects the flux available for a specific lithium line. This is largely due to the narrowness of most lines. For example, in the inset of Fig. 2.2, the Li line does not encounter any important Fe line for that specific (ρ,T) table; however, in the inset of Fig. 1 of Richer & Michaud (2005), which shows the same u interval for a different (ρ,T) table, the Li line is overlapped by a strong Fe line, and the available flux is consequently reduced.

One can alleviate these problems by combining a modified version of the opacity sampling method with the known position of all the line centers for LiBeB. In order to reduce the fluctuations, while preparing the spectra of, say, Li, for the calculations of $g_{\rm rad}$(Li), it was assumed that each Li line was spread uniformly over the Δu_G interval in which the Li line center occurs (i.e. the Li lines become square functions of width Δu_G and so it becomes impossible for the sampling to overlook them). This will leave fluctuations caused by random variations of the opacity background when the line center moves from one Δu_G interval to another (2), but the variations due to non optimal sampling (1) will be reduced significantly.

Note that if the frequency sampling is refined (e.g. 10^5 as in OP data) in order

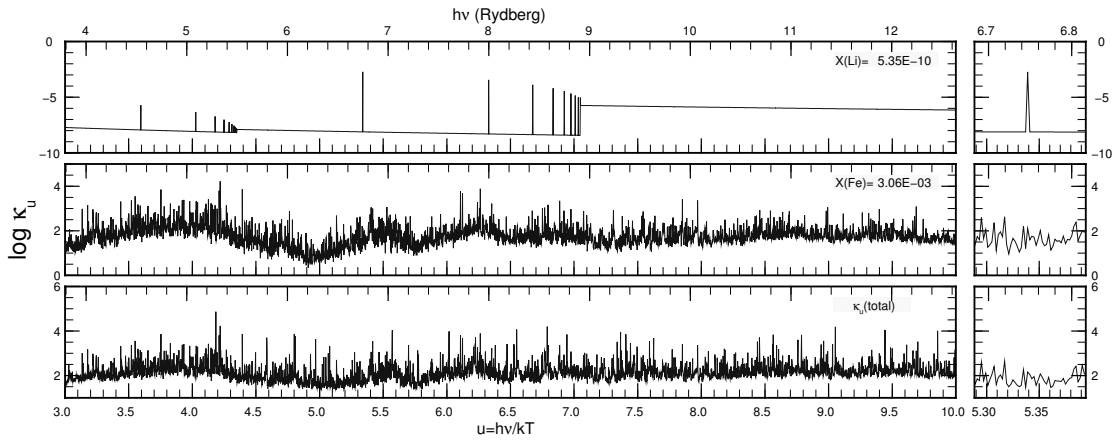

Figure 2.2: Opacity spectra for Li, Fe as well as the total opacity in $\mathrm{cm^2 g^{-1}}$ at a depth where $\log T = 5.3$ and $\log \rho = -4.6$. The u interval covers the range through which most of the flux passes. The spectrum is dominated by Fe lines. The inset on the right shows a zoom of the area which hosts the Li line which contributes the most to its g_{rad}.

to better represent the background spectra, errors due to the inexact position (in frequency) of each background feature remain. The line center positions for Fe, the main contributor to the total opacity in this region, are only known to about 1%.

The resulting error bars on g_{rad} are discussed in Sect. 3 of Richer & Michaud (2005). As an example, for Population I stars, there is a factor of 2 uncertainty for g_{rad}(Li). In Pop II stars, the uncertainty is much less important (e.g. only 3% for a star with $Z = 0.0001$).

The same errors and limitations should be expected for scandium around the minima of its g_{rad} since the radiative accelerations in these regions are computed with only a few narrow lines. Unfortunately, Sc is not included in OPAL data, and its g_{rad} must be calculated through alternate methods (LeBlanc & Alecian 2008).

2.3.1.2 Results

The radiative accelerations for Li and Be are shown in Fig. 2.3 for a star of 1.55 $\mathrm{M_\odot}$ with a mass loss rate of $1 \times 10^{-13}\,\mathrm{M_\odot yr^{-1}}$ as well as for a star of 1.47 $\mathrm{M_\odot}$

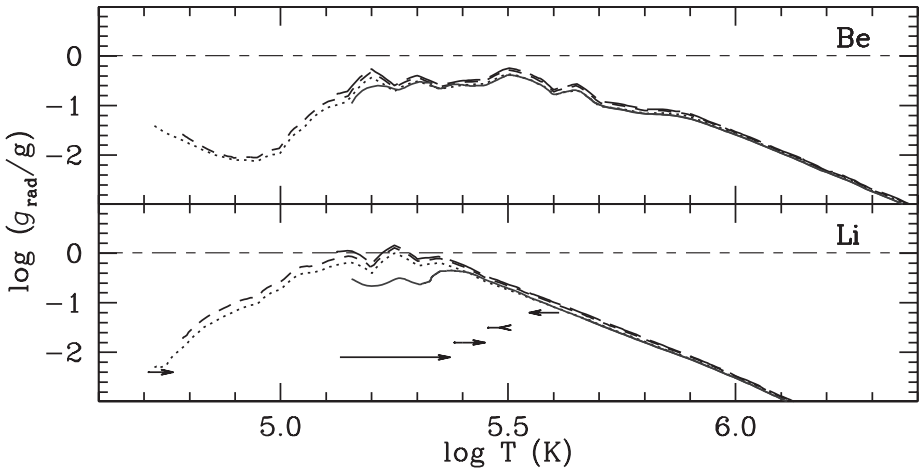

Figure 2.3: Variation of radiative accelerations with temperature for Li and Be at 100 Myr (dotted line), 700 Myr (dashed line) and 1.3 Gyr (long dashed line) in a 1.55 $M_\odot$ model with a mass loss rate of 1×10^{-13} $M_\odot yr^{-1}$ as well as at 100 Myr (solid line) for a 1.47 $M_\odot$ model with no mass loss. The curves extend to the bottom of the surface convection zone, on the left. Acceleration is normalized to local gravity. The horizontal arrows indicate the total movement of the bottom of the surface convection zone (BSCZ) for models of 1.40, 1.43, 1.45, 1.47 and 1.55 $M_\odot$ from top to bottom (see text below).

with no mass loss. For both models, the radiative accelerations for Be are below gravity throughout the radiative zone, and throughout evolution. However, $g_{\rm rad}$(Li) has a peak that approximately reaches gravity below the surface convection zone for the 1.55 $M_\odot$ model. Up to $\log T \simeq 5.4$, $g_{\rm rad}$ is seen to be almost solely temperature dependent as the curves for both models overlap.

In the 1.47 $M_\odot$ model, $g_{\rm rad}$(Li) has about the same value as in the 1.55 $M_\odot$ model for $\log T > 5.4$, but, for $\log T < 5.4$ it is reduced by the competition of Fe, which absorbs most of the flux where the Li lines are important. This occurs when mass loss is small enough for Fe to accumulate in and above this region, as is the case for the 1.47 $M_\odot$ model (or in the 1.50 $M_\odot$ model with a mass loss rate of 10^{-14} $M_\odot yr^{-1}$ shown in Fig. 2.5). On the other hand, $g_{\rm rad}$(Be) does not vary with Fe abundance likely because most Be lines, particularly the ones which contribute

the most to its $g_{\rm rad}$, lie outside of the frequency interval which is dominated by Fe lines.

The horizontal arrows in Fig. 2.3 show the total movement of the bottom of the surface convection zone (BSCZ) for 4 models without mass loss (1.40, 1.43, 1.45 and 1.47 $M_\odot$), as well as for a model of 1.55 $M_\odot$ with a mass loss rate of $10^{-13}\,M_\odot yr^{-1}$. The interval for which the BSCZ is plotted spans from 50 Myr to 625 Myr for all models except for the 1.47 $M_\odot$, model which goes from 50 Myr to 425 Myr (the simulation's last converged model). For most models, the depth of the BSCZ does not vary much between 50 and 625 Myr (most of the main–sequence lifetime before the age of the Hyades cluster); however, for the 1.47 $M_\odot$ model, the BSCZ moves significantly and extends over an interval in which $g_{\rm rad}$(Li) also varies significantly.

If we compare the curves for the 1.55 $M_\odot$ model with those shown in Fig. 1 of Richer & Michaud (1993), we first note the similarity in the temperature dependence of the curves. For Li, we have verified that they are nearly equal for $\log T > 5.4$. The maxima occur at very nearly the same temperature as well. However, the maximum values of $g_{\rm rad}$(Li) and $g_{\rm rad}$(Be) are respectively about 2 and 6 times larger in Richer & Michaud (1993). Furthermore, their results show very smooth curves compared to the many variations seen in our calculations.

Although there is a slight difference in stellar mass (a 1.54 $M_\odot$ model is shown in Fig. 1 of Richer & Michaud 1993), this cannot account for the relatively large differences close to the maximum. There are nonetheless a few other explanations. Our calculations were carried out with integrations over complete OPAL spectra for all species at each time step and each mesh point. Since these spectra were not available in 1993, the calculations of Richer & Michaud (1993) were done using averaged spectra whose frequency dependence (Eq. [18] of Borsenberger et al. 1979) did not include the frequency dependence of Fe lines, particularly near $T \simeq 2 \times 10^5\,K$, where $g_{\rm rad}$(Li) is affected the most. From Fig. 2.2, one can see that

Fe lines dominate the region where Li lines are strongest. As Fe lines which occur near Li lines were absent in the old opacities, the available flux for Li lines is very different (see Sect. 2.3.1.1).

Moreover, the evolution of individual metal abundances and its impact on local opacity are *not* included in the calculations of Richer & Michaud (1993). This is particularly important in AmFm stars since heavier metals such as iron and nickel tend to accumulate below the surface convection zone when mass loss is not too strong.

2.4 Mass loss

We first discuss how to include mass loss in evolutionary models (Sect. 2.4.1). In Sect. 2.4.2 we discuss a few theoretical analyses of coronal and radiatively driven winds followed by a brief look into separated winds[3] (Sect. 2.4.3).

2.4.1 Treatment of mass loss

Mass loss is assumed spherical and chemically unseparated. If we simply apply mass conservation arguments, the net result of mass loss is the appearance of an outward flowing interior velocity due to the wind:

$$v_w(r) = -\frac{\dot{M}}{4\pi r^2 \rho}\frac{m_r}{M_*} \tag{2.6}$$

where ρ is the local density, m_r is the mass interior to r and $\dot{M} < 0$. It should be pointed out that the m_r/M_* factor in this equation has often been overlooked, but it will be shown to be a consequence of mass conservation (see Sect. 2.4.1.1). Even for small mass loss rates, the ρ^{-1} dependence leads to large velocities in the outer layers of the star. To avoid numerical instabilities due to the cancellation of

[3]In this paper, mass loss is *separated* when the abundances in the wind are not the same as in the photosphere. On the contrary, mass loss is *unseparated* when the abundances in the wind are the same as in the photosphere.

two large quantities in the convective envelope (wind velocities and large turbulent velocities used to enforce convective mixing) and in order to have a Neumann surface boundary condition (no flux), mass loss was implemented as described in Charbonneau (1993). The main physical considerations are that the surface convection zone (SCZ) be fully mixed, and that the atmosphere be mixed with it by overshooting. Therefore, the ejected mass has the same composition as the SCZ. The mechanism by which mass is ejected from the star becomes irrelevant so long as the correct amount of mass is removed from the star. For each chemical species, the resulting transport equation is:

$$\begin{aligned} \rho\frac{\partial c}{\partial t} &= -\nabla\cdot[-\rho D\nabla\ln c+\rho(\mathbf{U}+\mathbf{U}_w)c] \\ &\quad +\rho(S_{nuc}+S_w)c, \end{aligned} \tag{2.7}$$

with a Neumann condition imposed at the surface and with $\mathbf{U}_w$ and S_w defined as:

$$\mathbf{U}_w = \begin{cases} v_w\hat{\mathbf{e}}_\mathbf{r} \text{ under the SCZ,} \\ 0 \text{ in the SCZ;} \end{cases} \tag{2.8}$$

$$S_w = \begin{cases} 0 \text{ under the SCZ,} \\ \frac{\dot{M}}{M_{\mathrm{CZ}}} \text{ in the SCZ.} \end{cases} \tag{2.9}$$

Here, c is the time and depth dependent composition, D the total diffusion coefficient, $\mathbf{U}$ the advective part of the atomic diffusion velocity, $\mathbf{U}_w$ the interior velocity due to the wind, M_{CZ} the mass of the SCZ, $\dot{M}$ the mass loss rate, S_{nuc} a source/destruction term linked to nuclear reactions and S_w is a sink term linked to mass loss. The mass is simply removed from the surface convection zone which, given the assumed mixing, is equivalent to losing it through the stellar surface. The mass of the star is also continuously updated so that all quantities that depend on stellar mass are correctly calculated.

2.4.1.1 Mass flux equation

Mass loss has the effect of ejecting (or *peeling*) the outermost layers of a stellar model. The model must then be reconverged with a slightly reduced mass. This scenario can be described within the formalism of operator splitting. If a mass $\Delta M_{\rm loss}$ is removed in a given time step Δt, one needs to reconverge a model of mass $M_1 = M_0 - \Delta M_{\rm loss}$ at time $t_1 = t_0 + \Delta t$ *with the composition of the star kept unchanged as a function of* m_r*, the independent variable which is defined as the sphere of constant mass,* m_r. Mass loss does not modify the abundance profiles with respect to m_r, although there is a change with respect to the stellar surface. For example, an abundance peak at the point $M_0 - \Delta M_{\rm loss}$ (or $\Delta M_{\rm loss}$ below the surface before peeling), finds itself at M_1 (or at the surface) after the peeling but the mass interior to this point, m_r, has not changed.

To implement mass loss in a stellar evolution code, one can imagine the solution process to be broken down into 2 steps. In a first step, the model can be converged at a time t_1 as if there were no mass loss, with the composition changes due to nuclear reactions and diffusion processes. Then, the grid at t_1 is reinterpreted as corresponding to a mass $M_1 = M_0 - \Delta M_{\rm loss}$ with all variables expressed as a function[4] of m_r/M_* except for the composition which is kept unchanged as a function of m_r. The star is then reconverged a second time at t_1 with a mass M_1 and with the concentration profiles which include the effect of mass loss. As more mass is lost, the model inches toward less massive structures, and so evolution progressively corresponds to that of a lower mass star. This is a correct description of mass loss which in practice is as accurate as the operator splitting procedure is accurate.

However, going from the m_r/M_0 to the m_r/M_* grid while keeping c_i as a function of m_r implies interpolating. In practice, performing interpolations on c_i during

[4]Here $M_1 = M_*$ at t_1 and similarly $M_0 = M_*$ at t_0.

computations can introduce unwanted numerical diffusivity. It is relatively easy to show that these interpolations on c_i resulting from mass loss can be avoided by introducing a local mass flux into the conservation equation, while keeping the grid constant (i.e. the grid points have the same values of m_r/M_* in spite of M_* varying from M_0 to M_1).

Let us consider the concentration on a grid point (m_r/M_*) at t_1 as a function of the concentration on the same grid point at t_0. The grid points shift on the m_r axis. Then

$$c_i\left(m_{r1}\right) = c_i\left(m_{r0}\right) + \frac{\partial c_i}{\partial m_r}\Delta m_r \tag{2.10}$$

which is a simple Taylor series development and where

$$\Delta m_r = m_{r1} - m_{r0}. \tag{2.11}$$

By definition, m_{r1} is the position on the m_r axis, of the grid point $\frac{m_{r0}}{M_0}$ after a $\Delta M_{\rm loss}$ mass loss so that one may write:

$$\frac{m_{r1}}{M_1} = \frac{m_{r0} + \Delta m_r}{M_0 - \Delta M_{\rm loss}} = \frac{m_{r0}}{M_0} \tag{2.12}$$

which can trivially be solved to give:

$$\Delta m_r = -\frac{m_{r0}}{M_0}(\Delta M_{\rm loss}). \tag{2.13}$$

Now we substitute equation (2.13) in equation (2.10), replace $\Delta M_{\rm loss}$ by $-\dot{M} \times \Delta t$ and simplify:

$$c_i\left(m_{r1}\right) = c_i\left(m_{r0}\right) + \frac{\partial c_i}{\partial m_r}\frac{\mathrm{d}\,M_*}{\mathrm{d}t}\frac{m_{r0}}{M_0}\Delta t. \tag{2.14}$$

The second term on the right has the same effect on c_i as the introduction of a flux term[5] (caused by mass loss $\times\frac{m_r}{M_0}$) in a conservation equation. The flux $4\pi\rho r^2 U_W$

[5]Often abusively called a "wind" term in this context. It seems preferable to restrict the use

given by equation

$$-4\pi\rho r^2 U_w = \frac{\mathrm{d}\, M_*}{\mathrm{d}t}\frac{m_r}{M_*}. \tag{2.15}$$

must then be introduced in the conservation equation in order to take into account the effect of the m_r shift caused by the peeling of surface layers while keeping the same grid as a function of $m_r/\, M_*$ when M_* changes due to mass loss. This simple argument justifies the introduction of a mass flux to model the effect of mass loss on element separation in stellar atmospheres or envelopes (Vauclair, 1975; Michaud et al., 1983; Alecian, 1996).

For smaller mass loss rates, structural effects of mass loss are often negligible to the extent that only the shift of c_i remains and mass loss may be viewed as a mass flux going through a star of constant mass (i.e. it is not necessary to change the stellar mass during evolution calculations). Consider the case of the present Sun. Assuming that it is constant in time, its current mass loss rate of $2 \times 10^{-14}\,\mathrm{M}_\odot/\mathrm{yr}$ leads to a loss of $10^{-4}\ \mathrm{M}_\odot$ up to the Sun's age which for most purposes corresponds to negligible structural changes. This is only $\sim 1/300$ of the mass of the superficial convection zone.

Since we are not certain about the nature of the winds at the surface of A and F stars, the present models do not take into account any energy dissipation which would be required to produce these winds.

2.4.2 Stellar winds of A and F stars

This study will use observed surface abundances to constrain mass loss since the stellar winds associated with A and F stars are not well known. The winds could be radiative, coronal, a combination of both or even completely negligible. Comparisons with stellar wind models are difficult. Indeed, even the hottest A stars maintain a thin surface H convection zone, and stars as early as A7 (and

of "wind" to the region above the photosphere.

possibly earlier, see Neff & Simon 2008; Simon & Landsman 1997) can support active coronas and chromospheres which could harbor solar type winds. It is also plausible that both mechanisms act simultaneously. A few properties of coronal and radiatively driven winds for A and F stars will be reviewed in the two following subsections, in so far as they relate to chemical separation.

2.4.2.1 Coronal winds

With simple physical considerations, it is possible to obtain an approximate value of the mass loss rate above which coronal winds are necessarily unseparated. For a spherically symmetrical mass loss, the wind velocity (Eq. [2.6] with $M_r = M_*$) may be compared to the maximal downward diffusion velocity (given by the gravitational settling velocity without any contribution from radiative accelerations). Equating the two gives an evaluation of the maximum mass loss that allows for separation to occur. One may then write:

$$v_w = \frac{\frac{-\mathrm{d}M_*}{\mathrm{d}t}}{4\pi r^2 \rho} = D_{ip}\frac{A_i g m_p}{kT}. \tag{2.16}$$

which can be rewritten as:

$$\frac{-1}{M_*}\frac{\mathrm{d}M_*}{\mathrm{d}t} = \frac{2.4\times10^{-15}A_i T_5^{1.5}}{Z_i^2}[\mathrm{yr}^{-1}] \tag{2.17}$$

($T_5 = T/10^5\,\mathrm{K}$) where A_i and Z_i are the atomic mass and atomic number respectively of element i and where the Coulomb term in the calculation of D_{ip} is replaced by an approximate value. This applies both in the atmosphere and in the outer parts of the wind solution. For a solar type wind, assuming an isothermal corona of $T = 10^6\,\mathrm{K}$, one obtains a limiting mass loss rate $\simeq 10^{-13}\,\mathrm{M}_\odot\mathrm{yr}^{-1}$(see Michaud et al. 1987). The dependence on T is valid when the gas is fully ionized. In the cooler atmospheres of early A stars (say at $10^4\,\mathrm{K}$), He is mainly neutral, neverthe-

less the limiting mass loss rate is approximately the same in the atmosphere as in the corona since the diffusion coefficients are larger by a factor of $200 - 300$ than those of ionized He (Michaud et al. 1978). The separation observed in the solar wind ($\dot{M} \simeq 10^{-14}\,\mathrm{M_\odot yr^{-1}}$) agrees roughly with this analysis. As previously mentioned, observations show that elements which are neutral at $T = 10^4\,\mathrm{K}$ are $\simeq 2-3$ times less abundant in the corona than in the photosphere (Meyer, 1985, 1996). Most agree that the separation occurs somewhere in the solar chromosphere immediately above the photosphere and could therefore have an impact on observed photospheric abundances. For instance, Geiss & Buergi (1986, in their model 4) find that matter which arrives at 1 AU has the same He to H ratio as at the wind's base. Since there is no net separation within the solar wind, it is premature to infer that all coronal type winds are chemically differentiated. Moreover, wind structures in A star coronas would probably be quite different since many metals that are neutral in G and F star photospheres are ionized in A star photospheres. It is thus very difficult to compare the solar wind to other coronal winds, particularly for hotter stars.

2.4.2.2 Radiatively driven winds

Babel (1995) found that for stars within $8000 \leq T_{\mathrm{eff}} \leq 14000\,\mathrm{K}$, all radiatively driven winds must be fully separated. In these stars the Coulomb coupling is not sufficient to redistribute the momentum acquired by the heavier, radiatively accelerated elements onto the bound, more abundant H and He (Springmann & Pauldrach, 1992; Owocki & Puls, 2002; Krtička et al., 2003). Since only metals are ejected from the star, the mass loss rates are much smaller: between $10^{-16}\,\mathrm{M_\odot yr^{-1}}$ and $10^{-17}\,\mathrm{M_\odot yr^{-1}}$. However, the multicomponent hydrodynamical model put forth in Babel (1995) and Babel (1996) only considers an average metal, rather than solving for each metal individually, therefore metal-specific mass loss rates are not known. Furthermore, the interaction of radiatively driven winds with magnetic

fields as well as convection is still poorly understood. This is particularly important for A stars, and the consequent uncertainties require us to be cautious before constraining our analysis with these results. For cooler stars, such as F stars, radiative accelerations are not believed to be able to generate significant mass loss (Abbott, 1982).

Unglaub (2008) found that radiatively driven winds of sdB stars must be separated (accelerated metals cannot drag H and He) if the mass loss is smaller than $10^{-12}\,M_{\odot}yr^{-1}$ (10 times larger than the approximate value obtained in Sect. 2.4.2.1). However, although the author's calculations are quite thorough, they are not complete in so far as some other poorly understood factors could play a significant role in determining wind properties. How does convection or magnetic fields, particularly flux tubes, affect the wind structure and velocity? Furthermore, the omission of line shadowing in the calculations could have a significant impact on the author's results[6]. In fact, the author stipulates in Sect. 6.2 of his article that including line shadowing could diminish $g_{\rm rad}$ by a factor of 100 for the stronger photoshperic lines, thus leading to an overestimation of $\dot{M}$ by a factor of 10.

2.4.3 Unseparated vs. separated mass loss

The object of this study is to constrain the effects of mass loss *solely* via observed abundance anomalies. To do so, we use simple wind models in order to minimize the arbitrariness of the analysis. Accordingly, most calculations were done assuming simple unseparated winds, although a few calculations were also carried out assuming separation in the wind in order to assess potential effects. Three cases of separated winds were considered: (1) only metals are ejected, (2) the separation mimics the solar wind with H treated as a high-FIP (First Ionization Potential; Meyer 1985) element and (3) the separation again mimics the solar wind

[6]Line shadowing occurs when the wind velocity is not sufficient to Doppler shift the wind's line centers away from flux attenuated photospheric line centers, thus reducing radiative accelerations. This is often true until the wind reaches the sonic point.

but with H as a low-FIP element.

In case 1, all metals are ejected with the same composition as the stellar surface, while H and He remain bound. For this scenario, mass loss rates were varied from 10^{-17} to $5 \times 10^{-16}\,M_{\odot}yr^{-1}$ in order to account for the fact that only metals are leaving the star (around 2% of the superficial mass fraction).

The other scenarios (2 and 3) consider chemical separation in the solar wind as established by Meyer (1985), who found that elements with a FIP smaller than 9eV were approximately 4 times more abundant relative to hydrogen in the corona than in the photosphere, while higher-FIP elements, including hydrogen, kept their photospheric abundances. Although this scenario is generally favored, Meyer (1996) questioned his own results a decade later by implying that instead of having overabundant low-FIP elements in the wind, higher-FIP elements, including H, could be depleted in the corona[7]. Both configurations are investigated: case 2 has H as a bound high-FIP element, and case 3 has it as a low-FIP element. Our approach was to divide all elements into two groups: low-FIP elements (below 11 eV) and high-FIP elements (He, C, N, O, Ne, Cl and Ar). All low-FIP elements were depleted 4 times faster than high-FIP elements.[8]

Numerically, in cases (2) and (3), the destruction term in Eq. [2.9] was multiplied by a factor of 4 in the SCZ for all low-FIP elements. A weight term, which was continuously updated as concentrations changed in the SCZ, was added to the denominator for normally depleted high-FIP elements to account for the fact that their destruction is not, in this case, proportional to the total mass loss rate multiplied by individual concentration (Eqs. [2.7] and [2.9]) since their relative concentration in the photosphere is not the same as in the wind. The interior wind velocities are not affected since the $v_{\rm wind}$ term does not depend on relative concen-

[7]This question remains unanswered (see Feldman & Widing 2003 for a complete review).

[8]Helium is assumed to have a 1:1 ratio with high-FIP elements, since the observations which suggest that He would have a ratio of 1:4 with these elements are questioned (see Feldman & Widing 2003).

trations, but simply on the mass loss rate.

2.5 Evolutionary models

In Fig. 2.4, the evolution of $T_{\rm eff}$, L, $\log g$, the depth of the surface convection zone as well as the surface Fe abundance are shown for a number of models. The chosen masses were selected to span the observed $T_{\rm eff}$ range associated with AmFm stars and Li gap stars (Preston 1974; Boesgaard & Tripicco 1986). The lower limit also corresponds to the least massive star on the main sequence for which we predict relatively large surface abundance anomalies (see Sect. 2.5.3). All models are shown for the same mass loss rate ($10^{-13}\,{\rm M}_{\odot}{\rm yr}^{-1}$). As will be seen in the next section, this mass loss rate has an effect, though very moderate, on the structure via abundance changes (the effect on He abundance for instance can increase the depth of the surface convection zone). This mass loss rate also allows surface abundance anomalies which are compatible with observed abundance anomalies for Am stars (see Sect. 2.5.3).

The main–sequence lifetime ranges from about 500 Myr for the 2.5 $M_{\odot}$ model to more than 3 Gyr for the 1.3 $M_{\odot}$ model. The Fe surface abundance is intimately coupled with the movement of the surface convection zone; for the models with the thinnest SCZ, Fe is predicted to be overabundant over most of the MS lifetime (in the 2.5 $M_{\odot}$ model by a factor of about 3).

All models of at least 1.5 $M_{\odot}$ are marked by a rapid Fe abundance peak which occurs at the beginning of the main sequence. The rise of X(Fe), which is related to the depth change of the surface convection zone as the star stabilizes (see Fig. 2.4f), is so rapid that it is not resolved in Fig. 2.4f. Similarly, there is a sharp spike towards the end of the MS for most models which is once again correlated with the sharp variation in SCZ depth (in this case the most important variation is for the 1.7 $M_{\odot}$ model, which has a difference of a factor of 2.5 in Fe abundance

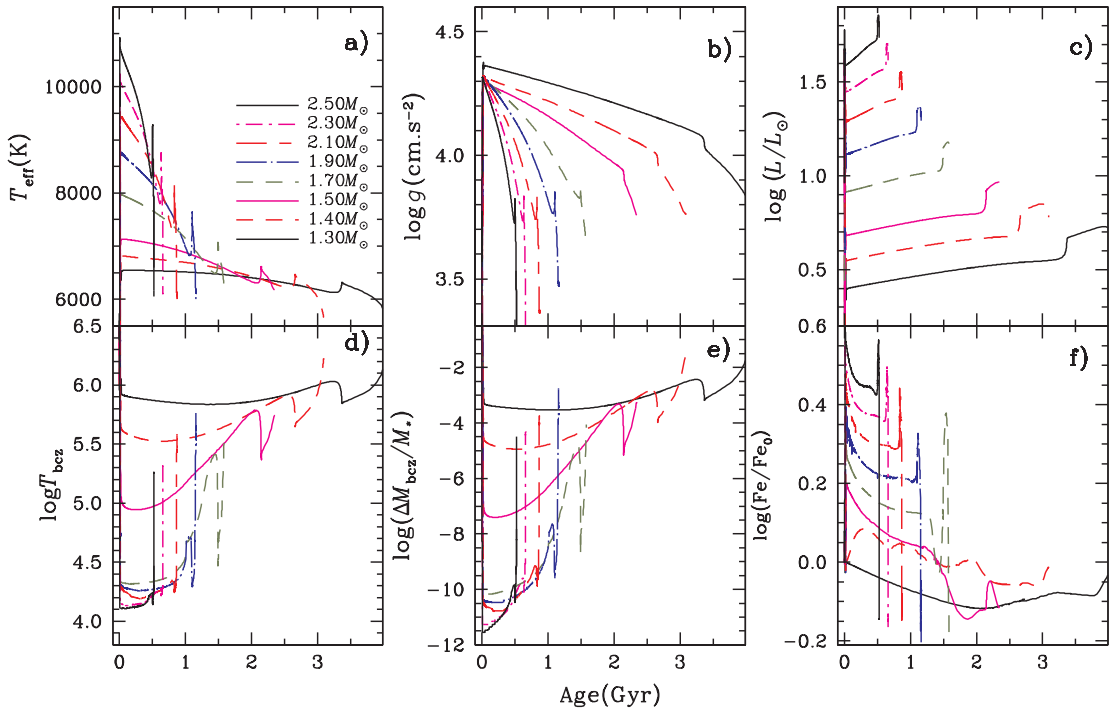

Figure 2.4: Evolution of $T_{\rm eff}$ (a), $\log g$ (b), luminosity (c), temperature (d) and mass at the bottom of the surface convection zone (e), as well as the surface Fe abundance (f) for selected masses that span the range of AmFm stars. All models are shown for a mass loss rate of $10^{-13}\,{\rm M}_{\odot}{\rm yr}^{-1}$. The curves are identified in panel (a). Vertically, they have the same order in panels (a), (c) and (f), but are in reverse order in panels (b), (d) and (e).

within less than 100 Myr). As we will see in the following sections, these variations are larger when the mass loss rate is smaller. The HR diagram for these models is shown in Fig. 2.1. For clarity, only two evolutionary tracks are shown from the initially homogeneous pre-main–sequence up to the subgiant branch (the others are shown from the beginning of the main–sequence, although their evolution is calculated from the pre-main–sequence). Diffusion and its effects on surface abundances appear well before the arrival on the main–sequence (a thorough investigation of diffusion on the pre-main–sequence will be discussed in Vick et al., in preparation).

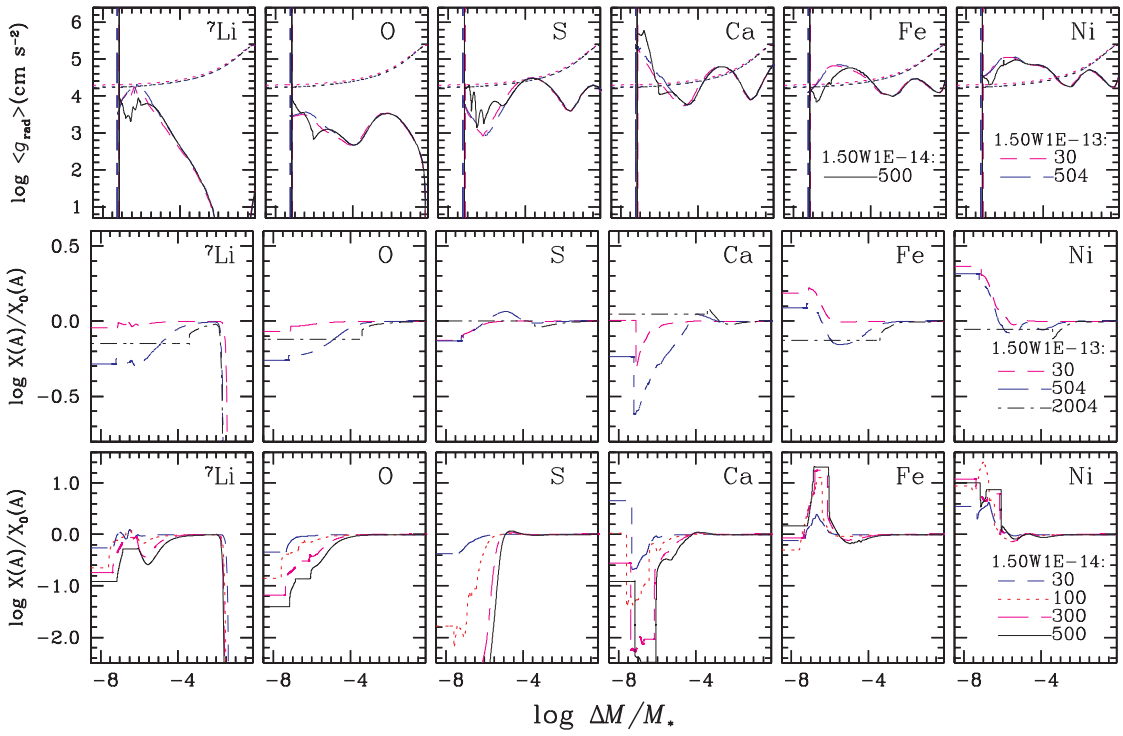

Figure 2.5: [Top row] Radiative accelerations (solid line) and local gravity (dotted line) for a few selected elements in a 1.5 $M_\odot$ model with two different mass loss rates. For the 1.50W1E-13 model, the radiative accelerations are shown for 2 ages (30 and 503 Myr), while they are only shown at 500 Myr for the 1.50W1E-14 model. The vertical lines show the position of the bottom of the surface H-He convection zone. The corresponding internal abundance variations at different ages (in Myr) are shown for both the 1.50W1E-13 model [middle row] and the 1.50W1E-14 model [bottom row].

2.5.1 Radiative accelerations, internal abundance variations and structure

In Figs. 2.5 and 2.6 the radiative accelerations as well as the corresponding spatial abundance variations for a few selected elements are shown for models of 1.5 $M_\odot$ and 2.5 $M_\odot$. These masses approximately correspond to the lower and higher $T_{\rm eff}$ limits of AmFm stars.

The MS lifetime of the 1.5 $M_\odot$ model is about 2 Gyr whereas the 2.5 $M_\odot$ star

has a MS lifetime of about 520 Myr (see Fig. 2.4). The 1.5 $M_\odot$ model with a mass loss rate of $1 \times 10^{-14}\,M_\odot yr^{-1}$ (see bottom panel of Fig. 2.5) was stopped at 575 Myr because the solution became numerically unstable.

Throughout most of the stellar envelope, the mass loss rate does not significantly affect the resulting $g_{\rm rad}$s, as seen in the upper row of Fig. 2.5. However, if mass loss is small enough to permit iron peak accumulation below the SCZ, as is the case for the 1.50W1E-14 model, then all $g_{\rm rad}$s will be affected by competition in the region where metals have accumulated.

We present in Sect. 5.1.1 and Sect. 5.1.2 approximate equations which will facilitate the interpretation of the detailed solutions shown in Figs. 2.5 and 2.6, which will be discussed in Sect. 5.2.

2.5.1.1 The interior wind solution

Consider the approximate solution to Eq. [2.7], in a regime for which the $\frac{\partial c}{\partial t}$ term is small compared to the others (which is true over most of the MS lifetime). Then one may write:

$$\nabla \cdot [- \rho D \nabla \ln c + \rho(\mathbf{U} + \mathbf{U}_w)c] = 0 \tag{2.18}$$

if nuclear terms are negligeable, which is true for the stellar envelope, and $S_{\rm w} = 0$, which is true outside the surface convection zone. In one dimension, and in the absence of turbulence (so that D becomes D_{12}, the diffusion coefficient in a hydrogen and helium background) Eq. [2.18] becomes:

$$\mathcal{F}(r) = r^2 \left[-\rho D_{12} \frac{\partial c}{\partial r} + \rho(U + U_{\rm w})c \right] = cst \tag{2.19}$$

where $\mathcal{F}(r)$ is constant as a function of r and U is approximately given by Eq. [9] from Michaud et al. 1983, with a slight correction[9]:

$$U \simeq v_{\rm D} = D_{12}\left[-\left(A-\frac{Z}{2}-\frac{1}{2}\right)\frac{m_{\rm p}g}{kT} + \frac{m_{\rm p}Ag_{\rm rad}}{kT} + \alpha_T\frac{\partial \ln T}{\partial r}\right]. \tag{2.20}$$

Here A and Z are the atomic mass and charge number respectively, and α_T is the thermal diffusion coefficient[10]. Since the g and $g_{\rm rad}$ terms are multiplied by A while the abundance gradient term (in Eq. [2.19]) is not, only very large abundance gradients can affect the diffusion velocity. Therefore, the internal abundance distribution approximately satisfies the relation:

$$\mathcal{F}(r) = cst \simeq r^2\rho(U+U_{\rm w})c \tag{2.21}$$

which expresses the conservation of particle flux throughout the stellar envelope. In this discussion, for the purpose of illustration, one may also neglect the term involving $\frac{\partial \ln T}{\partial r}$ because it is not dominant in the relevant regions of the envelope (although it is always included in our calculations).

The implications of flux conservation are illustrated in Fig. 2.7 for three atomic species (Ca, Mn and Ni) from the 2.5 $M_\odot$ model of Fig. 2.6. For all three species, the flux is always positive as may be seen from the top row. While $g_{\rm rad}$(Ca) is smaller than gravity at some mass shells (middle row), the downward diffusion velocity of Ca is never larger than the wind velocity (see Fig. 2.10) so that it is dragged by the wind toward the surface. In general, as long as the absolute value of the diffusion velocity is smaller than the wind velocity, the concentration simply increases in order to conserve the flux (as implied by Eq. [2.21])[11]. This equation may then be

[9] $\frac{m_{\rm p}}{kT}$ had been erroneously forgotten in the 2nd and 3rd terms.
[10] This equation is not used for the calculations. For more details see Turcotte et al. (1998b).
[11] This resembles the results for oxygen which are discussed in Landstreet et al. (1998).

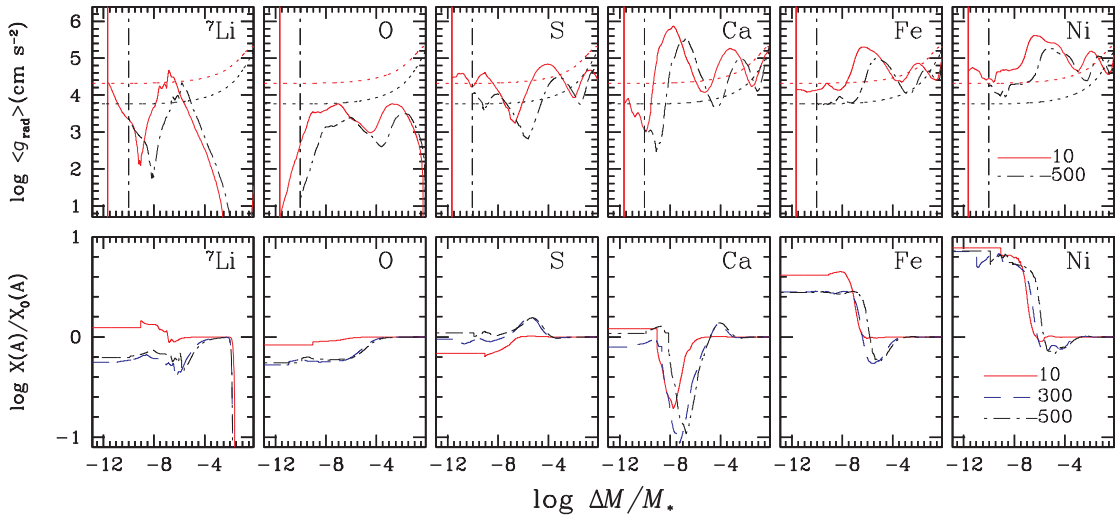

Figure 2.6: [Top row] Radiative accelerations (solid line) and local gravity (dotted line) in a 2.5 $M_\odot$ model with a mass loss rate of $1\times10^{-13}\,M_\odot yr^{-1}$. The corresponding internal abundance variations are shown at three ages [bottom panel]. All curves are identified by their age (in Myr). The vertical lines show the position of the bottom of the surface H convection zone.

used here for all three species. As may be seen from the bottom row, after 3 Myr, the concentration has adjusted only down to $\Delta M/M_*\simeq 3\times10^{-7}$. Therefore, below this depth, the local flux (top row) mainly reflects the local $g_{\rm rad}$. After about 10 Myr however, the abundance has adjusted to carry the flux which arrives from deep inside the star (down to $\log\Delta M/M_*\simeq -6$). This may be evaluated using $\Delta M \simeq \dot{M}\times t$ for a mass loss rate of $10^{-13}\,M_\odot yr^{-1}$. After 100 Myr, the concentration has adjusted to the flux down to $\log\Delta M/M_*\simeq -5$ and the concentration becomes the mirror image of $g_{\rm rad}$ from the surface to that depth as may be seen by comparing the middle and bottom rows. There are Ca overabundances at $\log\Delta M/M_* = -8.5$ and -4.5, which occur at $g_{\rm rad}$(Ca) minima (see also Fig. 2.6), while the minimum abundance occurs at the maximum of $g_{\rm rad}$(Ca). However, if the wind velocity were not larger than the settling velocity, a gradient could develop to conserve the flux. If this gradient cannot become large enough to conserve flux, then the $\partial c/\partial t$ term (in Eq. [2.7]), which is required to be zero in the kinematic approximation becomes

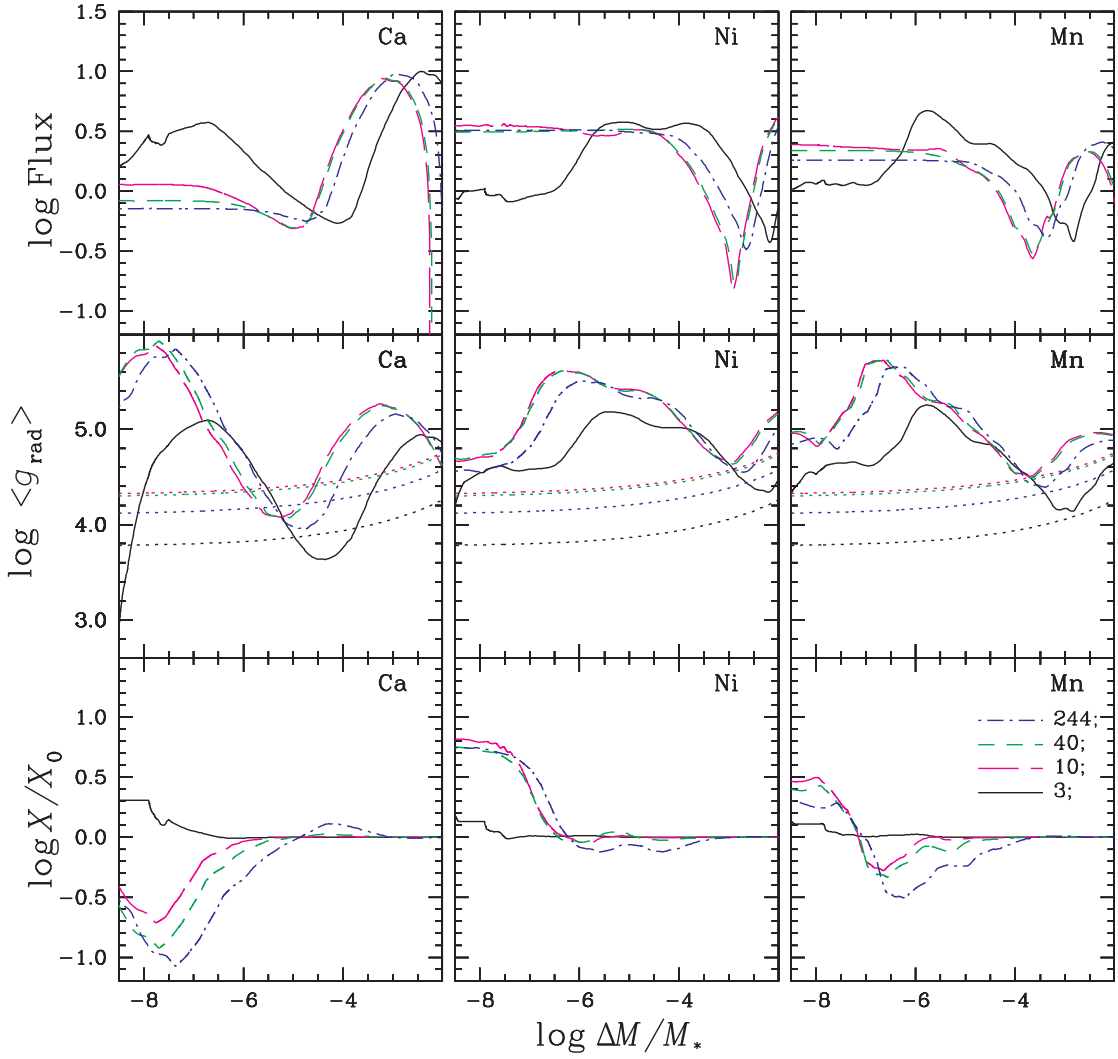

Figure 2.7: Comparison of the normalized local flux with radiative accelerations and internal abundances for 3 elements at 4 different ages (in Myr) for a 2.5 $M_\odot$ model with a mass loss rate of $10^{-13}\,M_\odot yr^{-1}$. In the middle row, $\log g$ is identified at different ages by the dotted lines.

important, and the approximation leading to Eq. [2.21] becomes invalid.

The net elemental flux toward the surface quickly becomes nearly constant in time once the local abundance has adjusted itself to conserve the flux. The remaining slow variation in time of the flux comes from the variation of $g_{\rm rad}$ where the matter originated, deep in the star, at $\Delta M \simeq \dot{M} \times t$.

2.5.1.2 The kinematic approximation

By following the analysis of Michaud & Charland (1986), the surface abundance of elements which are pushed upwards by $g_{\rm rad}$ and/or dragged by the wind throughout the stellar envelope can be approximated by using a simple kinematic equation *so long as the evolutionary effects and the contribution of* $\frac{\partial c}{\partial t}$ *are small (i.e. there is no significant accumulation).* The problem of determining surface abundances thereby reduces to a kinematic problem. The only required quantity is the local velocity and, consequently, the radiative acceleration. Elements which originated at r_1 at $t = 0$ arrive at r_{cz}, the radius at the bottom of the surface convection zone at a time t_1 given by:

$$t_1 = \int_{r_1}^{r_{cz}} \frac{dr}{v_{\rm w} + v_{\rm D}}. \tag{2.22}$$

Because of flux conservation, the flux of an element A entering the convection zone at t_1 is then given by:

$$\phi(t_1, A) = c_0(A, r_1)(v_{{\rm D},r_1} + v_{{\rm w},r_1})\rho_{r_1}\frac{r_1^2}{r_{cz}^2}, \tag{2.23}$$

where $c_0(A, r_1)$ is the initial abundance of A at r_1 and $v_{\rm D1}$, $v_{\rm w1}$ and ρ_1 are evaluated at r_1. This is valid for the region above which $v_{\rm w} + v_{\rm D} > 0$ and for $t < t_{0A}$, the time required for the element A to migrate from the point where $v_{\rm w} + v_{\rm D} \simeq 0$ to the bottom of the convection zone. Since diffusion timescales are much longer than convective mixing time scales, the convection zone is assumed thoroughly mixed up to the bottom of the wind forming region. Within the context of unseparated mass loss, the evolution of the abundance of A in the surface convection zone, $c_{\rm cz}(A)$ can then be approximated by:

$$M_{\rm cz}\frac{\partial c_{\rm cz}(A)}{\partial t} = -\dot{M}c_{\rm cz}(A) + 4\pi r_{\rm cz}^2\phi(t_1, A), \tag{2.24}$$

where M_{cz} and r_{cz} are respectively the mass of the superficial convective zone and the radius at the bottom of this convection zone. Eq. [2.24] is *not* used for our calculations, but is used to interpret the results.

2.5.2 Discussion: Internal variations

By comparing Figs. 2.5 and 2.6, it is clear that the same mass loss rate leads to quite different internal concentration variations in stars of different mass. There are two main reasons for this. First, in the more massive star, the surface convection zone is much thinner, therefore the radiative zone is extended upward into regions where the diffusion timescales are much shorter. Second, because of the ${T_{\rm eff}}^4$ dependence of the photon flux, most $g_{\rm rad}$s are stronger in more massive stars.

For both models, diffusion mainly affects the outer 10^{-3} of the star's mass; the point above which the effects of atomic diffusion become visible on Figs. 2.5 and 2.6 will be defined as *the point of separation*. Atomic diffusion can also act deeper in the star (e.g. in the core), though in A and F main–sequence stars, its effects are much smaller below than above the point of separation.

2.5.2.1 The 1.5 $M_\odot$ models

For the 1.5 $M_\odot$ model with a mass loss rate of $1 \times 10^{-13}\,M_\odot{\rm yr}^{-1}$ (henceforth designated 1.50W1E-13 for short), internal anomalies are small. Iron reaches an overabundance of 1.5, and nickel of 2.0. Lithium, oxygen and calcium decrease from the point of separation up to the bottom of the surface convection zone. Differences in $g_{\rm rad}$ lead to differences in their behavior. Due to a strong $g_{\rm rad}$ immediately below the surface CZ, Ca is most underabundant in that region, since Ca is pushed into the convection zone by both $g_{\rm rad}$ and the wind while little arrives from below because of the minimum in its $g_{\rm rad}$ at $\log \Delta M/M_* \sim -4.5$. At 500 Myr, its underabundance reaches a factor of 4 while the Li underabundance below the SCZ is about -0.3 dex.

In the lower row of Fig. 2.5, one sees that when the wind is 10 times smaller,

the internal variations are much stronger since the advection by $v_{\rm wind}$ is not strong enough to prevent elemental accumulation. Lithium has an interesting behavior: it has a local maximum where its $g_{\rm rad}$ equals gravity. The underabundances of Li and O drop to -0.95 and -1.35 dex respectively, while underabundances greater than 2 dex are reached for S and Ca. Through Eq. [2.21], when $U_{\rm w}$ is smaller, the change in U due to $g_{\rm rad}$ has a larger effect on concentration. This is particularly true for Fe: due to a dip in $g_{\rm rad}$ (see Fig. 2.5), it accumulates near $\log \Delta M/M_* = -6.5$ (where $T = 200\,000$ K). The overabundances of Fe and Ni reach 1.25 and 1.45 dex respectively. The implications of this accumulation are analyzed in Fig. 2.8. The local opacity bump in the region between $\log \Delta M/M_* \simeq -6.0$ and -6.8 leads to the appearance of an iron peak convection zone ($\nabla_r - \nabla_{ad}$ changes sign) at around 70 Myr which survives until the end of the simulation. Fe and Ni reinforce each other. Only the $10^{-14}\,{\rm M}_\odot{\rm yr}^{-1}$ model becomes convective; doubling the mass loss rate reduces the Fe accumulation enough for the iron peak convection zone not to appear.

In fact, a noteworthy transition occurs in internal solution types between the 1.50W1E-14 and 1.50W2E-14 models (Fig. 2.8). In the 1.50W1E-14 model, Fe is overabundant where $g_{\rm rad}({\rm Fe}) > g$, whereas Fe is minimal at the $g_{\rm rad}({\rm Fe})$ maximum in the 1.50W2E-14 model (similarly, Ca is minimal at the $g_{\rm rad}({\rm Ca})$ maximum in the 2.50W1E-13 model shown in Fig. 2.7). This is due to the relationship between $v_{\rm wind}$ and the settling velocities for each individual species; if the settling velocity dominates locally, the element will accumulate locally, and the solution will behave as does Fe in the 1.50W1E-14 model. When $v_{\rm wind}$ dominates throughout the envelope, the solution is determined by flux conservation, as shown in Fig. 2.7. This transition separates the solution in which the surface abundances reflect matter which is advected from deep inside the star ($v_{\rm wind} > v_{\rm sett}$) from the solution in which the surface reflects variations at the bottom of the SCZ (as in the models of Watson 1971 and Alecian 1996). This transition occurs only for elements whose

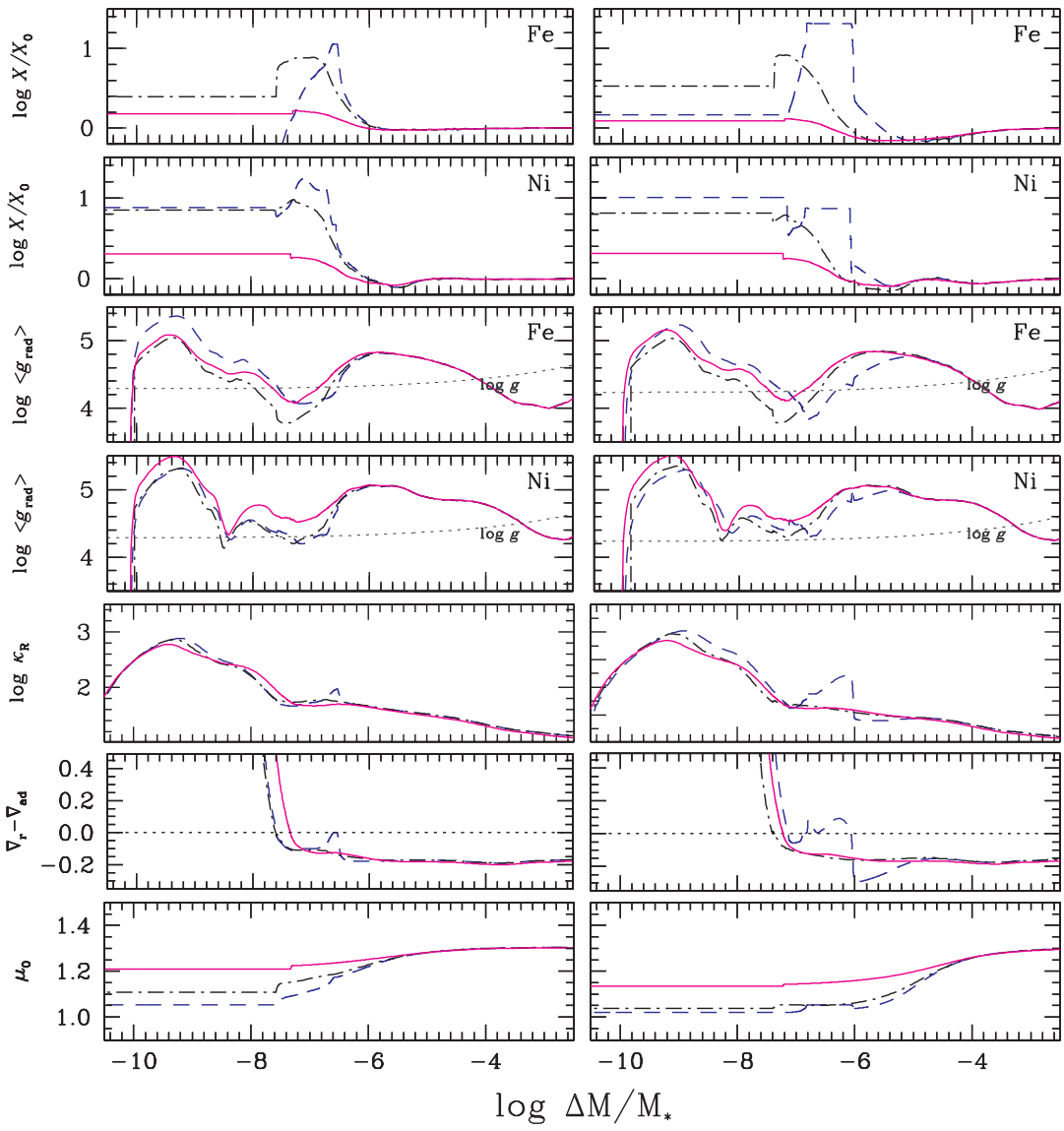

Figure 2.8: Internal abundances (Fe, Ni), radiative accelerations (Fe, Ni), Rosseland opacity, the difference between the radiative and adiabatic temperature gradients as well as the mean molecular weight per nucleus for three 1.5 $M_\odot$ models with different mass loss rates ($10^{-14}\,M_\odot yr^{-1}$ [dashed line], $2\times10^{-14}\,M_\odot yr^{-1}$ [dot-dashed line] and $10^{-13}\,M_\odot yr^{-1}$ [solid line]) at 70 Myr (left column) and 500 Myr (right column). At this mass, the Fe peak convection zone (between $\log \Delta M/M_* = -6$ and -7) only appears for the mass loss rate of $10^{-14}\,M_\odot yr^{-1}$. The H-He convection zones remain linked for all mass loss rates.

$g_{\rm rad}$ has a minimum smaller than gravity close to the bottom of the SCZ.

A large enough mass loss rate also affects the position of the bottom of the surface H-He convection zone by keeping He from sinking. Since it also modifies the accumulation of metals, mainly iron and nickel, its effect is complex: the relative position of the bottom of the convection zone for the three mass loss rates in Fig. 2.8 is different at 70 and 500 Myr.

The inversion of the molecular weight gradient (bottom row of Fig. 2.8 at 500 Myr), which eventually follows the appearance of the iron accumulation around 200 000 K, has been suggested to affect the presence of the iron peak convection zone (Théado et al. 2009). In the present calculations however, the iron peak convection zone appears (as seen at 70 Myr) before the inversion appears so that while the size of the convection zone could be affected by the μ gradient inversion, its appearance cannot be affected. This will be further discussed in Sect. 2.8.

2.5.2.2 The 2.5 $M_\odot$ models

Large overabundances of iron peak elements are obtained in the 2.5 $M_\odot$ models (Fig. 2.6): Ni and Fe are overabundant by factors of 7.5 and 4 respectively. Calcium on the other hand is found to be up to 10 times underabundant around $\log \Delta M/M_* = -6.5$, where its $g_{\rm rad}$ is near a maximum. This may seem counter intuitive but is a consequence of Eq. [2.21]. Since the flux is conserved, where $v_{\rm D}$ is large and positive, c decreases, which is precisely what happens for Ca just below the convection zone (see Figs. 2.6 and 2.7 and the last two paragraphs of Sect. 2.5.1.1).

Wind and diffusion velocities are compared in Fig. 2.10. The wind velocity decreases more rapidly than the diffusion velocity as $\log \Delta M/M_*$ increases. For instance, the absolute value of the ^{4}He settling velocity is 50 times smaller than the larger of the two wind velocities at $\log \Delta M/M_* = -12$ but equals it at $\log \Delta M/M_* = -4.5$. For smaller mass loss rates the settling velocity dominates

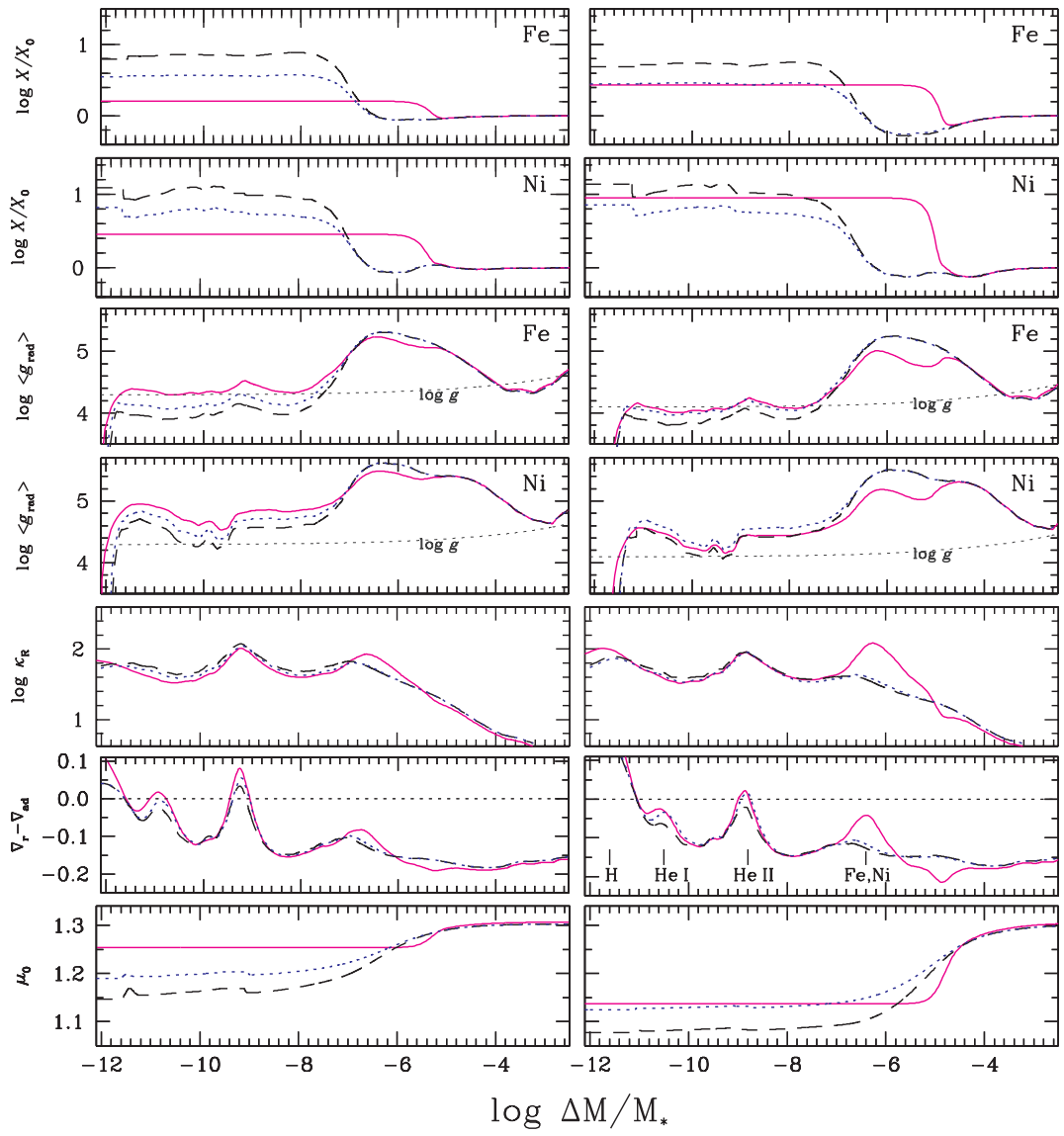

Figure 2.9: Internal abundances (Fe, Ni), radiative accelerations (Fe, Ni), Rosseland opacity, the difference between the radiative and adiabatic temperature gradients as well as the mean molecular weight per nucleus for two 2.5 $M_\odot$ models with different mass loss rates ($10^{-13}\,M_\odot yr^{-1}$ [dotted line] and $5\times10^{-14}\,M_\odot yr^{-1}$ [dashed line]) as well as a model with turbulence [solid line] at 30 Myr (left column) and around 250 Myr (right column). The maxima in the ∇_r-∇_{ad} row are mainly due to opacities from H, He I, He II and Fe/Ni from left to right respectively.

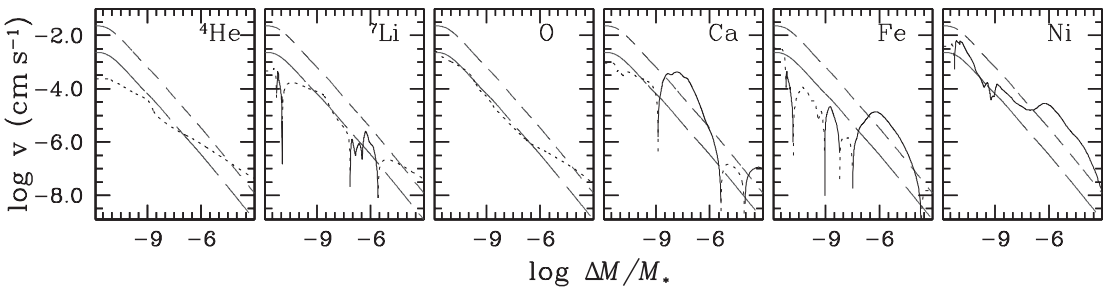

Figure 2.10: Wind velocities (long dashed line: $10^{-14}\,\mathrm{M_\odot yr^{-1}}$; dashed line: $10^{-13}\,\mathrm{M_\odot yr^{-1}}$) and diffusion velocities (solid when positive, towards the surface, and dotted when negative) of a few selected elements in two 2.50 $\mathrm{M_\odot}$ models at 300 Myr. For most species, wind velocities decrease more rapidly inwards than diffusion velocities.

closer to the surface. Calcium has an upward diffusion velocity over the interval $-9 < \log \Delta M/M_* < -6$ and it is up to ten times larger than the wind velocity. Fe and Li have smaller upward diffusion. Those velocities determine local concentration via Eq. [2.21] (see the end of Sect. 2.5.1.1).

Fig. 2.9 allows an analysis of the effect of varying mass loss rates on surface convection zones and to distinguish the effects of mass loss from those of turbulence (see Sect. 2.6). The abundances and g_{rad} of both Fe and Ni are presented since they are the main contributors to the appearance of the iron peak convection zones in 1.5 $\mathrm{M_\odot}$ models. In 2.5 $\mathrm{M_\odot}$ models however, iron convection zones do not appear for the two mass loss rates considered. The Fe and Ni abundances remain slightly below solar where g_{rad}(Fe) and g_{rad}(Ni) are largest so that they do not lead to an increase of opacity where they could contribute most to opacity. The wind velocity is ten times larger than the diffusion velocity of Fe for $\log \Delta M/M_* \geq -8$ so that Eq. [2.21] forces the solution to be nearly constant over that range. This is to be contrasted with their behavior in 1.5 $\mathrm{M_\odot}$ models.

Even a small mass loss rate difference can have important effects on the stellar structure in 2.5 $\mathrm{M_\odot}$ models. For both mass loss rates considered, the He I convec-

tion zone disappears early in the evolution, at around 30 Myr (see the sixth row of Fig. 2.9). The He II convection zone on the other hand only disappears in the model with the smaller mass loss rate, the 2.50W5E-14 model, at around 200 Myr. This is because the inward diffusion velocity of He dominates the wind velocity at a shallower depth than in the 2.50W1E-13 model (see Fig. 2.10), so that a more pronounced He underabundance develops to conserve the flux.

2.5.3 Surface abundance variations

2.5.3.1 The 1.5 $M_\odot$ models

The evolution of surface abundances is shown for several 1.5 $M_\odot$ models in the upper two rows of Fig. 2.11. For the 1.50W1E-12 model, the largest anomaly encountered, which is for Ni, reaches a mere 0.05 dex, and it is quickly flattened after a brief period. Such a mass loss rate effectively wipes out any surface effects of chemical separation. In the 1.5W1E-14 model, some of the calculated underabundances are very large (greater than 2 dex for S as well as C and Si, which are not shown). With the exception of Fe, all iron peak elements are overabundant throughout the simulation. Both Ni and Mn become more than 1 dex overabundant at around 500 Myr and 50 Myr respectively.

Iron surface abundances are particularly interesting for this model since it is the only one to have an iron surface underabundance which spans 500 Myr[12]. This is due to the accumulation of iron under the surface convection zone, and the subsequent appearance of an iron peak convection zone (see Fig. 2.8). Although not shown here, a separate iron peak convection zone is expected for all simulations for masses between 1.47 $M_\odot$ and 3.0 $M_\odot$ when the mass loss rate is equal to or below $\sim 10^{-14}\,M_\odot yr^{-1}$.

The 1.50W2E-14 and 1.50W5E-14 models generate surface iron overabundances

[12]We may assume however that if the simulation had not encountered significant instabilities, the shown iron abundance trend would have continued and iron would have become overabundant.

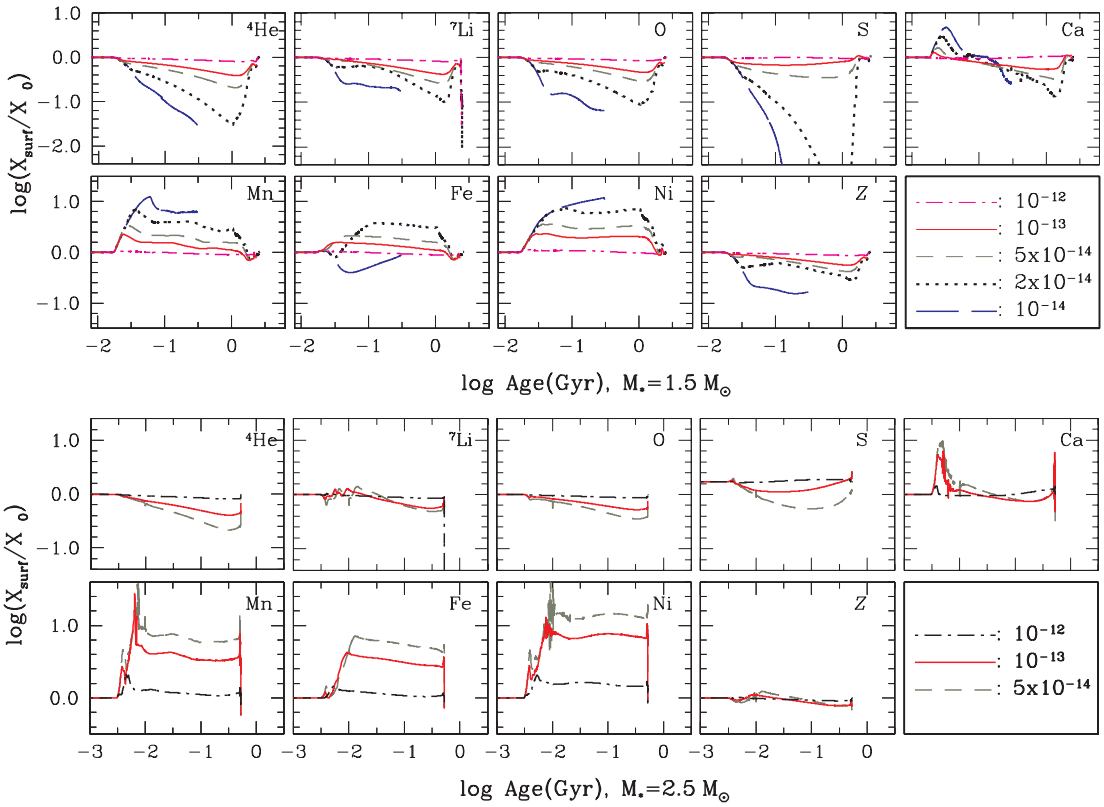

Figure 2.11: Surface abundance variations for five 1.50 $M_\odot$ models [top 2 rows] as well as three 2.50 $M_\odot$ [lower 2 rows] models with $Z_0 = 0.02$ and varying amounts of mass loss (in $M_\odot yr^{-1}$). The model was ended at around 550 Myr due to numerical instabilities which were caused by the severe underabundances of many elements (of which S is shown). It is also the only model which leads to the appearance of a separate iron peak convection zone. In the bottom panel, the two models with smaller mass loss rates lead to a surface metallicity which has a maximum around 10 Myr before falling below Z_0 around 100 Myr.

of about 0.5 and 0.35 respectively at 300 Myr. The calcium abundance is particularly interesting since for all models, an overabundance is predicted at the beginning of the main sequence evolution followed by an underabundance. The underabundance is present over a much larger fraction of the evolution than the overabundance. The Ca calculations are compared in Fig. 2.12 with those carried out by Alecian (1996). His calculations were undertaken in static stellar models;

therefore, evolutionary effects were not included. There are also slight differences in $T_{\rm eff}$ between our calculations ($T_{\rm eff} \simeq 7200\,{\rm K}$ at the beginning of diffusion but decreases as the star evolves) and his simulations ($T_{\rm eff} = 7500\,{\rm K}$). There are also differences in $g_{\rm rad}({\rm Ca})$: his calculated $g_{\rm rad}({\rm Ca})$ has a peak which is 10 times smaller than obtained in a model of similar $T_{\rm eff}$ with our code. Results are compared in Fig. 2.12 for three mass loss rates. In all three cases, the maximum anomaly as well as the overall behavior of the curves correspond well. The overabundance peaks are however not quite so wide in our calculations as in his. The agreement seems satisfactory.

2.5.3.2 The 2.5 $M_\odot$ models

In the 2.5 $M_\odot$ models (lower two rows of Fig. 2.11), the surface abundances of heavier metals (say $Z > 17$) can be characterized by two distinct episodes: a steep abundance spike, followed by a smooth decline. The initial peaked episode around 10 Myr shows matter which was above $\log \Delta M/M_* \simeq -6$ at the onset of diffusion, advected to the surface by the stellar wind.

As discussed at the end of Sect. 2.5.1.1, the initial flux distribution reflects $g_{\rm rad}$ since, originally, the concentration is the same throughout the envelope; then, as time elapses, the internal abundances naturally evolve in such a way that flux is conserved throughout the envelope (see Fig. 2.7). In so far as the $\partial c/\partial t$ term is negligible (i.e. flux is conserved), the surface reflects the point in the initial flux distribution which is dragged by $v_{\rm wind}$. Therefore, when the initial internal flux profile of an element has important variations near the surface due to strong variations in $g_{\rm rad}$ (as is the case for Ca and Ni, see Fig. 2.6 and 2.7), these variations appear on the surface in a time which is related to the mass loss rate.

Quantitatively, in the 2.50W1E-13 model (solid line), a given element's surface abundance at 100 Myr depends on the initial flux variations (caused by $g_{\rm rad}$ varia-

tions at $t = 0$)[13] at a depth of $\Delta M \simeq \dot{M} \times t = 10^{-13}\,\mathrm{M_\odot yr^{-1}} \times 10^8\,\mathrm{yr} \simeq 10^{-5}\,\mathrm{M_\odot}$. In Fig. 2.11, the slight bump in surface Ni abundance around 100 Myr for the 2.50W1E-13 model reflects the small bump in the initial flux distribution of Ni around $\log \Delta M/M_* \simeq -5$ (see Fig. 2.7).

The previous example is an application of Eq. [2.22] and shows that the time it takes for a given internal variation to reach the surface is inversely proportional to the mass loss rate. This is further illustrated by the fact that the surface Ni abundance peak around 10 Myr appears earlier as the mass loss rate increases (see Fig. 2.11). The dilution by the convection zone (Eq. [2.24]) is relatively small because it has a relatively small mass. Also, the rapid variations seen around this Ni abundance peak reflect the many internal flux variations which were above $\log \Delta M/M_* \simeq -6$ at $t = 0$. For a mass loss rate of $10^{-13}\,\mathrm{M_\odot yr^{-1}}$, these variations all reach the surface within 10^7 yr.

As a consequence, the nearer an internal flux variation is to the surface at $t = 0$, the quicker it appears at the surface, and the quicker it disappears. A flux variation that spatially spans from the surface to $\log \Delta M/M_* = -7$ at $t = 0$ appears and disappears at the surface in less than one million years for a mass loss rate of $10^{-13}\,\mathrm{M_\odot yr^{-1}}$.

The amplitude of the surface variations also depends on the mass loss rate; as the mass loss rate increases, each internal variation of the flux at $t = 0$ manifests itself at the stellar surface with a smaller amplitude since more enriched/depleted matter is evacuated from the SCZ (Eq. [2.24]). This is illustrated by the decreasing amplitude of the initial surface abundance spikes for Mn and Ni as the mass loss rate increases (Fig. 2.11).

The conservation of the flux down to $\log \Delta M/M_* \simeq -5.5$ to -6.5 (depending on the age and mass loss rate) has another important consequence: diffusion be-

[13] Remember that at $t = 0$, the flux distribution is essentially proportional to the local abundance multiplied by the local g_{rad} since the composition is homogeneous.

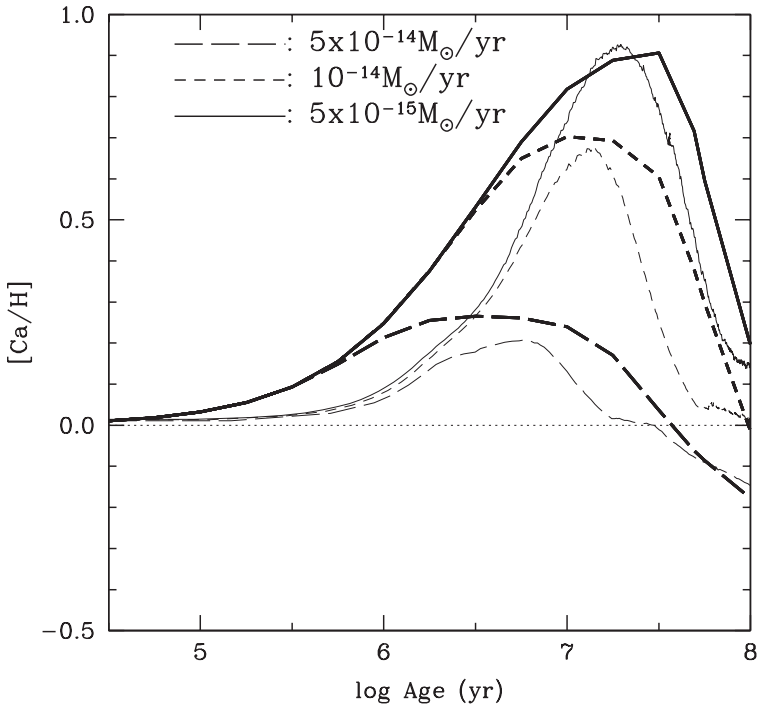

Figure 2.12: Evolution of Ca surface abundances for 1.5 $M_\odot$ models with different mass loss rates. The calculations from Alecian (1996) are shown in bold.

tween the surface convection zones (i.e. between the H and either of the two He convection zones) has practically no influence on the surface abundances. Matter which originates from between the H and He convection zones ($\log \Delta M/M_* \simeq -10$) appears at the surface within 10^3 years for a mass loss rate of $10^{-13}\,M_\odot yr^{-1}$. The detailed calculation of chemical transport between these zones is then not required in order to accurately obtain the surface abundance solution. To verify the accuracy of this assertion a model was calculated with homogenized abundances between all surface convection zones, and it was found that the surface solution was practically identical to the surface solution obtained when separation was allowed between SCZs. After a mere 3 Myr of a star's main–sequence life with a mass loss rate of 10^{-13} $M_\odot yr^{-1}$, anomalies which appear at the surface reflect the separation which occurs below $\log \Delta M/M_* = -7$. Hence, *for most of the main–sequence lifetime*

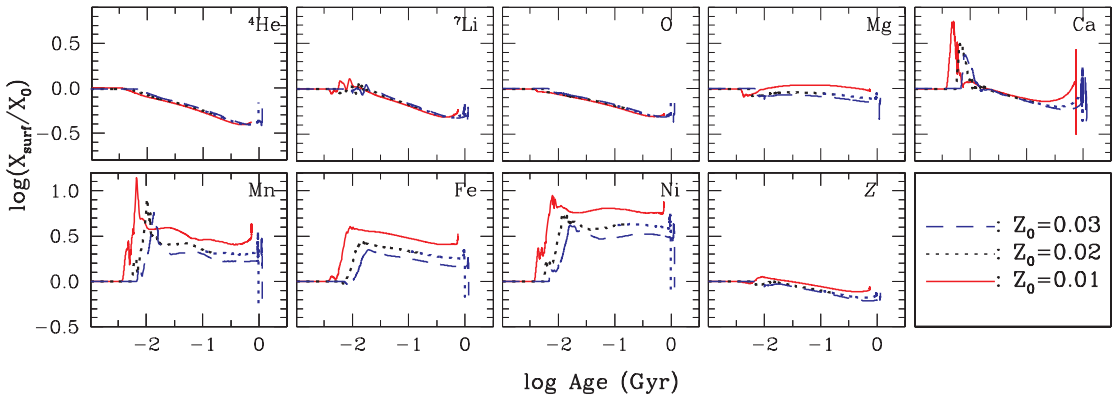

Figure 2.13: The effect of varying initial metallicity on the evolution of abundance anomalies at the surface of a 2.0 $M_\odot$ star with a mass loss rate of $10^{-13}\,M_\odot yr^{-1}$. Models are shown for $Z_0 = 0.01$ (solid), $Z_0 = 0.02$ (dashed line) and $Z_0 = 0.03$ (long dashed line). The original abundance of Li is assumed independent of Z_0.

of models compatible with observations, the surface abundance solution depends on the separation which takes place around $\log \Delta M/M_* \simeq -5.5$ *to* -6.5.

This is analogous to the turbulence models of Richer et al. (2000), in which surface abundances depend solely on the separation which occurs below 200 000 K. In our calculations, however, abundance variations are present throughout the stellar envelope because no mixing is enforced outside of convection zones. In that respect, in the presence of mass loss, it is clear that the chemical separation responsible for the AmFm phenomenon involves up to $\log \Delta M/M_* = -5$ of the star's mass.

2.5.3.3 The effect of Z, age and $T_{\rm eff}$

In Fig. 2.13, one sees that the main features of the time evolution of surface abundances are similar for three different initial metallicities. However varying the initial metallicity can have an important effect on the amplitude of surface anomalies, though not for all elements. For elements such as CNO, varying Z_0 has relatively little effect on the surface abundance anomalies since these elements are not supported by the radiation field. For heavier iron peak elements, supported by

the radiation field, the ramifications are much more apparent since their lines are often saturated and flux sharing becomes prevalent. In fact, the lower metallicity models have larger anomalies, when compared to the original abundances of the model, since the same flux is shared among fewer atoms. Also, the abundance peaks appear earlier during evolution as Z decreases since the $g_{\rm rad}$ profiles with respect to $\Delta M/M_*$ are shifted toward the surface as Z decreases. However the situation is different if one compares to a fixed set of abundances. By comparing Figs. 2.11 and 2.13 one notes that a reduction of mass loss by a factor of 1.5 approximately compensates for a reduction of Z_0 from 0.03 to 0.02 for the absolute final abundance of Fe and other elements which are supported. It however amplifies the effect of the reduction for elements which are not supported by $g_{\rm rad}$ such as CNO.

Figure 2.14 shows the surface abundances as a function of atomic number for a 2.5 $M_\odot$ model at five different ages. A large overabundance of Ti (1.3 dex) occurs as early as 5 Myr because $g_{\rm rad}$(Ti) has a maximum near the surface, and the bump it causes in the original flux is dragged by the wind. The same occurs for Cr and Mn but to a lesser extent. There is also a slight overabundance of Li which appears at this age. At 9 Myr, the Ti overabundance has weakened and most iron peak elements reach their highest values: Fe peaks at 0.65 dex and Ni peaks at 1.0 dex. Throughout the star's main–sequence evolution, the surface abundances change only slightly, as highlighted by the similarity in the curves at 70 and 250 Myr. Until the final dredge-up (i.e. the post turn-off increase in SCZ mass), which begins around 520 Myr, the iron peak abundances decrease only slightly. For instance, Fe only drops 0.15 dex over the entire main–sequence lifetime. The changes will be slightly more significant for underabundant elements because they are not supported by the radiation field, and so the amplitude of the underabundances is largely dependant on time (due to settling). For CNO, the surface underabundances appear around 9 Myr and continuously decrease down to about -0.40, -0.38 and -0.35 dex for C, N and O respectively, after which

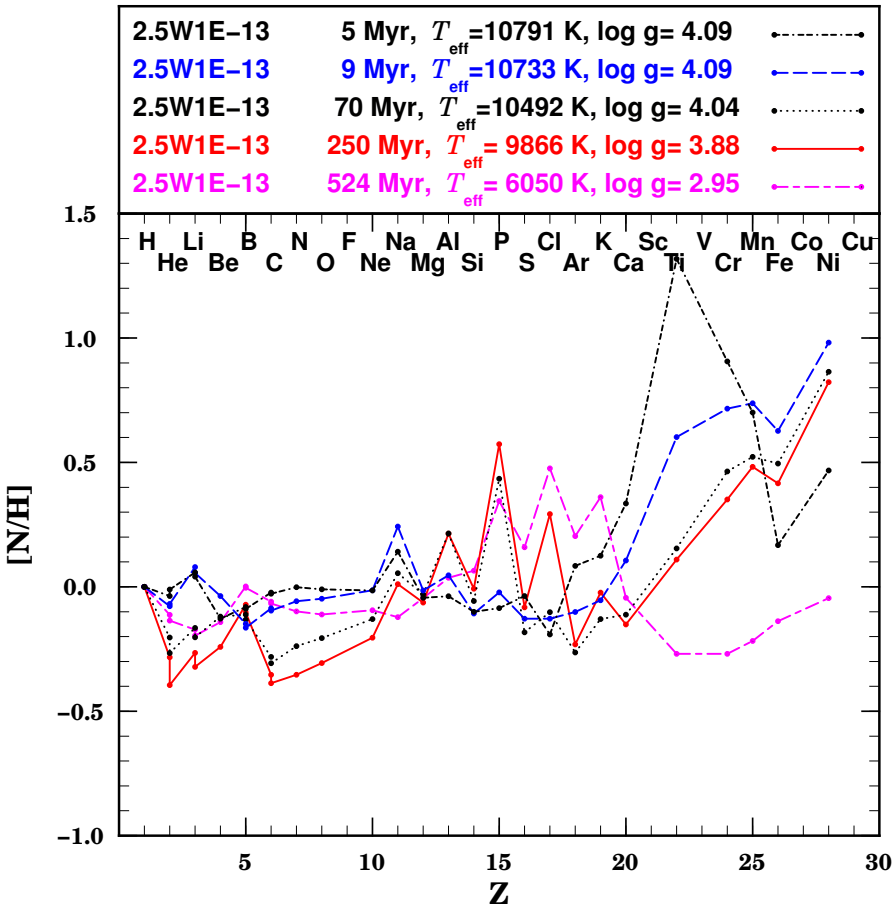

Figure 2.14: Surface abundance anomalies at five ages (5, 9, 70, 250 and 524 Myr) for a 2.50 $M_\odot$ star with a mass loss rate of $10^{-13}\,M_\odot yr^{-1}$.

dredge-up begins. *At all times, the surface abundances reflect the matter which is exposed by the wind at the specific age.* With that in mind, one notes from the curve at 524 Myr, that the material at $\log \Delta M/M_* \simeq -2$ has not yet reached the surface since LiBeB abundances have not yet dipped due to material advecting to the surface from regions where they burn (see Fig. 2.6). At this age, the surface convection zone extends down to $\log \Delta M/M_* = -4.5$, and while iron peak elements are now underabundant, an overabundance has appeared for S (and a few species of similar atomic mass) because of the dredge up of the maximum of its abundance at $\log \Delta M/M_* \sim -5.2$ (see Fig. 2.6, one also notes the underabundances of Fe and

Ni near $\log \Delta M/M_* \sim -5$ which explain their underabundance at 524 Myr). This time dependent behavior is compared to models with turbulence in Sect. 2.6.

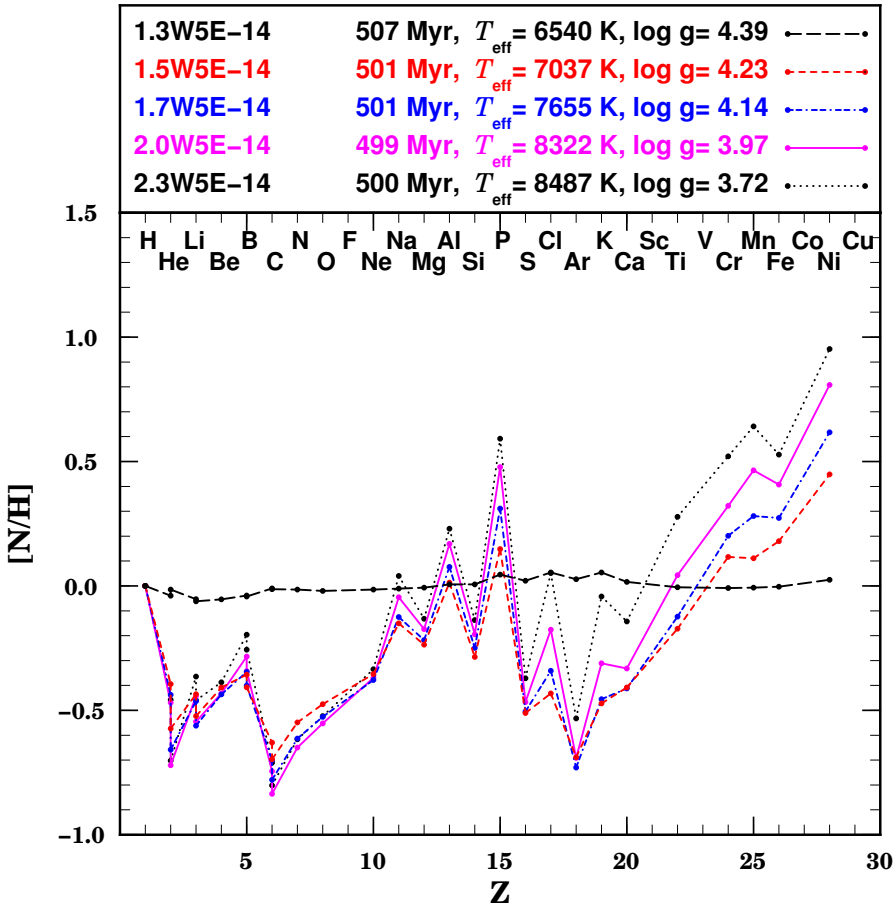

Figure 2.15: The effect of varying $T_{\rm eff}$ (or stellar mass) on the surface abundance profiles of 5 models at 500 Myr for a mass loss rate of 5×10^{-14} $M_\odot yr^{-1}$.

Figure 2.15 shows the superficial abundances at 500 Myr for models of different masses with the same mass loss rate (5×10^{-14} $M_\odot yr^{-1}$). The 1.3 $M_\odot$ has much smaller anomalies than the others. At a given age, stars of 1.5 to 2.3 $M_\odot$ have very similar underabundances of elements from He to Ne, since for a given mass loss rate, they essentially depend on time. Iron peak overabundances increase as $T_{\rm eff}$ increases. This is partly caused by the increase of $g_{\rm rad}$ with $T_{\rm eff}$ as well as by the reduction of the mass of the surface convection (if the SCZ is more massive,

the anomalies will be reduced by dilution). This behavior is different from what is obtained in turbulence models, and will also be discussed in Sect. 2.6.

2.5.3.4 Stars of the lithium gap

The surface Li abundances for stars of the lithium gap without mass loss are shown in Fig. 2.16. The models heavier than 1.45 $M_\odot$ ceased converging before the end of their main–sequence lifetime because of numerical instabilities. In the absence of mass loss, the H-He and iron peak convection zones are split by the appearance of a thin radiative zone for all models of 1.47 $M_\odot$ or more. Variations within this layer appear at the surface of the 1.47 $M_\odot$ model near 200 Myr.

A close inspection of Fig. 2.16 shows a distinct separation between the 1.46 $M_\odot$

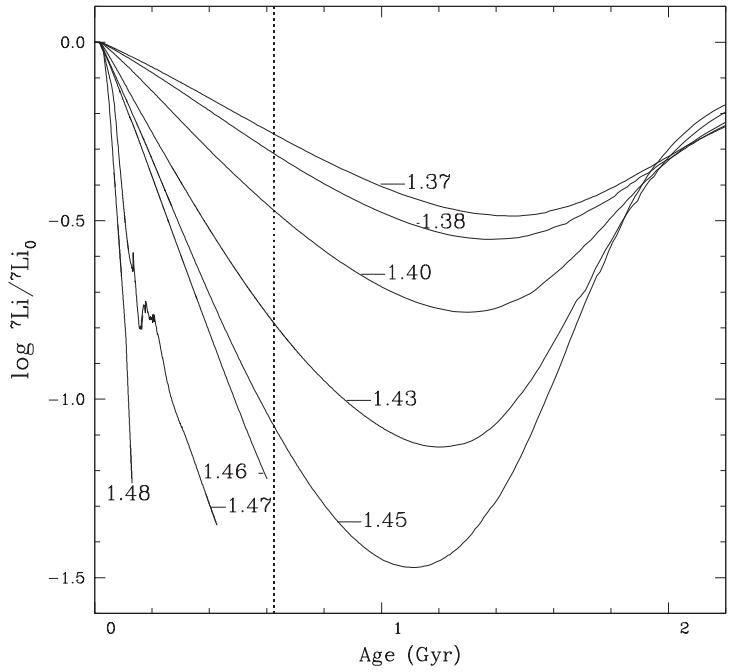

Figure 2.16: Evolution of ^{7}Li surface abundances for models with masses ranging from 1.37 $M_\odot$ to 1.48 $M_\odot$ with no mass loss and $Z_0 = 0.02$. The vertical line indicates 625 Myr, the age of the Hyades open cluster. This can be compared to Fig. 6 of Richer & Michaud (1993).

and 1.47 $M_\odot$ models; the 1.46 $M_\odot$ model behaves more like the 1.45 $M_\odot$ model while the 1.47 $M_\odot$ model's behaviour most resembles the 1.48 $M_\odot$ model. Again, this is because of the appearance of a radiative zone immediately above the iron peak CZ in the 2 heavier models.

The abundances obtained near the age of the Hyades open cluster ranged from -0.25 dex for the 1.37 $M_\odot$ model to -1.25 dex for the 1.46 $M_\odot$ model. Lithium is underabundant for all models throughout evolution.

By comparing these results with those shown in Fig. 6 of Richer & Michaud (1993), one first notices that the curves have very similar behavior in time; the minima occur at nearly the same age and the curve shapes are nearly identical. However, the underabundances obtained in our calculations are systematically smaller. For instance, their 1.43 $M_\odot$ model is 250 times underabundant around 1.23 Gyr, while our 1.43 $M_\odot$ model is only 14 times underabundant at the same age. A careful analysis of the results determined that the difference was principally due to the difference in the mass of the SCZ. If the convection zone is homogeneous and emptied through its bottom, then:

$$\frac{d(X\Delta M_{\rm cz})}{dt} = X w_i \rho \tag{2.25}$$

where X is the mass fraction in the SCZ (and on the surface), $\Delta M_{\rm cz}$ the mass in the SCZ, w_i the diffusion velocity and ρ the density immediately below the SCZ. By integrating this equation and comparing diffusion time scales for the different values of $M_{\rm cz}$, the differences in surface lithium abundances for models of the same mass can be explained by the difference in $M_{\rm cz}$. This difference in CZ mass is mainly due to the inclusion of metal diffusion in our models. In fact, the increased opacity in our models due to heavy metal accumulation considerably increases opacity at the BSCZ, thereby extending it inwards.

In Fig. 2.17, the surface lithium abundances are shown for different isochrones of

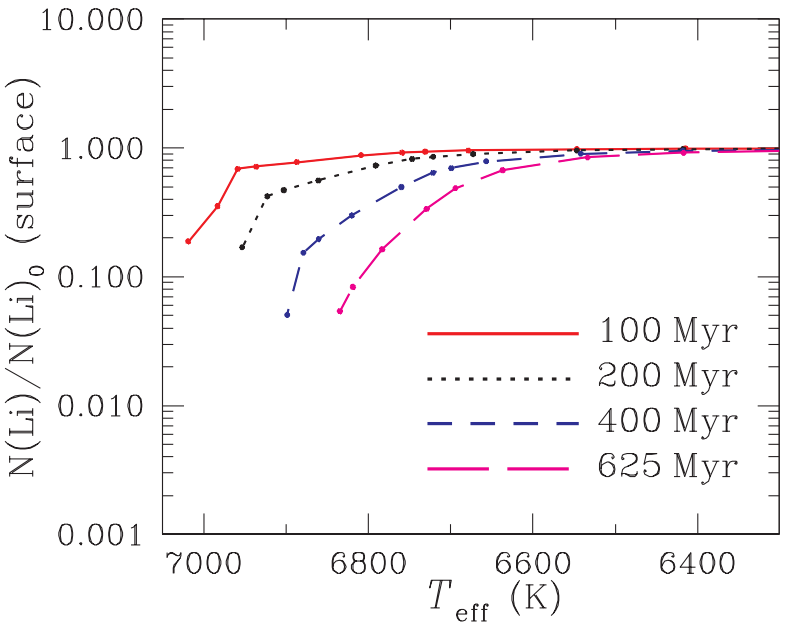

Figure 2.17: The $T_{\rm eff}$-$X_{\rm Li}$ relation at different ages for the models shown in Fig. 2.16. Each point represents a calculated model. This plot can be compared directly to Fig. 8 of Richer & Michaud (1993).

the models shown in Fig. 2.16. The gap position evolves toward cooler temperatures with time. At 100 Myr, only stars of 6900 K have significant underabundances, while at 625 Myr, stars as cool as 6700 K have important underabundances.

At 100, 200 and 400 Myr, the gap obtained in the present calculations is 50-80 K hotter than the gap of the same metallicity shown in Fig. 8 of Richer & Michaud (1993). Our gap is also slightly deeper, as the surface lithium on the hotter end of our isochrones keeps decreasing where surface lithium in the isochrones of Richer & Michaud (1993) start increasing. This is a result of the smaller $g_{\rm rad}$(Li) obtained in our models (see Sect. 2.3.1.2, in particular Fig. 2.3): the competition with Fe decreases $g_{\rm rad}$(Li) by a factor of 2, so that it doesn't reach g in the hotter models of our isochrones. Therefore, lithium is not supported in our diffusion only model.

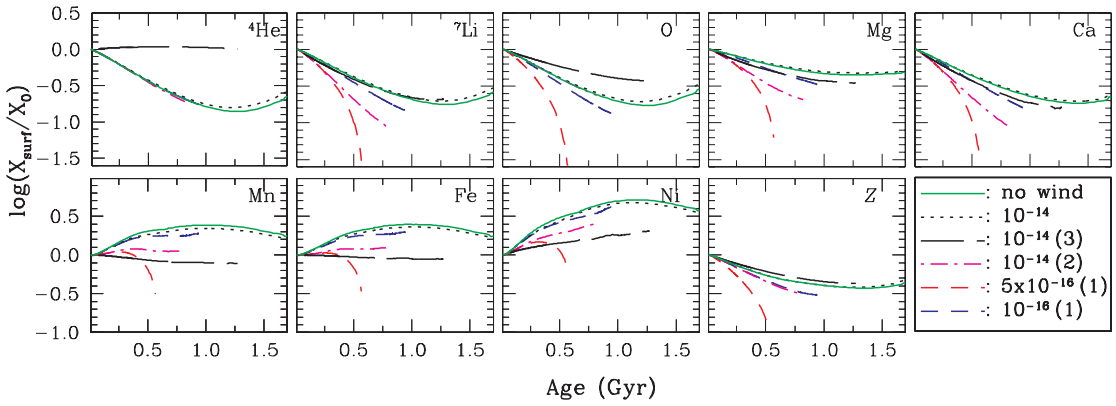

Figure 2.18: Surface abundance evolution for selected elements of 1.40 $M_\odot$ models with different types of wind solutions: one model with no mass loss (solid line), one model with a homogeneous mass loss rate of $10^{-14}\,M_\odot yr^{-1}$(dotted line), and 4 models with separated mass loss. For the separated winds, the configuration is indicated by a number (1, 2 or 3) which is explained in Sect. 2.4.3 and in the text below.

2.5.3.5 Separated winds

The effects of various separated wind configurations on surface abundances of 1.4 $M_\odot$ models are illustrated in Fig. 2.18. Along with the 1.40W1E-14 unseparated mass loss model and the pure diffusion model (no wind), three cases of separated winds were considered, as described in Sect. 2.4.3.

In contrast to unseparated mass loss (dotted line) which, when comparing to the pure diffusion model (solid line) in Fig. 2.18, *reduces surface anomalies for all elements*, separated mass loss can affect underabundant and overabundant elements differently. In case 1, for which all metals are ejected with the same relative concentration as in the atmosphere whereas H and He remain bound, a mass loss rate of $1 \times 10^{-16} M_\odot/\mathrm{yr}$[14] leads to *smaller* overabundances and *larger* underabundances than unseparated mass loss. This is because in case 1, the internal wind term this mass loss leads to is negligeable (see Eq. 2.6). Therefore, for underabun-

[14]This is smaller than the rate of metal depletion for the unseparated model 1.40W1E-14, since $Z \times \dot{M} = 1.999 \times 10^{-16}\,M_\odot yr^{-1}$.

dant elements, the surface convection zone is drained from its bottom (because the wind is too weak to support downward diffusing elements), as well as from its top (i.e. mass loss at the stellar surface). Overabundant elements, on the other hand, are depleted through the surface, while the bottom of the surface convection zone is replenished by atomic diffusion. When the mass loss rate is increased to $5 \times 10^{-16}\,\mathrm{M_\odot yr^{-1}}$ for case 1, the overabundances can rapidly evolve into underabundances since, without the wind providing sufficient replenishment from deeper inside the star, the elemental depletion at the surface quickly dominates the replenishement at the bottom of the convection zone. For the model with a mass loss rate of $5 \times 10^{-16}\,\mathrm{M_\odot yr^{-1}}$ underabundances of Li and Fe reach $-1.5\,\mathrm{dex}$ and $-0.95\,\mathrm{dex}$ respectively at 570 Myr, whereas for the $10^{-16}\,\mathrm{M_\odot yr^{-1}}$, the Li underabundance reaches $-0.55\,\mathrm{dex}$ around 625 Myr, while Fe has an overabundance of $0.45\,\mathrm{dex}$. Generalized underabundances are attainable in the context of case 1.

In case 2, all low-FIP elements are depleted 4 times more rapidly than H and other high-FIP elements. Consequently, in comparison to the anomalies obtained for the 1.40W1E-14 model, the anomalies for the low-FIP elements (of which Li, Mg, Ca, Mn, Fe and Ni are shown) are greater for underabunt elements and smaller for overabundant elements, as in case 1. The Fe overabundance is reduced to $0.2\,\mathrm{dex}$ around 625 Myr, and the Li underabundance reaches $-0.6\,\mathrm{dex}$ at the same age. However, for O, which is a high-FIP element, the curve is tucked in between the pure diffusion and unseparated mass loss curves (and is therefore impossible to see on the figure), which is what could be expected, since the rate of depletion as seen by O, a high-FIP element, is smaller than $10^{-14}\,\mathrm{M_\odot yr^{-1}}$ because the lost mass has a higher concentration of low-FIP elements (see Sect. 2.4.3).

Finally, in case 3, for which H is included among the low-FIP elements, the results are quite different: the depletion of H at the surface leads to an important increase of He. Since the He abundance at the surface remains slightly above its original value throughout the simulation, the stellar structure is changed as

the H-He SCZ is much deeper on the main–sequence than for any of the other models. Around 625 Myr, Fe is barely underabundant, while Li is underabundant by -0.5 dex[15]. At 625 Myr, the model in case 3 is 100 K hotter than the three other models at the same age.

2.6 Comparison to turbulence models

As previously mentioned, models with turbulence (Richer et al., 2000; Richard et al., 2001; Michaud et al., 2005) have been quite successful at reproducing observed properties of AmFm stars both on the surface (i.e. abundance anomalies) and in the interior (pulsation properties of δ Scuti stars, see Turcotte et al. 2000). These models with turbulence put forth a scenario in which chemical separation takes place below 200 000 K, as opposed to the scenario in which chemical separation immediately below the H convection zone is responsible for AmFm abundance anomalies (Watson 1971; Alecian 1996). The models calculated with mass loss offer an alternative scenario which is in fact a hybrid of both these scenarios. On the one hand, no external mixing is enforced outside of convection zones, which allows for chemical separation to occur throughout the stellar interior. However, for most of the main–sequence lifetime, the surface abundance is modulated by matter which is advected from deep inside the star (while in turbulence models, it is mixed to that depth). In order to determine which of these scenarios must be favored, it is paramount to differentiate the models so as to enable observational tests.

Even when surface abundances are quite similar in turbulent and mass loss models, the interior behaves differently. This can be seen by comparing the 2.50W1E-13 and 2.50T5.2D1M-4 models in Fig. 2.19 and Fig. 2.20. In Fig. 2.19, which compares the internal concentrations of all 28 elements for a model with turbulent mixing and a model with mass loss, there is a stark contrast in the internal distribu-

[15]For a given element, [X/H] is about 0.1 dex larger than $\log(X_{\rm surf}/X_0)$ because of the surface underabundance of H.

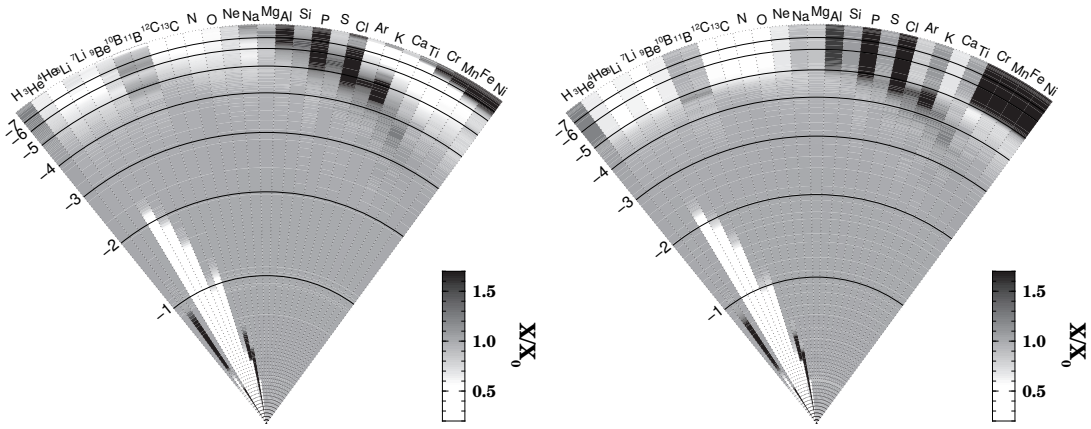

Figure 2.19: Gray coded concentrations of two 2.50 $M_\odot$ models at 500 Myr. The scale of the radius is linear although the value on the left hand side indicates $\log \Delta M/M_*$. The contrast is identified in the right insert and spans the interval from 0.3 to 1.7 times the original elemental abundances. The anomalies affect the outer 25 % of the radius. Nuclear effects appear for lighter elements near the stellar core. For the calculations shown in the left panel, the competing process is mass loss while it is turbulence in the right panel. For these two models, the surface abundances are nearly the same (see Fig. 2.20).

tion of elements heavier than Ar, even though the surface abundances are quite similar for most atomic species (see Fig. 2.20). The Fe abundance in the interval $\log \Delta M/M_* \simeq -6$ to -5 is $4-5$ times larger in the turbulence model. The same can be said for Ni which, between $\log \Delta M/M_* = -7$ and -5, differs by about a factor of 10. This has an important effect on the local Rosseland opacity. These internal differences could therefore allow for some asteroseismological tests which could help differentiate between the two models.

With respect to pulsations, one notes that around 250 Myr, the age of Sirius (Liebert et al. 2005), the He II convection zone is still present in the turbulence model as well as in the 2.50W1E-13 model, but not in the 2.50W5E-14 model (see Fig. 2.9). As seen in the $\log \kappa_R$ panel, opacities are quite similar in the He II convection zones for the 2.50W1E-13 and the turbulence models, therefore, the mass loss model could be compatible with observed pulsation properties of δ Scuti

stars (Turcotte et al. 2000). Further investigation is required to determine if the He II opacity bump in the 2.50W5E-14 model is sufficient to drive kappa mechanism oscillations.

During evolution there are phases in which important surface abundance differences differentiate models with mass loss from those with turbulence. For instance, Fig. 2.14 can be compared directly to Fig. 15 of Richer et al. (2000). The most glaring difference is the surface behavior shortly after the onset of diffusion. In the turbulence model, abundance anomalies appear slowly and gradually at the surface, whereas large anomalies appear at the surface as early as 5 Myr in the mass loss model. This is because all chemical separation that occurs near the surface, where timescales are short, will rapidly be advected to the surface by the wind[16] (see discussion in Sect. 2.5.3.2). In the turbulence models, mixing is enforced throughout the upper envelope, and effectively prevents any chemical separation near the surface. Likewise, the abundances immediately following the turn-off are also different; while overabundant iron peak elements such as Mn and Fe can become underabundant as the SCZ exposes regions in the envelope with important gradients (as is the case at 524 Myr), the internal variations in the turbulence context are much less important (as an example, compare the Fe underabundance around $\log \Delta M/M_* \simeq -5$ in our Fig. 2.6 and Fig. 4 of Richer et al. 2000), and so the variations at the surface will also be smaller. On the main–sequence however, the differences between the two models are relatively quite small.

Similarly, for the $T_{\rm eff}$ dependence, Fig. 2.15 can be compared directly to Fig. 16 of Richer et al. (2000). The most glaring difference is the behaviour of iron peak elements. By comparing the models with masses between 1.7 and 2.3 $M_\odot$ in both figures, one notes that in the turbulence regime, the iron peak surface distribution is the same for all $T_{\rm eff}$s at a given age, while there is more significant variations for

[16] This will be discussed in further detail in a forthcoming paper which will look into the effects of diffusion on the pre-main–sequence.

the same elements in the mass loss models within the same stellar mass interval. On the contrary, the lighter elements show less variations in the mass loss models in comparison to the models with turbulence in the same mass interval.

2.7 Comparison to observations

In order to constrain stellar models, and to determine whether turbulence or mass loss is the dominant macroscopic process reducing surface abundance anomalies, it is imperative to compare our results with observations. In order to carry out an accurate comparison one needs to constrain age, mass and initial composition, which as shown in the previous section, all affect surface abundances. To reduce the arbitrariness of the comparison, we chose three open cluster stars for which we have a good evaluation of the initial metal content as well as of the approximate age. We will also compare our results to the field star Sirius A and the binary system *o* Leonis.

In the following sections, [N/H] has its usual meaning:

$$[\mathrm{N/H}] = \log(\mathrm{N/H})_\star - \log(\mathrm{N/H})_\odot. \tag{2.26}$$

As mentioned in Sect. 2.2, this paper is part of a series of papers starting with Turcotte et al. (1998b), where the mixing length used was calibrated using the Sun for given boundary conditions, as well as helium and metal content. For consistency, the same boundary condition, solar composition and mixing length are used for Pop I stars. Our models lead to abundance variations, or *anomalies*, relative to those original abundances. A number of observers have similarly determined anomalies by differential methods with respect to solar abundances. Moreover, in the model atmospheres used for abundance determinations, most observers used the solar abundance mix either from Anders & Grevesse (1989) or Grevesse et al. (1996). Because determinations were sometimes obtained with different solar photospheric

abundances by different observers and sometimes with differential methods, their abundance determinations relative to the Sun (i.e. the anomalies) are used, when available, rather than absolute abundances. The uncertainty that inaccuracies in solar abundances lead to will be discussed in Sect. 2.8.

2.7.1 Field stars

Sirius A is the most studied hot Am star ($T_{\rm eff} \simeq 9800\,$K), with a mass of about 2.14 $M_\odot$ and an age of approximately 250 Myr (Gatewood & Gatewood 1978; see also Sect. 4.1 of Richer et al. 2000). Figure 2.20 shows surface abundance determinations for 19 chemical species (16 of which are included in our calculations) from 8 different papers.

First, for most elements, there is considerable scatter among observers. For instance, there is a 0.3 dex difference in Si abundance, as well as a 0.4 dex difference in Fe abundance, which is the most carefully determined element. We compared this data to 3 models with mass loss (2.50W1E-12, 2.50W1E-13 and 2.50W5E-14) as well as to the model with turbulence from Richer et al. (2000) which best reproduced the data (2.50T5.2D1M-4). Of the 16 observed elements which are included in our calculations, 12 (He, Li, O, Na, Mg, Si, P, Ca, Ti, Cr, Fe and Ni) are well reproduced by both the turbulence model and the 2.50W1E-13 model. It is interesting to note that Bertin et al. (1995) determined, from Mg II lines, that the observed mass loss rate of Sirius A is between 1.5×10^{-12} and 2×10^{-13}. The overall fit is also just as good for the 2.50W5E-14 model since it is also able to reproduce the carbon abundance, though it perhaps overevaluates the iron peak abundances. The S abundance is not at all reproduced by our calculations; however, the observer gives little credibility to its value (Hill, 1995). It is clear that the model with a mass loss rate of 10^{-12} $M_\odot yr^{-1}$does not lead to the observed surface abundance pattern. Finally, surface abundance observations are not sufficiently accurate to enable a differentiation between turbulence and mass loss models.

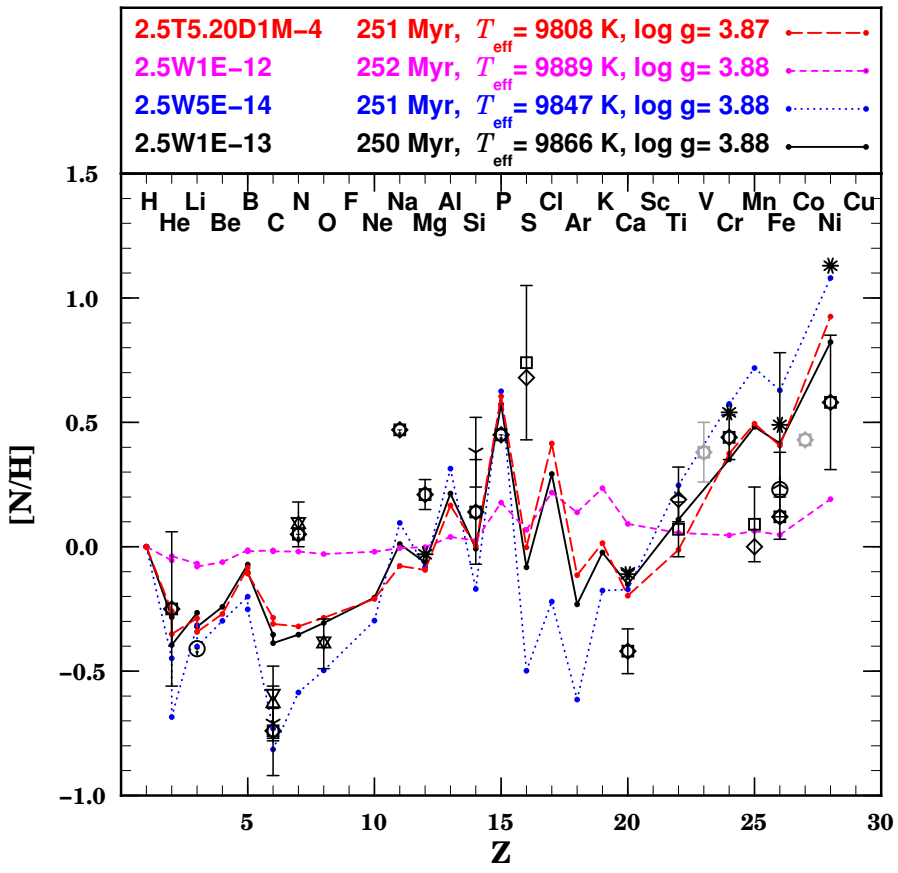

Figure 2.20: Confronting models to observations of the surface abundances of Sirius A (also known as α CMa, HR 2491 or HD 48915). *Circles*, Burkhart & Coupry (1991); *Upright open triangles*, Roby & Lambert (1990); *inverted open triangles*, Lambert et al. (1982); *three-point stars*, Lemke (1989); *inverted three-point stars*, Lemke (1990); *squares*, Hill (1995); *diamonds*, Hill & Landstreet (1993); *asterisks*, Hui-Bon-Hoa et al. (1997). Calculated values are shown for 3 models with mass loss (2.50W5E-14, 2.50W1E-13 an 2.501E-12), as well as the model with turbulence (2.50T5.2D1M-4) which represents the best fit from Fig. 18 of Richer et al. (2000). All models were calculated with a solar ($Z = 0.02$) initial metallicity and are shown at an age of 250 Myr. Vanadium, scandium and cobalt are grayed out since they are not included in our calculations. The internal abundance distributions of the 2.50W1E-13 and 2.50T5.2D1M-4 models are shown in Fig. 2.19.

In Michaud et al. (2005), the binary system o Leonis (HD 83808/83809) has been interpreted as consisting of two AmFm stars with masses of 2.12 and 1.87 $M_\odot$ (Griffin, 2002). The authors show that two models with turbulent mix-

ing, of 2.24 and 1.97 $M_\odot$ respectively, are able to reproduce the observed features (namely both positions in the H-R diagram as well as surface abundances) of the A and B components of the binary system within the observational error bars. Similarly, models of 2.20 and 1.90 $M_\odot$ with a mass loss rate of $5 \times 10^{-14}\,M_\odot yr^{-1}$ are able to reproduce the H-R position of both components. At the age indicated by the squares (750 Myr and 750.5 Myr), the A component is in the rapid evolution stage that follows the depletion of hydrogen in the core (the luminosity change is related to the star's adjustment to H-shell burning). At this age, the B component is still in the slowly evolving MS stage, which explains why both circles overlap on the graph.

The two squares in Fig. 2.21 show that the Fe abundance can vary between -0.2 dex and 0.6 dex within the $T_{\rm eff}$ error bar for the A component, while the corresponding Ca surface abundance varies from -0.18 to -0.4. Throughout most of this interval, the 2.20 $M_\odot$ model has anomalies which are typical of Am stars (Fe overabundance coupled with a Ca underabundance). For either of the values for the A component, the 1.90 $M_\odot$ model has an overabundance of Fe of 0.4 dex coupled with an underabundance of Ca which attains -0.3 dex, both typical Am star anomalies as well.

Both the turbulent model of Michaud et al. (2005) and the mass loss model can reproduce the AmFm character of components A and B. While the AmFm character of component A can be fitted by the turbulent model for its exact observed $T_{\rm eff}$, the mass loss model only generates typical AmFm iron overabundances for a part of the error bar on the hot side of the observed $T_{\rm eff}$.

2.7.2 Open cluster stars

In Fig. 2.22, we compare our results to observed abundance determinations for the hot Am star 68 Tau ($T_{\rm eff} \simeq 9050$ K, Netopil et al. 2008) from the Hyades open cluster. The cluster age has been quoted between 625 Myr (Perryman et al.

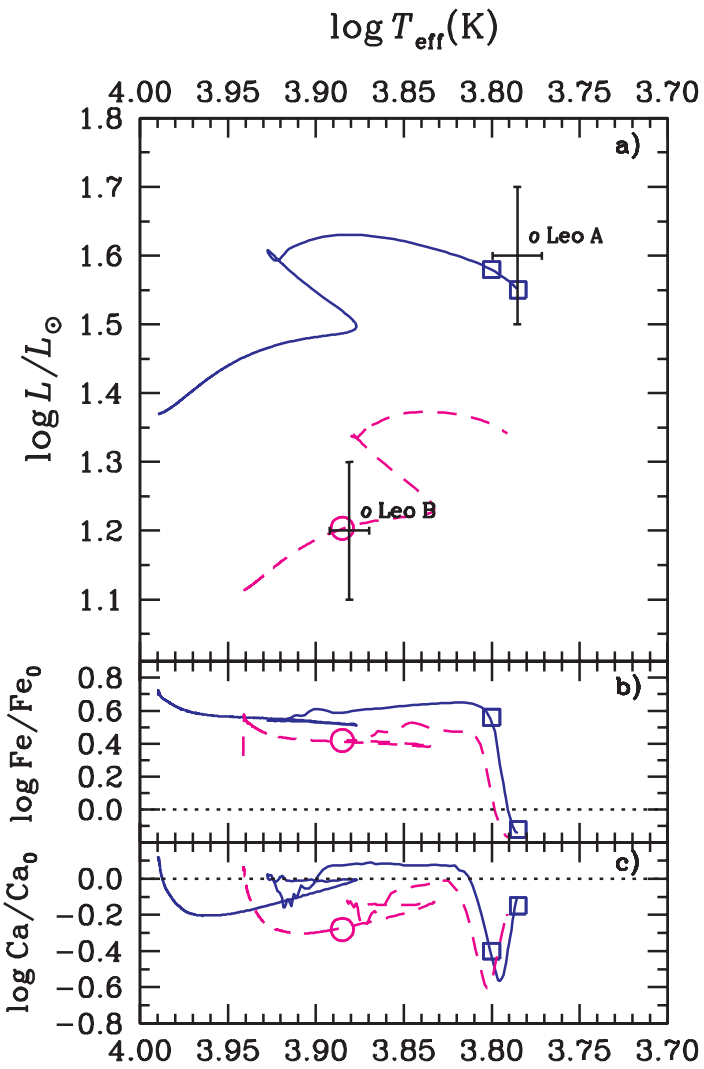

Figure 2.21: A model of 2.2 $M_\odot$ with a mass loss rate of $5\times10^{-14}\,M_\odot yr^{-1}$ (solid line) and a model of 1.9 $M_\odot$ with the same mass loss rate (dashed line) are plotted in an H-R diagram (a). The observed position in the H-R diagram of the primary and secondary components of *o* Leonis (with error bars) are shown with crosses. The squares indicate two possible positions on the primary's evolution path which fall within observational error bars. The circle indicates the position of the secondary at the age of the primary indicated by the square. The surface values of Fe and Ca are shown relative to their original values in (b) and (c).

1998) and 783 Myr by Varenne & Monier (1999). Its quoted metallicity has also

ranged between $Z_0 \simeq 0.024$ (Perryman et al. 1998; Gratton 2000) [17] and $Z_0 = 0.03$ (Cayrel et al. 1985) using F and G star iron abundances as indicators. In order to reflect this metallicity, the selected models have been calculated with an initial metallicity of $Z_0 = 0.03$, which was also used in models from Richer et al. (2000)[18]. We have attempted to make a compromise between fitting age and $T_{\rm eff}$: three models have a mass of 2.50 $M_\odot$ and one has a mass of 2.30 $M_\odot$. The 2.50W1E-13Z0.03 and 2.50W5E-14Z0.03 models are on a short $T_{\rm eff}$ upswing which arises as hydrogen nears depletion in the core (in Fig. 2.21 for instance, it is the segment which immediately follows the main–sequence, spanning from $\log T_{\rm eff} \simeq 3.87$ at its bottom to $\log T_{\rm eff} \simeq 3.93$ at its top). In terms of stellar age, this upswing only lasts 3 Myr before the star starts its descent onto the red giant branch. While it has very little effect on surface abundances, models were chosen at this age in order to be closer to the star's surface temperature. Given the large spread in abundances between observers, the fit is almost perfect with the 2.30W1E-13Z0.03 model, which is slightly cooler and younger, yet is still on the main–sequence. Of 15 observed elements, only Na, Al and Mn (arguably just Al) are not reproduced. The fit is as good if not better (because of Ni) than the fit obtained with the model with turbulence. The 2.50W1e-13Z0.02 model was added in order to illustrate the effect of reducing initial metallicity on absolute abundances (see also Fig. 2.13). The fit with observations is better than for the 2.50W1-13Z0.03 model, since the iron peak abundances with respect to solar abundances are smaller in the lower metallicity model. By comparing these two curves one can conclude that, for a given mass loss rate, a 0.18 dex reduction of initial metallicity can, at most, lead to a 0.18 dex reduction for elements which are not supported, such as C, N and O, and a 0.09 dex reduction for elements which are supported such as Fe. See also

[17] Using the Hyades iron enrichment factor of Gratton (2000) to multiply the metallicity determined by Asplund et al. (2009) for the solar mixture, the Hyades metallicity becomes $Z_0 \simeq 0.019$. The actual value would likely lie somewhere between 0.019 and 0.03. The curve with $Z_0 = 0.02$ in Fig. 2.22 illustrates the impact of uncertainties.

[18] Of course, [N/H] at $t = 0$ for models with $Z_0 = 0.03$ is above solar for all metals.

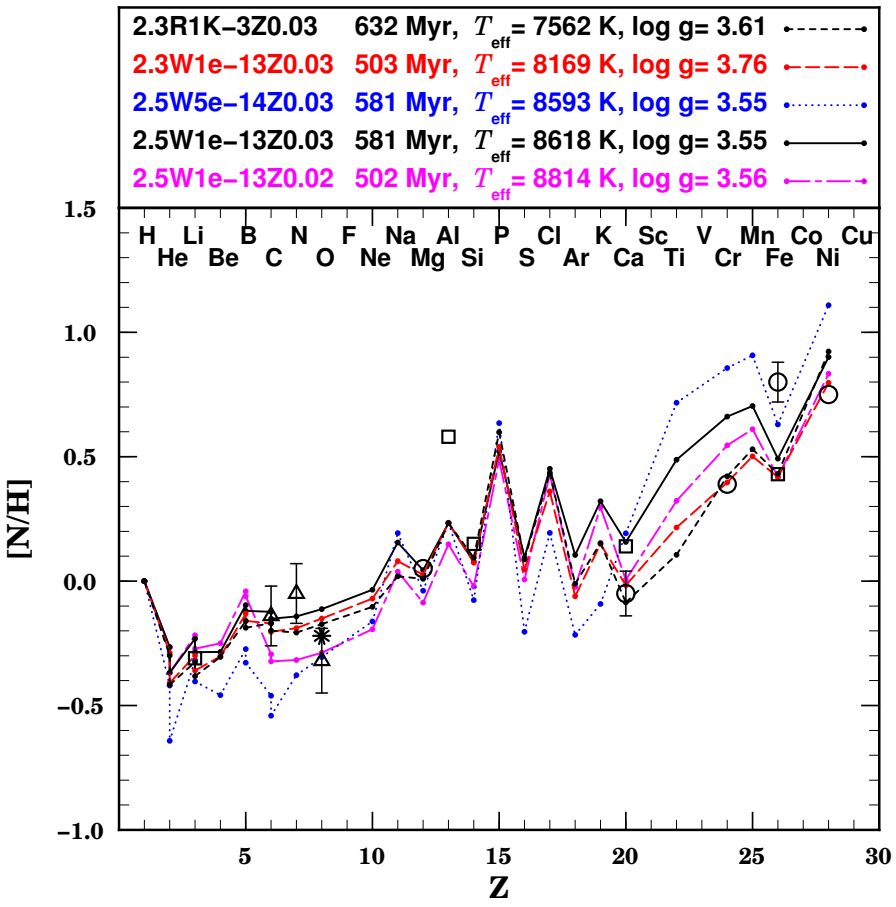

Figure 2.22: Observed surface abundances of 68 Tau (also known as vB 56, HR 1389 or HD 27962), the hottest star (blue straggler) from the Hyades open cluster. *Circles*, Hui-Bon-Hoa & Alecian (1998); *triangles*, Roby & Lambert (1990); *squares*, Burkhart & Coupry (1989); *asterisks*, Takeda & Sadakane (1997). Calculated values are shown for 4 models with varying mass loss rates as well as the model with turbulence which best reproduced the data (2.30R1K-3Z0.03, see Richer et al. 2000). One model was calculated with $Z_0 = 0.02$, while all other models were calculated with an initial metallicity of $Z_0 = 0.03$. Metallicity is indicated in the model name.

Sect. 2.5.3.3.

In Fig. 2.23, we compare 2 models of 1.9 $M_\odot$ with mass loss as well as a model with turbulence to the observations of the star HD 73045 ($T_{\rm eff} \simeq 7500$ K) from the Praesepe open cluster which has an approximate age of 800 Myr and a solar metal-

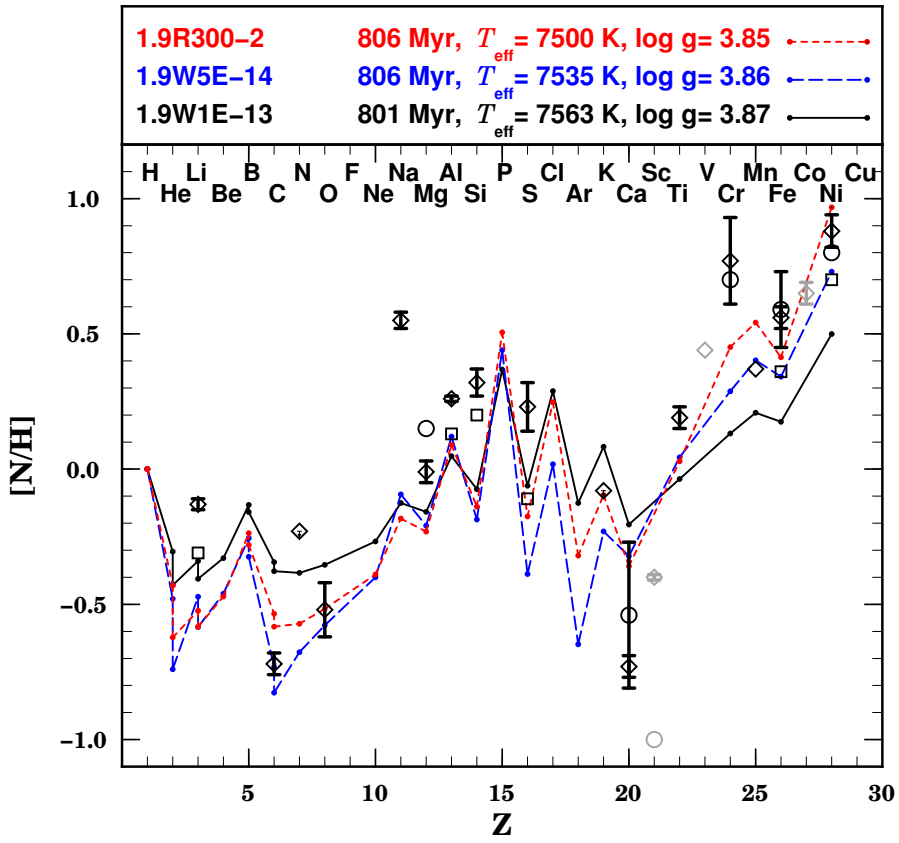

Figure 2.23: Observed surface abundances of HD 73045 ($T_{\rm eff} \simeq 7500\,{\rm K}$) of the Praesepe open cluster which has an approximate age of 800 Myr. *Circles*, Hui-Bon-Hoa & Alecian (1998); *squares*, Burkhart & Coupry (2000); *diamonds*, Fossati et al. (2007). Curves correspond to models listed at the top of the figure. All models were computed with solar initial abundances ($Z_0 = 0.02$).

licity. There are 15 observed elements which can be compared to our simulations, although 3 determinations (N, K and Mn), result from a single line and therefore could be inaccurate. Again, note the large discrepancies between observers. Only the 1.90W5E-14 and the turbulence model can reproduce either the overabundant iron peak elements or the underabundances of C and O. The abundances of Na and Si are not reproduced by either of the models.

Finally, we have compared our models to observations of the Coma Berenices star HD 108486 (Fig. 2.24). Coma Berenices is an open cluster with an age of about

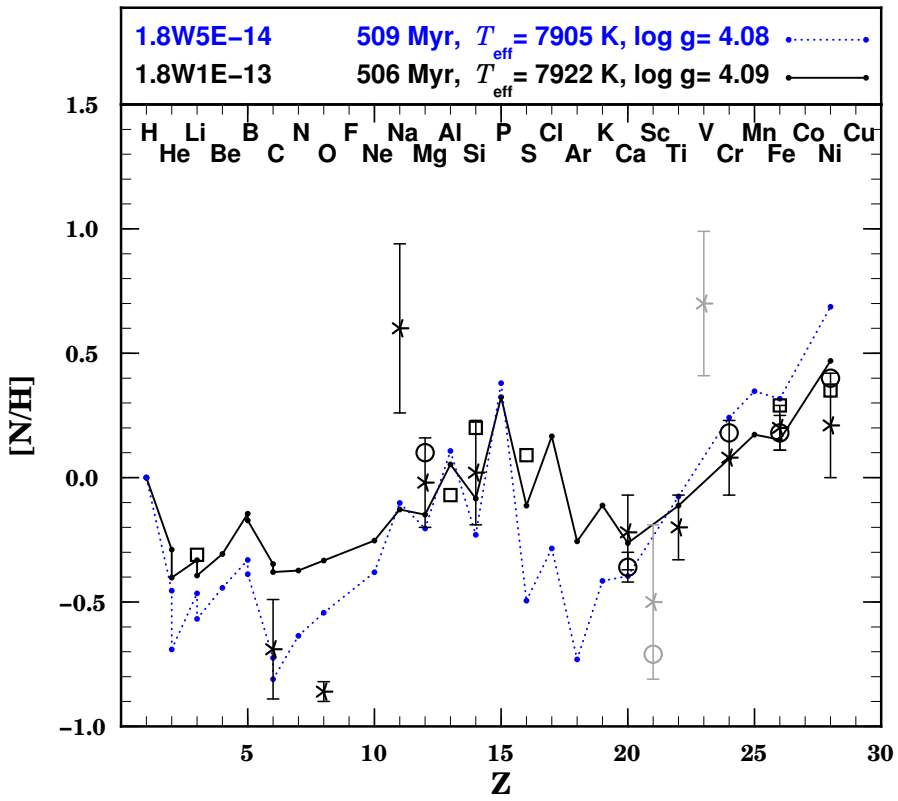

Figure 2.24: Observed surface abundances of HD 108486 ($T_{\rm eff} \simeq 8180$ K) of the Coma open cluster which has an approximate age of 500 Myr. *Circles*, Hui-Bon-Hoa & Alecian (1998); *squares*, Burkhart & Coupry (2000); *five-point stars*, Gebran et al. (2008). Curves correspond to models listed at the top of the figure. All models were computed with solar initial abundances ($Z_0 = 0.02$).

500 Myr and with a metallicity which is about solar. We have matched the star's $T_{\rm eff}$ and age quite well with two 1.8 $M_\odot$ models with mass loss. Except for O and Na, which are not reproduced by any of the two models, most elements are fitted by both models. Assuming error bars for S and Al which are similar to those for other elements, we can state that 10 of the 13 abundances can be reproduced by the 1.80W1E-13 model, and 9 by the 1.80W5E-14 model.

Although we have opted not to add any extra figures, our results are also compatible with observations of Ca overabundances (see Fig. 2.12) in very young open clusters such as the Pleiades (Gebran & Monier, 2008; Hui-Bon-Hoa & Alecian,

1998) and α Persei (Hui-Bon-Hoa, 1999). This is noteworthy since models with turbulence do not predict such an overabundance (see Figs. 10 of Richer et al. 2000).

2.7.2.1 Lithium gap

In Fig. 2.25, models with and without mass loss are compared to lithium, beryllium, calcium and iron observations in and around the Hyades lithium gap. Lithium determinations are shown for F stars and AmFm stars (normal A stars and other peculiar A stars are omitted). Iron and calcium abundances are shown only for stars which had a lithium determination. All beryllium abundances for F stars in Boesgaard & King (2002) are shown[19]. When multiple observations for the same star were available, the different determinations are connected by a line segment. This gives an evaluation of the uncertainty. All models calculated with mass loss rates of $5 \times 10^{-14}\,\mathrm{M_\odot yr^{-1}}$ and $1 \times 10^{-13}\,\mathrm{M_\odot yr^{-1}}$ which were still on the main–sequence at 625 Myr are shown. Models with a mass loss rate of $1 \times 10^{-14}\,\mathrm{M_\odot yr^{-1}}$ are omitted since they result in surface abundances which are very similar to diffusion only models (compare the diffusion only and 1.40W1E-14 models in Fig. 2.18). Therefore in the following discussion, results from diffusion only models can be assimilated to models with unseparated mass loss $\leq 1 \times 10^{-14}\,\mathrm{M_\odot yr^{-1}}$. All models were calculated with an initial metallicity of $Z_0 = 0.02$, although the metallicity of the Hyades is above solar ($Z = 0.024$, see Sect. 2.7.2). The original value of lithium was set to A(Li)=3.05. This value fits lithium determinations for the stars at the top of the cold side of the gap, which, since diffusion plays only a small role for these stars, probably reflect the cluster's original Li content (unless there is significant pre-main–sequence burning). Following the same logic, A(Be) was set

[19]Lithium abundances from Boesgaard & Tripicco (1986) and Boesgaard & Budge (1988) are preferred over the revised values from Boesgaard & King (2002) because there is a greater number of stars. Nonetheless, in the more recent paper, *all* previous determinations are revised upwards by 0.09 to 0.4 dex.

to 1.40.

According to our calculations, atomic diffusion in the absence of competing processes leads to an important reduction of surface lithium abundance. The smallest lithium anomaly was obtained for the 1.10 $M_\odot$ model, for which surface lithium was reduced by 0.015 dex at 625 Myr. The largest lithium reduction at 625 Myr is by about -1.4 dex (or a factor of 25), for the 1.46 $M_\odot$ model without mass loss. This does not quite reach the bottom of the gap of Boesgaard & Tripicco (1986)[20]. As seen in Fig. 2.16, the 1.47 $M_\odot$ model without mass loss would likely have reached a lower lithium abundance had it been able to converge up to the age of the Hyades, thus reconciling some of the difference. In fact, the mass of the model which would have attained the lithium gap minimum can be deduced from Fig. 2.3. Because Li is not supported until $g_{\rm rad} \simeq g$ just below the surface convection zone at 625 Myr, the heaviest model for which the BSCZ is located where $\log T \gtrsim 5.4$ throughout its evolution will represent the gap minimum, since it is for this model that Li is sinking fastest. From Fig. 2.3, while the 1.55 $M_\odot$ model is clearly on the hot side and the 1.43 $M_\odot$ model on the cold side, it is the 1.46 $M_\odot$ model that should be closest to the bottom of the gap. Furthermore, if the competition with Fe that is prescribed by the OPAL opacities and calculated in these models without mass loss is correct, then diffusion alone cannot explain the increase of Li on the hot side of the gap. The $g_{\rm rad}$(Li) in the atomic diffusion only models will remain smaller than g by a factor of at least 2. However, given the uncertainties discussed in Sect. 2.3.1.1 on the location of Fe lines, $g_{\rm rad}$(Li) could very well attain g near $\log T \simeq 5.3$, in which case lithium would be supported, and would consequently exhibit different surface behavior.

For the models without mass loss on the cold side of the gap, the Fe abundances are in agreement with observations up to about 6800 K, after which the calculated

[20]It has been suggested to revise these observations upwards by up to 0.4 dex (see the discussion in Sect. 2.1.2 of Michaud & Charbonneau 1991 and Boesgaard & King 2002). The maximum depletion encountered in the deepest part of the gap might so be closer to a factor of 50.

overabundances become too large. The discrepancy between the Fe curve and the observations for $T_{\rm eff} < 6700\,{\rm K}$ is related to our models having a solar initial metallicity, whereas the Hyades stars were formed in a metal rich environment.

The models with mass loss rates of $5 \times 10^{-14}\,{\rm M}_{\odot}{\rm yr}^{-1}$ and $10^{-13}\,{\rm M}_{\odot}{\rm yr}^{-1}$ cannot explain the depletion encountered within the gap. However, given reasonable error bars, they are consistent with the almost constant lithium and beryllium abundances observed for $T_{\rm eff} > 7200\,{\rm K}$. Both mass loss rates lead to models which reproduce the observed Fe abundances between $6000 \leq T_{\rm eff} \leq 8200\,{\rm K}$ and, in particular, the increase in Fe abundance for $T_{\rm eff} > 7200\,{\rm K}$, which is compatible with the AmFm character of these stars. Given the large discrepancies in determinations, most Ca abundances are also compatible with the models with mass loss.

Neither the calculated gap minimum nor the shoulder on the cold side of the gap match the observed position in $T_{\rm eff}$. By comparison to Fig. 9 of Richer & Michaud (1993), their calculated depth for the gap ($-1.6\,{\rm dex}$) resembles the depth obtained in our calculations ($-1.4\,{\rm dex}$, see discussion in Sect. 2.5.3.4). The shoulder on the cold side of the gap obtained in the present calculations matches the curve they obtained with $Z_0 = 0.02$ within $\pm 50\,{\rm K}$. Accordingly, as also seen in this same Fig. 9, if we had chosen $Z_0 = 0.03$ ([Fe/H]$=+0.18$), some of the $150\,{\rm K}$ difference would have been recuperated as the gap minimum would have been shifted toward cooler temperatures by 50-80 K. There is also a $\pm 50 - 100\,{\rm K}$ uncertainty on the observed position of the gap (see discussion in Sect. 2.1.2 of Michaud & Charbonneau 1991). The uncertainty on the age of the Hyades (from 625 to 783 Myr, see Sect. 2.7.2) could also account for some of the difference as illustrated in Fig. 2.17. As the age of the isochrones increases, the $T_{\rm eff}$ at which lithium abundances fall off also decreases. The real problem in explaining the Li gap with atomic diffusion is not with the exact $T_{\rm eff}$ of the gap nor its depth, but rather with the calculated Fe overabundances which are not observed, and the related difficulty in calculating $g_{\rm rad}({\rm Li})$ on the hot side of the gap due to Fe lines.

2.8 General discussion and conclusion

2.8.1 Summary of results

Evolutionary models including both atomic diffusion and unseparated mass loss explain the main abundance anomalies of AmFm stars (Sect. 2.7.2). When mass loss is assumed to be the only macroscopic process competing with atomic diffusion, observed abundance anomalies from open cluster stars as well as Sirius A and o Leonis constrain mass loss rates to $2-5$ times the solar mass loss rate. As shown in Sects. 2.7.1 and 2.7.2 models involving mass loss are as capable as models involving turbulence in explaining observations of AmFm stars. This is because in both instances, the important separation occurs at the same depth ($\Delta M/M_* \simeq 10^{-6} - 10^{-5}$) for most of the main–sequence life. Whether the mass loss model is to be preferred over the turbulence model is difficult to assess given the large observational uncertainties. However, as shown in Fig. 2.19, the internal distribution of elements is different between the two cases for most elements. With differences reaching a factor of $4-5$ for abundant elements such as Fe, there should be effects on local opacities and thus on pulsations. Asteroseismic tests could perhaps distinguish between the two[21].

In the mass loss regime, chemical separation affects up to $10^{-5}\,\mathrm{M}_\odot$ of a star's mass or, equivalently, 20 to 25% of the stellar radius (see Fig. 2.6 and Fig. 2.19). For any given element, as long as the wind velocity is greater in amplitude than the downward settling velocity, the local abundance solution is determined by flux conservation; local abundances adjust as the flux quickly becomes constant throughout the outer envelope (see Fig. 2.7). As a result, the surface abundances depend on matter which is advected from deep inside the star (see discussion in Sect. 2.5.3.2). This differs from the models of Watson (1971) and Alecian (1996) in which surface

[21] Carrier et al. (2007) did not detect pulsations which could have been a signature of iron accumulation in the Am star HD209625.

abundances depend on the outer $10^{-10}\,M_\odot$. This can also be contrasted to the solution obtained in the models with weak or *fully separated* mass loss presented in Sects. 2.5.2.1 and 2.5.3.5.

When flux is conserved throughout the envelope, abundance gradients which form near the surface, between surface convection zones for example, have no effect on the surface solution once the star has arrived on the main–sequence (see discussion in Sects. 2.5.3.2 and 2.5.3.3). In this instance, if the age of interest is greater than $M_{\rm BSCZ}/\dot{M}$, where $M_{\rm BSCZ}$ is the mass above the bottom of the deepest surface convection zone, one can obtain a nearly similar surface solution by approximating that abundances are homogeneous from the surface to the bottom of the deepest SCZ. However, early in the evolution, only matter from superficial layers has had time to be advected, and thus surface abundances obtained here depend on separation that occurred close to the surface as first studied for Ca by Alecian (1996, see also Sect. 2.5.3.1) and confirmed observationally (see end of Sect. 2.7.2). This favors models involving mass loss rather than turbulence. Likewise, variations obtained near the surface, which do not appear in models with turbulence, have an effect on the PMS (Fig. 2.14) and will be discussed in a forthcoming paper.

In all models heavier than 1.47 $M_\odot$ without mass loss or with an unseparated mass loss rate $\leq 1 \times 10^{-14}\,M_\odot{\rm yr}^{-1}$, the accumulation of Fe and Ni around $T = 200\,000$ K leads to the appearance of a thin radiative layer which separates the iron peak convection zone from the surface H-He convection zone. This accumulation forms before the appearance of a small inversion of the local molecular weight gradient (see Sect. 2.5.2.1). The inclusion of thermohaline convection as suggested by Théado et al. (2009) could have an effect on abundances in the region, though convection occurs even when there is no molecular weight gradient inversion. This would require further investigation. Nonetheless, the appearance (or not) of the iron peak convection zone does not have a significant effect on the surface solution, nor does it appear in models with mass loss which adequately reproduce observed

abundance anomalies of AmFm stars (Sect. 2.7).

Since this paper is a part of a series which explores the various macroscopic processes which compete with atomic diffusion in AmFm stars, it is important that the models be as similar as possible to those used in previous calculations (e.g. those with turbulence) in order to isolate the effects due specifically to mass loss. This is one of the primary motivations for using the same initial solar abundances as in previous calculations, rather than the revised Asplund et al. (2005, 2009) abundances (see also the discussion in Sect.2.2). Varying too many things at once could obscure results and introduce further uncertainty. Furthermore, there is a controversy on solar abundances, since helioseismology strongly favors the older (Grevesse et al., 1996) over the newer (Asplund et al., 2005, 2009) composition. One may then view the abundance differences between the two sets as an evaluation of uncertainty. Since solar abundances are used throughout this paper, the uncertainty on solar abundances leads to uncertainties on the absolute values of all abundances. As shown in Fig. 2.22, a factor of 1.5 reduction (or 0.18 dex) of the original Z leads to a similar reduction (0.18 dex) of the expected abundances of atomic species that are not supported, as well as a smaller reduction of 0.09 dex for species such as Fe which are supported by $g_{\rm rad}$. The fit for the abundances of 68 Tau is about the same for both values of Z as seen in Fig. 2.22. Equivalently, compensating the change of Fe abundance would require reducing the mass loss rate from $10^{-13}\,{\rm M}_{\odot}{\rm yr}^{-1}$ to $7\times10^{-14}\,{\rm M}_{\odot}{\rm yr}^{-1}$ according to the results shown on Fig. 2.11. This may be viewed as the uncertainty on the mass loss rate resulting from the uncertainty of solar abundances[22].

[22]To significantly improve the evaluation of the effect of changing to another set of solar abundances would require first recalibrating the mixing length using a solar model, then carrying out calculations for AmFm stars for both turbulence and mass loss, as well as reanalyzing observations of AmFm star abundances using the new solar abundances. This is outside the scope of the present paper.

2.8.2 Further implications

Atomic diffusion alone *cannot* explain all characteristics of the Hyades lithium gap, nor can unseparated mass loss. The cold side of the gap can only be reproduced by diffusion only models or models with $\dot{M} \leq 1 \times 10^{-14}\,\mathrm{M_{\odot}yr^{-1}}$, whereas the hot side of the gap and the AmFm character of stars for $T_{\rm eff} \geq 7200\,\mathrm{K}$ *require* a stronger mass loss rate. Moreover, separated mass loss (see Sects. 2.5.3.5 and 2.7.2.1) seems required to explain observed Li underabundances near the bottom of the gap as well as reduce the calculated Fe overabundances. In Fig. 2.18, in comparison to the *diffusion only* model, the curve for case 2 shows both larger underabundances of Li as well as smaller overabundances of Fe. Well tuned *fully separated mass loss* (case 1) could do the same. Similarly, the model for case 3 has a nearly flat Fe surface abundance coupled with similar Li underabundances to the *diffusion only* model. It does not seem justified to further speculate on the role of separated winds in Li gap stars until we have a better understanding of separation mechanisms within stellar winds. Since radiative forces generally increase with $T_{\rm eff}$, the above mentioned increase in mass loss rate seems possible if winds of A and hot F stars are radiative in nature. Since a star's $T_{\rm eff}$ changes over time, a mass loss rate which depends on $T_{\rm eff}$ (or on L_*) could also vary in time (Swenson & Faulkner, 1992). Such effects were not introduced in order to limit the number of adjustable parameters.

The competition between atomic diffusion and meridional circulation in 2-D should lead to solutions which resemble those obtained with mass loss, since meridional circulation leads to an additional advective term in the transport equation (Eq. 2.7). Therefore, because the internal distribution of elements in the mass loss regime differs considerably from the variations encountered in the turbulent mixing regime (see discussion in Sect. 2.6), internal distributions due to meridional circulation could also differ significantly from those encountered via turbulence. Hence, when building stellar models, one should be cautious when replacing meridional

circulation, which is an advective process, by turbulent mixing. A careful study of the atomic diffusion of metals within the context of meridional circulation, such as the one carried out for helium in Quievy et al. (2009), could help determine the implications of such an approximation. This could perhaps lead to asteroseismic tests which could distinguish between models using rotationally induced turbulence (Talon et al. 2006) and those using meridional circulation (Charbonneau & Michaud 1988), which are both used to explain the disappearance of the AmFm character for rotation velocities greater than $100\,\mathrm{km\,s^{-1}}$.

Observations of rapid p-mode oscillations in many Ap stars (Kurtz 1978) and in particular in Przybylski's star (see also Mkrtichian et al. 2008) have led to a number of studies of the oscillation mechanisms. In particular, Vauclair et al. (1991) suggested that unseparated mass loss acting solely in polar regions, where the magnetic field is strongest, could induce helium gradients which are compatible with oscillation generating models (Balmforth et al. 2001). Although differences between our stellar model and the one of Vauclair et al. (1991) could have an effect on the predicted anomalies (notably the absence of convection due to magnetic braking/freezing in the latter), our calculations suggest anomalies would reach inwards to about 25 % of the star's radius and could have an important effect on opacities. Though it would depend on the strength of the overall mass loss rate, which will be smaller than the mass loss rate at the poles, a similar He depletion could be coupled with overabundances of iron peak elements around $200\,000\,\mathrm{K}$ and perhaps iron convection. It is not clear whether magnetic braking/freezing or thermohaline convection can stabilize iron peak convection. Unfortunately, we are not able to investigate this scenario any further since our models require spherical symmetry.

Perhaps asteroseismology will allow us to answer some of these questions, while revealing the relative importance of meridional circulation, turbulence and mass loss within chemically peculiar stars.

Acknowledgments

We would like to thank G. Alecian as well as the anonymous referee for useful comments which allowed us to improve the paper. M.Vick thanks the Département de physique de l'Université de Montréal for financial support, as well as everyone at the GRAAL in Montpellier for their amazing hospitality. We acknowledge the financial support of Programme National de Physique Stellaire (PNPS) of CNRS/INSU, France. This research was partially supported by NSERC at the Université de Montréal. Finally, we thank the Réseau québécois de calcul de haute performance (RQCHP) for providing us with the computational resources required for this work.

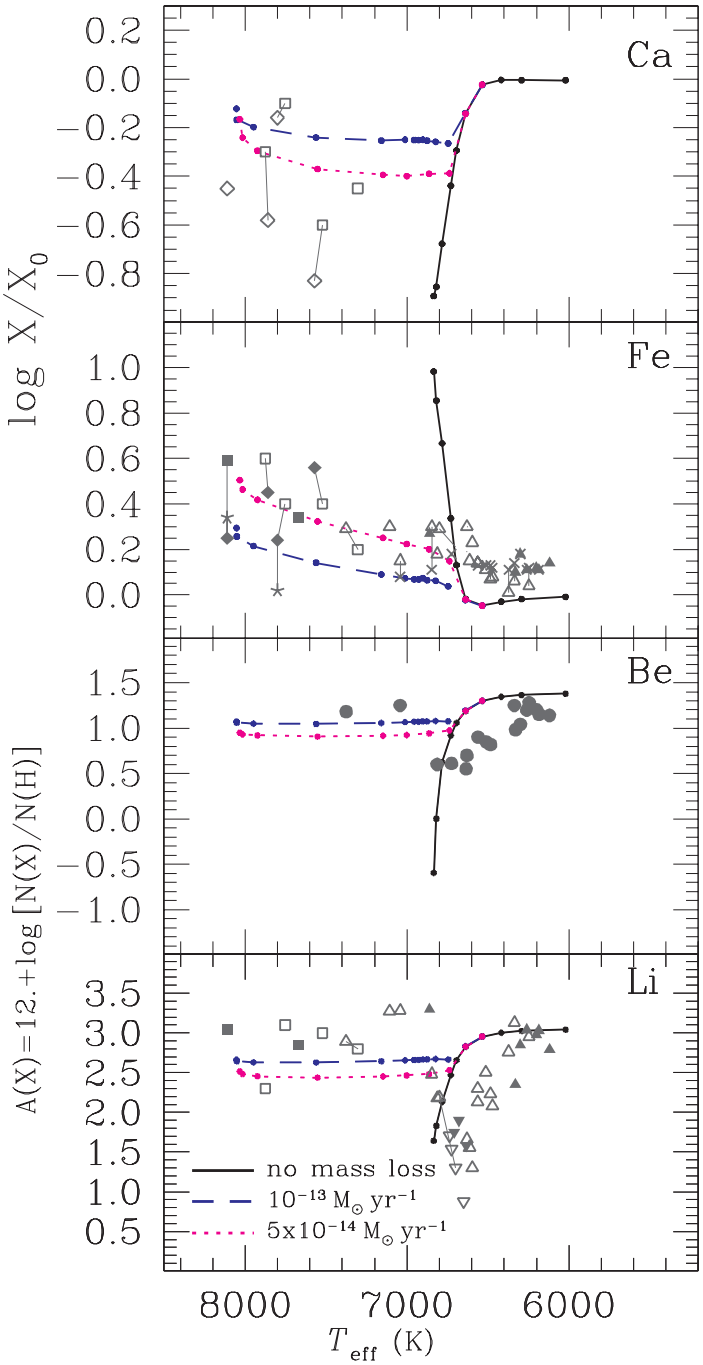

Figure 2.25: Lithium, beryllium, iron and calcium abundances for models with and without mass loss at 625 Myr, the approximate age of the Hyades open cluster. All models were calculated with an initial metallicity of $Z_0 = 0.02$ and the original Li abundance was set at N(Li)=3.05. The Li observations are from (△, and ▽ for upper-limits) Boesgaard & Tripicco (1986), (▲ and ▼) Boesgaard & Budge (1988), (□) Burkhart & Coupry (1989) and (■) Burkhart & Coupry (2000). Be abundances are taken from (●) Boesgaard & King (2002). Additional calcium and iron abundances are also shown for all stars with lithium determinations: (×) Boesgaard & Friel 1990; (⋆) Takeda & Sadakane 1997; (◇) Hui-Bon-Hoa & Alecian 1998. All stars with multiple determinations are connected by a line segments. Calculated models are indicated by dots along the curves.

CHAPITRE 3

ANOMALIES D'ABONDANCES DANS LES ÉTOILES DE LA PRÉ-SÉQUENCE PRINCIPALE

Abundance anomalies in pre–main-sequence stars
Stellar evolution models with mass loss

Mathieu Vick[ac], Georges Michaud[b], Jacques Richer[c], Olivier Richard[a],

Accepted in: *Astronomy & Astrophysics*, 10 October 2010

Abstract

The effects of atomic diffusion on internal and surface abundances of A and F pre–main-sequence stars with mass loss are studied in order to determine at what age the effects materialize, as well as to further understand the processes at play in HAeBe and young ApBp stars.

Self-consistent stellar evolution models of 1.5 to 2.8 $M_\odot$ stars with atomic diffusion (including radiative accelerations) for all species within the OPAL opacity database were computed and compared to observations of HAeBe stars.

Atomic diffusion in the presence of weak mass loss can explain the observed abundance anomalies of pre–main-sequence stars, as well as the presence of binary systems with metal rich primaries and chemically normal secondaries such as V380

[a]GRAAL UMR5024, Université Montpellier II, CC072, Place E. Bataillon, 34095 Montpellier Cedex 05, France

[b]LUTH, Observatoire de Paris, CNRS, Université Paris Diderot, 5 Place Jules Janssen, 92190 Meudon, France

[c]Département de physique, Université de Montréal, C.P. 6128 Succ. Centre-Ville, Montréal, QC, H3C 3J7, Canada

Ori and HD72106. This is in contrast to turbulence models which do not allow for abundance anomalies to develop on the pre–main-sequence. The age at which anomalies can appear depends on stellar mass.

For A and F stars, the effects of atomic diffusion can modify both the internal and surface abundances before the onset of the main–sequence. The appearance of important surface abundance anomalies on the pre–main-sequence does not require mass loss, though the mass loss rate affects their amplitude. Observational tests are suggested to decipher the effects of mass loss from those of turbulent mixing. If abundance anomalies are confirmed in pre–main-sequence stars they would severely limit the role of turbulence in these stars.

Subject headings: Diffusion — stars: chemically peculiar — stars: mass–loss — stars: pre–main-sequence — stars: evolution — stars: abundances

3.1 Astrophysical context

The recent availability of magnetic field data from instruments such as ESPaDOnS at the Canada-France-Hawaii Telescope and Narval at the Bernard Lyot Telescope has allowed stellar physicists to explore long standing questions in stellar physics. A flurry of recent studies have specifically focused on observing globally organized magnetic fields in intermediate mass pre–main-sequence (PMS) stars in order to determine the origin of magnetic fields in the chemically peculiar Ap/Bp stars (Donati et al., 1997; Alecian et al., 2005; Wade et al., 2005; Catala et al., 2007; Alecian et al., 2008a,b; Folsom et al., 2008; Alecian et al., 2009). This is particularly interesting since A and B type stars have, at most, a very thin convective envelope, which is probably not sufficient to generate solar type, dynamo driven, magnetic fields. With this in mind, the favored hypothesis used to explain the presence of important magnetic fields (from 100 G to 10 kG) in A and B main–sequence (MS) stars is the fossil field theory. In this context, the magnetic field

would either have originated in the molecular cloud from which the star was born, or would have been generated by a dynamo process in the core during the star's earliest evolutionary stages. To test this hypothesis, the above mentioned studies have concentrated their efforts on characterizing magnetic fields in Herbig (HAeBe) stars (Herbig, 1960), which are believed to be the PMS progenitors of Ap/Bp stars (Wade et al., 2005).

In some cases, namely for HD72106, RS Cha and V380 Ori, binarity allows us to probe the effects of chemical separation since both stars likely had the same initial composition. In fact, for at least two of these systems, the secondary has a solar metallicity, whereas the heavier primary star has an above solar metallicity and is likely chemically anomalous. Since atomic diffusion timescales generally decrease when stellar mass increases, chemical separation could perhaps offer an explanation.

Furthermore, a more thorough analysis may allow to characterize other phenomena at play within these stars. What can the observed abundances tell us on the various processes, such as convection, mass loss and magnetic fields, which compete with atomic diffusion? And on what timescales can we expect significant surface abundance anomalies? This paper will address both of these questions.

In Vick et al. (2010) (hereafter Paper I), stellar evolution models with mass loss were introduced and shown to reproduce observed surface abundance anomalies for many AmFm stars. However, observed abundance anomalies do not allow to determine whether it is mass loss or turbulence which is competing with atomic diffusion within the radiative zone of these stars. It was nonetheless established that the surface anomalies of AmFm stars were modulated by chemical separation which occurs deep within the star. Indeed, for both the mass loss models and models with turbulent mixing (Richer et al., 2000; Richard et al., 2001, and references therein), chemical separation near $\log \Delta M/M_* \simeq -5$ to -6 is responsible for the anomalous surface behavior. For PMS stars on the other hand, chemical separation

which occurs at this depth cannot explain observed abundance anomalies since the timescales are much too long. In mass loss models, chemical separation occurring near the surface leads to anomalies which appear at the surface within a few Myr, and could therefore reconcile observations.

In the following analysis, and in our calculations, mass loss is considered in *non rotating* stars, since in such stars, mass loss could be the only process competing with atomic diffusion within the stable radiative zones. An outline of the main aspects of our evolution code is found in Sect. 3.2. The stellar models will be presented in Sect. 3.3, with particular attention to the various effects of mass loss and atomic diffusion in the interior (Sect. 3.3.1) and at the surface (Sect. 3.3.2) of PMS stars. In Sect. 3.4, the models are compared to observations of various HAeBe stars. Finally, in Sect. 3.5, the implications of our results on the processes involved in HAeBe and, by extension, in ApBp stars will be discussed.

3.2 Calculations

The detailed description of the stellar evolution code used for these computations can be found in Paper I and references therein. At age zero, all models are fully convective with the abundance mix prescribed in Table 1 of Turcotte et al. (1998b). Opacities are continuously updated for every mesh point as abundances evolve. The only adjustable parameter, the mixing length parameter α, was calibrated by fitting the current radius and luminosity of the Sun (see model H of Turcotte et al. 1998b). Radiative accelerations are taken from Richer et al. (1998) with corrections due to redistribution from Gonzalez et al. (1995) and LeBlanc et al. (2000). The introduction of mass loss and its impact on transport are discussed extensively in Sect. 4 of Paper I.

No extra mixing is enforced outside of convection zones. The effects of atomic diffusion materialize as soon as radiative zones naturally appear as the models

evolve toward the MS. These effects become more important as the radiative zone expands toward the surface, where atomic diffusion timescales are much shorter.

The unseparated[1] mass loss rates considered range from 10^{-14} to $10^{-13}\,M_{\odot}yr^{-1}$: mass loss rates which lead to surface abundances compatible with observations of many AmFm stars. Due to uncertainties related to the nature of winds for A and F stars (see discussion in Sect. 4.2 of Paper I), we have chosen to limit our investigation to unseparated winds in order to avoid introducing additional adjustable parameters.

Finally, this paper is part of a series of papers starting with Turcotte et al. (1998b), where the mixing length used was calibrated using the Sun for given boundary conditions, helium and metal abundances. For consistency, and in order to isolate the effects of the processes of interest, the same boundary condition, solar composition and mixing length are used for all calculations of Pop I stars (see also Sect. 2 of Paper I).

3.3 Evolutionary models

In Fig. 3.1, the position in the Hertzsprung–Russell (HR) diagram, the evolution of $\Delta M_{\rm BSCZ}$[2], $T_{\rm eff}$ as well as of the surface abundances of He, ^{7}Li, Ca and Fe are shown for four stellar models with the same mass loss rate ($5 \times 10^{-14}\,M_{\odot}yr^{-1}$). Due to numerical instabilities related to the complete disappearance of the surface convection zone, the 2.80W5E-14[3] model could not be converged up to the main–sequence. Therefore, in order to complete the HR diagram, the curve was continued using a 2.80W1E-13 model. In this case, the effect of doubling the mass loss rate on the position in the HR diagram is smaller than the width of the line. Its effect on surface abundances will be discussed in Sect. 3.3.2.

[1] Having the same composition as the photosphere.

[2] BSCZ: bottom of surface convection zone.

[3] The expression 2.80W5E-14 corresponds to a $2.80\,M_{\odot}$ model with a mass loss rate of $5 \times 10^{-14}\,M_{\odot}yr^{-1}$.

The exact definition of the MS and, by extension, the PMS is somewhat arbitrary. The definition given by Iben (1965) stipulates that the *zero age* main–sequence (ZAMS) begins when the thermal-gravitational energy is reduced to one percent of the luminosity of the star, although this may depend on such things as the treatment of convection (Cox, 1968). According to this definition, immediately after of the end of the PMS, indicated by a ($\times$) in Fig. 3.1*c*, $T_{\rm eff}$ and L begin varying much more slowly. The time spent on the PMS varies from $\sim$4 Myr for the 2.80W5E-14 model to $\sim$19 Myr for the 1.50W5E-14 model.

3.3.1 Radiative accelerations, internal abundances and structure

Even on the PMS, the internal structure and abundances vary significantly between 1.5 $M_\odot$ and 2.8 $M_\odot$. In Fig. 3.2, convection zones are shown for models of different mass as they arrive on the ZAMS (see also Fig. 3.1*b*). The internal distribution of convection zones is strongly correlated with stellar mass. For the 1.50 $M_\odot$ model, the SCZ includes the linked H and He convection zones and is never shallower than $\log \Delta M/M_* = -7.2$ (see also Fig. 3.1*b*). For the 1.90W5E-14 model, the surface convection zones separate into a linked H$-$He I CZ and a deeper He II CZ, while a separate He I CZ materializes in the heavier 2.50W5E-14 model. All convection zones disappear completely in the 2.80W5E-14 model before it has even arrived on the MS (see Fig. 3.1*b*). Finally, over the entire PMS phase, the opacity bump near $\log \Delta M/M_* \sim -7.2$ resulting from iron peak element accumulation is not large enough to induce an iron peak convection zone for any of the three models, though iron peak opacity might extend the SCZ slightly inward for the 1.50W5E-14 model. If the mass loss rate is $\leq 10^{-14}\,M_\odot {\rm yr}^{-1}$, an iron convection zone may appear after the PMS (see Fig. 5 of Paper I).

Significant abundance variations appear in the interior of our PMS models. For example, in the 2.50W5E-14 model (bottom row of Fig. 3.3), a 1.1 dex Ca overabundance develops at $\log \Delta M/M_* \simeq -9.4$ as early as 4 Myr. It might seem puzzling

however that such an overabundance transforms into a strong underabundance which reaches below 1 dex at 30 Myr. Why should the behavior at 4 Myr be so different from the rest of the star's evolution and why does a strong overabundance develop in a region where $g_{\rm rad}$(Ca) is below gravity? The reason stems from the fact that the wind progressively advects matter from deeper within the star. That depth is simply given by:

$$\Delta M \simeq \dot{M} t. \tag{3.1}$$

So, at 4 Myr, the wind brings to the surface matter which originates from $4 \times 10^6\,{\rm yr} \cdot 5 \times 10^{-14}\,{\rm M}_\odot{\rm yr}^{-1} = 2 \times 10^{-7}\,{\rm M}_\odot \sim 10^{-7} M_*$. Correspondingly, one sees in the top row of Fig. 3.3 that the flux is nearly constant from the surface down to that depth (except over CZs), while it is clearly not constant below that depth. Naturally, the depth above which the flux is conserved due to advection from the wind increases with age (compare the curves at 4, 30 and 300 Myr). In order to conserve the flux, X(Ca) at 4 Myr increases above $\Delta M/M_* \sim 10^{-7}$ to compensate for the decrease in $g_{\rm rad}({\rm Ca})$[4]. This process can be described by:

$$\mathcal{F}(r) = cst \simeq r^2 \rho (U + U_{\rm w}) c \tag{3.2}$$

where $\mathcal{F}(r)$ is the local flux at radius r, ρ is the local density, U and $U_{\rm w}$ are the advective part of the atomic diffusion velocity and wind velocity respectively, and c is concentration[5]. Although gravity is stronger than $g_{\rm rad}$ over a fraction of the stellar envelope for all elements shown in Fig. 3.3, the downward diffusion velocity is never larger than the wind velocity (see Fig. 3.4 for an example with a 1.9 $\rm M_\odot$ model). Therefore, as long as the absolute value of the wind velocity is larger than the downward diffusion velocity, any given element is dragged toward the surface, and its local abundance adjusts in order to conserve flux. Notice that the fraction

[4]The same type of solution was obtained for oxygen in Landstreet et al. (1998).

[5]This equation is derived and discussed in Sect. 5.1.1 of Paper I.

of the envelope ΔM which can be described by Eq. [3.2] increases with time since the wind progressively advects more mass toward the surface.

With this in mind, one can understand that at $t = 4\,\mathrm{Myr}$, the increase of $X(\mathrm{Ca})$ above $\Delta M/M_* \sim 10^{-7}$ is generated by the large flux arriving from regions where $g_{\mathrm{rad}}(\mathrm{Ca})$ is larger than gravity and which is conserved even as $g_{\mathrm{rad}}(\mathrm{Ca})$ decreases toward the surface. As time passes, Ca arrives at the surface from deeper within the star, where $g_{\mathrm{rad}}(\mathrm{Ca})$ is much smaller than its value at $\Delta M/M_* \sim 10^{-7}$, so that the flux is smaller, the flux conservation applies over a larger mass and the surface abundance consequently decreases. This shows the importance of a solution over the whole star, as done here, since applying an inner boundary condition at $\Delta M/M_* \sim 10^{-7}$ would lead to an erroneous solution after 4 Myr.

On the PMS, the internal concentration variations are much smaller for ^{7}Li, O and Fe than for Ca. However, after the star arrives on the MS, as illustrated by the curve at 30 Myr, larger variations appear, including a nearly $\sim$0.8 dex overabundance of Fe which spans from the surface down to $\log \Delta M/M_* \sim -8$.

As shown in Fig. 3.4, for a mass loss rate of $10^{-14}\,\mathrm{M_\odot yr^{-1}}$, the downward diffusion velocity is greater than the wind velocity for some elements, whereby the flux conservation regime as described by Eq. [3.2] cannot be extended to all elements. The regime shift approximately occurs at $2 \times 10^{-14}\,\mathrm{M_\odot yr^{-1}}$ (see Fig. 5 of Paper I and corresponding discussion). This mass loss rate also marks the limit below which iron accumulation near $T \sim 200\,000\,\mathrm{K}$ can lead to iron peak convection (see Fig. 5 of Paper I).

3.3.2 Surface abundances

An element's surface abundance depends on age, stellar mass and mass loss rate. In Fig. 3.1, the surface abundances of He, ^{7}Li, Ca and Fe are shown for models of 1.5, 1.9, 2.5 and 2.8 $\mathrm{M_\odot}$ with a mass loss rate of $5 \times 10^{-14}\,\mathrm{M_\odot yr^{-1}}$. As stellar mass increases, anomalies appear at the surface earlier. For instance, at around

3 Myr the 2.80W5E-14 model has a 0.6 dex overabundance of Ca while all other models still have their initial abundances (Fig. 3.1*g*). The same can be said for Fe overabundances or He underabundances, which appear later in smaller stellar mass models. Nonetheless, it is evident that for a given element, the overall shape of the surface abundance evolution curve is very similar for the three heavier models. This is due to two things: the appearance of a separate He II CZ, as well as flux conservation as described in the previous section.

For all four elements shown in Fig. 3.1, the initial, short-lived abundance maxima are caused by evolutionary effects. The appearance of a radiative zone which separates the He II CZ from the SCZ allows for chemical separation to occur near the surface. The direction of the anomaly is determined by $g_{\rm rad}$-g within that region (between $\log \Delta M/M_* \sim -10.5$ and -9), and thus He, ^{7}Li and Ca become underabundant, whereas Fe develops an overabundance (compare middle panel of Fig. 3.3 with Fig. 3.1). Following this brief episode, the surface abundance is determined by flux conservation, and so results from chemical separation occurring deeper within the star. For instance, the subsequent, gradual X(Fe) increase results from the wind slowly advecting matter which originated below $\log \Delta M/M_* \sim -7$ (for the 2.50W5E-14 model), where $g_{\rm rad}$(Fe) is greater than g. Similarly, the variations of $X(^7{\rm Li})$ which materialize at the surface are due to variations seen in $g_{\rm rad}(^7{\rm Li})$ between $\log \Delta M/M_* \sim -7.5$ and -6.

The amplitude of the anomalies also depends on stellar mass. The Ca overabundance that materializes on the PMS in the three heavier models reaches 0.65 dex for the 1.90W5E-14 model, while it reaches 1.1 dex in the 2.50W5E-14 model. The He and ^{7}Li underabundances, as well as the initial Fe overabundance follow the same dependence. The 1.50W5E-14 model behaves differently since most of the mass interval from $\log \Delta M/M_* \sim -7.5$ and -6 is mixed by convection (see Fig. 3.2).

3.3.2.1 Effect of varying the mass loss rate

Generally, increasing the mass loss rate lowers the amplitude of surface abundance anomaly extrema, as sinking elements are further advected toward the surface while supported elements are more effectively evacuated. In Fig. 3.5, the surface abundances are shown for a 1.9 $M_\odot$ model with four different mass loss rates. For this model, the PMS ends near 10 Myr (see Fig. 3.1*c*). For the 1.90W5E-14 and 1.90W1E-13 models, He, O and S decrease slowly and monotonously, while Li oscillates around its initial value. A calcium overabundance occurs at $\sim$7 Myr, after which X(Ca) returns to its original value near the end of the PMS. Iron peak elements are overabundant for both models throughout the PMS and onto the MS, with Fe maxima of 0.4 and 0.6 dex for the 1.90W1E-13 and 1.90W5E-14 models respectively. For all elements, maximum amplitudes are smaller when the mass loss rate is larger.

The 1.90W1E-14 behaves quite differently: large anomalies appear very rapidly, especially for sinking elements; ^{7}Li and O underabundances reach -1.2 and -2 dex respectively, while Ca is more than 100 times underabundant as soon as chemical separation reaches the surface. This is because, in contrast to the other two mass loss rates, the wind generated by a mass loss rate of $10^{-14}\,M_\odot yr^{-1}$ is not strong enough to dominate inward diffusion for most sinking elements. In Fig. 3.4, for instance, one can see that for this mass loss rate, the inward diffusion velocity of ^{7}Li, O and Ca is greater or equal to the wind velocity over an important fraction of the upper layers. On the other hand, supported elements behave as in the other two models, though with larger overabundances (at least up to the age of the last converged model). This is logical since the weaker wind cannot evacuate as much of the metal rich material which has accumulated in the SCZ.

On the PMS, and for this stellar mass, only the 1.90W1E-14 model generates sufficient anomalies to cause Z to vary significantly from its original value. The

1.90W1E-12 model only allows very small abundance anomalies at the surface (~ 0.1 dex).

3.3.2.2 Comparison to turbulence models

In the models of Richer et al. (2000), turbulent mixing down to $T \sim 200\,000$ K, the depth of the iron peak CZ, is assumed to be the process which competes with atomic diffusion in the stellar interior. However, due to efficient mixing, abundance anomalies do not appear at the surface of these models until they have arrived on the MS. The significant overabundance of Ca in mass loss models (Fig. 3.1*f*, see also Alecian 1996), is not obtained in the above mentioned models with turbulence, and so could be used as an observational test for young stars.

3.4 Comparison to observations

Confronting our models to observations can offer constraints on mass loss rates as well as on mixing processes near the surface, such as convection. However, in order to compare models with observations, one must try to fit various parameters simultaneously, including age, mass (or $T_{\rm eff}$) and initial surface composition. To reduce the arbitrariness of the comparison, we chose three binary systems, since both components of such systems should have the same age and initial abundances. Unfortunately, determining this age and initial abundance mix is difficult. For all three systems, the age deduced by observers was determined using model isochrones in which many assumptions were necessary. For instance, in all three cases atomic diffusion was neglected, and large mass loss or accretion rates ($\sim 10^{-8}\,{\rm M}_{\odot}{\rm yr}^{-1}$) were assumed. For this reason, we believe that it is preferable to fit the position in the HR diagram from this study rather than use the age determined by other isochrones. As for initial abundances, two of the systems have a chemically "normal" secondary which offers a glimpse into the initial metal content, even though

"normal" abundances can mean different things depending on the solar mix used as a reference[6]. However, assuming that both components of a given binary system have the same initial abundances allows us to make a differential comparison of surface abundances and conclude that differences between the two are caused by internal processes such as atomic diffusion. The chosen original abundances aren't crucial for our analysis since our objective here is to show *when* abundance anomalies appear on the PMS, which is not very sensitive to the initial abundances used to construct the models (see Fig. 13 and Sect. 8.1 of Paper I).

In Fig. 3.1, models are compared to three observed binary systems: V380 Ori (■), HD72106 (▲) and RS Cha (●), which are all believed to be HAeBe stars. For the Ae star V380 Ori (Alecian et al. 2009), the 2.87 $M_\odot$ primary and 1.6 $M_\odot$ chemically normal secondary are compared to the 2.80W5E-14 and 1.50W5E-14 models respectively. Within the error bars, the fit in the HR diagram is very good and the corresponding age of the primary is ∼2.7 Myr (the age given in Alecian et al. 2009 is 2±1 Myr). The 2.80W5E-14 model has developed overabundances of Fe and Ca which reach ∼ 0.3 dex and ∼0.6 dex respectively. Though this model could only be converged until 2.8 Myr, it has already developed anomalies which explain the high metallicity ([M/H]=0.5) determined in Alecian et al. (2009). As illustrated in Fig. 3.6, most metals heavier than $Z \geq 15$ are overabundant by a factor of ∼2−3, while CNO are barely underabundant. Lithium becomes −0.2 dex underabundant. At the best fitting age for the primary, the 1.50W5.14 model still has its initial abundances, which also agrees with observations. The potential effect of a magnetic field, which is observed in the primary, will be discussed in Sect. 3.5.

For HD 72106, the 2.4 $M_\odot$ primary and the 1.9 $M_\odot$ secondary are compared to the 2.50W5E-14 and 1.90W5E-14 models respectively. In the HR diagram, the fit

[6]There is still much debate on the newer Asplund et al. (2005) and Asplund et al. (2009) initial solar abundance mix for which abundances of CNO are significantly lower than the older solar mix of Grevesse et al. (1996); the latter are in better agreement with helioseismology models (Delahaye & Pinsonneault 2006).

is not perfect, especially for the primary, though this was also problematic in Fig. 4 of Folsom et al. (2008). In fact, these authors suggest that at a determined age of $6-13$ Myr (our best fit model is between 5–7 Myr), the primary is most likely on the ZAMS rather than the PMS. Nonetheless, they found that the primary was chemically anomalous with important overabundances of iron peak elements and a strong underabundance of He, while the secondary is almost solar. In the best fitting models for the primary (5–7 Myr), iron overabundances vary from about 0.1 to 0.3 dex, while Ca overabundances vary from about 1 dex down to about 0.3 dex. For the same age interval, the He underabundance varies from -0.1 to -0.15 dex. These amplitudes are smaller than the observed values. This could be due to the mass loss rate being too large (see Fig. 3.5). The presence of a magnetic field and of phase variations (see Fig. 9 of Folsom et al. 2008) do not justify trying to achieve a better fit. A precise model would require 2 or 3 D calculations. Furthermore, some uncertainty remains on the exact amplitudes since all their abundances were determined simultaneously by fitting the observed spectra for a single averaged phase. Over this same age interval, the secondary still has its initial abundances, which agrees with observations.

For RS Cha, the 1.89 $M_\odot$ primary and the 1.87 $M_\odot$ secondary may be compared to the 1.90W5E-14 model. In the HR diagram, the slight discrepancy with the model can be explained by the slight difference in stellar mass. Within reasonable error bars, the model is either chemically normal (up to 6.7 Myr), or has developed an overabundance of Ca of about 0.4 dex accompanied by small underabundances of ^{7}Li and He of -0.11 dex and -0.05 dex respectively. This model does not seem to explain the iron enrichment factor of 1.5 obtained by the authors. However, in contrast to the two previous binary systems, both these stars have the same composition; therefore, there is no difference in composition between the stars to explain, and so the initial abundances could be responsible for the abundance anomalies with respect to the solar composition. The X-ray emission observations

of Mamajek et al. (1999) suggest that accretion could play a role. A smaller mass loss rate would also lead to larger anomalies.

Other young single HAeBe stars which are not shown in Fig. 3.1 may also be compared to our models, though less reliably, since we do not know the luminosity. The star HD 104237 has a mass of about 2.3 $M_\odot$ ($T_{\rm eff} = 8000$ K) and an approximate age of 2 Myr (van den Ancker et al. 1998), as well as a magnetic field of about 50 G (Donati et al., 1997, 2000). It is an HAeBe star for which Acke & Waelkens (2004) found that Si, Cr and Fe abundances were solar, which agrees with our results since even the heavier 2.50W5E-14 model is roughly normal until 3 Myr (see Fig. 3.1). Similarly, HD 190073, which has an age of 1.2±0.6 Myr and a mass of 2.85±0.25 $M_\odot$ ($T_{\rm eff} = 9250$ K), was also found to be roughly solar (Acke & Waelkens 2004). Within the timescales shown in Fig. 3.1, this is also compatible with our results. Finally, though it has just recently embarked on the MS, the young magnetic Bp cluster star NGC 2244-344 which has $T_{\rm eff} \simeq 15\,000$ K and an age of 2 Myr (Bagnulo et al. 2004) can also be compared to our results. A rough extrapolation suggests that the observed ∼1 dex overabundances of Si and Fe and ∼2 dex overabundances of Ti and Cr, as well as the ∼1 dex underabundance of He could simply be the result of chemical separation which began on the PMS.

3.5 General discussion and conclusions

Though it is often assumed negligible for A and F type PMS stars, chemical separation resulting from atomic diffusion can affect both the surface and interior of these young stars. The mass in convection zones (Fig. 3.2) and internal concentrations (Fig. 3.3) can be modified *before* stars arrive on the MS. The amplitude of the internal concentration variations depends on stellar mass. Equivalently, the age at which abundance anomalies appear at the surface also depends on stellar mass. In the presence of weak mass loss, and for models with no turbulent mixing, rota-

tion or magnetic fields, significant internal variations and surface anomalies (both exceeding factors of 10 for some elements) appear as early as $\sim$2 Myr in early-type A stars, and $\sim$20-25 Myr in cooler F stars.

Mass loss only slightly affects the age at which abundance anomalies occur at the surface, although its inclusion in our calculations was necessary in order to evolve models to ages of interest. This being said, mass loss does affect the maximum amplitude of surface anomalies (see Fig. 3.5); a mass loss rate $\geq 10^{-12}\,M_{\odot}yr^{-1}$ nearly flattens surface abundance anomalies, whereas mass loss rates $\leq 10^{-14}\,M_{\odot}yr^{-1}$ allow strong underabundances of elements which are not supported by the radiation field, and may allow the appearance of an iron peak CZ.

The important Ca overabundance materializing in our models of PMS stars, which is not obtained in similar models with turbulence, could help distinguish between these two scenarios (see Sect. 3.3.2.2). If abundance anomalies observed on the surface of A and F type PMS stars are in fact due to chemical separation, this strongly favors the mass loss model as presented in this paper and should be confirmed by asteroseismology (see also Sect. 6 of Paper I). More precise determinations of individual elemental abundances may also allow further differentiation.

Atomic diffusion coupled with a mass loss rate which is compatible with observations of AmFm stars may elucidate why there are PMS binary systems such as V380 Ori and HD72106 for which the primary is chemically anomalous while the secondary remains roughly normal (see Sect. 3.4). Since diffusion timescales vary more rapidly with stellar mass than with mass loss rate (compare Figs. 3.1 and 3.5), smaller mass loss rates (or atomic diffusion on its own) may also explain these systems. More precise observations of individual elements are required to further constrain mass loss rates. Observed abundance anomalies in other single PMS stars and young ApBp stars may also result from atomic diffusion (Sect. 3.4), without the need for other more exotic explanations. This being said, many PMS stars have observed magnetic fields, strong accretion rates (from stellar disks) or both.

These phenomena could also have an effect on transport in the external regions of the star.

A magnetic field can impact chemical transport through its effects on rotation via magnetic braking, by modifying convection in the atmosphere (Cattaneo et al. 2003), as well as by affecting atomic diffusion velocities (Alecian & Stift 2006). In single stars for which rotation cannot be slowed by tidal forces, strong magnetic fields may be the only process which sufficiently reduces rotation to allow chemical separation. Although it has to our knowledge never been shown that magnetic fields can completely eliminate convection, their topologies can induce horizontally dependent convection and abundance profiles (Babel & Michaud 1991), in addition to anisotropic mass loss and/or accretion (Théado et al. 2005). Until these processes are better understood, and magnetic field geometries are better constrained for individual stars, it would be ill-advised to introduce additional magnetic field related parameters into our calculations. The effects of magnetic fields on chemical transport may best be grasped through comparative mapping of superficial magnetic fields and abundances as done for roAp stars in Kochukhov & Wade (2010) and Lüftinger et al. (2010), as well as for HAeBe stars in Folsom et al. (2008).

Accretion also affects elemental distribution in the atmospheres of stars. For accretion rates greater than approximately $10^{-12}\,M_{\odot}yr^{-1}$, the abundance profiles in the atmosphere, and in the interior, simply reflect those of the accreted material (Turcotte & Charbonneau 1993). For accretion rates of about $10^{-14}\,M_{\odot}yr^{-1}$, the atmospheric abundances will be similar to the accreted material, while abundance gradients due to atomic diffusion may form below the SCZs. In both cases, as soon as the star stops accreting, chemical separation resulting from atomic diffusion dominates within 1 Myr.

In terms of stellar modeling, HAeBe stars are extremely complex: stellar winds, accretion, rotation and magnetic fields complicate simulations. Current models cannot account for all these processes without invoking multiple parameters which

may blur any actual physics taking place within these stars. Though there are other processes involved, it is shown that atomic diffusion can lead to abundance anomalies on the PMS, and that neglecting its effects could have an impact on calibrating atmosphere models.

3.6 Acknowledgments

M. Vick would like to thank E. Alecian and C. Folsom for some very insightful discussions. He also thanks the Département de physique de l'Université de Montréal for financial support, as well as everyone at the GRAAL in Montpellier for their amazing hospitality.We acknowledge the financial support of Programme National de Physique Stellaire (PNPS) of CNRS/INSU, France. This research was partially supported by NSERC at the Université de Montreál. Finally, we thank the Réseau québécois de calcul de haute performance (RQCHP) for providing us with the computational resources required for this work.

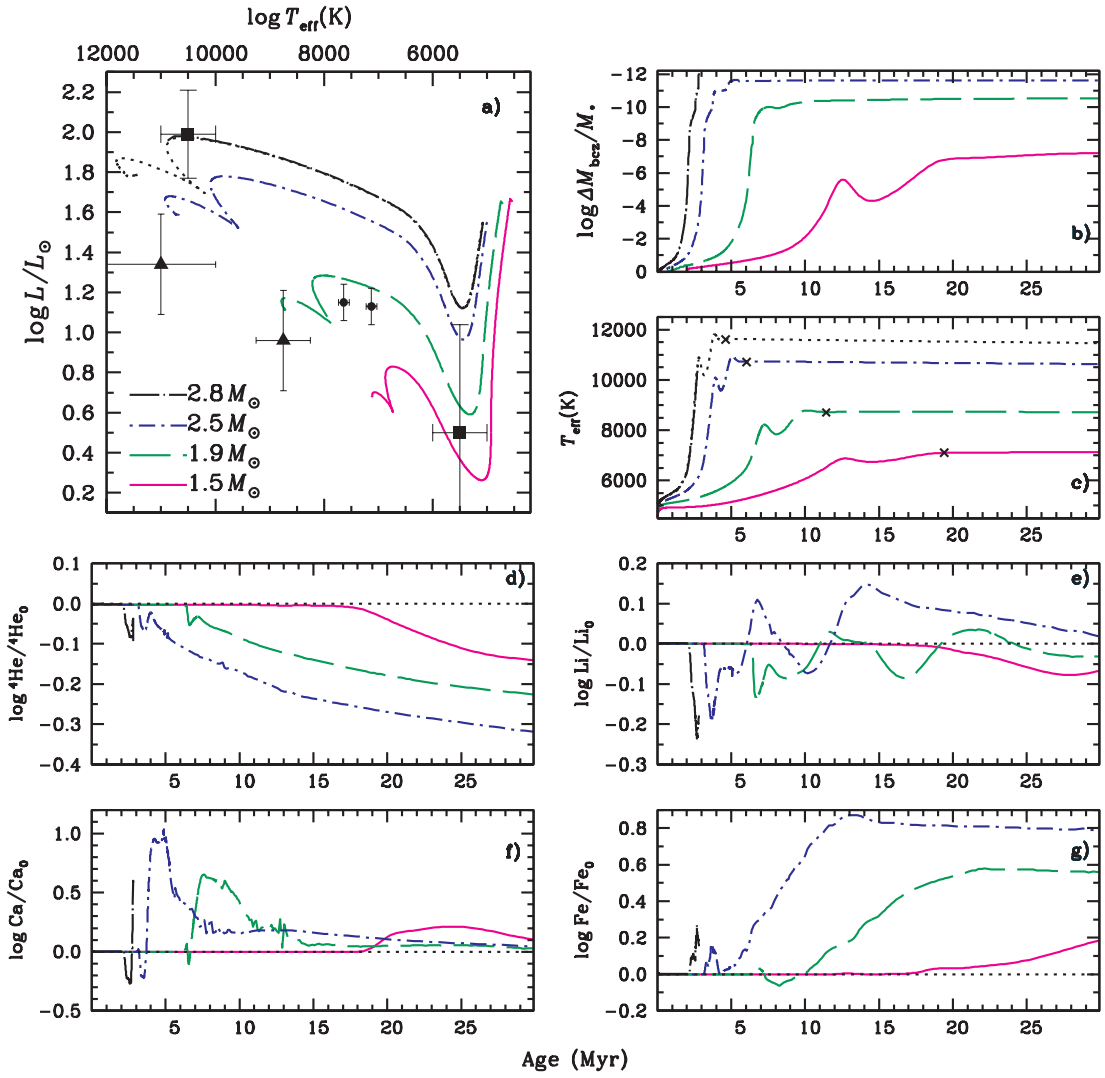

Figure 3.1: The position in the HR diagram *(a)* is shown for four models with a mass loss rate of $5 \times 10^{-14}\,\mathrm{M_\odot yr^{-1}}$. The curves end (on the left) at 30 Myr, age at which all the models are on the main–sequence. The dotted segment of the 2.80 $\mathrm{M_\odot}$ curve represents a model with a mass loss rate of $10^{-13}\,\mathrm{M_\odot yr^{-1}}$ and was added in *(a)* and *(c)* in order to facilitate extrapolation, though it was not added in other panels for which the mass loss rate has an effect. Observations are shown in the HR diagram for three sets of binary stars: (■) V380 Ori (Alecian et al. 2009); (▲) HD72106 (Folsom et al. 2008); (●) RS Cha (Alecian et al. 2005). The evolution of the bottom of the surface convection zone *(b)*, $T_{\rm eff}$ *(c)*, as well as the abundances of He *(d)*, ^{7}Li *(e)*, Ca *(f)* and Fe *(g)* are also shown. In panel *(c)*, (×) marks the approximate end of the PMS.

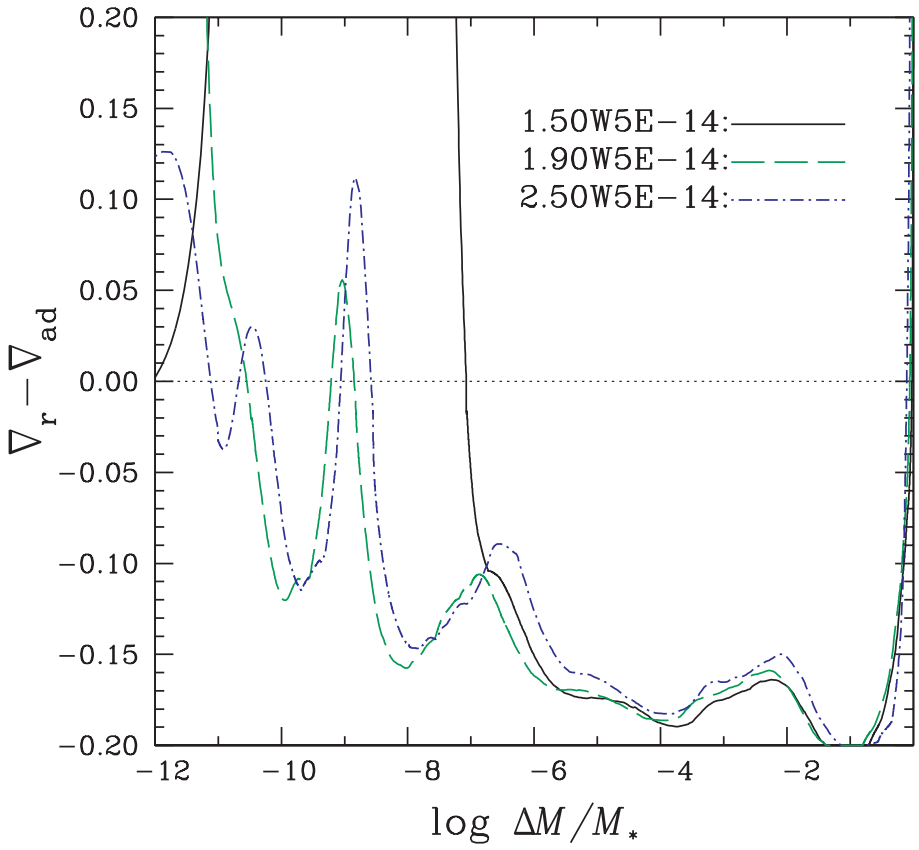

Figure 3.2: Internal variation of $\nabla_{\rm r} - \nabla_{\rm ad}$ for three models with a mass loss rate of $5 \times 10^{-14}\,{\rm M}_\odot{\rm yr}^{-1}$ at the onset of the ZAMS. The surface is at $\log \Delta M/M_*$=−12 and transport is convective when $\nabla_{\rm r} - \nabla_{\rm ad} > 0$. For different masses, the position of convection zones in relation to $\log \Delta M/M_*$ changes slightly, though it is constant in relation to T.

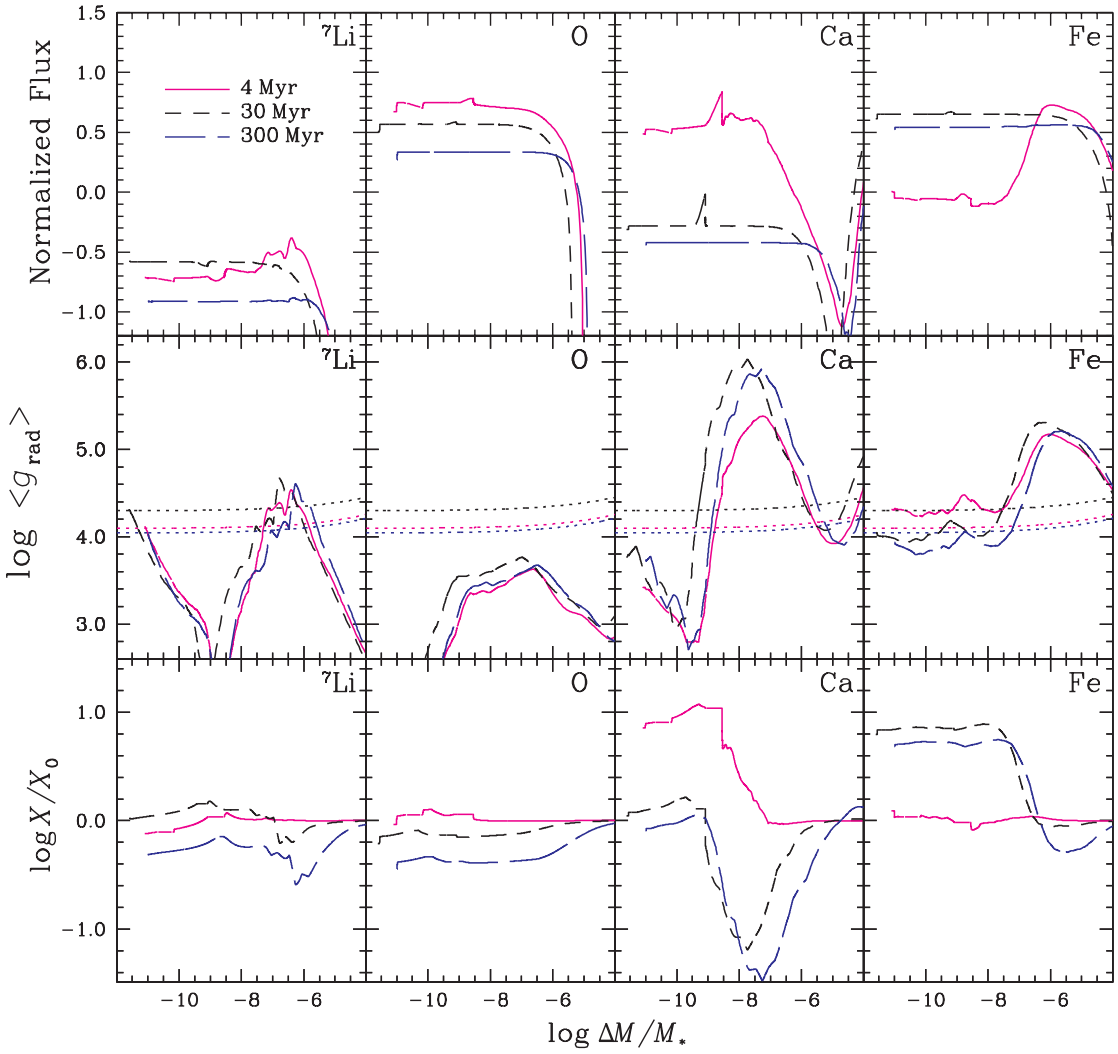

Figure 3.3: Comparison of the normalized local flux with radiative accelerations and internal abundances of ^{7}Li, O, Ca and Fe at 3 different ages for the 2.50W5E-14 model. The curves end (on the left) at the bottom of the surface convection zone. In the middle row, the dotted line represents gravity.

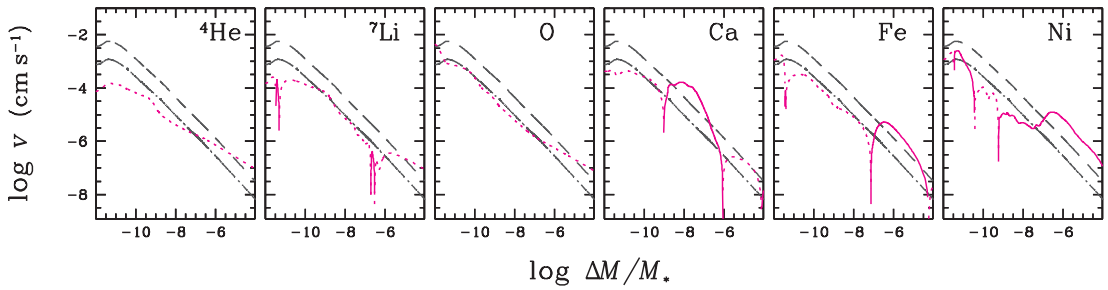

Figure 3.4: Wind velocities (dot-dashed line: $10^{-14}\,M_{\odot}yr^{-1}$; dashed line: $5 \times 10^{-14}\,M_{\odot}yr^{-1}$) and diffusion velocities (solid when positive, toward the surface, and dotted when negative) of a few selected elements in a $1.90\,M_{\odot}$ model near the ZAMS. For most species, wind velocities decrease more rapidly inwards than diffusion velocities.

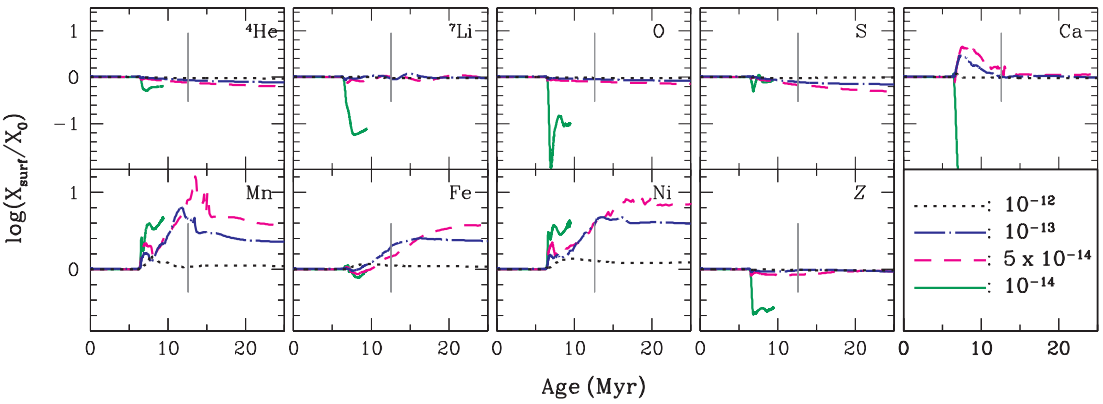

Figure 3.5: Surface abundance variations for models of $1.9\,M_{\odot}$ with different mass loss rates which are identified in the lower right panel in $M_{\odot}yr^{-1}$. The vertical line indicates the approximate end of the PMS.

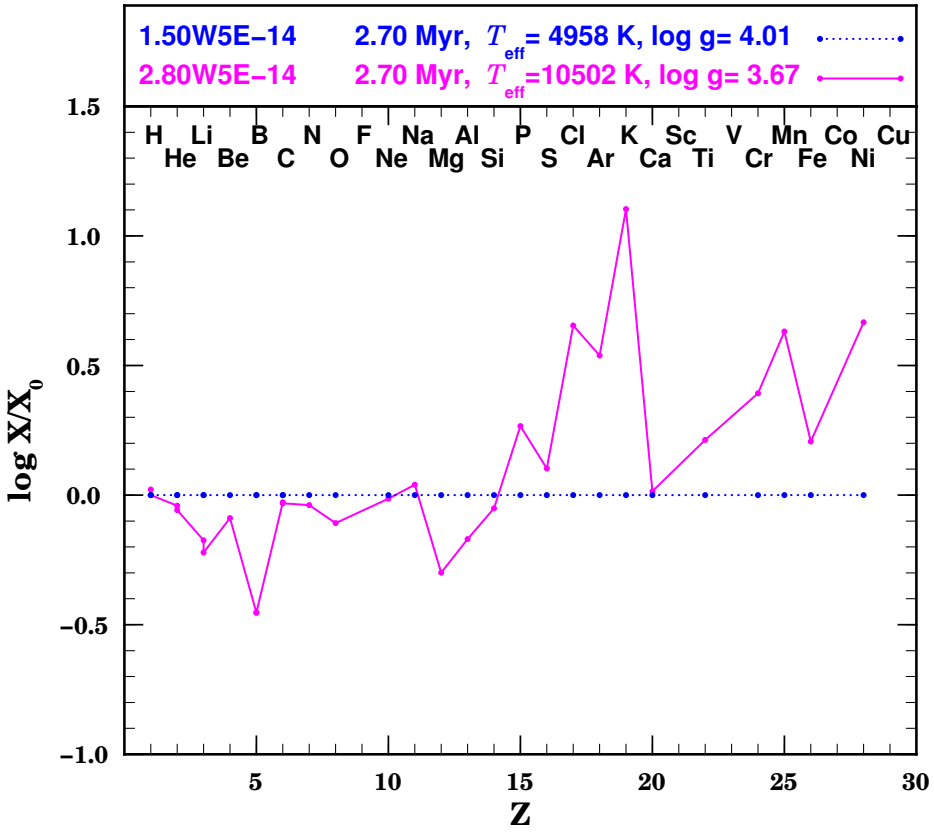

Figure 3.6: Surface abundances for models representing the components of the binary star V380 Ori. The models were chosen at the age which best fits the primary in the HR diagram (Fig. 3.1*a*). In both models, the mass loss rate is $5 \times 10^{-14}\,\mathrm{M}_{\odot}\mathrm{yr}^{-1}$.

CHAPITRE 4

LES ÉTOILES DE POPULATION II ET LE PLATEAU DE SPITE

Population II stars and the Spite plateau
Stellar evolution models with mass loss

Mathieu Vick[ac], Georges Michaud[b], Jacques Richer[c], Olivier Richard[a],

Abstract

Models with masses between 0.6 and 0.8 $M_\odot$ were calculated with unseparated mass loss in order to constrain its potential role in metal poor dwarfs.

Self-consistent evolutionary models including all the effects of atomic diffusion and radiative accelerations for 28 chemical species were computed and compared to previous models with mass loss as well as models with turbulent mixing.

For models with an initial metallicity of $[Fe/H]_0 = -2.31$, mass loss rates of about $10^{-12}\,M_\odot yr^{-1}$ lead to surface abundance profiles which are very similar to those obtained in models with turbulence. These models with turbulence are able to reproduce observations of galactic halo lithium abundances, as well as lithium and other elemental abundances from metal poor globular clusters such as NGC 6397.

[a]GRAAL UMR5024, Université Montpellier II, CC072, Place E. Bataillon, 34095 Montpellier Cedex 05, France

[b]LUTH, Observatoire de Paris, CNRS, Université Paris Diderot, 5 Place Jules Janssen, 92190 Meudon, France

[c]Département de physique, Université de Montréal, C.P. 6128 Succ. Centre-Ville, Montréal, QC, H3C 3J7, Canada

The internal solution obtained in models with mass loss is slightly different from the internal solution in models with turbulent mixing. The mass loss rates required to reproduce plateau-like lithium abundances are difficult to justify, however.

Subject headings: Diffusion — stars: chemically peculiar — stars: mass-loss — stars: evolution — stars: abundances — stars: Pop II

4.1 Astrophysical context

Population II stars can be used as tracers for exploring the universe's chemical evolution. Still, in order to correctly connect the chemical properties of the early Universe to the composition of the oldest observed stars, one must be able to map the evolution of their current abundances back to their original values. Doing so could help elucidate numerous questions pertaining to Big Bang nucleosynthesis, the nature of the first supernovae, as well as the age of the Universe.

The nearly constant Li abundance of most low-metallicity ($[\mathrm{Z/H}] < -1.5$) halo field stars between ($6300\,\mathrm{K} > T_{\mathrm{eff}} > 5500\,\mathrm{K}$) – otherwise known as the Spite plateau (Spite & Spite 1982; Spite et al. 1984) – has puzzled astronomers for decades. Originally, many inferred that this plateau was representative of the Universe's original Li abundance, though it was promptly shown that this could not be the case (Michaud et al. 1984). Precise observations of the cosmic microwave background, namely those from the *Wilkinson Microwave Anisotropic Background* (WMAP, see Spergel et al. 2007), have now lead to a primordial lithium abundance of $A(^7\mathrm{Li})$[1]$= 2.65^{+0.05}_{-0.06}$ (Cyburt et al. 2003; Steigman 2007), or even higher, $A(^7\mathrm{Li}) = 2.72^{+0.05}_{-0.05}$ (Cyburt et al. 2008), while the lithium content in metal poor dwarfs, ranging from $A(^7\mathrm{Li}) = 2.0$ to 2.4 (Bonifacio et al. 2007; Asplund et al. 2006; Charbonnel & Primas 2005; Meléndez & Ramírez 2004; Bonifacio 2002), is a factor of $2-3$ lower. Even though Population III stars destroyed some of the primordial lithium (Piau et al. 2006), this cannot explain the large discrepancy (Ryan et al. 1999).

[1] $A(\mathrm{Li}) = \log[N(\mathrm{Li})/N(\mathrm{H}) + 12]$.

Changing the standard Big Bang nucleosynthesis model is another possible explanation, though it seems hypothetical (Ichikawa et al. 2004; Coc et al. 2004; Cumberbatch et al. 2007). This leads many to believe that the solution stems from within the stars themselves. Possible stellar explanations may include destruction via differential rotation in the context of gravity waves (Talon & Charbonnel 2004; Charbonnel & Talon 2005), rotational mixing (Vauclair 1988; Charbonnel et al. 1992; Pinsonneault et al. 1999), as well as settling via atomic diffusion (Deliyannis et al. 1990; Profitt & Michaud 1991; Salaris et al. 2000; Richard et al. 2005). That being said, the higher Li content of subgiant (SG) stars compared to main–sequence (MS) stars in globular clusters (GC) such as NGC 6397 (Korn et al. 2007; Lind et al. 2009; González Hernández et al. 2009) favors a model in which the lithium is not destroyed, but simply sinks below the photosphere prior to dredge-up.

Additional constraints may stem from claimed observations of ^{6}Li (Asplund et al. 2006), which, with a thermonuclear destruction cross section 60 times larger than the heavier isotope, would severely constrain the stellar destruction of ^{7}Li. These observations remain very uncertain (Cayrel et al. 2007). Also, many recent studies have also claimed that below [Fe/H]$\simeq -2.5$, Li abundances lie significantly below the Spite plateau abundance and with increased scatter (Boesgaard et al. 2005; Asplund et al. 2006).Though this was also obtained by Aoki et al. (2009) and Sbordone et al. (2010), other observations suggest that there might simply be a lower plateau abundance for extremely metal poor (EMP) stars (Meléndez et al. 2010).

Although the surface convection zone (SCZ) of galactic Population II stars homogenizes abundances down to depths at which atomic diffusion is relatively slow, the long lifetimes of these stars, which reach the age of the Universe, allows for the effects of chemical separation to materialize at the surface. However, models which allow atomic diffusion to take place unimpeded lead to lithium underabundances which are too large at the hot end of the plateau (Michaud et al. 1984). By

enforcing additional turbulent mixing below the SCZ, models of metal poor stars with gravitational settling and radiative accelerations are able to reproduce many observations of halo and globular cluster stars (Richard et al., 2002b; VandenBerg et al., 2002; Richard et al., 2002a, 2005; Korn et al., 2006). These same models were also successful in explaining abundance anomalies in AmFm (Richer et al. 2000; Richard et al. 2001) and horizontal branch stars (Michaud et al. 2007, 2008).

In Vauclair & Charbonnel (1995), gravitational settling inhibited by an unseparated and constant mass loss rate of $\sim 3 \times 10^{-13}\,\mathrm{M_{\odot}yr^{-1}}$ leads to near constant lithium abundances, even at the hot end of the plateau. However, these calculations, which will be further discussed in Sect. 4.4, did not include the effects of radiative accelerations, nor did they follow atomic diffusion in detail for many individual elements; therefore, further inspection is warranted.

In Vick et al. (2010) and Vick et al. (submitted), hereafter Papers I and II respectively, stellar evolution models with mass loss were introduced and shown to reproduce observed surface abundance anomalies for many AmFm and chemically anomalous HAeBe binary stars. To further validate the model and to help constrain the relative importance of mass loss with respect to turbulent mixing in stars, the present mass loss models will be compared to models with turbulence from Richard et al. (2002b) and Richard et al. (2005), namely the T6.09 models, which are able to reproduce observations of galactic halo stars, as well as globular cluster stars.

In the following analysis, and in our calculations, mass loss is considered in *non rotating stars*, since in such stars it might be the only process competing with atomic diffusion. To our knowledge, mass loss rates have never been observed in Population II MS stars, likely due to their small amplitudes; therefore, mass loss rates will be constrained solely via surface abundance anomalies. In Sect. 4.2, the evolutionary calculations will be presented, while the results will be discussed in Sect. 4.3. In Sects. 4.4 and 4.5, the models with mass loss will be compared to previous evolutionary models of metal poor dwarfs with mass loss, as well as to

models with turbulence. Conclusions will follow in Sect. 4.6.

4.2 Calculations

The stellar evolution models were calculated as detailed in Paper I and references therein. Atomic diffusion is computed self-consistently with radiative accelerations from Richer et al. (1998) and corrections for redistribution from Gonzalez et al. (1995) and LeBlanc et al. (2000). Chemical transport is computed for all 28 chemical species included in the OPAL database (Iglesias & Rogers 1996). The models are evolved from the pre–main-sequence (PMS) with the abundance mix prescribed in Richard et al. (2002b) for $Z_0 = 0.00017$ (or equally, [Fe/H]$= -2.31$). With respect to the solar abundance mix used in Papers I and II for Population I stars, the relative abundances of alpha elements are increased as appropriate for Population II stars (VandenBerg et al. 2000). The introduction of mass loss and its impact on transport is outlined in Paper I.

No extra mixing is enforced outside of convection zones. The effects of atomic diffusion materialize as soon as radiative zones appear as the models evolve toward the MS. These effects become more important as the radiative zone expands toward the surface, where atomic diffusion becomes more efficient, and the convection zone becomes less massive, thereby reducing the dilution of anomalies.

The unseparated[2] mass loss rates considered range from 10^{-13} to 10^{-12} $M_{\odot}yr^{-1}$, with the former value leading to surface abundances compatible with observations of many AmFm stars. Due to uncertainties related to the nature of winds for Population II stars (see also discussion in Sect. 4.2 of Paper I), we have chosen to limit our investigation to unseparated winds in order to avoid introducing additional adjustable parameters.

In order to fully constrain the effects of mass loss, we have chosen to use the

[2]In this context, unseparated refers to the abundances in the wind being the same as in the photosphere.

same boundary condition (Krishna-Swamy 1966), and mixing length parameter, α, as in Papers I and II (see also Sect. 2 of Paper I and VandenBerg et al. 2008). Most models in Richard et al. (2002b,a) and Richard et al. (2005) were computed with the Eddington gray atmosphere surface boundary condition (see also Turcotte et al. 1998b). The main effect is to change the value of α. In both cases, the mixing length is calibrated using the Sun so that very little difference remains in solar type models. Therefore, though the different boundary conditions might lead to a different evolution of SCZ depths and masses (see Fig. 9 of Richard et al. 2002b), the remaining slight difference does not play a role in models with turbulence since the separation which modulates surface abundances usually occurs deeper. As will be shown in Sect. 4.3, the same is true for the models with mass loss presented in this paper since separation also occurs deeper within the star.

4.3 Evolutionary models

Evolutionary models of masses ranging from 0.6 to 0.8 $M_\odot$, an interval of masses which spans the Spite plateau, are shown in a Hertzprung-Russell diagram (H-R) in Fig. 4.1. All the models have an initial metallicity of $Z_0 = 0.00017$, and a mass loss rate of $10^{-12}\,M_\odot yr^{-1}$. Figure 4.1 also shows the evolution of $T_{\rm eff}$, gravity, the depth (in mass, $M_{\rm BSCZ}$, and in temperature, $T_{\rm BSCZ}$) of the bottom of the SCZ as well as the central H mass fraction. At 12 Gyr and 13.5 Gyr, the assumed lower and upper limits on the age of halo dwarfs, the 0.79 and 0.77 $M_\odot$ models are respectively at the MS turnoff.

For all models, the variations in surface convection zone depth have an impact on surface abundance evolution since the efficiency of atomic diffusion, or equivalently the diffusion velocity, varies with depth. Throughout the MS, $M_{\rm BSCZ}$ decreases until H is exhausted in the stellar core (i.e. until turnoff). Although this, and other parameters, depend on the mass loss rate, the effect is slight (see

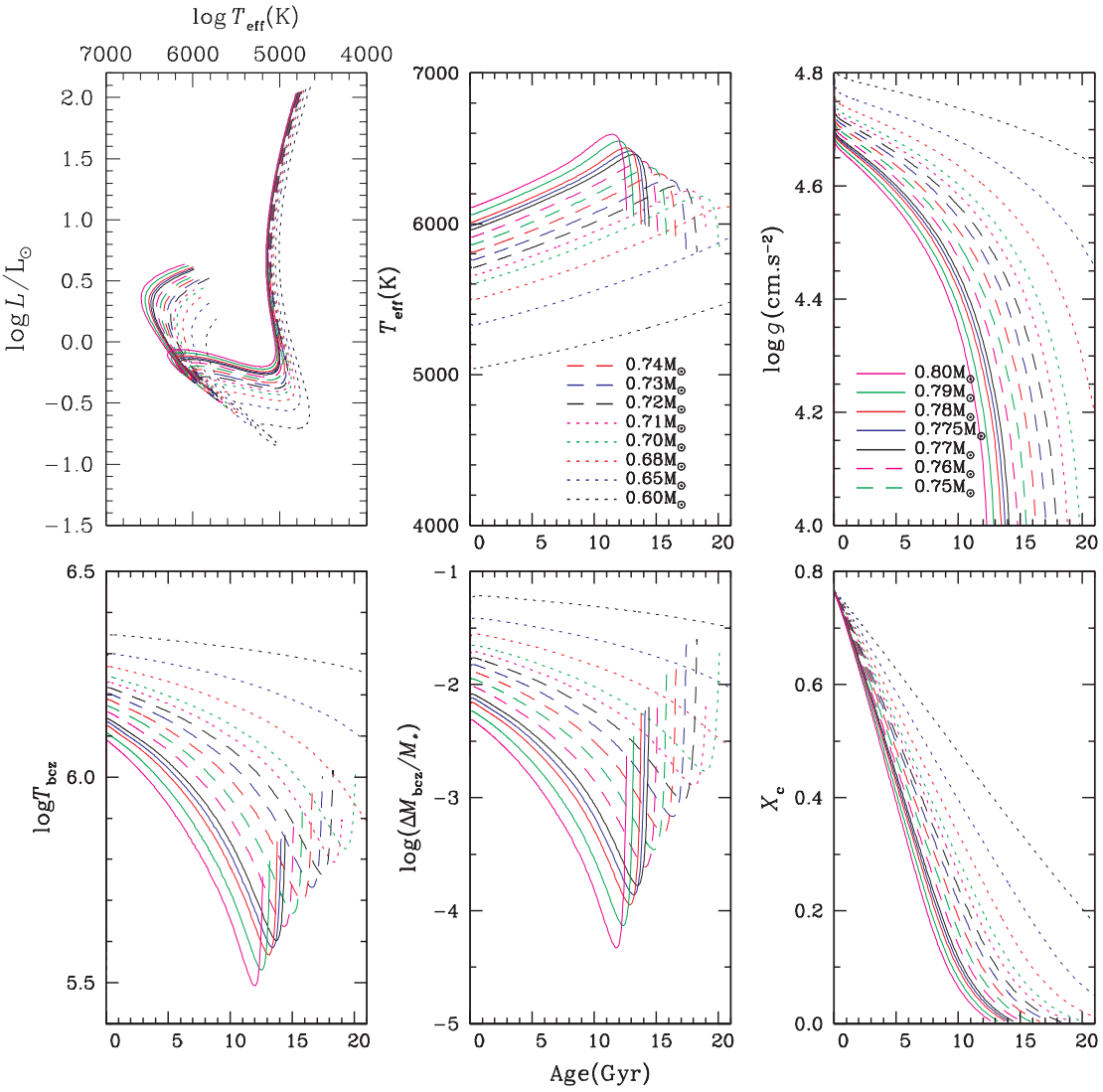

Figure 4.1: The position in the Hertzprung-Russell diagram as well as the evolution of $T_{\rm eff}$, $\log g$, the temperature at the base of the SCZ ($T_{\rm BSCZ}$), the mass at the base of the SCZ ($M_{\rm BSCZ}$) and the mass fraction of hydrogen in the core ($X_{\rm c}$) for stars of $0.6 - 0.8\,{\rm M}_\odot$ with $Z_0 = 0.00017$ and $\dot{M} = 10^{-12}\,{\rm M}_\odot{\rm yr}^{-1}$.

Fig. 4.2). Just before the MS turnoff, there is a $\sim 125\,{\rm K}$ difference in $T_{\rm eff}$ between the $0.8\,{\rm M}_\odot$ model with *diffusion only* and the 0.80W1E-12 model[3], while the difference falls to about 15 K between the *diffusion only* and 0.80W1E-13 models. The

[3]0.80W1E-12 refers to a $0.80\,{\rm M}_\odot$ model with a mass loss rate of $1 \times 10^{-12}\,{\rm M}_\odot{\rm yr}^{-1}$.

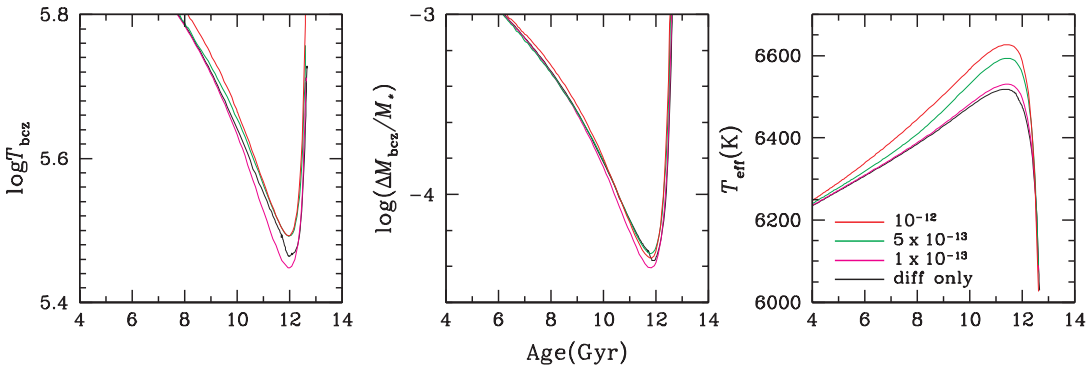

Figure 4.2: The impact of mass loss rate on the evolution of the depth (in temperature and mass) of the SCZ as well as on $T_{\rm eff}$ for 0.8 $M_\odot$ models.

effect on stellar age at the turnoff, or equivalently, on the stellar lifetime, is smaller than the line width. While $M_{\rm BSCZ}/M_*$ varies by a factor of 100 ($\log \Delta M/M_*$ goes from ~ -2.3 to -4.3) on the MS for a 0.80 $M_\odot$ model (Fig. 4.1), the maximum effect of adding mass loss is below 0.08 dex.

4.3.1 Radiative accelerations and internal abundance variations

Within very short time scales, convection homogenizes abundances from the bottom of the SCZ to the stellar surface; therefore, the competition between radiative acceleration ($g_{\rm rad}$) and gravity below the surface convection zone determines an element's surface abundance. In Fig. 4.3, the internal variations of $g_{\rm rad}$ and g are shown for the 0.80W1E-12 model[4]. The changes in $g_{\rm rad}$ over time are due principally to structure changes, since the abundances in Population II stars with $[{\rm Fe/H}]_0 = -2.31$ are never large enough to cause saturation[5]. For other stellar masses, the contribution of changes in $g_{\rm rad}$ to the dependence of surface abundances on stellar mass—which will be discussed in Sect. 4.3.2— are not as important as

[4]This model mass was chosen specifically in order to facilitate comparison with the models and figures from Richard et al. (2002b).

[5]The mass loss rate also has little to no effect on $g_{\rm rad}$ for this same reason, and because its effects on the structure are very small (see Fig. 4.2).

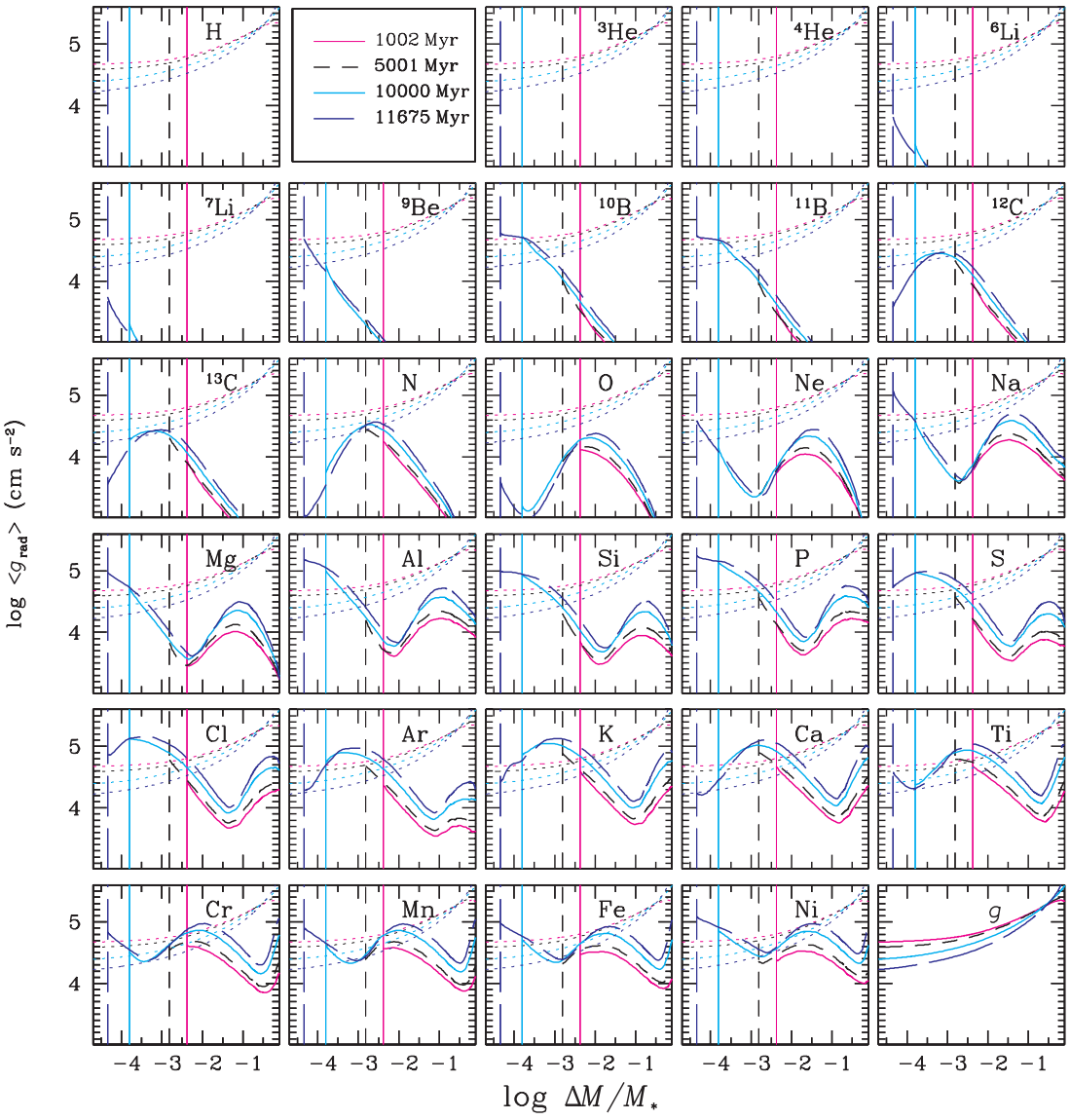

Figure 4.3: Radiative accelerations and gravity (dotted lines) at four different ages for a 0.8 $M_\odot$ model with $\dot{M} = 10^{-12}\,M_\odot yr^{-1}$. The vertical lines indicate the position of the bottom of the SCZ.

the contribution of changes in SCZ mass and depth (Fig. 4.1).

For many elements, including He, Li and O, the radiative acceleration is always smaller than gravity. These elements are underabundant at the surface until dredge-

up. Other elements such as Be, Mg and Fe have local $g_{\rm rad}$ maxima just below the SCZ, which, at 11 675 Myr, causes their surface abundances to increase.

Since, in these stars, a given element's abundance does not affect its $g_{\rm rad}$, the internal $g_{\rm rad}$ variations can be related to its ionization state; H-like configurations lead to local maxima, while He-like configurations lead to local minima. As we move toward elements with more electrons when not ionized, the H-like state is encountered at greater depths. Carbon for instance, is in a H-like configuration at $\log \Delta M/M_* \sim -3$, while for Si, this occurs near $\log \Delta M/M_* \sim -1$. Some elements, including Fe and Ni, never quite reach the H-like state[6]. Unlike the H-like maxima, the second local $g_{\rm rad}$ maxima, which is clearly distinguishable for all elements heavier than S, is usually greater than or equal to gravity. This $g_{\rm rad}$ increase corresponds to configurations between F-like and Li-like.

The internal abundance variations caused by the radiative accelerations shown in Fig. 4.3 are plotted in Fig. 4.4. For the 0.80W1E-12 model, all internal variations caused by atomic diffusion are smaller than 0.2 dex (in contrast to the ones caused by thermonuclear destruction and creation which are encountered near and around the stellar core for $Z < 8$). For this mass loss rate, all elements are underabundant below the SCZ, and down to about $\log \Delta M/M_* \sim -0.5$. Below this point, elements heavier that O become slightly overabundant due to gravitational settling. Therefore, for these elements, there are underabundances of up to a factor of 1.6 over the outer half of the stellar mass and overabundances of a few percent over the inner half.

For models without mass loss, internal abundance variations become much greater (Fig. 4.5). In the 0.80 $M_\odot$ *diffusion only* model, some elements become over 1 dex overabundant (Cl and K), while other elements become -0.8 to -1 dex underabundant (^{4}He, ^{7}Li, O and Na). These variations can be linked directly to variations

[6]To be more precise, in the stellar core, these elements arrive at an equilibrium between multiple ionization configurations, including the hydrogenic state.

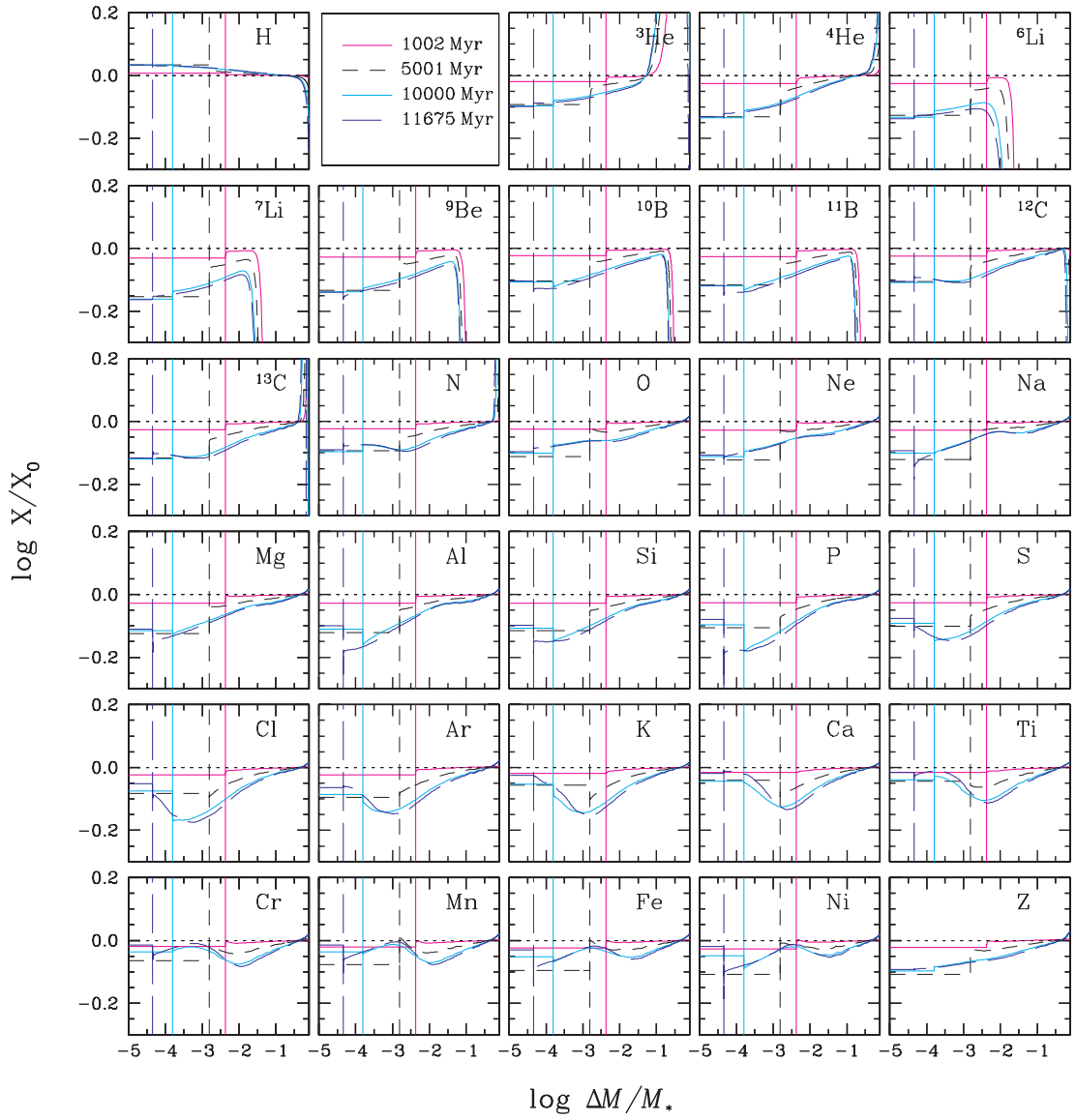

Figure 4.4: Internal abundance variations for the same model and ages seen in Fig. 4.3. The vertical lines indicate the position of the bottom of the SCZ. At 11 675 Myr, ^{7}Li is completely depleted by thermonuclear reactions below $\log \Delta M/M_* = -2$ (about 99% of the stellar mass).

in $g_{\rm rad}$. For example, the Ni underabundance which begins at $\log \Delta M/M_* \sim -2.5$, and reaches up to the BSCZ, is caused by the increase in its $g_{\rm rad}$ over the same depth interval. In this region, Ni is pushed into the SCZ, thus causing the Ni

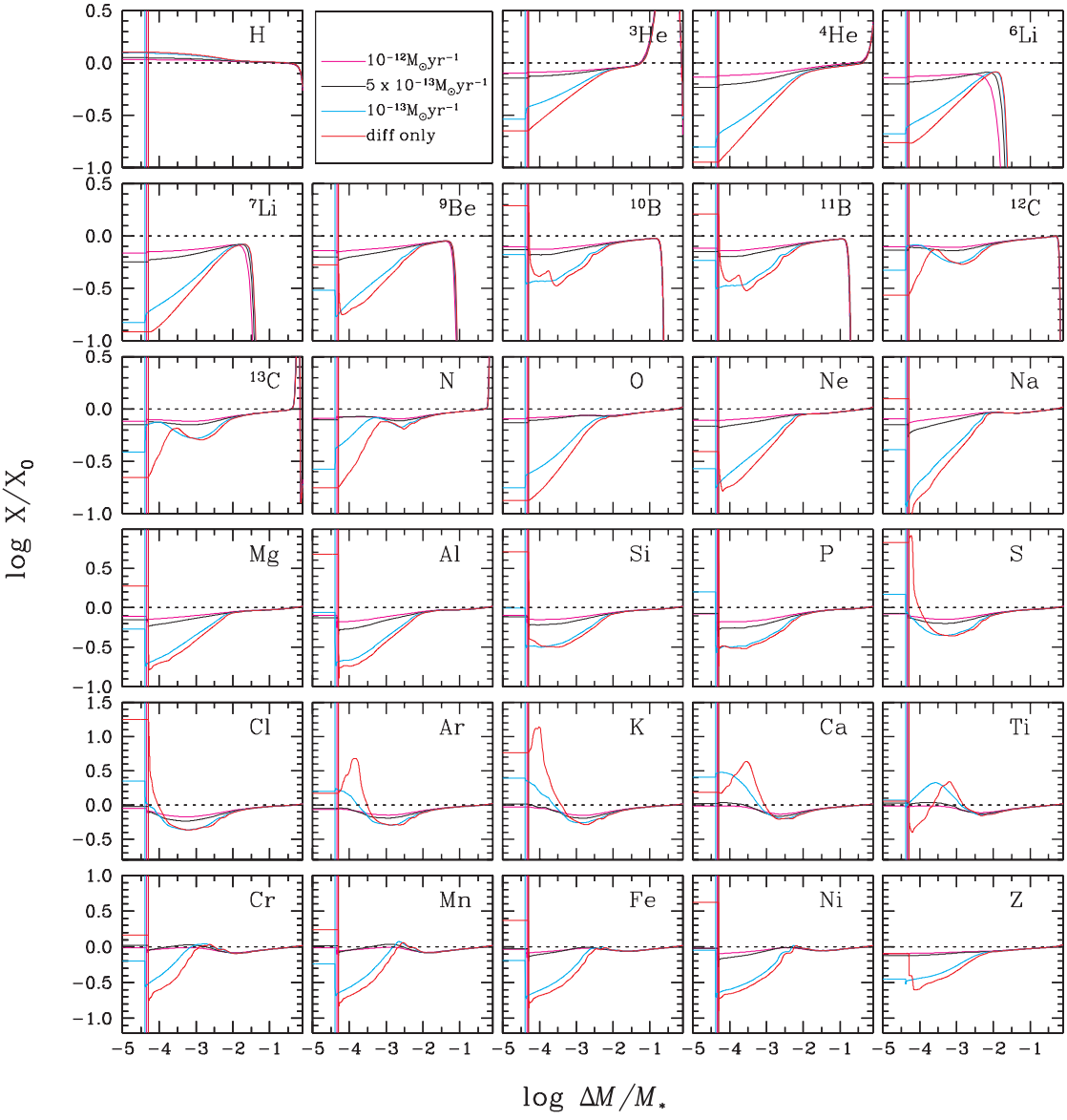

Figure 4.5: The impact of mass loss rate on internal abundance profiles for 0.80 $M_\odot$ models. The models are shown just before turnoff near 11.675 Myr. Atomic diffusion affects mainly the outer 10^{-2} of the stellar mass.

abundance to increase at the surface and decrease below the SCZ. On the contrary, Ca becomes overabundant near $\log \Delta M/M_* = -3.5$ for the 0.80 $M_\odot$ *diffusion only* model since $g_{\rm rad}$(Ca) has a local maximum just below this depth.

In general, mass loss has the effect of reducing internal anomalies. For example, a mass loss rate of $10^{-13}\,M_{\odot}yr^{-1}$ reduces the underabundances of ^{4}He and ^{7}Li immediately below the BSCZ by $\sim$0.2 dex, while a mass loss rate of $10^{-12}\,M_{\odot}yr^{-1}$ reduces them by $\sim$0.8 dex (Fig. 4.5). Mass loss also has the effect of advecting elements for which $v_{\rm wind}$ is greater than the downward diffusion velocity. For example, at 10 Gyr—or 10^{10}yr—matter which is advected by a mass loss rate of $10^{-13}\,M_{\odot}yr^{-1}$ will have moved $\sim 10^{-3}M_{*}$ nearer the surface.

In fact, when mass loss is added, there are two possible types of internal solutions: those dominated by atomic diffusion and those dominated by mass loss (see also Sect. 5.1.1 of Paper I). For any given model with mass loss, an element's internal abundance solution is determined by the mass loss rate wherever the associated velocity, $v_{\rm wind}$, is greater in amplitude than the settling velocity $v_{\rm sett}$. For example, in Fig. 4.6, one first notes that the depth at which $|v_{\rm wind}| \simeq |v_{\rm sett}|$, which we will call the point of separation, depends on the element and on the stellar age (through structure changes). For the 0.80W1E-12 model, mass loss dominates the internal solution of ^{7}Li from the surface down to $\log \Delta M/M_{*} \sim -1.2$, while this occurs nearer $\log \Delta M/M_{*} \sim -0.9$ for Ni. As discussed in Sect. 5.1.1 of Paper I, the consequence is that local abundances above the point of separation are not determined by the local $g_{\rm rad}$, but rather adjust in order to conserve the flux arriving from just below the point of separation. If the wind dominated solution extends down to ΔM, which is given by $\Delta M = \dot{M} \times t$, the surface abundance reflects $g_{\rm rad}/g$ at ΔM. If we come back to the previous example, at 10 Gyr—or 10^{10}yr— and for a mass loss rate of $10^{-13}\,M_{\odot}yr^{-1}$, the surface reflects $g_{\rm rad}/g$ at $\sim 10^{-3}M_{*}$.

For smaller mass loss rates, or when the settling velocity dominates locally, abundances reflect local variations in $g_{\rm rad}$, and can therefore accumulate, as is the case for Ca in the 0.80W1E-13 model in Fig. 4.5.

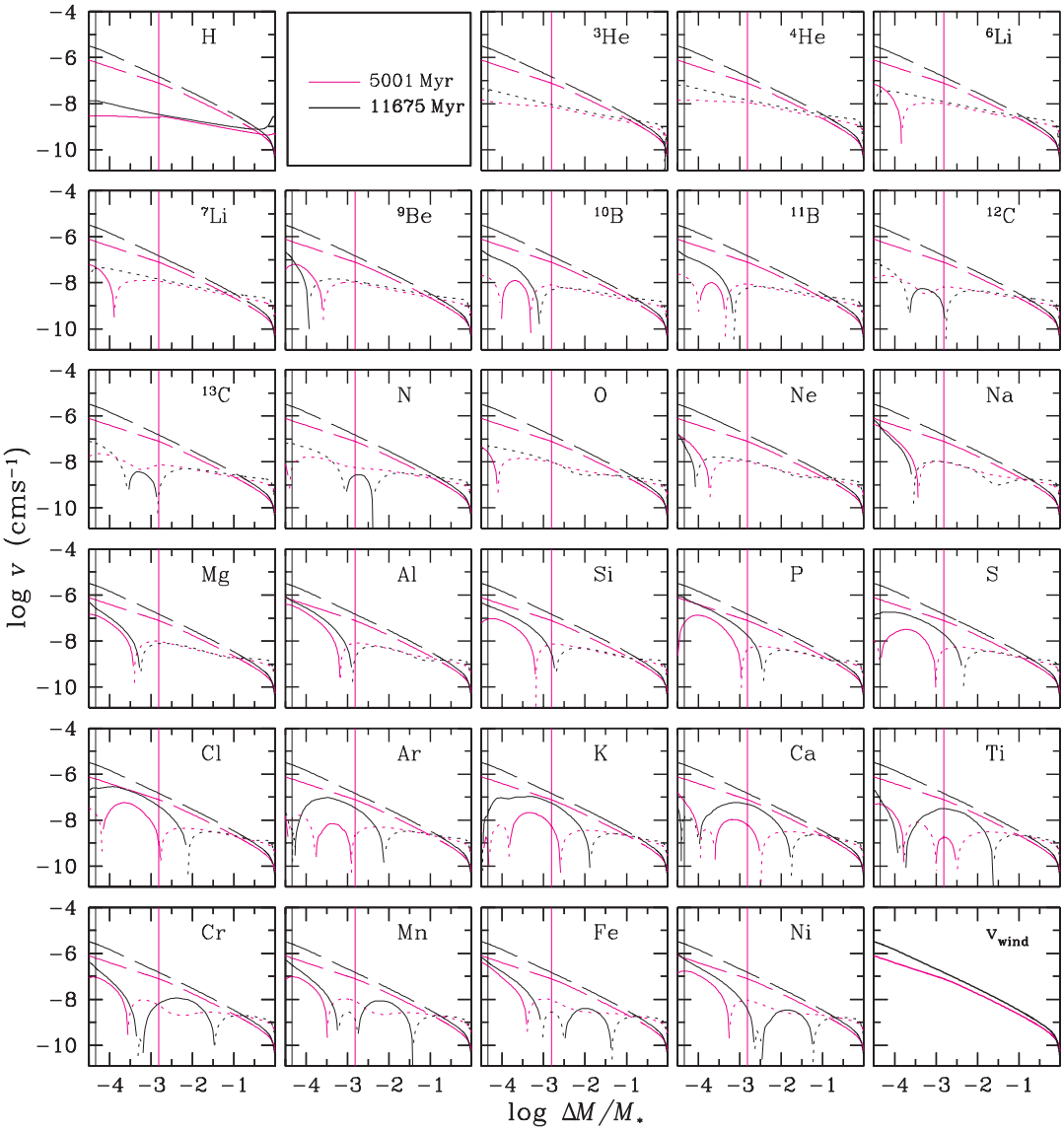

Figure 4.6: Wind velocity (long dashed line) and diffusion velocities (solid when positive, towards the surface, and dotted when negative) in the 0.80W1E-12 model at two different ages.

4.3.2 Surface abundance variations

For a given metallicity, surface abundances depend on stellar mass, age as well as on the mass loss rate. The age and stellar mass dependance are clearly demon-

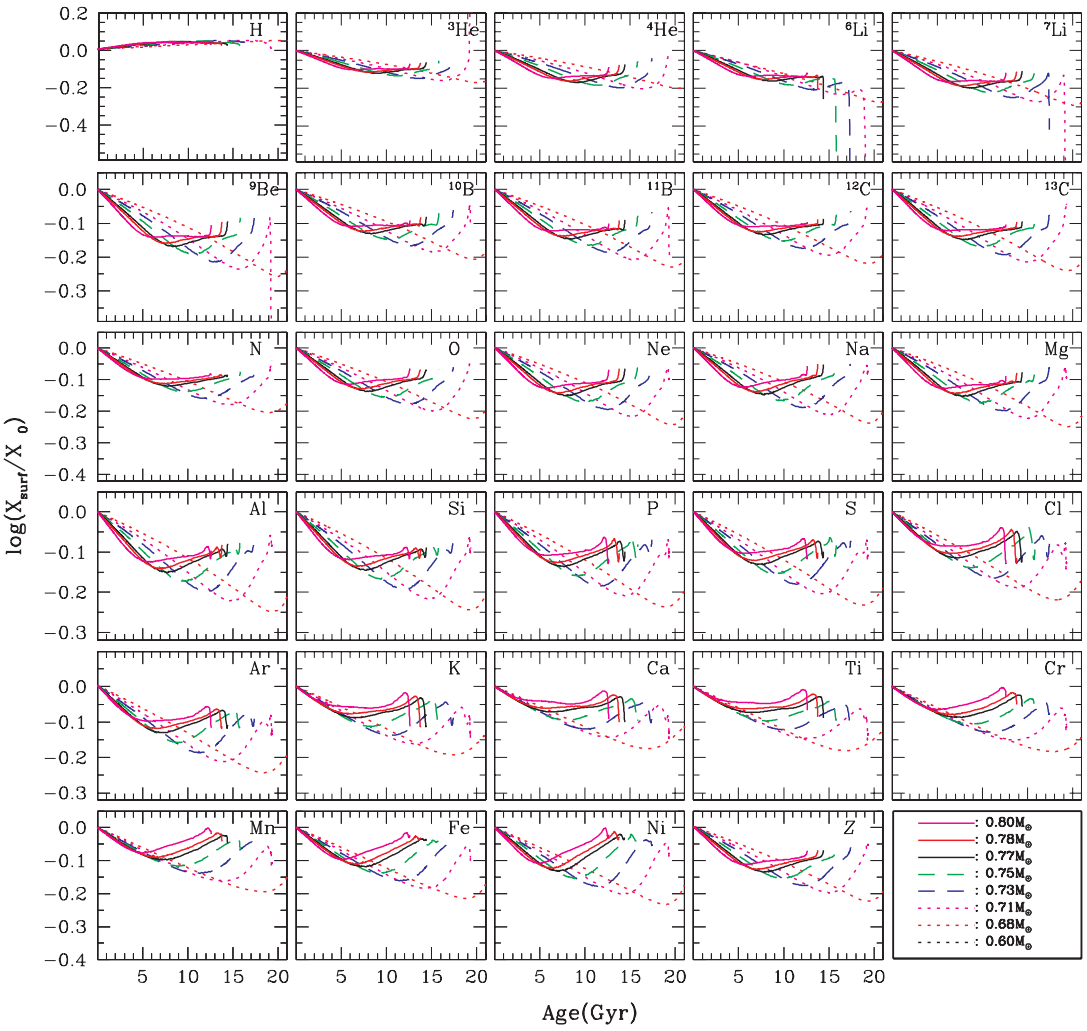

Figure 4.7: Evolution of surface abundance anomalies for selected stellar masses with a mass loss rate of $10^{-12}\,\mathrm{M}_{\odot}\mathrm{yr}^{-1}$.

strated in Fig. 4.7, which shows the evolution of surface abundances for selected models with a mass loss rate of $10^{-12}\,\mathrm{M}_{\odot}\mathrm{yr}^{-1}$. First, for this mass loss rate, all elements are underabundant throughout MS evolution, and until dredge up advects layers which are affected by thermonuclear reactions. The maximum underabundance amplitudes increase as stellar mass decreases, simply because settling becomes more important for models with longer lifetimes. Over a large fraction of the stellar lifetime, the overall *shape* of the surface abundance solution is quite

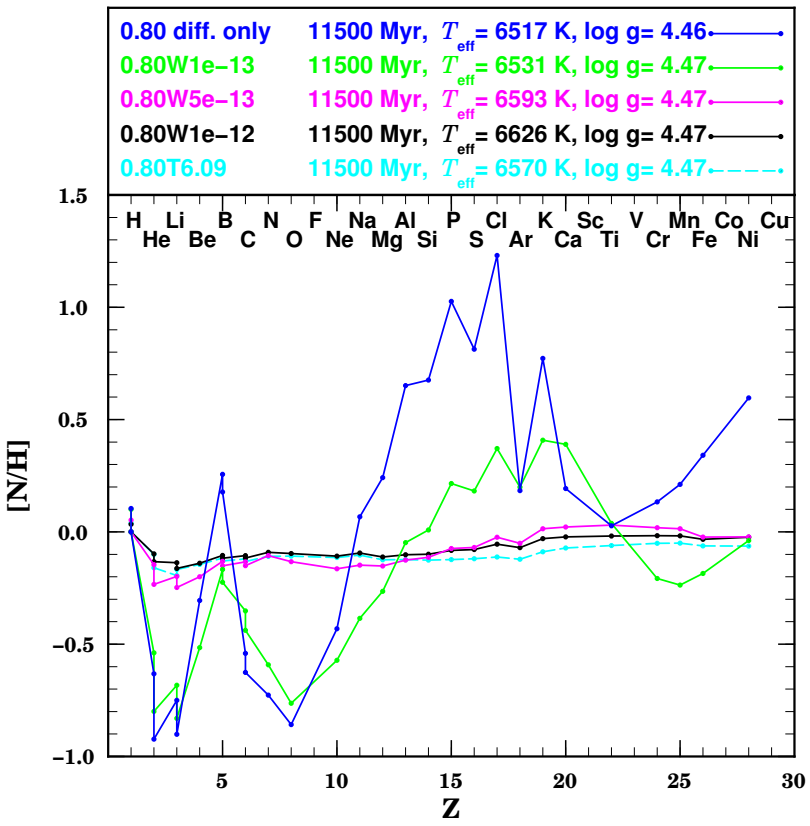

Figure 4.8: Comparison of the surface abundance anomalies for $0.8\,M_\odot$ models with and without mass loss as well as with the T6.09 turbulent parametrization. At 11.5 Myr, these models are just before turnoff.

similar for all masses since the overall shape of $g_{\rm rad}$ does not vary significantly over this mass interval.

The mass loss rate also affects the surface abundance, since supported elements are expelled through the surface, and sinking elements encounter advection from $v_{\rm wind}$. For $0.80\,M_\odot$ models near turnoff (Fig. 4.8), a mass loss rate of $10^{-13}\,M_\odot{\rm yr}^{-1}$ reduces He, Li and O underabundances obtained in the *diffusion only* model by a little more than 0.1 dex, while also reducing overabundances of Cl and P by about 0.8 dex. For this mass loss rate, the effect is greater for supported elements, since the wind velocity is not large enough to overcome settling. For other elements, the

effect is not so linear: the overabundances of Fe and Ni become underabundances, while Ca and Ti become more overabundant for a short period of time. For Ca and Ti, this is because $v_{\rm wind}$ has an effect just below the SCZ, where $g_{\rm rad} \simeq g$ (Fig. 4.3); therefore, instead of accumulating below the SCZ, they are pushed into it. Similarly, mass loss advects the layers just below the BSCZ, where Fe and Ni abundances are smallest, into the SCZ (see Fig. 4.5). For the two larger mass loss rates, the surface anomalies are reduced to factors mostly below about 0.2 dex. While the 0.80W1E-12 has generalized underabundances, the 0.80W5E-13 model has small overabundances of elements from K to Mn.

4.3.2.1 Surface lithium abundances

Figure 4.9 shows lithium and iron isochrones for the *diffusion only* model, models with mass loss rates of $10^{-12}\,{\rm M}_\odot{\rm yr}^{-1}$ and $5 \times 10^{-13}\,{\rm M}_\odot{\rm yr}^{-1}$, as well as the T6.09 models at 12 Gyr and 13.5 Gyr. In the *diffusion only* model, large Fe and Li anomalies are obtained around the turnoff: lithium decreases by a factor of up to 10 at 12 Gyr, while Fe becomes overabundant by a factor of 5. For the mass loss rate of $5 \times 10^{-13}\,{\rm M}_\odot{\rm yr}^{-1}$, the maximum lithium underabundance is reduced to -0.35 dex, whereas Fe overabundances are transformed into underabundances by factors below -0.25 dex. For the $10^{-12}\,{\rm M}_\odot{\rm yr}^{-1}$ model, the maximum amplitudes are further reduced. While the anomalies in the *diffusion only* model near turnoff are much smaller at 13.5 Gyr, than at 12 Gyr, this effect is not as important for lithium, and is unnoticeable for both models with mass loss.

Below $\sim$6000 K, the lithium isochrones with and without mass loss differ only slightly for pre-turnoff stars—with lithium depletions between -0.12 and -0.14 dex near $T_{\rm eff} = 5400$ K—since the SCZ is too deep for mass loss to have an effect. Though all three isochrones have decreasing lithium abundances for models hotter than $\sim$6000 K, the underabundance amplitudes decreases as the mass loss rate increases. At 12 Gyr, the lithium abundance begins increasing again near 6200 K

and 6400 K for the models with $10^{-12}\,M_\odot yr^{-1}$ and $5 \times 10^{-13}\,M_\odot yr^{-1}$ respectively. This is due to SCZ retraction, which exposes layers for which v_{wind} is dominant.

The *diffusion only* lithium isochrones do not exhibit plateau-like behaviour. On the other hand, the mass loss isochrones are much flatter: the $5 \times 10^{-13}\,M_\odot yr^{-1}$ model has a scatter of about $\sim$0.1 dex and the $10^{-12}\,M_\odot yr^{-1}$ model has a scatter of about $\sim$0.05 dex with respective plateau average values of about -0.3 dex and -0.25 dex below the initial ^{7}Li abundance.

4.4 Comparison to previous models with mass loss

In previous evolutionary calculations for Population II stars with mass loss, Vauclair & Charbonnel (1995) found that both mass loss rates of $10^{-12.5}$ ($\simeq 3 \times 10^{-13}$) and $10^{-12}\,M_\odot yr^{-1}$ lead to lithium abundances that increase monotonically (by at most 0.5 dex for the smaller mass loss rate) with T_{eff} for 6 models ranging from 0.60 to 0.80 $M_\odot$. They suggest that the larger mass loss rate completely wipes out the effects of atomic diffusion, and leads to a primordial lithium abundance of $A(\mathrm{Li}) = 2.5 \pm 0.1$, which is determined from the surface abundance of their hottest model.

Unfortunately, a direct comparison to their results is impossible, since the stellar models are too different. These differences include Y_0, Z_0, α_{MLT}, the surface boundary condition, and the diffusion of metals. As a result, the SCZ evolution is very different. By comparing the internal lithium profile of the *diffusion only* model in Fig. 4.10 with the one from Fig. 4 of Vauclair & Charbonnel (1995), one sees that at 10 Gyr, the SCZ (i.e. the flat part of both solutions) is about 4 times more massive in their models. Furthermore, their 0.75 $M_\odot$ models are still on the MS (with their T_{eff} still increasing) at 18 Gyr, while our 0.75 $M_\odot$ models have already evolved toward the subgiant branch at 15 Gyr. The difference in Y_0 is not large enough to explain this significant discrepancy[7].

[7] Though not shown, this was verified by evolving models with $Y_0 = 0.2484$, which, due to

That being said, despite the limitations in a direct comparison of the models with mass loss, some general results can be discussed. For instance, at 10 Gyr, they found that the surface lithium abundance for the $10^{-12.5}\,M_{\odot}yr^{-1}$ model was 0.12 dex larger than in the $10^{-12}\,M_{\odot}yr^{-1}$ model, since the stronger mass loss rate reaches into the lithium burning layers. Our models also suggest that the strongest wind drags some material from the lithium depleted layers outward. Indeed, from Fig. 4.10, the wind velocity for the $10^{-12}\,M_{\odot}yr^{-1}$ model at 10 Gyr dominates the settling velocity down to $\log \Delta M/M_{*} = -1$, the point of separation, which is well into the burning layers. However, at 10 Gyr, this has not yet reached the surface since at 10^{10}yr, a mass loss rate of $10^{-12}\,M_{\odot}yr^{-1}$ has only exposed to the surface layers which are above $\sim 10^{-2}M_{*}$. In the same way, mass loss advected all mass above the point of separation by $\sim 10^{-2}M_{*}$, thus explaining the difference in the depths at which Li falls to zero in the *diffusion only* and $10^{-12}\,M_{\odot}yr^{-1}$ models.

Futhemore, the shape of the internal solutions in both sets of models is very different; for $10^{-12}\,M_{\odot}yr^{-1}$, they obtain a nearly flat solution from the BSCZ down to Li burning layers, whereas our solution suggests an important atomic diffusion induced gradient below the SCZ. In order to verify that the difference was not simply due to evolutionary effects, namely SCZ mass, this result was compared to smaller mass models with the same mass loss rate (the 0.73W1E-12, 0.70WE1-12 and 0.68W1E-12 models). Even in models with more massive SCZs, the abundance gradient remains, since it is formed below $\log \Delta M/M_{*} \sim -2$, the point above which the wind has imposed the conservation of flux. The reason for these differences is not evident.

Finally, while they obtain *no* effects of chemical separation in all models with $10^{-12}\,M_{\odot}yr^{-1}$, lithium settling leads to $\sim$0.15 dex surface abundance reductions (at 12 Gyr) in *all* our models (see Fig. 4.9). In terms of isochrone shape, they obtain

the smaller H mass fraction in the core, left the MS only 1 Gyr earlier than for models with $Y_0 = 0.2352$. The models from Vauclair & Charbonnel (1995) have $Y_0 = 0.2403$

a monotonic linear increase from the cooler stars to the hotter ones (Figs. 5 and 6 of Vauclair & Charbonnel 1995), while our isochrones dip between $6400\,\mathrm{K} \geq T_{\mathrm{eff}} \geq 6000\,\mathrm{K}$ (Fig. 4.9).

Some of the differences are related to the difference in models, namely the M_{BSCZ} evolution. Other differences could include the fact that the wind term in their diffusion equation does not include the often overlooked flux factor (m_r/M_*) which is required in evolutionary models (see Eq. [6] of Paper I)[8].

4.5 Comparison to models with turbulence

Along with describing the effects of mass loss on Population II evolutionary models with mass loss, this paper's main objective is to contrast models with mass loss to the ones with turbulence presented in Richard et al. (2002b). In particular, the goal is to see if a specific mass loss rate can reproduce the surface behavior exhibited in the T6.09 models, which are compatible with observations of halo dwarf Li abundances (Richard et al. 2005).

In Fig. 4.8, the 0.80T6.09 and 0.80W1E-12 models are shown to be very similar. Abundances of ^{4}He and ^{7}Li are about 0.02 dex smaller in models with turbulence, whereas elements with $Z > 12$ are on average about 0.03-0.04 dex smaller (with a maximum of about 0.05 dex for Ar). The differences in surface abundances of elements from Be to Mg are smaller than the line width.

In terms of lithium and iron isochrones, as shown in Fig. 4.9, the differences are just as small. Both types of models lead to nearly flat abundances (above $T_{\mathrm{eff}} = 5800\mathrm{K}$), and their plateau value is nearly the same. At 12 Gyr, the maximum difference in Fe abundance, which occurs near $T_{\mathrm{eff}} \simeq 6100\mathrm{K}$, is about 0.07 dex, though this could be due to the absence of turbulent models in this region. Similarly, for models hotter than $T_{\mathrm{eff}} = 5800\mathrm{K}$, the maximum difference in ^{7}Li abundances, which occurs at $T_{\mathrm{eff}} \simeq 6100\mathrm{K}$, is of 0.1 dex, and could again be explained

[8] At $\log \Delta M/M_* = -2$, this factor changes v_{wind} by 1%, and by 10% at $\log \Delta M/M_* = -1$.

by the T6.09 isochrone's poor resolution. Below $T_{\rm eff} = 5800$K, the fit is not as good, likely due to lithium destruction. The discrepancy is greater than 0.3 dex, although again, resolution is not sufficient to correctly evaluate the difference.

Whereas the surface behaviour is quite similar for most models with T6.09 and $10^{-12}\,{\rm M}_\odot{\rm yr}^{-1}$, the internal solutions are a little different. By comparing Fig. 4.4 with Fig. 8 of Richard et al. (2002b), one notes that in the 0.80W1E-12 model, abundances change gradually from the bottom of the SCZ down to about $\log \Delta M/M_* = -1$, with most variations between 0.1 and 0.15 dex. However, in the 0.80T6.09 model at turnoff, abundances are constant from the surface down to just below $\log \Delta M/M_* = -2$.

4.6 Conclusion

Evolutionary models with atomic diffusion and unseparated mass loss explain some characteristics observed in galactic halo dwarfs. A mass loss rate of $5 \times 10^{-13}\,{\rm M}_\odot{\rm yr}^{-1}$ leads to surface lithium isochrones which exhibit plateau-like behaviour with a maximum scatter of about 0.1 dex around an average value which is -0.3 dex below the initial lithium abundance (Fig. 4.9). For models with mass loss rates of $10^{-12}\,{\rm M}_\odot{\rm yr}^{-1}$, the lithium isochrones are even flatter with a scatter of about 0.05 dex around an average value about -0.25 dex lower than the initial abundance.

While mass loss does not have a significant impact on a star's structural properties, its effects on abundances, both in the interior and on the surface, can be important. In the interior, abundance profiles are either dominated by atomic diffusion—and reflect local variations in $g_{\rm rad}$—or are dominated by the wind—and adjust in order to conserve the flux coming from below (Sect. 4.3.1). A mass loss rate of $10^{-13}\,{\rm M}_\odot{\rm yr}^{-1}$ reduces internal anomalies by up to a factor of 6-7, while a mass loss rate of $10^{-12}\,{\rm M}_\odot{\rm yr}^{-1}$ reduces all anomalies to below 0.2 dex (Fig. 4.5). At

the surface, these two mass loss rates lead to similar reductions (Fig. 4.8). While the $10^{-12}\,M_{\odot}yr^{-1}$ models lead to generalized underabundances for all elements, smaller mass loss rates allow for overabundances to develop at the surface.

The mass loss models presented in this paper differ significantly from those presented in Vauclair & Charbonnel (1995) (Fig. 4.10). Although some of this difference can be attributed to differences in input parameters, other discrepancies are more difficult to explain (Sect. 4.4).

With respect to the T6.09 models from Richard et al. (2002b), the models with mass loss are very similar above $T_{\rm eff} = 5800$K, especially the models with a mass loss rate of $10^{-12}\,M_{\odot}yr^{-1}$ (Figs. 4.8 and 4.9). Below this temperature, turbulence leads to greater lithium destruction.

Unfortunately, even for mass loss rates of $10^{-12}\,M_{\odot}yr^{-1}$, the stellar winds implicated in these calculations are barely detectable through direct observation. Furthermore, despite the fact that acceleration processes for these types of winds are poorly understood, it is difficult to justify mass loss rates which are 100 times larger than the solar mass loss rate ($\sim 10^{-14}\,M_{\odot}yr^{-1}$). It is unlikely that winds in Population II stars are driven by radiation; therefore, if these stars host solar-like winds, one could hope to observe solar-like coronae and/or X-ray emission.

As a next step, these models could be extended to the red giant branch in order to further constrain the effects of mass loss in Population II giants, for which mass loss has extensively been observed and studied (Origlia et al. 2007). It would also be interesting to see if mass loss would affect, or even eliminate, the effects of atomic diffusion (Michaud et al. 2010) and/or of thermohaline mixing (Charbonnel & Zahn 2007).

Acknowledgments

M.Vick would like to thank the Département de physique de l'Université de Montréal for financial support, as well as everyone at the GRAAL in Montpellier for their amazing hospitality. We acknowledge the financial support of Programme National de Physique Stellaire (PNPS) of CNRS/INSU, France. This research was partially supported by NSERC at the Université de Montréal. Finally, we thank the Réseau québécois de calcul de haute performance (RQCHP) for providing us with the computational resources required for this work.

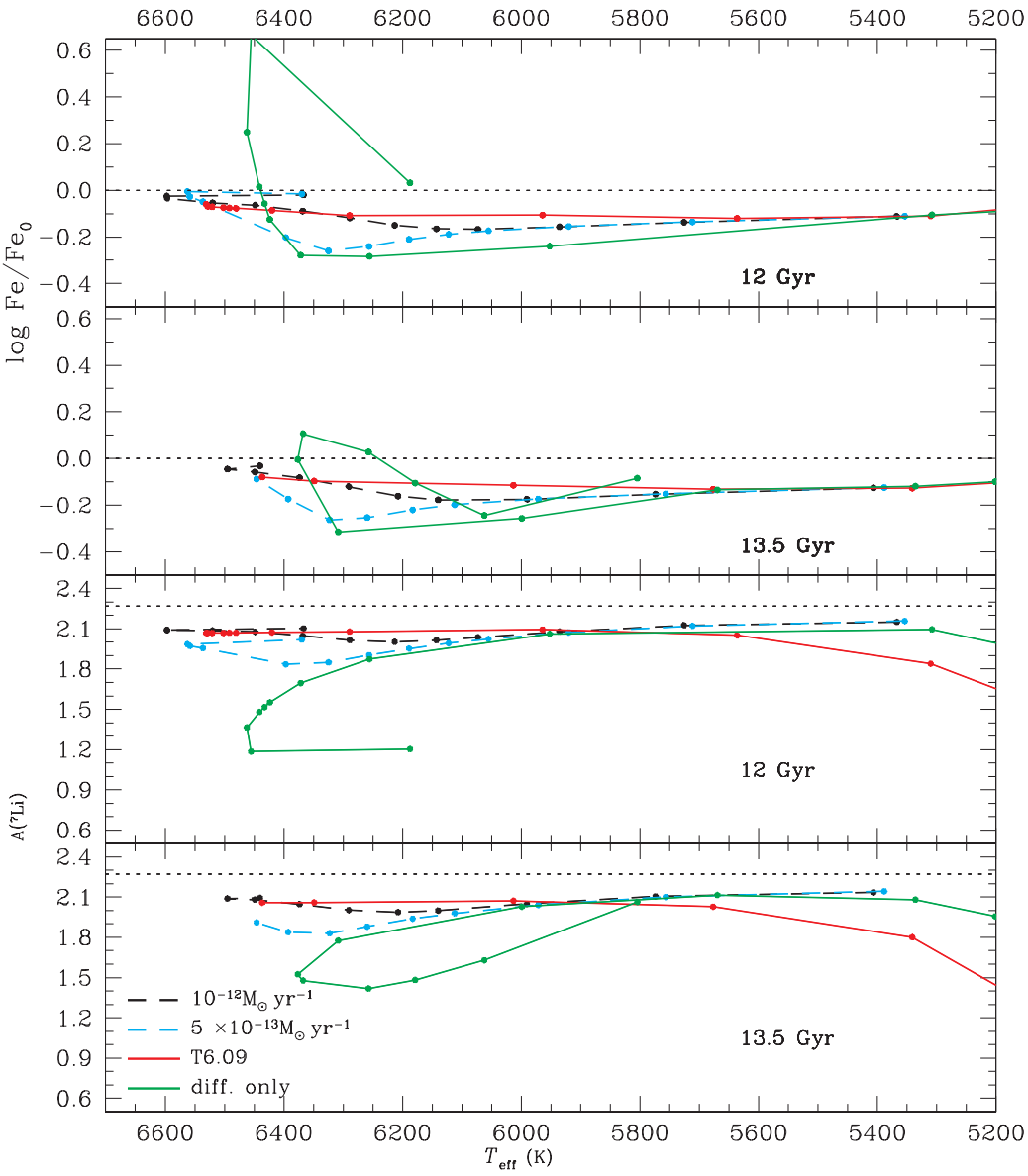

Figure 4.9: Lithium and iron surface abundance isochrones at 12 Gyr and 13.5 Gyr for models with and without mass loss as well as the T6.09 models from Richard et al. (2002b). The continuous lines link calculated models (dots). The horizontal dotted line at $A(^7\mathrm{Li}) = 2.27$ indicates the initial lithium abundance for all models. The model masses are not the same for every isochrone. For instance, most *diffusion only* models were converged along the subgiant branch, whereas the models with mass loss were not. The T6.09 isochrones are discussed in Sect. 4.5. The horizontal dashed line represents the initial ^{7}Li abundance.

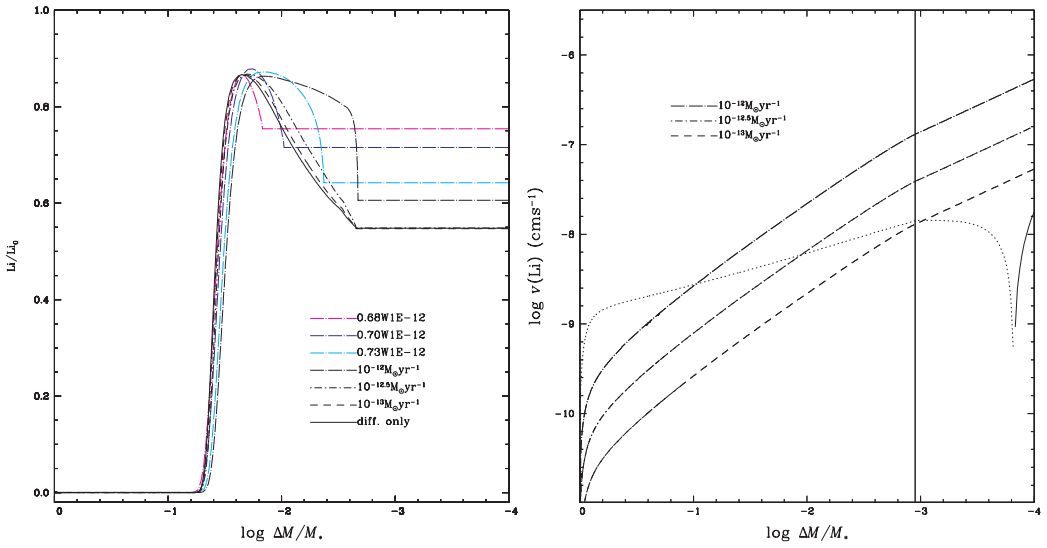

Figure 4.10: [Left panel] Internal lithium profiles for $0.75\,M_\odot$ models with and without mass loss. Three models of different mass were added (coloured curves) in order to verify the solution for the 0.80W1E-12 model. [Right panel] A comparison of diffusion and wind velocities for the $0.75\,M_\odot$ models. All models are shown at 10 Gyr. The left panel can be compared to Fig. 4 of Vauclair & Charbonnel (1995).

CHAPITRE 5

CONCLUSION

Des modèles évolutifs avec diffusion atomique et perte de masse permettent d'expliquer plusieurs anomalies d'abondances observées en surface des étoiles AmFm, HAeBe et de Population II. Dans ces modèles, le transport de 28 espèces chimiques est calculé de façon self-consistente en tenant compte de tous les effets de la diffusion atomique et des accélérations radiatives. La séparation chimique qui en résulte affecte jusqu'à 30% du rayon de l'étoile. À la surface, la perte de masse a pour effet de réduire les anomalies d'abondances causées par la diffusion atomique, alors qu'à l'intérieur de l'étoile, la perte de masse conduit à une stratification radiale des éléments qui diffère de la solution obtenue dans les modèles avec turbulence de Richer et al. (2000) et de Richard et al. (2002b). Des tests observationnels, reposant surtout sur l'astérosismologie, sont proposés afin de contraindre davantage l'importance relative de ces deux processus dans les étoiles CP et de Population II.

Pour les étoiles AmFm, des taux de perte de masse de $2.5-5$ fois le taux de perte de masse solaire mènent à des anomalies compatibles avec plusieurs observations d'étoiles d'amas et du champ, incluant des surabondances des éléments du pic du Fe de facteurs $2-3$, ainsi que des sousabondances de l'hélium et de CNO de facteurs $1.5-2.5$ (voir Sects. 2.7.1 et 2.7.2). Ces anomalies proviennent de la séparation chimique qui se manifeste profondément dans l'étoile (entre $\log \Delta M/M_* \sim -5$ et -6). D'ailleurs, nous avons montré que la séparation est déterminée par le rapport $g/g_{\rm rad}$ à la même profondeur que dans les modèles avec turbulence (Sect. 2.5), ce qui explique pourquoi nous obtenons des abondances en surface similaires. Ces mêmes taux de perte de masse ne permettent pas d'expliquer la brèche du lithium dans les Hyades, d'où la nécessité d'invoquer un autre processus qui explique la chute

abrupte de l'abondance en surface du Li dans les étoiles entre $6000 \leq T_{\rm eff} \leq 6400\,{\rm K}$ (Sect. 2.7.2.1). D'autres solutions possibles incluent une perte de masse séparée ou un taux de perte de masse qui varie d'un facteur ~ 5 dans ce même intervalle de $T_{\rm eff}$, bien que cette dernière solution soit plus difficile à justifier. Pour qu'il y ait suffisamment d'accumulation des éléments du pic du Fe pour générer de la convection à 200 000 K, le taux de perte de masse doit être $\lesssim 10^{-14}\,{\rm M_\odot yr^{-1}}$, mais ce taux de perte de masse génère des anomalies en surface nettement supérieures aux amplitudes observées (Sect. 2.7).

Les mêmes modèles évolutifs expliquent aussi les anomalies d'abondances observées en surface d'étoiles HAeBe de systèmes binaires (voir Sect 3.4). Contrairement au cas des étoiles AmFm, les anomalies en surface de ces étoiles de la PMS résultent de la séparation chimique qui se déroule plus près de la surface (vers $\log \Delta M/M_* \sim -7$, voir Sect. 3.3.1). Elles apparaissent vers $\sim$2 Myr pour les étoiles A chaudes et vers $\sim$20-25 Myr pour les étoiles F plus froides et s'élèvent à des facteurs de 1.5 à 10. Si ces anomalies, qui se développent avant la MS, sont dues à la diffusion atomique, cela limite le rôle que le mélange turbulent tel que présenté dans Richer et al. (2000) pourrait jouer dans ce type d'étoiles. Pour approfondir cette analyse, les effets du champ magnétique doivent être cernés davantage. Il est possible que la turbulence ne soit suffisamment réduite sur la PMS que si un champ magnétique impose la stabilité de l'enveloppe. Des observations précises de plus d'éléments individuels, notamment du Ca, pourraient aussi permettre d'approfondir l'analyse.

Dans les étoiles de Population II, la perte de masse mène à une stratification interne des éléments qui diffère de celle obtenue dans les modèles avec turbulence. Par contre, des taux de perte de masse jusqu'à 100 fois plus forts que le taux de perte de masse solaire sont requis pour que $A(^7{\rm Li})$ varie aussi peu en fonction de $T_{\rm eff}$ que le suggère le plateau de Spite observé pour les étoiles du halo galactique. Bien que la source de la perte de masse ne soit pas connue, nous pouvons difficile-

ment justifier un taux si élevé, ce qui présage la présence d'un autre processus qui limite les anomalies d'abondances en surface. Ces processus incluent la circulation méridienne et le transport turbulent causé par la rotation différentielle, la diffusion thermohaline et/ou les ondes de gravité.

Sur la MS, une perte de masse $\gtrsim 2\times10^{-14}\,\mathrm{M_\odot yr^{-1}}$ conduit à des profils d'abondances internes modulés par la conservation du flux. Dans ce régime, l'abondance locale d'un élément (Sect. 2.5.2, 3.3.1 et 4.3.1) s'ajuste afin d'assurer la conservation du flux partout où $v_{\rm wind} > v_{\rm sett}$. La stratification radiale des éléments correspondante pourrait s'apparenter à la solution obtenue pour des processus advectifs comme la circulation méridienne en 2 ou 3-D, alors qu'elle diffère de celle obtenue par des processus diffusifs tel le mélange rotationnel en 1-D (voir Sect. 2.8.1). L'astérosismologie pourrait permettre de distinguer ces deux solutions internes.

L'observation directe — ou l'amélioration des observations indirectes — de vents en surface d'étoiles A, F et de Population II permettrait de contraindre davantage les modèles, à la fois au niveau des taux utilisés et par rapport à l'inclusion éventuelle de la perte de masse à partir de principes premiers. Des modèles de vents plus complets pourraient aussi permettre de déterminer si les taux exigés pour expliquer les anomalies d'abondances peuvent nous en apprendre sur les processus d'accélération. Les observations et les modèles semblent suggérer que les $T_{\rm eff}$ les plus froides pour lesquelles la perte de masse serait accélérée par la radiation se retrouvent parmi les étoiles A, tout comme la limite supérieure des $T_{\rm eff}$ qui permettraient les vents coronaux. Il reste donc à déterminer où exactement se situent ces limites et si elles se recoupent. Pour le moment, relancer l'exploration de modèles avec vents séparés n'est pas à prévoir puisque le nombre de paramètres est trop élevé. En fait, tel que montré dans la Sect. 2.5.3.5, la perte de masse sélective peut être ajustée de sorte à reproduire — ou à peu près reproduire — un profil recherché quelconque. Par ailleurs, malgré certains efforts récents (voir entre autre Krtička et al. 2006), les incertitudes demeurent importantes au niveau des modèles de vent

séparé et ce, même pour le Soleil (voir Sect. 2.4.3).

Au niveau des abondances en surface, les observations ne permettent pas de suffisamment contraindre les modèles. D'une part, il faudrait augmenter le nombre d'éléments observés et de l'autre, il faudrait augmenter la précision des déterminations d'abondances. Tel que montré dans les Figs. 2.20–2.25, il y a des écarts significatifs entre observateurs pour un même élément et pareillement pour la détermination de la $T_{\rm eff}$. Du côté des modèles, l'insertion d'une ou de plusieurs terres rares dans le code évolutif permettrait de comparer à un plus grand nombre d'observations.

Dans le but de bien contraindre les effets de la perte de masse, les modèles présentés dans cette thèse dressent un portrait simple des étoiles CP : pas de rotation, pas de champ magnétique. Mais cela ne reflète certainement pas toute la réalité ; bien qu'elles tournent lentement, les étoiles AmFm tournent tout de même et les étoiles HAeBe ont, parfois, des champs magnétiques et, parfois, de l'accrétion. Néanmoins, à ce stade, incorporer ces processus dans les modèles évolutifs impliquerait des paramètres ajustables. Alors, y gagnerions-nous vraiment ? Une prochaine étape pourrait explorer l'inclusion additionnelle de la circulation méridienne.

La continuation naturelle de cette étude mènerait à la comparaison des modèles évolutifs avec perte de masse aux observations d'étoiles BHB et sdB. Pour ce faire, l'évolution sur la MS et la branche des géantes (GB) des étoiles de Population II servirait de condition initiale pour les modèles. Sur la GB, la perte de masse est bien contrainte puisqu'il existe plusieurs observations de perte de masse en surface de ces étoiles. D'ailleurs, plusieurs relations empiriques, telle celle de Reimers (1975, 1977), permettent de relier le taux de perte de masse à la luminosité de l'étoile et ce, pour un intervalle important de masses et de métallicités. Il serait donc intéressant de savoir en quoi la perte de masse affecterait, ou peut-être même éliminerait, les effets de la diffusion atomique (Michaud et al. 2010) et de la convection thermohaline (Charbonnel & Zahn 2007) dans le géantes de faible masse.

Et donc, pour conclure, la perte de masse ou la turbulence ? Nous prenons le point de vue que l'identification du principal processus en compétition avec la diffusion atomique est encore à déterminer puisque l'importance d'un processus physique dont la contribution dépend d'un paramètre ajustable est toujours incertaine.

BIBLIOGRAPHIE

Abbott, D. C. 1982, ApJ, 259, 282

Abt, H. A. 2000, ApJ, 544, 933

Abt, H. A. & Levy, S. G. 1985, ApJS, 59, 229

Abt, H. A. & Morrell, N. I. 1995, ApJS, 99, 135

Acke, B. & Waelkens, C. 2004, A&A, 427, 1009

Adelman, S. J. 1973, ApJ, 183, 95

Alecian, E., Catala, C., van't Veer-Menneret, C., Goupil, M., & Balona, L. 2005, A&A, 442, 993

Alecian, E., Catala, C., Wade, G. A., Donati, J.-F., Petit, P., Landstreet, J. D., Böhm, T., Bouret, J.-C., Bagnulo, S., Folsom, C., Grunhut, J., & Silvester, J. 2008a, MNRAS, 385, 391

Alecian, E., Goupil, M., Lebreton, Y., Dupret, M., & Catala, C. 2007, A&A, 465, 241

Alecian, E., Wade, G. A., Catala, C., Bagnulo, S., Boehm, T., Bohlender, D., Bouret, J.-C., Donati, J.-F., Folsom, C. P., Grunhut, J., & Landstreet, J. D. 2008b, A&A, 481, L99

Alecian, E., Wade, G. A., Catala, C., Bagnulo, S., Böhm, T., Bouret, J., Donati, J., Folsom, C. P., Grunhut, J., & Landstreet, J. D. 2009, MNRAS, 400, 354

Alecian, G. 1986, A&A, 168, 204

Alecian, G. 1996, A&A, 310, 872

Alecian, G. & Stift, M. J. 2006, A&A, 454, 571

Aller, L. H. & Chapman, S. 1960, ApJ, 132, 461

Anders, E. & Grevesse, N. 1989, Geochim. Cosmochim. Acta, 53, 197

Anthony-Twarog, B. J., Deliyannis, C. P., Twarog, B. A., Croxall, K. V., & Cummings, J. D. 2009, AJ, 138, 1171

Aoki, W., Barklem, P. S., Beers, T. C., Christlieb, N., Inoue, S., García Pérez, A. E., Norris, J. E., & Carollo, D. 2009, ApJ, 698, 1803

Asplund, M., Grevesse, N., & Sauval, A. J. 2005, in Astronomical Society of the Pacific Conference Series, Vol. 336, Cosmic Abundances as Records of Stellar Evolution and Nucleosynthesis, ed. T. G. Barnes, III & F. N. Bash, 25

Asplund, M., Grevesse, N., Sauval, A. J., & Scott, P. 2009, ARA&A, 47, 481

Asplund, M., Lambert, D. L., Nissen, P. E., Primas, F., & Smith, V. V. 2006, ApJ, 644, 229

Babcock, H. W. 1958, ApJS, 3, 141

Babel, J. 1994, A&A, 283, 189

—. 1995, A&A, 301, 823

—. 1996, A&A, 309, 867

Babel, J. & Michaud, G. 1991, ApJ, 366, 560

Babel, J. & Montmerle, T. 1997, A&A, 323, 121

Bagnulo, S., Hensberge, H., Landstreet, J. D., Szeifert, T., & Wade, G. A. 2004, A&A, 416, 1149

Balachandran, S. 1995, ApJ, 446, 203

Balmforth, N. J., Cunha, M. S., Dolez, N., Gough, D. O., & Vauclair, S. 2001, MNRAS, 323, 362

Basu, S., Chaplin, W. J., Elsworth, Y., New, R., Serenelli, A. M., & Verner, G. A. 2007, ApJ, 655, 660

Behr, B. B. 2003, ApJS, 149, 67

Bertin, P., Lamers, H. J. G. L. M., Vidal-Madjar, A., Ferlet, R., & Lallement, R. 1995, A&A, 302, 899

Boesgaard, A. M., Armengaud, E., King, J. R., Deliyannis, C. P., & Stephens, A. 2004, ApJ, 613, 1202

Boesgaard, A. M. & Budge, K. G. 1988, ApJ, 332, 410

Boesgaard, A. M. & Friel, E. D. 1990, ApJ, 351, 467

Boesgaard, A. M. & King, J. R. 2002, ApJ, 565, 587

Boesgaard, A. M., Stephens, A., & Deliyannis, C. P. 2005, ApJ, 633, 398

Boesgaard, A. M. & Tripicco, M. J. 1986, ApJ, 302, L49

Bonifacio, P. 2002, A&A, 395, 515

Bonifacio, P., Molaro, P., Sivarani, T., Cayrel, R., Spite, M., Spite, F., Plez, B., Andersen, J., Barbuy, B., Beers, T. C., Depagne, E., Hill, V., François, P., Nordström, B., & Primas, F. 2007, A&A, 462, 851

Borsenberger, J., Praderie, F., & Michaud, G. 1979, A&A, 76, 287

Boyer, M. L., Woodward, C. E., van Loon, J. T., Gordon, K. D., Evans, A., Gehrz, R. D., Helton, L. A., & Polomski, E. F. 2006, AJ, 132, 1415

Braithwaite, J., Akgün, T., Alecian, E., Kholtygin, A. F., Landstreet, J. D., Mathis, S., Michaud, G., Portnoy, J., Alecian, G., Bychkov, V. D., Bychkova, L. V., Drake, N., Fabrika, S. N., Reisenegger, A., Steinitz, R., & Vick, M. 2010, Highlights of Astronomy, 15, 161

Brancazio, P. J. & Cameron, A. G. W. 1967, Can. J. Phys., 45, 3297

Brown, A., Veale, A., Judge, P., Bookbinder, J. A., & Hubeny, I. 1990, ApJ, 361, 220

Burgers, J. S. 1969, in Flow Equations for Composite Gases (New York : Academic Press)

Burkhart, C. & Coupry, M. F. 1989, A&A, 220, 197

—. 1991, A&A, 249, 205

—. 2000, A&A, 354, 216

Caffau, E., Ludwig, H., Steffen, M., Ayres, T. R., Bonifacio, P., Cayrel, R., Freytag, B., & Plez, B. 2008, A&A, 488, 1031

Cannon, A. J. 1901, Harvard Ann., 28, 129

Carrier, F., Eggenberger, P., Leyder, J., Debernardi, Y., & Royer, F. 2007, A&A, 470, 1009

Carroll, B. W. & Ostlie, D. A. 1996, An Introduction to Modern Astrophysics (An Introduction to Modern Astrophysics, by B.W. Carroll and D.A. Ostlie. Benjamin Cummings, 1996. ISBN 0-201-54730-9.)

Castor, J. I., Abbott, D. C., & Klein, R. I. 1975, ApJ, 195, 157

Catala, C., Alecian, E., Donati, J., Wade, G. A., Landstreet, J. D., Böhm, T., Bouret, J., Bagnulo, S., Folsom, C., & Silvester, J. 2007, A&A, 462, 293

Cattaneo, F., Emonet, T., & Weiss, N. 2003, ApJ, 588, 1183

Cayrel, R., Burkhart, C., & C., V. 1991, in IAU Symposium 145, ed. G.Michaud & A.Tutukov, 99–105

Cayrel, R., Cayrel de Strobel, G., & Campbell, B. 1985, A&A, 146, 249

Cayrel, R., Spite, M., Spite, F., Vangioni-Flam, E., Cassé, M., & Audouze, J. 1999, A&A, 343, 923

Cayrel, R., Steffen, M., Chand, H., Bonifacio, P., Spite, M., Spite, F., Petitjean, P., Ludwig, H., & Caffau, E. 2007, A&A, 473, L37

Charbonneau, P. 1993, ApJ, 405, 720

Charbonneau, P. & Michaud, G. 1988, ApJ, 327, 809

—. 1991, ApJ, 370, 693

Charbonnel, C. & Primas, F. 2005, A&A, 442, 961

Charbonnel, C. & Talon, S. 2005, Sci, 309, 2189

Charbonnel, C., Vauclair, S., & Zahn, J. 1992, A&A, 255, 191

Charbonnel, C. & Zahn, J. 2007, A&A, 467, L15

Coc, A., Vangioni-Flam, E., Descouvemont, P., Adahchour, A., & Angulo, C. 2004, ApJ, 600, 544

Cowley, C. R. 1993, in Astronomical Society of the Pacific Conference Series, Vol. 44, IAU Colloq. 138 : Peculiar versus Normal Phenomena in A-type and Related Stars, ed. M. M. Dworetsky, F. Castelli, & R. Faraggiana, 18–+

Cox, J. P. 1968, Principles of stellar structure - Vol.1 : Physical principles ; Vol.2 : Applications to stars (New York : Gordon and Breach, 1968)

Cranmer, S. R. 2008, in Astronomical Society of the Pacific Conference Series, Vol. 384, 14th Cambridge Workshop on Cool Stars, Stellar Systems, and the Sun, ed. G. van Belle, 317–+

Cumberbatch, D., Ichikawa, K., Kawasaki, M., Kohri, K., Silk, J., & Starkman, G. D. 2007, Phys. Rev. D, 76, 123005

Cyburt, R. H., Fields, B. D., & Olive, K. A. 2003, Phys. Lett. B, 567, 227

—. 2008, Journal of Cosmology and Astro-Particle Physics, 11, 12

Delahaye, F. & Pinsonneault, M. H. 2006, ApJ, 649, 529

Delahaye, F., Pinsonneault, M. H., Pinsonneault, L., & Zeippen, C. J. 2010, ArXiv e-prints

Deliyannis, C. P., Demarque, P., & Kawaler, S. D. 1990, ApJS, 73, 21

Donati, J., Mengel, M., Carter, B. D., Marsden, S., Collier Cameron, A., & Wichmann, R. 2000, MNRAS, 316, 699

Donati, J., Semel, M., Carter, B. D., Rees, D. E., & Collier Cameron, A. 1997, MNRAS, 291, 658

Feldman, U. & Widing, K. G. 2003, Space Science Reviews, 107, 665

Feldman, W. C., Asbridge, J. R., Bame, S. J., & Gosling, J. T. 1977, in The Solar Output and its Variation, ed. O. R. White, 351

Folsom, C. P., Wade, G. A., Kochukhov, O., Alecian, E., Catala, C., Bagnulo, S., Böhm, T., Bouret, J.-C., Donati, J.-F., Grunhut, J., Hanes, D. A., & Landstreet, J. D. 2008, MNRAS, 391, 901

Fossati, L., Bagnulo, S., Monier, R., Khan, S. A., Kochukhov, O., Landstreet, J., Wade, G., & Weiss, W. 2007, A&A, 476, 911

Fowler, W. A., Burbidge, E. M., Burbidge, G., & Hoyle, F. 1965, ApJ, 142, 423

Gatewood, G. D. & Gatewood, C. V. 1978, ApJ, 225, 191

Gebran, M. & Monier, R. 2008, A&A, 483, 567

Gebran, M., Monier, R., & Richard, O. 2008, A&A, 479, 189

Geiss, J. & Buergi, A. 1986, A&A, 159, 1

Gonzalez, J.-F., LeBlanc, F., Artru, M.-C., & Michaud, G. 1995, ApJ, 297, 223

González Hernández, J. I., Bonifacio, P., Caffau, E., Steffen, M., Ludwig, H., Behara, N. T., Sbordone, L., Cayrel, R., & Zaggia, S. 2009, A&A, 505, L13

Gratton, R. 2000, in Astronomical Society of the Pacific Conference Series, Vol. 198, Stellar Clusters and Associations : Convection, Rotation, and Dynamos, ed. R. Pallavicini, G. Micela, & S. Sciortino, 225–+

Grevesse, N., Noels, A., & Sauval, A. J. 1996, in Astronomical Society of the Pacific Conference Series, Vol. 99, Cosmic Abundances, ed. S. S. Holt & G. Sonneborn, 117

Griffin, R. E. 2002, AJ, 123, 988

Grundahl, F., Catelan, M., Landsman, W. B., Stetson, P. B., & Andersen, M. I. 1999, ApJ, 524, 242

Heber, U. 2009, ARA&A, 47, 211

Herbig, G. H. 1960, ApJS, 4, 337

Hill, G. M. 1995, A&A, 294, 536

Hill, G. M. & Landstreet, J. D. 1993, A&A, 276, 142

Hui-Bon-Hoa, A. 1999, A&A, 343, 261

—. 2000, A&AS, 144, 203

Hui-Bon-Hoa, A. & Alecian, G. 1998, A&A, 332, 224

Hui-Bon-Hoa, A., Burkhart, C., & Alecian, G. 1997, A&A, 323, 901

Hui-Bon-Hoa, A., LeBlanc, F., & Hauschildt, P. H. 2000, ApJ, 535, L43

Iben, Jr., I. 1965, ApJ, 141, 993

Ichikawa, K., Kawasaki, M., & Takahashi, F. 2004, Physics Letters B, 597, 1

Iglesias, C. A. & Rogers, F. 1996, ApJ, 464, 943

Kato, S. 1966, PASJ, 18, 374

Khalack, V. R., Leblanc, F., Behr, B. B., Wade, G. A., & Bohlender, D. 2008, A&A, 477, 641

Khalack, V. R., Leblanc, F., Bohlender, D., Wade, G. A., & Behr, B. B. 2007, A&A, 466, 667

Kochukhov, O. & Wade, G. A. 2010, A&A, 513, A13+

Korn, A. J., Grundahl, F., Richard, O., Barklem, P. S., Mashonkina, L., Collet, R., Piskunov, N., & Gustafsson, B. 2006, Nat, 442, 657

Korn, A. J., Grundahl, F., Richard, O., Mashonkina, L., Barklem, P. S., Collet, R., Gustafsson, B., & Piskunov, N. 2007, ApJ, 671, 402

Krishna-Swamy, K. S. 1966, ApJ, 145, 176

Krtička, J., Kubát, J., & Groote, D. 2006, A&A, 460, 145

Krtička, J., Owocki, S. P., Kubát, J., Galloway, R. K., & Brown, J. C. 2003, A&A, 402, 713

Kudritzki, R. P., Pauldrach, A., Puls, J., & Abbott, D. C. 1989, A&A, 219, 205

Kurtz, D. W. 1978, Information Bulletin on Variable Stars, 1436, 1

—. 1982, MNRAS, 200, 807

Lambert, D. L., Roby, S. W., & Bell, R. A. 1982, ApJ, 254, 663

Lamers, H. J. G. L. M. & Cassinelli, J. P. 1999, Introduction to Stellar Winds (Introduction to Stellar Winds, by Henny J. G. L. M. Lamers and Joseph P. Cassinelli, pp. 452. ISBN 0521593980. Cambridge, UK : Cambridge University Press, June 1999.)

Landstreet, J. D. 1982, ApJ, 258, 639

Landstreet, J. D., Barker, P. K., Bohlender, D. A., & Jewison, M. S. 1989, ApJ, 344, 876

Landstreet, J. D., Dolez, N., & Vauclair, S. 1998, A&A, 333, 977

Langer, N., El Eid, M. F., & Fricke, K. J. 1985, A&A, 145, 179

Lanz, T. & Catala, C. 1992, A&A, 257, 663

LeBlanc, F. & Alecian, G. 2008, A&A, 477, 243

LeBlanc, F., Michaud, G., & Richer, J. 2000, ApJ, 538, 876

Lemke, M. 1989, A&A, 225, 125

—. 1990, A&A, 240, 331

Liebert, J., Young, P. A., Arnett, D., Holberg, J. B., & Williams, K. A. 2005, ApJ, 630, L69

Lind, K., Primas, F., Charbonnel, C., Grundahl, F., & Asplund, M. 2009, A&A, 503, 545

Lüftinger, T., Kochukhov, O., Ryabchikova, T., Piskunov, N., Weiss, W. W., & Ilyin, I. 2010, A&A, 509, A71+

Maeder, A. 1997, A&A, 321, 134

Mamajek, E. E., Lawson, W. A., & Feigelson, E. D. 1999, ApJ, 516, L77

Maury, A. C. 1897, Harvard Ann., 28, 1

Meléndez, J., Casagrande, L., Ramírez, I., Asplund, M., & Schuster, W. J. 2010, A&A, 515, L3+

Meléndez, J. & Ramírez, I. 2004, ApJ, 615, L33

Meyer, J.-P. 1985, ApJS, 57, 173

Meyer, J.-P. 1996, in Astronomical Society of the Pacific Conference Series, Vol. 99, Cosmic Abundances, ed. S. S. Holt & G. Sonneborn, 127

Michaud, G. 1970, ApJ, 160, 641

—. 1986, ApJ, 302, 650

Michaud, G. & Charbonneau, P. 1991, Space Science Reviews, 57, 1

Michaud, G. & Charland, Y. 1986, ApJ, 311, 326

Michaud, G., Fontaine, G., & Beaudet, G. 1984, ApJ, 282, 206

Michaud, G. & Proffitt, C. R. 1993, in Astronomical Society of the Pacific Conference Series, Vol. 40, IAU Colloq. 137 : Inside the Stars, ed. W. W. Weiss & A. Baglin, 246–259

Michaud, G., Richard, O., Richer, J., & VandenBerg, D. A. 2004, ApJ, 606, 452

Michaud, G., Richer, J., & Richard, O. 2005, ApJ, 623, 442

—. 2007, ApJ, 670, 1178

—. 2008, ApJ, 675, 1223

—. 2010, A&A, 510, A104+

Michaud, G., Tarasick, D., Charland, Y., & Pelletier, C. 1983, ApJ, 269, 239

Mkrtichian, D. E., Hatzes, A. P., Saio, H., & Shobbrook, R. R. 2008, A&A, 490, 1109

Monier, R. 2005, A&A, 442, 563

Neff, J. E. & Simon, T. 2008, ApJ, 685, 478

Netopil, M., Paunzen, E., Maitzen, H. M., North, P., & Hubrig, S. 2008, A&A, 491, 545

Nissen, P. E., Asplund, M., Hill, V., & D'Odorico, S. 2000, A&A, 357, L49

Norris, J. 1971, ApJS, 23, 213

Origlia, L., Rood, R. T., Fabbri, S., Ferraro, F. R., Fusi Pecci, F., & Rich, R. M. 2007, ApJ, 667, L85

Owocki, S. & Murdin, P. 2000, Encyclopedia of Astronomy and Astrophysics

Owocki, S. P. & Puls, J. 2002, ApJ, 568, 965

Palacios, A., Talon, S., Charbonnel, C., & Forestini, M. 2003, A&A, 399, 603

Paquette, C., Pelletier, C., Fontaine, G., & Michaud, G. 1986, ApJS, 61, 177

Parker, E. N. 1958, ApJ, 128, 664

—. 1960, ApJ, 132, 821

Perryman, M. A. C., Brown, A. G. A., Lebreton, Y., Gomez, A., Turon, C., de Strobel, G. C., Mermilliod, J. C., Robichon, N., Kovalevsky, J., & Crifo, F. 1998, A&A, 331, 81

Piau, L., Beers, T. C., Balsara, D. S., Sivarani, T., Truran, J. W., & Ferguson, J. W. 2006, ApJ, 653, 300

Pinsonneault, M. H., Kawaler, S. D., Sofia, S., & Demarque, P. 1989, ApJ, 338, 424

Pinsonneault, M. H., Walker, T. P., Steigman, G., & Narayanan, V. K. 1999, ApJ, 527, 180

Preston, G. W. 1974, ARA&A, 12, 257

Profitt, C. R. & Michaud, G. 1991, ApJ, 371, 584

Quievy, D., Charbonneau, P., Michaud, G., & Richer, J. 2009, A&A, 500, 1163

Randich, S., Primas, F., Pasquini, L., Sestito, P., & Pallavicini, R. 2007, A&A, 469, 163

Reimers, D. 1975, Memoires of the Societe Royale des Sciences de Liege, 8, 369

—. 1977, A&A, 61, 217

Richard, O., Michaud, G., & Richer, J. 2001, ApJ, 558, 377

—. 2002a, ApJ, 580, 1100

—. 2005, ApJ, 619, 538

Richard, O., Michaud, G., Richer, J., Turcotte, S., Turck-Chièze, S., & VandenBerg, D. A. 2002b, ApJ, 568, 979

Richer, J. & Michaud, G. 1993, ApJ, 416, 312

Richer, J. & Michaud, G. 2005, in EAS Publications Series, Vol. 17, EAS Publications Series, ed. G. Alecian, O. Richard, & S. Vauclair, 53–59

Richer, J., Michaud, G., & Massacrier, G. 1997, A&A, 317, 968

Richer, J., Michaud, G., Rogers, F., Turcotte, S., & Iglesias, C. A. 1998, ApJ, 492, 833

Richer, J., Michaud, G., & Turcotte, S. 2000, ApJ, 529, 338

Roby, S. W. & Lambert, D. L. 1990, ApJS, 73, 67

Ryabchikova, T. A. 1991, in IAU Symposium, Vol. 145, Evolution of Stars : the Photospheric Abundance Connection, ed. G. Michaud & A. V. Tutukov, 149–+

Ryan, S. G., Norris, J. E., & Beers, T. C. 1999, ApJ, 523, 654

Salaris, M., Groenewegen, M. A. T., & Weiss, A. 2000, A&A, 355, 299

Sbordone, L., Bonifacio, P., Caffau, E., Ludwig, H., Behara, N. T., Gonzalez Hernandez, J. I., Steffen, M., Cayrel, R., Freytag, B., Van't Veer, C., Molaro, P., Plez, B., Sivarani, T., Spite, M., Spite, F., Beers, T. C., Christlieb, N., Francois, P., & Hill, V. 2010, ArXiv e-prints

Schramm, D. N., Steigman, G., & Dearborn, D. S. P. 1990, ApJ, 359, L55

Seaton, M. J., Yan, Y., Mihalas, D., & Pradhan, A. K. 1994, MNRAS, 266, 805

Sigut, T. A. A., Landstreet, J. D., & Shorlin, S. L. S. 2000, ApJ, 530, L89

Simon, T. & Landsman, W. B. 1997, ApJ, 483, 435

Smith, V. V., Lambert, D. L., & Nissen, P. E. 1998, ApJ, 506, 405

Spergel, D. N., Bean, R., Doré, O., Nolta, M. R., Bennett, C. L., Dunkley, J., Hinshaw, G., Jarosik, N., Komatsu, E., Page, L., Peiris, H. V., Verde, L., Halpern, M., Hill, R. S., Kogut, A., Limon, M., Meyer, S. S., Odegard, N., Tucker, G. S., Weiland, J. L., Wollack, E., & Wright, E. L. 2007, ApJS, 170, 377

Spite, F. & Spite, M. 1982, A&A, 115, 357

Spite, M., Spite, F., & Maillard, J. P. 1984, A&A, 141, 56

Springmann, U. W. E. & Pauldrach, A. W. A. 1992, A&A, 262, 515

Steigman, G. 2007, Annual Review of Nuclear and Particle Science, 57, 463

Swenson, F. J. & Faulkner, J. 1992, ApJ, 395, 654

Takada-Hidai, M. 1991, in IAU Symposium, Vol. 145, Evolution of Stars : the Photospheric Abundance Connection, ed. G. Michaud & A. V. Tutukov, 137–+

Takeda, Y. & Sadakane, K. 1997, PASJ, 49, 367

Talon, S. & Charbonnel, C. 1998, A&A, 335, 959

—. 2003, A&A, 405, 1025

—. 2004, A&A, 418, 1051

—. 2005, A&A, 440, 981

Talon, S., Richard, O., & Michaud, G. 2006, ApJ, 645, 634

Tassoul, J. & Tassoul, M. 1982, ApJS, 49, 317

Théado, S. & Vauclair, S. 2003, ApJ, 587, 784

Théado, S., Vauclair, S., Alecian, G., & Le Blanc, F. 2009, ApJ, 704, 1262

Théado, S., Vauclair, S., & Cunha, M. S. 2005, A&A, 443, 627

Thiam, M., Leblanc, F., Khalack, V., & Wade, G. A. 2010, MNRAS, 405, 1384

Townsend, R. H. D. & Owocki, S. P. 2005, MNRAS, 357, 251

Turcotte, S. & Charbonneau, P. 1993, ApJ, 413, 376

Turcotte, S., Michaud, G., & Richer, J. 1998a, ApJ, 504, 559

Turcotte, S., Richer, J., Michaud, G., & Christensen-Dalsgaard, J. 2000, A&A, 360, 603

Turcotte, S., Richer, J., Michaud, G., Iglesias, C. A., & Rogers, F. 1998b, ApJ, 504, 539

Unglaub, K. 2008, A&A, 486, 923

van den Ancker, M. E., de Winter, D., & Tjin A Djie, H. R. E. 1998, A&A, 330, 145

VandenBerg, D. A., Edvardsson, B., Eriksson, K., & Gustafsson, B. 2008, ApJ, 675, 746

VandenBerg, D. A., Richard, O., Michaud, G., & Richer, J. 2002, ApJ, 571, 487

VandenBerg, D. A., Swenson, F. J., Rogers, F. J., Iglesias, C. A., & Alexander, D. R. 2000, ApJ, 532, 430

Varenne, O. & Monier, R. 1999, A&A, 351, 247

Vauclair, S. 1975, A&A, 45, 233

—. 1988, ApJ, 335, 971

Vauclair, S. & Charbonnel, C. 1995, A&A, 295, 715

Vauclair, S., Dolez, N., & Gough, D. O. 1991, A&A, 252, 618

Vauclair, S. & Vauclair, G. 1982, ARA&A, 20, 37

Vick, M., Michaud, G., Richer, J., & Richard, O. 2010, A&A, 521, A62+

Wade, G. A., Drouin, D., Bagnulo, S., Landstreet, J. D., Mason, E., Silvester, J., Alecian, E., Böhm, T., Bouret, J.-C., Catala, C., & Donati, J.-F. 2005, A&A, 442, L31

Wade, G. A., Ryabchikova, T. A., Bagnulo, S., & Piskunov, N. 2001, in Astronomical Society of the Pacific Conference Series, Vol. 248, Magnetic Fields Across the Hertzsprung-Russell Diagram, ed. G. Mathys, S. K. Solanki, & D. T. Wickramasinghe, 373–+

Watson, W. D. 1971, A&A, 13, 263

White, R. E., Vaughan, Jr., A. H., Preston, G. W., & Swings, J. P. 1976, ApJ, 204, 131

Wiese, W. L., Smith, M. W., & Glennon, B. M. 1966, Atomic transition probabilities. Vol. : Hydrogen through Neon. A critical data compilation (NSRDS-NBS 4, Washington, D.C. : US Department of Commerce, National Buereau of Standards, 1966)

Wood, B. E., Müller, H., Zank, G. P., & Linsky, J. L. 2002, ApJ, 574, 412

Wood, B. E., Müller, H., Zank, G. P., Linsky, J. L., & Redfield, S. 2005, ApJ, 628, L143

Zahn, J. 1992, A&A, 265, 115

Annexe A

Composition chimique des étoiles A et F des Hyades

Astronomy & Astrophysics manuscript no. gebran˙13273
June 29, 2010

Chemical composition of A and F dwarfs members of the Hyades open cluster⋆,⋆⋆

M. Gebran[1⋆⋆⋆], M. Vick[1,2], R. Monier[3] and L. Fossati[4,5]

[1] Groupe de Recherche en Astronomie et Astrophysique du Languedoc,UMR 5024, Université Montpellier II, Place Eugène Bataillon, 34095 Montpellier, France.
[redacted]
[2] Département de Physique, Université de Montréal, Montréal, PQ, H3C 3J7
[redacted]
[3]Laboratoire Universitaire d'Astrophysique de Nice, UMR 6525, Université de Nice - Sophia Antipolis, Parc Valrose, 06108 Nice Cedex 2, France.
[redacted]
[4]Institut für Astronomie, Universität Wien, Türkenschanzstrasse 17, 1180 Wien, Austria.
[redacted]
[5]Department of Physics and Astronomy, Open University, Walton Hall, Milton Keynes MK7 6AA, UK.
[redacted]

Received ; accepted

ABSTRACT

Aims. Abundances of **15** chemical elements have been derived for 28 F and 16 A stars members of the Hyades open cluster in order to set constraints on self-consistent evolutionary models including radiative and turbulent diffusion.
Methods. A spectral synthesis iterative procedure was applied to derive the abundances from selected high quality lines in high resolution high signal-to-noise spectra obtained with SOPHIE and AURELIE at the Observatoire de Haute Provence.
Results. The abundance patterns found for A and F stars in the Hyades resemble those observed in Coma Berenices and Pleiades clusters. In graphs representing the abundances versus the effective temperature, A stars often display abundances much more scattered around their mean values than the coolest F stars do. Large star-to-star variations are detected in the Hyades A dwarfs in their abundances of C, Na, Sc, Fe, Ni, Sr, Y and Zr, which we interpret as evidence of transport processes competing with radiative diffusion.
In A and Am stars, the abundances of Cr, Ni, Sr, Y and Zr are found to be correlated with that of iron as in the Pleiades and in Coma Berenices. The ratios [C/Fe] and [O/Fe] are found to be anticorrelated with [Fe/H] as in Coma Berenices. All Am stars in the Hyades are deficient in C and O and overabundant in elements heavier than Fe but not all are deficient in calcium and/or scandium. The F stars have solar abundances for almost all elements except for Si.
The overall shape of the abundance pattern of the slow rotator HD30210 cannot be entirely reproduced by models including radiative diffusion and different amounts of turbulent diffusion.
Conclusions. While part of the discrepancies between derived and predicted abundances could be due to non-LTE effects, the inclusion of competing processes such as rotational mixing and/or mass loss seems necessary in order to improve the agreement between the observed and predicted abundance patterns.

Key words. stars: abundances - stars: main sequence - stars: rotation - diffusion - Galaxy: open clusters and associations: individual: Hyades

1. Introduction

Abundance determinations for A and F dwarfs in open clusters and moving groups aim at elucidating the mechanisms of mixing at play in the interiors of these main-sequence stars. This paper is the third in a series addressing the chemical composition of A and F dwarfs in open clusters of different ages. The objectives of this long-term project are twofold: first, we wish to improve our knowledge of the chemical composition of A and F dwarfs, and secondly we aim to use these determinations to set constraints on particle transport processes in self consistent evolutionary models. The first paper (Gebran et al. 2008, hereafter Paper I) addressed the abundances of several chemical elements for 11 A and 11 F dwarf members of the Coma Berenices open cluster. In the second paper (Gebran & Monier 2008, Paper II), abundances were derived for the same chemical elements for 16 A and 5 F dwarf members of the Pleiades open cluster. In this study, we present a re-analysis of the A and F dwarf abundances in the Hyades open cluster, already addressed by Varenne & Monier (1999) using mono-order spectra on much more limited spectral ranges (three 70 Å wide spectral intervals). The new data we collected are high signal to noise and high resolution échelle spectra stretching over more than 3000 Å which enabled us to synthesize more lines with high quality atomic data (and

Send offprint requests to: M. Gebran
⋆ Tables 5 to 8 are only available in electronic format at the CDS.
⋆⋆ Based on observations at the Observatoire de Haute-Provence (France).
⋆⋆⋆ Present affiliation: Departament d'Astronomia i Meteorologia, Universitat de Barcelona, c/ Martì i Franquès, 1, 08028 Barcelona, Spain.

more elements) than in Varenne & Monier (1999). In this paper, abundances have been derived for **15 chemical elements (C, O, Na, Mg, Si, Ca, Sc, Ti, Cr, Mn, Fe, Ni, Sr, Y and Zr)** for 28 F and 16 A members of the Hyades cluster.

Open clusters are excellent laboratories to test stellar evolution theory. Indeed stars in open clusters originate from the same interstellar material, and thus have the same initial chemical composition and age. At a distance of ~46 pc (van Leeuwen 2007), the Hyades open cluster is the nearest star cluster and also the most analyzed of all clusters. Perryman et al. (1998) compared the observational HR diagram of the Hyades with stellar evolution models and obtained an estimation of the age of this cluster (~625 Myr) using a combination of Hipparcos data with ground-based photometric indexes. Boesgaard & Friel (1990) derived a metallicity for the Hyades slightly above solar (<[Fe/H]>=0.127±0.022 dex) from their analysis of Fe I lines in 14 F dwarfs. In a study of 40 Hyades G dwarfs, Cayrel de Strobel et al. (1997) also derived a mean metallicity of <[Fe/H]>=+0.14±0.05 dex. Abundances derived from calibration of Geneva photometry by Grenon (2000) (<[Fe/H]>=+0.14±0.01) also yield a slightly enhanced metallicity.

Several papers have addressed the chemical composition of A and F dwarfs in the Hyades open cluster. Carbon and iron abundances have been derived for 14 F stars by Friel & Boesgaard (1990) and Boesgaard & Friel (1990). Lithium abundances have been determined for several F, G and K dwarfs by Cayrel et al. (1984), Boesgaard & Tripicco (1986), Boesgaard & Budge (1988) and Thorburn et al. (1993). Garcia Lopez et al. (1993) have derived the oxygen abundances for 26 F dwarfs members of the Hyades cluster. Carbon, oxygen, sodium, magnesium, silicon, calcium, scandium, chromium, iron, nickel, yttrium and barium abundances have been derived for A stars by Takeda & Sadakane (1997), Hui-Bon-Hoa & Alecian (1998), Burkhart & Coupry (2000) and Varenne & Monier (1999). Most of these studies, at the exception of Varenne & Monier (1999), have focused mainly on the peculiar Am stars, leaving aside the normal A stars. For a given chemical element, large star-to-star variations were found among A stars in several open clusters like the Pleiades (Paper II) and Coma Berenices (Paper I) . Varenne & Monier (1999) found significant star-to-star variations in the abundances of O, Na, Ni, Y and Ba for A stars in the Hyades whereas the F dwarfs display much less dispersion. Similarly, star-to-star variations of [Fe/H], [Ni/H] and [Si/H] are larger for the A dwarfs than for the F dwarfs in the Ursa Major group (Monier 2005). This behavior was also observed in earlier works on field A stars (Holweger et al. 1986, Lambert et al. 1986, Lemke 1998, 1990, Hill & Landstreet 1993, Hill 1995, Rentzsch-Holm 1997 and Varenne 1999).

The incentive to reanalyze the chemical composition of A and F dwarfs of the Hyades is justified by the acquisition of higher quality spectra encompassing a much wider spectral range than used in Varenne & Monier (1999). This allowed us to model more lines of higher quality (ie. with more accurate atomic data) for most investigated chemical elements yielding more accurate abundances for several species.

We have also searched for correlations of the abundances of individual elements with that of iron, an issue not addressed in Varenne & Monier (1999). Furthermore, the state of the art of modelling the internal structure and evolution of A dwarfs has improved over the last ten years and we present here comparisons of new models to the observed pattern of abundances.

The selection of the stars and the data reduction are described in §2. The determination of the fundamental parameters ($T_{\rm eff}$ and $\log g$) and the spectrum synthesis computations are discussed in (§3). As in Papers I and II, the behavior of the abundances of the analysed chemical elements in A and F dwarfs have been investigated in §4 with respect to effective temperature ($T_{\rm eff}$), projected rotational velocity ($v_{\rm e} \sin i$) and the iron abundance ([Fe/H]). In §5, the found abundance patterns are compared to recent evolutionary models including self consistent treatment of particle transport (Turcotte et al. 1998b; Richer et al. 2000 and Richard et al. 2001). The abundance pattern of the Am star, HD 30210, is modelled in detail using the latest prescriptions in the Montreal code (Richer et al., 2000). Conclusions are gathered in §6.

2. Program stars, observations and data reduction

Our observing sample consists of 28 F and 16 A members of the Hyades cluster brighter than V=7 (the same sample selected by Varenne & Monier 1999). At the distance of the Hyades, V=7 mag corresponds to the latest F dwarfs (F8-F9). A Hertzsprung–Russell (HR) diagram of the Hyades, shown in Fig.1, was constructed using the effective temperatures we derived in section 3 , the V magnitudes retrieved from SIMBAD and appropriate bolometric corrections. We adopted a cluster distance of 46.5±0.3 pc (van Leeuwen 2007), a reddening of 0.010±0.010 mag (WEBDA[1]) and the bolometric corrections given by Balona (1994). The uncertainty on the bolometric correction is of the order of 0.07 mag, leading to a typical uncertainty in $M_{\rm bol}$ of about 0.15 mag, corresponding to an uncertainty of about 0.05 dex in $\log L/L_{\odot}$. In the HR diagram of Fig. 1 the Am stars are depicted as filled squares, the normal A stars as filled circles and the F stars as filled triangles, the spectroscopic binaries as open squares. We did not correct the luminosities of the binaries since the contribution to the total flux due to the secondary is not known.

The age of the cluster can be estimated by adjusting isochrones by Marigo et al. (2008), including overshooting and calculated for a metallicity of Z = 0.025 dex, which corresponds roughly to the mean of the recent determinations by Perryman et al. (1998), Castellani et al. (2002), Percival et al. (2003), Salaris et al. (2004), Taylor (2006), Holmberg et al. (2007) plus the value given in WEBDA. Fig.1 displays two isochrones: one corresponding to the age given in WEBDA ($\log t$ = 8.9 - full line) and our best fit corresponding to a slightly lower age ($\log t$ = 8.8 - dashed line), which agrees quite nicely with the determination by Perryman et al. (1998): t=625±50 Myr. We are inclined to rule out a lower metallicity which would lead to a much lower value of the age (models without overshooting would lead to a much lower age). Following Landstreet et al.(2007), we have also derived $M/M_{\odot}$, fractional age (fraction of time spent on the Main Sequence noted as τ) and their uncertainties for each star and collected them in online Table 7. In Fig. 1, the star HD 27962 (= 68 Tau) is located at a much higher effective temperature than the other A dwarfs of similar luminosities. Mermilliod (1982) confirmed its membership to the Hyades and proposed that HD 27962 is a blue straggler with the spectral characteristics of an Am star. Abt (1985) assigned a spectral type Am (A2KA3HA5M) to HD 27962.

[1] www.univie.ac.at/webda/

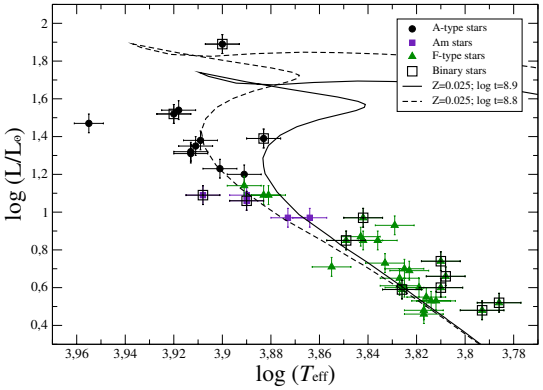

Fig. 1. HR diagram of the Hyades cluster. The two isochrones are calculated with the age given in WEBDA (log t=8.9 - full line) and our best fit (log t=8.8 - dashed line.)

The A stars were observed using SOPHIE, the échelle spectrograph at the Observatoire de Haute-provence (OHP). SOPHIE spectra stretch from 3820 to 6930 Å in 39 orders with two different spectral resolutions: the high resolution mode HR (R=75000) and the high efficiency mode HE (R=39000). All A stars were observed in the HR mode. The observing dates, exposure times and Signal to Noise ratios achieved for each A star are collected in Table 2. On good nights, an exposure time of 25 minutes typically yielded well exposed spectra with signal-to-noise ratios ranging from 300 to 600, depending on the V magnitude. As we did not get enough observing time to observe the F stars with SOPHIE as well, we have used the mono-order AURELIE spectra obtained by Varenne & Monier (1999). For each F star, three spectral regions centred on λ6160 Å, λ5080 Å and λ5530 Å had been observed at resolutions 30000 (V $\geq$ 6) or 60000 (V $\leq$ 6) and signal to noise ratios close to 200.
The fundamental data for the selected stars are collected in Table 1. The van Bueren and Henry Draper identifications appear in columns 1 and 2, the spectral type retrieved from SIMBAD or from Abt & Morell (1995) in column 3 and the apparent magnitudes in column 4. Effective temperatures ($T_{\rm eff}$) and surface gravities (log g), derived from *uvbyβ* photometry (see section 3), appear in columns 5 and 6. The derived projected rotational velocities and the microturbulent velocities are in columns 7 and 8. Comments about binarity and pulsation appear in the last column. The apparent rotational velocities range from 11 km.s^{-1} to 165 km.s^{-1}, only 7 stars rotate faster than 100 km.s^{-1}.
Inspection of the CCDM catalogue (Dommanget & Nys 1995) reveals that 13 among the 16 A stars are in binary or multiple systems. All of these stars are primaries and the components are much fainter (1 mag< Δm <9.5 mag). Only the case of **HD27962** (CCDM J04255+1755 AB) has to be accounted for because its companion (component B) is three magnitudes fainter than A and at only 1.4" from A. In case of F stars, 13 among the 28 stars belong to multiple systems. Six of them have nearby companions whose angular distance was probably less than the fiber angular size on the sky (3 arcsec) and who are only three magnitudes fainter than the brightest star we analysed. The spectral types of these companions is unknown. For the F stars, these are:
- **HD26015** = CCDM J04077+1510A has a companion at about 4" with Δm = 2.8 mag
- **HD27383** = CCDM J04199+1631AB: components A and B are very close with Δm = 2.0 mag
- **HD27991** = CCDM J04257+1557AP: companion P is quoted to be at 0.1" with Δm = 0.7 mag
- **HD28363** = CCDM J04290+1610AB is a spectroscopic binary whose angular separation is not specified with a Δm = 1.0 mag
- **HD30810** = CCDM J04512+1104AB is a triple star whose component B has same magnitude as A, no angular separation is provided.
For these six stars, we believe that the light of the companions might have contaminated the spectra of the brightest components we analysed. The effects are probably most pronounced for the F stars HD26015, HD27383, HD27991, HD28363 and HD30810.
The SOPHIE spectra were reduced using IRAF (Image Reduction and Analysis Facility, Tody 1993) in order to properly correct for scattered light. The sequence of IRAF procedures, which follows the method devised by Erspamer & North (2002), is fully described in Paper I.

Table 2. Observing log for the A stars of the Hyades open cluster.

HD	spectral type	exposure time (s)	S/N	Date
27628	A3m	1500	350	10/04/06
27819	A7V	1200	498	10/04/06
27934	A7V	900	591	10/04/06
27962	A2IV	600	429	10/04/06
28226	A3m	1500	380	10/04/06
28319	A7III	300	429	10/04/06
28355	A7V	1500	427	10/04/06
28527	A6IV	1200	354	10/04/06
28546	A5m	1500	292	10/04/06
28910	A8V	1200	434	10/04/06
29388	A6V	600	561	10/05/06
29499	A5m	1320	476	10/05/06
29488	A5V	900	601	10/05/06
30210	Am	1320	474	10/05/06
30780	A7V	1200	549	10/05/06
32301	A7V	720	526	10/05/06

3. Abundance analysis: method and input data

The abundances of **15** chemical elements have been derived by iteratively adjusting synthetic spectra to the normalized spectra and minimizing the chi-square of the models to the observations. Spectrum synthesis is mandatory as the apparent rotational velocities range from 11 to 165 km.s^{-1}. Specifically, synthetic spectra were computed assuming LTE using Takeda's (1995) iterative procedure and double-checked using Hubeny & Lanz (1992) SYNSPEC48 code. This version of SYNSPEC calculates lines for elements up to Z=99.

3.1. Atmospheric parameters and model atmospheres

The effective temperatures and surface gravities were determined using the UVBYBETA code developed by Napiwotzki et al. (1993). This code is based on the Moon & Dworetsky (1985)'s grid, which calibrates the *uvbyβ* photometry in terms of $T_{\rm eff}$ and log g. The photometric data were taken from Hauck & Mermilliod (1998). The estimated errors on $T_{\rm eff}$ and log g, are ±125 K and ±0.20 dex, respectively (see Sec. 4.2 in Napiwotzki et al. 1993). The found effective temperatures and surface gravities are collected in table 1.

Table 1. Basic physical quantities for the programme stars.

vB	HD	Type	m_v	$T_{\rm eff}$ (K)	log g (cm.s^{-2})	$v_{\rm e} \sin i$ (km.s^{-1})	ξ_t (km.s^{-1})	Remarks
				A stars				
38	27628	A3m	5.72	7310	4.12	31.2	3.70	δ Scuti (d)
47	27819	A7V/A8V	4.80	8190	3.94	47.0	3.00	
54	27934	A7IV/A6V	4.22	8290	3.83	80.0	3.00	
56	27962	A2IV/Am	4.29	9025	3.95	11.3	2.80	Blue Straggler
67	28226	A3m	5.72	7465	4.09	83.0	3.30	
72	28319	A7III/A7IV	3.39	7950	3.70	65.0	2.70	SB (b), δScuti (d)
74	28355	A7V/A5m	5.03	7965	3.97	90.0	3.00	
82	28527	A6IV/A7V	4.78	8180	3.98	67.8	3.70	
83	28546	A5m	5.48	7765	4.20	27.5	3.80	SB (b)
95	28910	A8V/A7V	4.65	7640	4.02	110.0	2.60	SB (b), δScuti (d)
104	29388	A6V	4.27	8310	3.87	81.0	3.30	SB (b)
107	29499	A5m/A9III	5.39	7770	4.11	60.0	3.00	
108	29488	A5V/A6V	4.70	8150	3.80	118.0	2.60	
112	30210	A2m	5.37	8080	3.92	57.0	4.00	SB (b)
123	30780	A7V/A9V	5.11	7790	3.90	165.0	2.80	δ Scuti (d)
129	32301	A7V	4.64	8110	3.73	117.0	2.70	
				F stars				
6	24357	F4V	5.97	6975	4.13	65.5	2.10	
8	25102	F5V	6.37	6685	4.32	64.0	2.20	
11	26015	F3V	6.01	6860	4.46	29.7	1.80	
13	26345	F6V	6.62	6685	4.36	27.2	1.60	
14	26462	F4V	5.73	6945	4.14	18.6	1.50	SB (b)
20	26911	F5V	6.32	6810	4.26	62.1	2.20	
29	27383	F9V	6.88	6215	4.39	16.8	1.40	SB (b)
33	27459	F0V/F0IV	5.26	7785	3.98	73.0	3.10	δ Scuti (d)
35	27524	F5V	6.80	6515	4.24	72.5	2.10	
36	27534	F5V	6.80	6485	4.26	48.0	1.50	
37	27561	F5V	6.61	6710	4.35	22.2	1.60	
51	27848	F8	6.97	6565	4.33	37.7	1.50	
57	27991	F7V	6.46	6430	4.48	17.6	1.10	SB2 (c), SB(b)
75	28363	F8V	6.59	6325	4.43	16.0	1.00	SB3 (c), SB (b)
78	28406	F6V	6.92	6560	4.40	33.0	1.60	
84	28556	F0V	5.41	7635	4.07	83.5	3.30	
85	28568	F2	6.51	6710	4.40	64.0	1.90	
89	28677	F4V/F2V	6.02	7060	4.07	129.0	1.90	SB (b)
90	28736	F5V	6.40	6655	4.30	48.0	1.70	
94	28911	F2	6.62	6590	4.32	50.0	1.60	
100	29169	F5IV	6.02	6950	4.25	75.0	2.20	
101	29225	F8	6.65	6700	4.41	50.8	1.70	SB (b)
111	30034	F0V/A9IV	5.40	7600	4.05	100.0	2.60	
122	30810	F6V	6.76	6110	4.36	12.0	1.10	SB2 (c), SB (b)
124	30869	F5	6.25	6460	4.28	23.5	1.80	SB2 (a,c), SB (b)
126	31236	F3IV/F1V	6.37	7165	3.89	120.0	3.00	
128	31845	F5V	6.75	6550	4.37	33.7	1.90	
154	18404	F5IV	5.80	6740	4.37	26.5	1.70	
	Procyon	F5IV-V	0.34	6650	4.05	6.0	2.2	

References (a) (b) (c) and (d) are for Griffin et al. (1985), Perryman et al. (1998), Barrado & Stauffer (1996) and Solano & Fernley (1997) respectively.

The ATLAS9 (Kurucz 1992) code was used to compute LTE model atmospheres assuming a plane parallel geometry, a gas in hydrostatic and radiative equilibrium and LTE. The ATLAS9 model atmospheres contain 64 layers with a regular increase in $\log \tau_{Ross} = 0.125$ and were calculated assuming Grevesse & Sauval (1998) solar chemical composition. This ATLAS9 version uses the new Opacity Distribution Function (ODF) of Castelli & Kurucz (2003) computed for that solar chemical composition. Convection is calculated in the frame of the mixing length theory (MLT). We have adopted Smalley's prescriptions (Smalley 2004) fo the values of the ratios of the mixing length to the pressure scale height ($\alpha = \frac{L}{H_P}$) and the microturbulent velocities (constant with depth).

3.2. The linelist

For the A stars, the linelist used for spectral synthesis is the same as in Paper I. All transitions between 3000 and 7000 Å from Kurucz's gfall.dat[2] linelist were selected. The abundance analysis relies on more than 200 transitions for the

[2] http://kurucz.harvard.edu/LINELISTS/GFALL/

15 selected elements as explained in Paper I. The adopted atomic data for each elements are collected in Table 8 of Paper I where, for each element, the wavelength, adopted oscillator strength, its accuracy (when available) and original bibliographical reference are given. The two sodium lines at 5890 and 5896 Å were not used in this present paper. These lines are likely to be affected by **interstellar absorption and** non-LTE effects, an LTE treatment assuming depth independent microturbulence underestimates abundances (Takeda et al. 2009). For the F stars, the same linelist was used except for iron and magnesium since only FeI and MgI **lines** are available in the AURELIE spectra. We have used the same atomic data for these lines as those in Table 3 of Varenne & Monier (1999). Most of the lines studied here are weak lines formed deep in the atmosphere where LTE should prevail. They are well suited for abundance determinations. **We have also included data for hyperfine splitting for the selected transitions when relevant, using the linelist gfhyperall.dat[3]. However the moderate spectral resolution of the spectra and smearing out of spectra by stellar rotation clearly prevent us from detecting signatures of hyperfine splitting and isotopic shifts in our spectra.**

3.3. Spectrum synthesis

For each modelled transition, the abundance was derived iteratively using Takeda's (1995) procedure which minimizes the chi-square between the normalized synthetic spectrum and the observed one. **As explained in Paper I, Takeda's code consists in two routines. The first routine computes the opacity data and it is based on a modified version of Kurucz's Width9 code (Kurucz 1992a) while the second computes the normalized flux and minimizes the dispersion between synthetic and observed spectra (see Paper I for a complete description of the method).**

We first derived the rotational ($v_e \sin i$) and microturbulent (ξ_t) velocities using several weak and moderately strong FeII lines located between 4491.405 Å and 4508.288 Å and the MgII triplet at 4480 Å by allowing small variations around solar abundances of Mg and Fe as explained in Sec. 3.2.1 of Paper I. The weak iron lines are very sensitive to rotational velocity but not to microturbulent velocity while the moderately strong FeII lines are affected mostly by changes of microturbulent velocity. The MgII triplet is sensitive to both ξ_t and $v_e \sin i$. Once the rotational and microturbulent velocities were fixed, we then derived the abundance that minimized the chi-square for each transition of a given chemical element. These individual abundances may differ because of different levels of accuracies in the atomic data of each line and possibly because of deviations from LTE in a few of them. The derivation of the mean abundance from these individual abundances is explained in Sec. 3.5. The abundances were then double-checked using Hubeny & Lanz's (1992) SYNSPEC48 code.

As an example, we display in Fig. 2 the final synthetic spectrum which best fits several Fe II lines in the observed spectrum of HD28527 (A6IV) in the spectral interval 4513-4525 Å. In this region, the independent fit of each line yields only slightly different abundances. The displayed synthetic spectrum is computed for an iron abundance of +0.30 dex, which is the derived mean value in HD28527.

In the case of stars rotating faster than about 80 km/s, the following neighbouring lines blend: Ti II 4394.059 Å and Ti II 4395.051 Å, Mn I 4033.062 Å and 4034.483 Å and for the O I lines "triplet" at 6155.900 Å, 6156.750 Å and 6158.1 Å. In these cases, the abundances given in the electronic Table 8 are those that provide the best match to each blend.

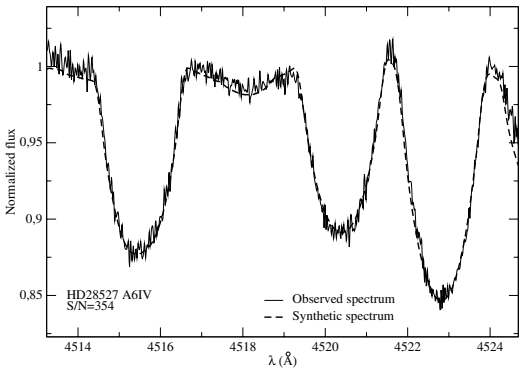

Fig. 2. A typical agreement between the observed spectrum (thin line) of HD28527 (A6IV) and the synthetic spectrum (dashed thick line) computed as explained in Sect. 3. Three iron (FeII) lines calculated for [Fe/H]=+0.30 dex, the mean iron abundance, are displayed in this figure.

3.4. Internal Consistency checks on the spectral energy distribution

For a few stars, we have checked the fundamental parameter determinations by modelling the entire spectral energy distribution from far UV to IR with the theoretical ATLAS9 flux computed for the derived fundamental parameters and the individual abundances. Fig. 3 exemplifies this check for HD 27819. The theoretical spectral energy distribution was computed with the LLmodel code (Shulyak et al. 2004). The observed spectral energy distribution was constructed from Adelman et al's (1989) spectrophotometry and IUE spectrophotometry: SWP04446 (low resolution) + LWP16605 (high resolution resampled to the LWP low resolution). The theoretical LLmodel spectral energy distribution, degraded to a spectral resolution comparable to that of the IUE low resolution spectra, follows nicely the overall shape of the observed flux distribution which leads credence to the adopted fundamental parameters and the derived abundances.

3.5. Mean abundances and uncertainties

Apparent rotational velocity, microturbulent velocity were determined for all sample stars. The abundances of **15** chemical elements were determined for most of the stars (when the selected lines were accessible with good signal-to-nois ratios). The abundances for A and F stars are collected in Online Tables 5 and 6. These abundances are relative to the sun[4]. Solar abundances are from Grevesse & Sauval (1998). **For each chemical element the final abundance is an average of the abundances derived from each line. The errors on the final abundances (labelled**

[3] http://kurucz.harvard.edu/LINELISTS/GFHYPERALL/

[4] $([\frac{X}{H}] = \log(\frac{X}{H})_\star - \log(\frac{X}{H})_\odot)$

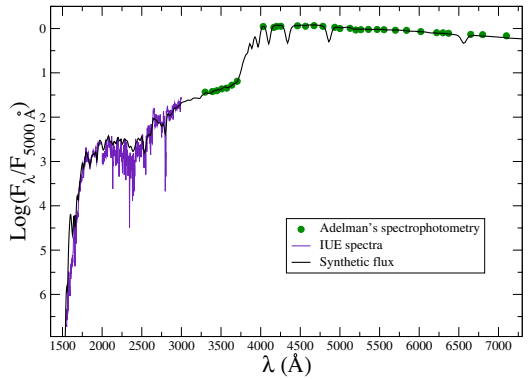

Fig. 3. Comparison of the LLmodel theoretical spectral energy distribution of HD27819 with the observed spectrophotometry of HD 27819 in the UV and the optical.

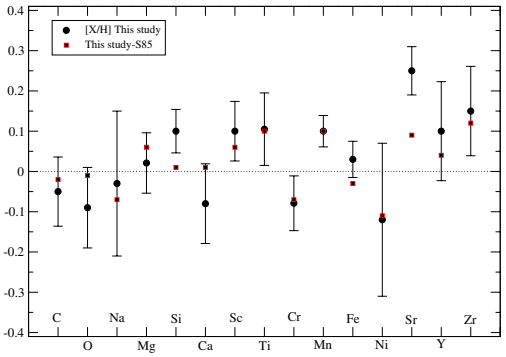

Fig. 4. Comparison of the abundances determined in this study and the one derived by Steffen 1985 (S85) for Procyon (red squares). The derived abundances are in black circles.

as σ) are standard deviation assuming a Gaussian distribution of the abundances derived from each line:

$$\bar{x} = \frac{\sum_i x_i}{N} \quad (1)$$

$$\sigma^2 = \frac{\sum_i (x_i - \bar{x})^2}{N} \quad (2)$$

where $\bar{x}$ is the mean value of the abundance, N the number of lines of the element and σ the standard deviation.
Accordingly the error on the abundance of a given element depends on the individual abundances derived from each line and usually varies from star to star. When only one transition was used to derive the abundance (for CI, OI[5], MgI, SiII, CaII, ScII and YII in F stars), the corresponding error was computed according to the formulation explained in Appendix A of Paper I. It consists into perturbating each of the 6 nominal parameters ($T_{\rm eff}$, log g, ξ_t, $v_e \sin i$, log gf and the continuum position) and repeating the fit for each line. The perturbations $\Delta(T_{\rm eff})$ and $\Delta(\log\ g)$ are 200 K and 0.20 dex, respectively (Napiwotzki et al. 1993). $\Delta(v_{\rm e} \sin i)$ is estimated as 5% of the nominal $v_e \sin i$ and $\Delta(\xi_t)$ is 1 km.s^{-1} (Gebran 2007). $\Delta(\log\ gf)$ depends on the accuracy of the considered lines. It varies from 3% to more than 50%. For more details concerning the accuracies on the oscillator strengths, see Tab. 8 (3rd column) of Paper I and Tab. 3 (3rd column) of Varenne & Monier (1999). The continuum placement error depends on the rotational velocity of the star and is fully explained in Paper I.
The difference between the nominal abundance and the one derived with the perturbated parameter yields the uncertainty affected to the given parameter. Considering that the errors are independent, the upper limit of the total uncertainty σ_{tot_i} for a given transition (i) is:

$$\sigma^2_{tot_i} = \sigma^2_{T_{\rm eff}} + \sigma^2_{\log g} + \sigma^2_{\xi_t} + \sigma^2_{v_e \sin i} + \sigma^2_{\log gf} + \sigma^2_{cont}. \quad (3)$$

Online Table 8 collects the abundances derived for each transition for each studied element in all A and F stars including Procyon (F5V) which served as control star for the spectral synthesis. In this table, the absolute values are represented ($\log(X/H)_\star$+12) and the wavelengths are in Å.

[5] Oxygen lines are blended in F stars because of the low resolution of AURELIE spectra, which is not the case of SOPHIE's A stars.

4. Results

We have first tested the spectrum synthesis on Procyon whose abundances are almost solar (Steffen 1985). For elements having lines on the 3 AURELIE spectral ranges, abundances agree weel. The derived abundances are displayed in Fig. 4. We have found nearly solar abundances for all the elements except for strontium. The differences between the abundances we derived and those derived by Steffen (1985) are depicted as squares in Fig. 4. They are less than 0.10 dex for 13 out of 15 elements and less than 0.15 dex for the remaining (Ni and Zr), typically less then the order of magnitude of the uncertainties. We found an apparent rotational velocity of 6 km.s^{-1} **and a microturbulent velocity of 2.2** km.s^{-1}**, in good agreement with Steffen's values ($v_e \sin i$=4.5** km.s^{-1} **and ξ_t=2.1** km.s^{-1}**, Steffen 1985).**

4.1. Abundance patterns and comparison with previous studies

Abundance patterns graphs where abundances are displayed against atomic number Z are particularly useful to compare the behaviour of A, Am and F stars for different chemical elements. The abundance patterns for A, Am and F stars are displayed in Figs. 5a-d. The pattern for A stars resembles that of the A stars in Coma Berenices and in the Pleiades (Papers I and II). Among the 9 A stars, the elements that exhibit the largest star-to-star variations are Sr, Y and Zr (1.0 to 0.8 dex) while C and Cr display the lowest variations (0.2 dex). The amplitudes of variations for the other elements, O, Na, Mg, Si, Ca, Sc, Ti, Mn, Fe and Ni range from 0.25 to 0.60 dex (see further discussion of individual elements).
The 7 Am stars display the characteristic jig-saw pattern with larger excursions around the solar composition than the A stars do. Almost all Am stars are heavily deficient in Sc, but not all are deficient in Ca and the deficiencies are more modest for this element. Almost all are more deficient in C and O than the A stars, and all are more enriched in iron peak elements and heavy elements (Sr and beyond). For all chemical elements, the star-to-

Fig. 5. Abundance patterns for the "normal" A (a), Am (b) and F (c,d) stars of the Hyades cluster. A maximum ±0.30 dex error bar is displayed. The horizontal dashed line represents the solar composition.

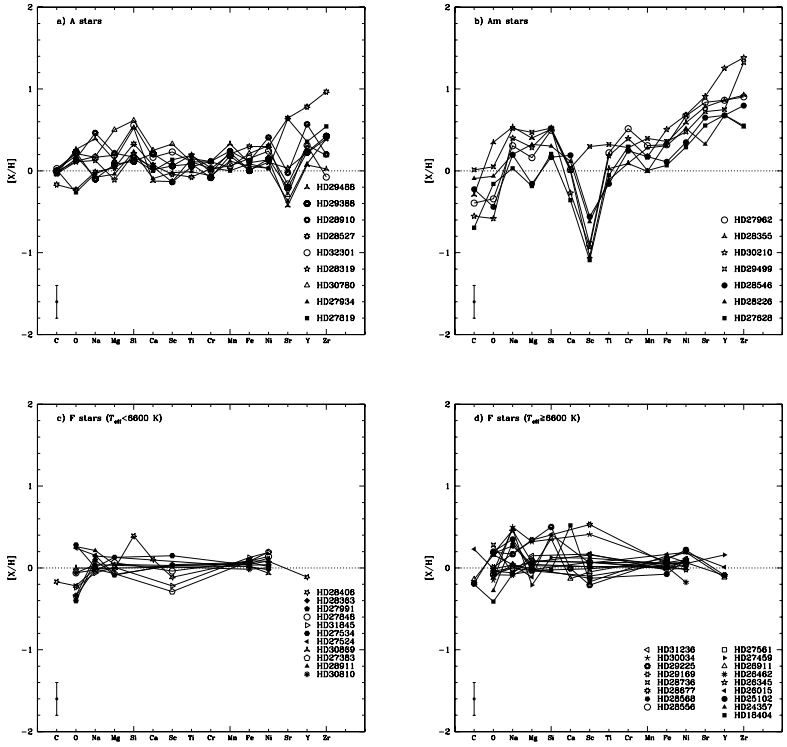

star variations of Am stars are usually larger than for the A stars. In contrast, F stars exhibit little scatter around the mean abundances. For clarity reasons, the abundances of F stars are sorted out in two graphs: the data for stars cooler than 6600 K appear in Fig. 5c, and for those hotter than 6600 K in Fig. 5d. At the age of the Hyades, a F star with a temperature of 6600 K has a 1.3-1.4 $M_{\odot}$ mass. As explained in sect. 5.1.2, the evolutionary models show that the effects of atomic diffusion are more pronounced in all stars earlier than F5 ($M_{\star}$ >1.3$M_{\odot}$) (Turcotte et al. 1998a). Sorting out the F stars into two groups ($T_{\rm eff}$<6600 K and $T_{\rm eff}$≥6600 K) helps to highlight the occurrence of diffusion in the most massive F stars.

Graphically, we have compared the abundances derived in this study (filled circles) with previous determinations for 9 stars in Figure 6. The abundances of Mg, Ca, Sc, Cr, Fe and Ni derived by Hui-Bon-Hoa & Alecian (1998) for HD27819, HD27962 and HD30210 are depicted as losanges, the abundances of Si and Fe in HD27819 and HD30210 derived by Burkhart & Coupry (2000) as empty triangles and those of C, O, Na, Mg, Si, Ca, Sc, Fe, Ni and Y derived by Varenne & Monier (1999) as empty squares. For all stars, the overall shapes of the abundance patterns agree well. Differences exist for individual elements mostly because of the use of different microturbulent velocities, rotational velocities, and in the case of A stars, different ionization levels.

We have also compared the derived iron abundances for F stars in this work with the compilation available in Perryman et al. (1998) in Table 3. The [Fe/H] determinations come from **Chaffee et al. (1971) (CCS), Boesgaard & Budge (1988) (BB), Boesgaard (1989) (B) and Boesgaard & Friel (1990) (BF)**, they mostly rely on adjustments of theoretical equivalent widths to observed ones. Differences arise from the usage of different effective temperatures with a fixed gravity (log g=4.5 dex), older version of Kurucz ATLAS model atmospheres, different microturbulent velocities (determined using Nissen's 1981 fit) and different neutral iron lines.

4.2. Comments on particular stars

Am stars are expected to be underabundant in light elements, underabundant in calcium and/or scandium as well as overabundant in iron-peak and heavy elements. HD27962 is the hottest A star in the Hyades, Mermilliod (1982) suggested that it may be a blue straggler on basis of its location on the HR diagram. Conti (1965) classified HD 27962 as an Am star based on the weakness of the scandium line at λ4246 Å and the strength of strontium line at λ4215 Å. Abt (1985) assigned a spectral type Am (A2KA3HA5M) to HD 27962. Our analysis shows that scandium is deficient by -0.90 dex and that iron-peak and heavy elements are enhanced in this star so that it has the characteristics of an Am star. Our analysis of HD28355

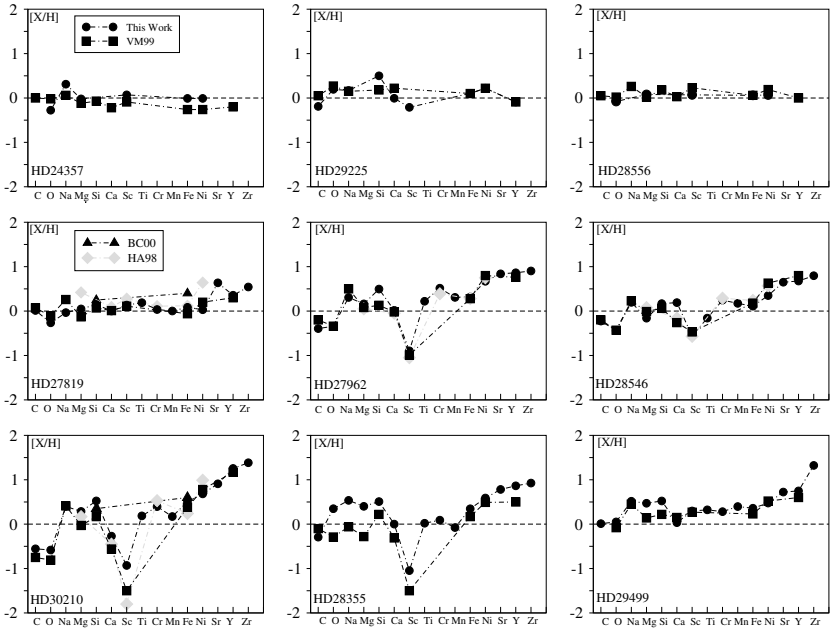

Fig. 6. Comparisons between the abundances derived in this work (filled circles), Varenne & Monier (1999) (VM99, open squares), Hui-Bon-Hoa & Alecian (1998) (HA98, filled diamonds) and Burkhart & Coupry (2000) (BC00, open triangles) for 9 stars of the Hyades cluster.

(A7V/A5m) also confirms its Am status as scandium is deficient by -1.05 dex and iron-peak and heavy elements are enhanced. Hauck (1977) had previously classified HD28355 as an Am star on basis of Geneva photometry. Both HD 27962 and HD 28355 are classified as Am in the catalog of Renson (1992). The seven stars represented in Fig. 5b are classified as Am in the catalog of Renson (1992). The abundances of all these stars except HD 29499 display the characteristic jig-saw pattern of Am stars: underabundances of light elements, of Ca and/or Sc and overabundances of metals and heavy elements. Our abundance analysis strongly suggest that HD29499 (A5m) may actually be a normal A star: it does not have Ca nor Sc deficiencies and is only moderately enriched in iron-peak and heavy elements.Its apparent rotational velocity is around 60 km.s^{-1}which is rather large for an Am star. Abt & Morrell (1995) have classified HD29499 as a giant star with metallic lines (A9III) but the surface gravity we found for HD 29499 suggests that it still be on the Main Sequence.

Table 3. Iron abundances comparisons.

Star	Reference	[Fe/H]	[Fe/H]$_{\rm this\ work}$
HD24357	BB	0.30	-0.014
HD25102	BB	0.20	-0.075
HD26015	BF	0.10	0.166
HD26345	BF	0.18	0.065
HD26462	BF	0.08	0.016
HD26911	BB	0.27	0.120
HD27383	CCS	0.23	0.082
HD27561	BF	0.16	0.048
HD27848	B	0.16	0.086
HD27991	BF	0.11	0.067
HD28406	BF	0.12	0.088
HD28736	BB	0.13	0.009
HD29225	BB	0.19	0.104
HD30810	CCS	0.16	-0.016
HD31845	BF	0.30	0.128

4.3. Behavior of the abundances of individual elements

As we have done for the Coma Berenices cluster (see Paper I), the behavior of the found abundances has been studied versus apparent rotational velocity ($v_{\rm e} \sin i$) and effective temperature ($T_{\rm eff}$). Any correlation/anticorrelation would be very valuable to theorists investigating the various hydrodynamical mechanisms affecting photospheric abundances. As we emphasized in Paper I, the existence of star-to-star variations with fundamental parameters can be established independently of errors in the absolute values of the oscillator strengths, since all stars will be affected in the same manner.

Second, we have searched whether the abundances of individual elements correlate with that of iron. **We expect the abundances of Fe, Ti, O, Cr, Mg, Mn, C, Ca and Ni to be fairly reliable as we synthesized several lines of quality A to D for these elements. For Y and Zr, several lines are available but their accuracy is unknown, the abundances of these elements should therefore be taken with caution. The abundances of Sr, derived from 2 transitions whose oscillator strengths**

Table 4. Mean abundances and dispersions.

Elements	F stars	σ_F	(Max-Min)$_{[\frac{X}{H}]}$	A stars	σ_A	(Max-Min)$_{[\frac{X}{H}]}$	Am stars	σ_{Am}	(Max-Min)$_{[\frac{X}{H}]}$
$[\frac{C}{H}]$	-0.09	0.16	0.43	-0.15	0.21	0.72	-0.32	0.27	0.71
$[\frac{O}{H}]$	-0.03	0.21	0.69	-0.03	0.27	0.93	-0.17	0.30	0.93
$[\frac{Na}{H}]$	0.11	0.18	0.59	0.20	0.20	0.64	0.31	0.23	0.50
$[\frac{Mg}{H}]$	0.03	0.11	0.55	0.15	0.21	0.68	0.18	0.21	0.66
$[\frac{Si}{H}]$	0.29	0.18	0.52	0.35	0.17	0.50	0.39	0.17	0.36
$[\frac{Ca}{H}]$	0.12	0.24	0.65	0.02	0.16	0.61	-0.04	0.17	0.55
$[\frac{Sc}{H}]$	0.03	0.18	0.82	-0.27	0.49	1.42	-0.69	0.64	1.39
$[\frac{Ti}{H}]$	-	-	-	0.08	0.13	0.48	0.06	0.13	0.48
$[\frac{Cr}{H}]$	-	-	-	0.14	0.16	0.60	0.27	0.21	0.42
$[\frac{Mn}{H}]$	-	-	-	0.17	0.12	0.47	0.18	0.13	0.47
$[\frac{Fe}{H}]$	0.05	0.05	0.24	0.19	0.14	0.50	0.29	0.17	0.44
$[\frac{Ni}{H}]$	0.07	0.09	0.40	0.33	0.21	0.65	0.51	0.26	0.39
$[\frac{Sr}{H}]$	-	-	-	0.29	0.46	1.33	0.68	0.61	0.58
$[\frac{Y}{H}]$	-0.04	0.10	0.28	0.54	0.32	1.18	0.82	0.42	0.57
$[\frac{Zr}{H}]$	-	-	-	0.60	0.41	1.46	0.93	0.53	0.83

have unknown inaccuracies, are likely to be inaccurate.
Abundances are displayed against $T_{\rm eff}$ in the left part of Figs. 8 to 12. Inspection of these figures reveal that there is no systematic slope (positive nor negative) and that for a large number of chemical elements, A stars display star-to-star variations in abundances larger than the typical uncertainty. Table 4 presents the mean abundance, the standard deviation and maximum spread for all chemical elements in **F, A (normal and Am) and Am stars**. Scatter around the mean value is more important in A stars than in F stars, namely for C, Na, Sc, Fe, Ni, Sr, Y and Zr. This behavior was already found in Coma Berenices and the Pleiades (see Papers I and II).
The abundances of C, O, Mg, Sc, Fe and **Y** are displayed versus $v_{\rm e}\sin i$ for A, Am and F stars in Fig. 7. For a given element, there is usually a considerable scatter in abundances at a given rotation rate. None of the derived abundances in this study exhibits a clear correlation nor anticorrelation with $v_{\rm e}\sin i$. Charbonneau & Michaud (1991) have analyzed the effect of meridional circulation on the chemical separation of elements in rotating stars. They showed that for stars rotating at less than $v_{\rm e}\sin i{\leq}100$ km.s^{-1}, no correlation should be expected between abundances and apparent rotational velocities. This prediction is verified by our findings (see Fig. 7). Even if we distinguish two velocity regimes ($v_{\rm e}\sin i{\leq}100$ km.s^{-1} and vsini$\geq$100 km.s^{-1}), we fail to find any dependence between the abundances of any of the **15** chemical elements and the apparent rotational velocity. Recently, Takeda et al. (2008) have found that the peculiarities (underabundances of C, O, and Ca) seen in slow rotators efficiently decrease with an increase of rotation and almost disappear at $v_{\rm e}\sin i{\geq}100$ km.s^{-1}. We confirm that for these chemical elements abundance anomalies vanish at $v_{\rm e}\sin i{\geq}100$ km.s^{-1}.

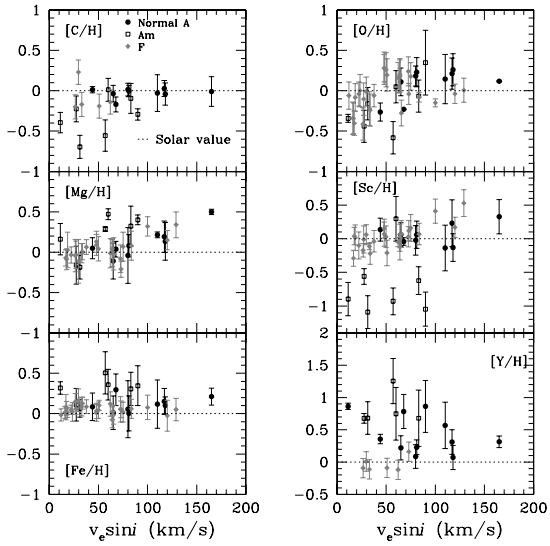

Fig. 7. Abundances of C, O, Mg, Sc, Fe and **Y** versus $v_e\sin i$ for A,Am and F stars.

Carbon and oxygen abundances display large star-to-star variation in A stars. No clear correlation was found between the abundances of C or O and [Fe/H]**. However, both** [C/Fe] **and** [O/Fe] **are anticorrelated with** [Fe/H]**. For the carbon lines used in our study, non-LTE abundance corrections for the A stars (7000 K**$<T_{\rm eff}<$**10000 K) are expected to be negative (Rentzsch-Holm 1996) and do not affect the star-to-star dispersion in** [C/H]**. Non-LTE corrections for oxygen abundances are negligible in the case of the OI lines considered here (see Paper I). Carbon and Oxygen tend to be more deficient in Am stars than in A stars of similar effective temperatures or rotation rate.**
For A stars, sodium abundances appear to be slightly correlated to the iron abundances as seen in Fig. 8. We found important star-to-star abundance variations in [Na/H]**. In Fig. 9, the scatter of** [Mg/H] **for both F and A stars does not exceed the typical uncertainty (0.20 dex) which suggests that there are no significant star-to-star variations in magnesium abundances. As mentioned in Paper I, the MgII** λ**4481 Å**

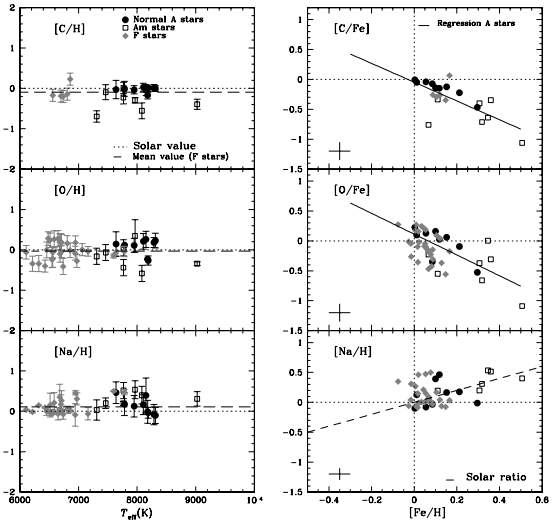

Fig. 8. Left panel: Abundances of carbon, oxygen and sodium versus effective temperature. The dotted line corresponds to the solar value and the dashed line to the mean value determined for the F stars of the cluster. Right panel: [C/Fe], [O/Fe] and [Na/H] versus [Fe/H]. The filled dots correspond to normal A stars, the open squares correspond to Am stars and the filled diamonds correspond to F stars. In the plot representing [Na/H] versus [Fe/H], the dashed line corresponds to the solar [Na/Fe] ratio. The error bars in the right panel represent the mean standard deviation for the displayed abundances.

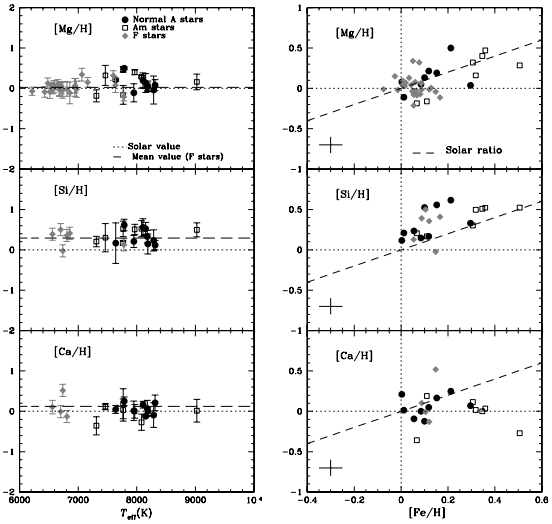

Fig. 9. Left panel: Abundances of magnesium, silicon and calcium versus effective temperature. The dotted line represents the solar value and the dashed one represents the mean abundance of F stars. Right panel: [Mg/H], [Si/Fe] and [Ca/H] versus [Fe/H]. The symbols are the same as in Figure 8. The dashed lines represent the solar ratios.

triplet yields higher abundances than other MgII lines, therefore we excluded this line from our analysis. The corrected [Mg/H**] abundances appear to be slightly correlated with [**Fe/H**]. The ratio [**Mg/Fe**] is close to solar for the A stars. The silicon lines synthesized in this work have low quality oscillator strengths and have not been updated for the recent values of the** $\log gf$ **of the NIST[6] database. The systematic found overabundances could be due to incorrect oscillator strengths, therefore the Si abundances should be viewed with caution. There does not seem to be significant star-to-star variations in [**Si/H**].**

Calcium abundance does not exhibit real star-to-star variations neither any clear correlation with repsect to [Fe/H**]. Not all Am stars are underabundant in calcium, only two of the 7 Am stars exhibit large underabundances in Ca. This result differs from Varenne & Monier's (1999) findings because of the use of different microturbulent velocities and ionisation level as explained in Sec.4.1. In Varenne & Monier (1999), the derived microturbulent abundances were larger (up to 5** $\mathrm{km.s^{-1}}$**) that those derived here, leading to lower abundances of calcium. Star-to-star variations in scandium abundance are clearly present for A stars (Fig. 10). Scandium is the most scattered of all analyzed elements. Scandium abundances do not appear to be correlated to iron abundances for both A and F stars. All Am stars except for HD 29499 are deficient in scandium and fall in the lower right part of Figure 10. The two stars, HD27962 and HD28355, for which we confirm the status as Am stars, are located in that region.**

Titanium, chromium and manganese abundances were derived for A stars only since none of the Ti, Cr and Mn lines observed with AURELIE have oscillator strengths accurate enough for abundance determinations. There does not seem to be significant star-to-star variation in [Ti/H**], [**Cr/H**] nor [**Mn/H**] for the A stars (Fig.10). The titanium abundances of the Hyades A stars do not appear to be correlated with the iron abundances. The chromium abundance appears to be only loosely correlated to that of iron.**

Iron abundances have been derived for all F and A stars of our sample. Neutral iron lines were used for F stars yielding a mean abundance of $<$ [Fe/H] $>_{\mathrm{F}}$**=0.05±0.05 dex. This value, which represents the average metallicity of the cluster, is almost 0.1 dex smaller than the value derived by Boesgaard & Friel (1990) from a different sample of 14 F Dwarfs (+0.127±0.022 dex using different FeI lines from ours). For the 16 A stars, 27 lines of FeII were synthesized. The normal A and Am stars scatter around their mean abundance with a maximum spread of about 0.50 dex, which is more than twice larger than the typical uncertainty on [**Fe/H**] is about 0.20 dex. This suggests real star-to-star variations in [**Fe/H**] among the Hyades A stars. Nickel behaves similarly to iron (see Fig. 11), the A stars display large star-to-star variations in [**Ni/H**] and the abundances are clearly correlated with the iron abundances, the correlation coefficient being close to 1.**

All Am stars appear to be overabundant in strontium. Star-

[6] http://www.nist.gov/

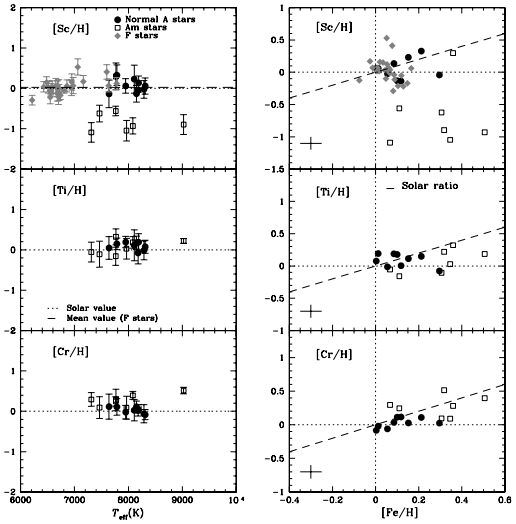

Fig. 10. Left panel: Abundances of scandium, titanium and chromium versus effective temperature. The dotted line represents the solar value and the dashed one represents the mean abundance of F stars. Right panel: [Sc/H], [Ti/Fe] and [Cr/H] versus [Fe/H]. The symbols are the same as in Figure 8. The dashed lines represent the solar ratios.

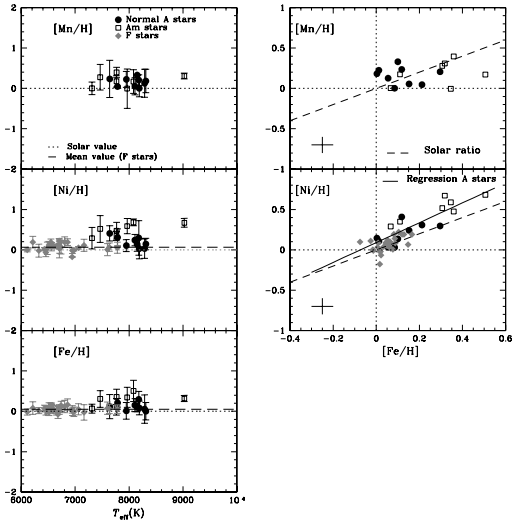

Fig. 11. Left panel: Abundances of manganese, iron and nickel versus effective temperature. The dotted line represents the solar value and the dashed one represents the mean abundance of F stars. Right panel: [Mn/H] and [Ni/H] versus [Fe/H]. The symbols are the same as in Figure 8. The dashed lines represent the solar ratios.

to-star variation in [Sr/H] **are clearly present. Strontium abundances are only loosely correlated with that of iron (right part of Fig. 12). Yttrium and zirconium are found overabundant in all A stars with a real star-to-star variations in [**Y/H] **and [**Zr/H] **(Figure 12). As for strontium, yttrium and zirconium abundances are correlated to [**Fe/H] **but appear to increase more rapidly than [**Fe/H] **(slope of 1.8 for Y and 2.1 for Zr).**

5. Discussion

5.1. Self-consistent evolutionary models

The derived abundances have been compared to the predictions of recent evolutionary models. These models are calculated with the Montréal stellar evolution code. The chemical transport problem is treated with all known physical processes from first principles, which includes radiative accelerations, thermal diffusion and gravitational settling (for more details see Turcotte et al. 1998b, Richard et al. 2001 and references therein). These models follow the chemical evolution of most elements as well as some isotopes up to $Z \leq 28$ (28 species in all). As the abundances change, the Rosseland opacity and radiative accelerations are continuously recalculated at each mesh point and for every time step during evolution which means that the treatment of particle transport is completely self-consistent. The spectra used to calculate the monochromatic opacities are taken from the OPAL database (Iglesias et al. 1996). The radiative accelerations are calculated as described in Richer et al. (1998) with corrections for the redistribution of momentum from Gonzalez et al. (1995)

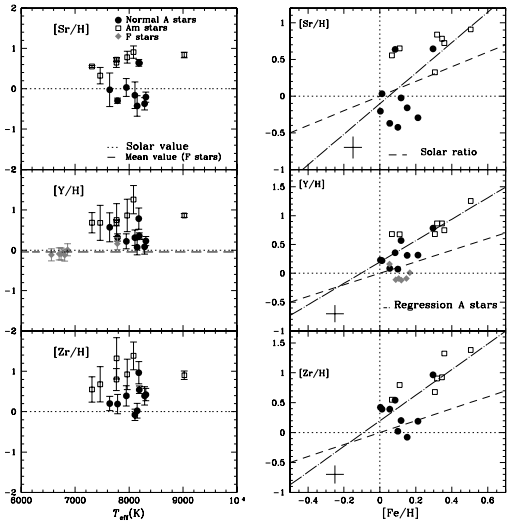

Fig. 12. Left panel: Abundances of strontium, yttrium and zirconium versus effective temperature. Right panel: [Sr/H], [Y/Fe] and [Zr/H] versus [Fe/H]. The symbols are the same as in Figure 8.

and LeBlanc et al. (2000). The mixing length parameter and initial helium abundance (α = 2.096 and Y_0 = 0.2779 respectively) are calibrated to fit the current luminosity and radius of the Sun (see Turcotte et al. 1998b, model H). Models are evolved from the pre-main sequence with a solar scaled abundance mix. The initial abundance ratios are given in Table 1 of Turcotte et al. (1998b). For the initial mass fraction of metals we used both Z_0 = 0.02, the solar metal content, and Z_0 = 0.024 (to represent the increased metallicity of the Hyades, Lebreton et al. 2001).

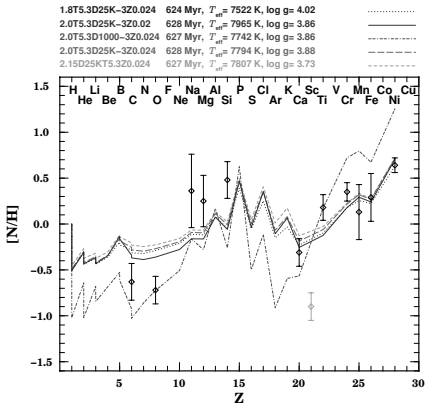

Fig. 13. Comparison of the predicted surface abundances for stars of 1.8, 2.0 and 2.15 $M_\odot$ with different turbulence prescriptions and different initial metallicities with those derived (depicted as diamonds with their respective uncertainties) for the Am star HD30210 ($T_{\rm eff}$ = 8082 K and $\log g$ = 3.92). The gray symbol for Sc indicates that it is not considered in the evolutionary models.

5.1.1. The A stars

The derived abundances in A stars are compared to the predictions of self-consistent evolutionary models calculated as in Richer et al. (2000). These models include an arbitrary parameter, the amount of mass mixed by turbulent mixing, in order to lower the effects of chemical separation and better fit the abundances of AmFm stars. The effect of turbulence is to extend the mixed mass below the surface convection zone, down to layers where atomic diffusion is less efficient (ie. where time scales are longer due to higher local density). *A priori*, the cause of turbulence is not considered, however it was found to be compatible with rotationally induced turbulence as calculated by Zahn 2005 and Talon et al. 2006. The surface abundances are shown to depend solely on the amount of mass mixed as well as initial metallicity. In Figure 13, we compare the predicted surface abundances for five models with masses of 1.8, 2.0 and 2.15 $M_\odot$ to the observed abundances of the Hyades A2m star HD30210 ($T_{\rm eff}$ = 8082 K and $\log g$ = 3.92 dex). The models are shown for both Z=0.02 and Z=0.024. To help interpret the chosen nomenclature, the 2.0T5.3D1000-3 corresponds to a 2.0 $M_\odot$ star for which the abundances are completely homogenized down to $\log T$ = 5.3. Below this point, as we move deeper inside the star, the turbulent diffusion coefficient $D_{\rm T}$ = 1000 $D_{\rm He}$ (the helium diffusion coefficient) decreases as ρ^{-3} (2.0T5.3D25K-3 would have the same behavior except that the turbulent coefficient $D_{\rm T}$ = 25000 $D_{\rm He}$ at $\log T$ = 5.3). It is clear from the plot that the amount of prescribed turbulence has an influence on the surface behavior. The model 2.0T5.3D1000-3 does not sufficiently impeed microscopic diffusion to reproduce most abundances. However, for all other models with greater turbulence, the predicted carbon and oxygen underabundances are not as important as the observed anomalies. The predicted slight underabundances of Na, Mg and Si are not observed in HD30210, but are observed in a few of the Am stars. However the silicon abundance is probably too large. The model that best fits the data is 2.15T5.3D25K-3Z0.024, which has a turbulence prescription which was equivalently able to reproduce the observations in Coma Berenices (see Figures 14 and 15 of Paper I). As in Paper I, models with less turbulence roughly replicate the observations for $Z < 12$ and the more turbulent models are better able to reproduce the heavier elements ($Z > 15$). The different metallicities do not lead to significant differences in the predicted abundance patterns, but do have an important effect on $T_{\rm eff}$.

5.1.2. The F-type stars

For the F dwarfs, we have compared the found abundances to the predicted surface abundances for C, O, Na, Mg, Fe and Ni using Turcotte's evolutionary models at 620 Myr (Turcotte et al. 1998a). These models, calculated for masses ranging from 1.1-1.5 $M_\odot$, treat radiative diffusion in detail but do not include macroscopic mixing processes (meridional circulation, turbulence or mass loss). They show that the effects of atomic diffusion, namely the appearance of surface abundance anomalies, can be expected in all stars earlier than F5 ($M_* > 1.3\ M_\odot$).
The found mean carbon abundance for F stars, <[C/H]>=-0.09 dex with very small dispersion, does not agree with predicted underabundance at 620 Myr ($\log$ age = 8.79 in Figure 7 of Turcotte et al. 1998a) and for a 1.4$M_\odot$ star, representative of the F stars analysed here. The oxygen abundances, which show large scatter for the F stars, can typically be underabundant by -0.41 dex or overabundant by up to 0.28 dex for a 1.4$M_\odot$ F star (roughly an effective temperature of 6700 K at the age of the Hyades). Again, they do not agree with the predicted surface underabundances [O/H] predicted by Turcotte et al. (1998a). The predicted solar Na abundances match reasonably well of our determinations for F stars. Magnesium is predicted to be slightly underabundant (Fig. 7 of Turcotte et al. 1998a), whereas for most F stars we find overabundances. Finally, iron and nickel are found to be mildly overabundant in case of F stars with $T_{\rm eff}\in$[6600K,6800K] (<[Fe/H]>=0.06 dex and <[Ni/H]>=0.11 dex). These results disagree with the overabundances of 0.5 and 0.8 dex respectively for a 1.4 $M_\odot$. As expected, these purely diffusive models typically predict too little C and O and too much iron-peak elements.

6. Conclusion

Selected high quality lines in new high resolution échelle spectra of 16 A and 28 F stars of the Hyades have been synthesized in a uniform manner to derive LTE abundances, a few of which have been corrected for Non-LTE effects whenever possible. Even when binary stars are removed, the abundances of several chemical elements for A stars and early F stars exhibit real star-to-star variations, significantly larger than for the late F stars. The largest spreads occur for Sc, Sr, Y, Zr while the lowest are for Mg, Si and Cr for A stars. Gebran et al (2008) and Gebran & Monier (2008) had already found similar behaviour in the Coma

Berenices and the Pleiades. The derived abundances do not depend on effective temperatures nor apparent rotational velocities as expected since the timescales of diffusion are much shorter than those of rotational mixing (Charbonneau & Michaud 1991). The abundances of Cr, Ni, Sr, Y and Zr are correlated with the iron abundance as was found for the Pleiades and Coma Berenices. The ratios [C/Fe] and [O/Fe] are anticorrelated with [Fe/H] (particularily true for normal A stars). Compared to normal A stars, all Am stars in the Hyades appear to be more deficient in C and O and more overabundant in elements heavier than Fe but not all are deficient in calcium and/or scandium. The F stars have nearly solar abundances for almost all elements except for Si and Ca. The Blue Straggler HD 27962 appears to have abundances characteristic of an Am star (scandium deficiency and enrichment in iron-peak and heavy elements). Conversely our abundance analysis of HD 29499 (A5m) yields normal abundances in Ca and Sc and only moderate enrichment in iron-peak and heavy elements suggesting that this star might be a normal A star. The detailed modelling of the A2m star HD 30210 including radiative diffusion and different amounts of turbulent diffusion reproduces the overall shape of the abundance pattern for this star but not individual abundances. Models with the least turbulence reproduce the abundances of the lightest ($Z < 12$) and those with most turbulence reproduce abundances of elements with $Z > 15$. For a few elements, the discrepancies between derived and predicted abundances could be due to Non-LTE effects. However, the inclusion of competing processes such as different prescriptions of rotational mixing (Zahn 2005) and/or different amounts of mass loss (Vick et al. , in preparation) could well improve the agreement between observed and predicted abundance patterns.

Acknowledgements. We warmly thank the OHP night staff for the support during the observing runs. This research has used the SIMBAD, WEBDA, VALD, NIST and Kurucz databases. MV thanks the Département de physique at l'Université de Montréal as well as the GRAAL at l'Université Montpellier II for financial support and the Réseau Québécois de Calcul de Haute Performance (RQCHP) for providing us with the computational resources required for this work. A special thanks to Georges Michaud and Olivier Richard for their careful reading of the manuscript and useful suggestions. LF received support from the Austrian Science Foundation (FWF project P17890-N2).

References

Abt, H. A., & Morrell, N. I. 1995, ApJS, 99, 135
Adelman S.J., Pyper D.M., Shore S.N., White R.E. & Warren W.H. 1989, A&AS, 81, 221
Alecian, G. 1996, A&A, 310, 872
Balona, L. A. 1994, MNRAS, 268, 119
Barrado y Navascues, D., & Stauffer, J. R. 1996, A&A, 310, 879
Burkhart, C., & Coupry, M. F. 2000, A&A, 354, 216
Boesgaard, A. M. 1989, ApJ, 336, 798
Boesgaard, A. M., & Tripicco, M. J. 1986, ApJ, 303, 724
Boesgaard, A. M., & Budge, K. G. 1988, ApJ, 332, 410
Boesgaard, A. M., & Friel, E. D. 1990, ApJ, 351, 467
Castellani, V., Degl'Innocenti, S., Prada Moroni, P. G. & Tordiglione, V. 2002, MNRAS, 334, 193
Cayrel, R., Cayrel, G., Campbell, B., & Dappen, W. 1984, Observational Tests of the Stellar Evolution Theory, 105, 537
Cayrel de Strobel, G., Crifo, F., & Lebreton, Y. 1997, Hipparcos - Venice '97, 402, 687
Cayrel de Strobel, G., Soubiran, C., & Ralite, N. 2001, A&A, 373, 159
Castelli, F., & Kurucz, R. L. 2003, IAU Symposium, 210, 20P
Chaffee, F. H., Jr., Carbon, D. F., & Strom, S. E. 1971, ApJ, 166, 593
Charbonneau, P., & Michaud, G. 1991, ApJ, 370, 693
Conti, P. S. 1965, ApJ, 142, 1594
Dommanget, J., & Nys, O. 1995, Bulletin d'Information du Centre de Donnees Stellaires, 46, 3
Erspamer, D., & North, P. 2002, A&A, 383, 227
Friel, E. D., & Boesgaard, A. M. 1990, ApJ, 351, 480
Garcia Lopez, R. J., Rebolo, R., Herrero, A., & Beckman, J. E. 1993, ApJ, 412, 173
Gebran, M., PhDThesis, 2007, UMII
Gebran, M., Monier, R., & Richard, O. 2008, A&A, 479, 189
Gebran, M., & Monier, R. 2008, A&A, 483, 567
Gigas, D. 1988, A&A, 192, 264
Gonzalez, J.-F., LeBlanc, F., Artru, M.-C., & Michaud, G. 1995, A&A, 297, 223
Grenon, M. 2000, HIPPARCOS and the Luminosity Calibration of the Nearer Stars, 24th meeting of the IAU, Joint Discussion 13, August 2000, Manchester, England, meeting abstract., 13,
Grevesse, N., & Sauval, A. J. 1998, Space Science Reviews, 85, 161
Griffin, R. F., Griffin, R. E. M., Gunn, J. E., & Zimmerman, B. A. 1985, AJ, 90, 609
Hauck, B. 1977, Revista Mexicana de Astronomia y Astrofisica, 2, 231
Hauck, B., & Mermilliod, M. 1998, A&AS, 129, 431
Hill, G. M. 1995, A&A, 294, 536
Hill, G. M., & Landstreet, J. D. 1993, A&A, 276, 142
Holmberg, J., Nordström, B. & Andersen, J. 2007, A&A, 475, 519
Holweger, H., Steffen, M., & Gigas, D. 1986, A&A, 163, 333
Hubeny, I., & Lanz, T. 1992, A&A, 262, 501
Hui-Bon-Hoa, A., & Alecian, G. 1998, A&A, 332, 224
Iglesias, C. A., & Rogers, F. J. 1996, ApJ, 464, 943
Kurucz, R. L. 1992, Revista Mexicana de Astronomia y Astrofisica, vol. 23, 23, 45
Lambert, D. L., McKinley, L. K., & Roby, S. W. 1986, PASP, 98, 927
Landstreet, J. D., Bagnulo, S., Andretta, V., Fossati, L., Mason, E., Silaj, J., & Wade, G. A. 2007, A&A, 470, 685
LeBlanc, F., Michaud, G., & Richer, J. 2000, ApJ, 538, 876
Lebreton, Y., Fernandes, J., & Lejeune, T. 2001, A&A, 374, 540 Badly placed ()'s.
Lemke, M. 1989, A&A, 225, 125
Lemke, M. 1990, A&A, 240, 331
Marigo, P., Girardi, L., Bressan, A. et al. 2008, A&A, 482, 883
Monier, R. 2005, A&A, 442, 563
Moon, T. T., & Dworetsky, M. M. 1985, MNRAS, 217, 305
Napiwotzki, R., Schoenberner, D., & Wenske, V. 1993, A&A, 268, 653
Nissen, P. E. 1981, A&A, 97, 145
Percival, S. M., Salaris, M. & Kilkenny, D. 2003, A&A, 400, 541
Perryman, M. A. C., Brown, A. G. A., Lebreton, Y., et al. 1998, A&A, 331, 81
Renson, P. 1992, Bulletin d'Information du Centre de Donnees Stellaires, 40, 97
Rentzsch-Holm, I. 1996, A&A, 312, 966
Rentzsch-Holm, I. 1997, A&A, 317, 178
Richard, O., Michaud, G., & Richer, J. 2001, ApJ, 558, 377
Richer, J., Michaud, G., Rogers, F., Iglesias, C., Turcotte, S., & LeBlanc, F. 1998, ApJ, 492, 833
Richer, J., Michaud, G., & Turcotte, S. 2000, ApJ, 529, 338
Salaris, M., Weiss, A. & Percival, S. M. 2004, A&A, 414, 163
Shulyak, D., Tsymbal, V., Ryabchikova, T., Stütz, Ch., & Weiss, W. W. 2004, A&A, 428, 993
Smalley, B. 2004, IAU Symposium, 224, 131
Solano, E., & Fernley, J. 1997, A&AS, 122, 131
Steffen, M. 1985, A&AS, 59, 403
Takeda, Y. 1995, PASJ, 47, 287
Takeda, Y., Han, I., Kang, D.-I., Lee, B.-C., & Kim, K.-M. 2008, Journal of Korean Astronomical Society, 41, 83
Takeda, Y., Kang, D.-I., Han, I., Lee, B.-C., & Kim, K.-M. 2009, arXiv:0907.1329
Takeda, Y., & Sadakane, K. 1997, PASJ, 49, 367
Talon, S., Richard, O., & Michaud, G. 2006, ApJ, 645, 634
Taylor, B. J. 2006, AJ, 132, 2453
Thorburn, J. A., Hobbs, L. M., Deliyannis, C. P., & Pinsonneault, M. H. 1993, ApJ, 415, 150
Turcotte, S., Richer, J., & Michaud, G. 1998, ApJ, 504, 559
Turcotte, S., Richer, J., Michaud, G., Iglesias, C. A., & Rogers, F. J. 1998, ApJ, 504, 539
van Leeuwen, F. 2007, Astrophysics and Space Science Library, 350,
Varenne, O. 1999, A&A, 341, 233
Varenne, O., & Monier, R. 1999, A&A, 351, 247
Vick, M., & Michaud, G. 2008, Contributions of the Astronomical Observatory Skalnate Pleso, 38, 135
Zahn, J.-P. 2005, EAS Publications Series, 17, 157

Table 8. continued.

HD30210

λC	log(C/H)$_\star$	λO	log(O/H)$_\star$	λNa	log(Na/H)$_\star$	λMg	log(Mg/H)$_\star$
4932.049	7.730	5330.700	8.210	4668.559	6.470	4390.510	7.860
5052.167	8.120	6155.900	8.207	4982.813	6.910	4481.1	7.792
		6156.750	8.207				
		6158.1	8.204				
λSi	log(Si/H)$_\star$	λCa	log(Ca/H)$_\star$	λSc	log(Sc/H)$_\star$	λTi	log(Ti/H)$_\star$
5055.984	7.810	5001.479	6.050	4314.083	2.200	4163.644	5.030
5978.930	8.300					4287.873	5.130
6347.110	7.990					4300.042	5.230
						4386.844	5.230
						4394.059	5.040
						4395.051	5.180
						4399.772	4.986
						4417.714	5.490
						4443.801	5.180
λCr	log(Cr/H)$_\star$	λMn	log(Mn/H)$_\star$	λFe	log(Fe/H)$_\star$	λNi	log(Ni/H)$_\star$
4592.049	5.940	4033.062	5.540	4273.326	7.633	4470.472	6.920
4634.070	6.007	4034.483	5.030	4296.570	8.067	4604.982	6.730
4812.337	5.868	4083.628	5.325	4416.830	7.910	5080.528	6.909
5237.329	6.085	4754.042	5.980	4491.405	7.990	5099.927	7.010
5308.440	6.070	4783.427	5.580	4508.288	8.107		
5313.590	6.180			4515.339	8.440		
				4520.224	8.280		
				4522.634	8.054		
				4541.524	7.940		
				4555.890	7.700		
				4666.758	7.510		
λSr	log(Sr/H)$_\star$	λY	log(Y/H)$_\star$	λZr	log(Zr/H)$_\star$		
4077.709	3.990	4883.684	3.246	4149.217	3.820		
4215.520	3.687	4900.120	3.948	4156.240	4.530		
		5087.416	3.170	4208.980	3.770		
				4496.980	3.650		

HD30780

λC	log(C/H)$_\star$	λO	log(O/H)$_\star$	λNa	log(Na/H)$_\star$	λMg	log(Mg/H)$_\star$
4932.049	8.570	5330.700	8.918	4668.559	6.640	4390.510	8.080
5052.167	8.320	6155.900	8.900	4982.813	6.067	4481.1	8.000
		6158.	8.920				
λSi	log(Si/H)$_\star$	λCa	log(Ca/H)$_\star$	λSc	log(Sc/H)$_\star$	λTi	log(Ti/H)$_\star$
5055.984	7.980	5001.479	6.417	4314.083	3.800	4163.644	4.935
5978.930	8.270	5019.971	6.640	4324.996	3.330	4287.873	5.165
		5285.266	6.650	5031.021	3.123	4300.042	4.710
				5239.813	3.580	4386.844	5.230
						4395.051	5.320
						4399.772	5.360
						4417.714	4.940
λCr	log(Cr/H)$_\star$	λMn	log(Mn/H)$_\star$	λFe	log(Fe/H)$_\star$	λNi	log(Ni/H)$_\star$
4592.049	5.980	4034.483	5.374	4273.326	7.330	4470.472	6.620
4634.070	5.807	4083.628	5.415	4296.570	7.670	4604.982	6.730
4812.337	5.790	4754.042	5.400	4416.830	7.860	5080.528	6.160
5237.329	5.360			4491.405	7.610	5099.927	6.530
5308.440	5.760			4508.288	7.670		
				4515.339	7.670		
				4520.224	7.630		
				4522.634	7.890		
				4541.524	7.720		
λSr	log(Sr/H)$_\star$	λY	log(Y/H)$_\star$	λZr	log(Zr/H)$_\star$		

Table 8. continued.

4077.709	2.570	4883.684	2.570	4149.217	2.510		
4215.520	2.700	4900.120	2.585	4156.240	2.990		
		5087.416	2.390				

HD32301

λC	log(C/H)$_\star$	λO	log(O/H)$_\star$	λNa	log(Na/H)$_\star$	λMg	log(Mg/H)$_\star$
4932.049	8.510	5330.700	9.338	4668.559	6.700	4390.510	7.540
5052.167	8.350	6155.900	8.890	4982.813	6.210	4427.994	7.660
5380.337	8.614					4481.1	7.997
5793.120	8.560						
λSi	log(Si/H)$_\star$	λCa	log(Ca/H)$_\star$	λSc	log(Sc/H)$_\star$	λTi	log(Ti/H)$_\star$
5055.984	7.940	5001.479	6.360	4314.083	3.970	4163.644	4.890
5978.930	7.890	5019.971	6.490	4324.996	3.510	4287.873	4.600
6347.110	8.370	5285.266	6.490	5031.021	3.430	4300.042	4.680
				5239.813	2.987	4386.844	5.480
				5526.790	2.930	4395.051	5.476
						4399.772	5.440
λCr	log(Cr/H)$_\star$	λMn	log(Mn/H)$_\star$	λFe	log(Fe/H)$_\star$	λNi	log(Ni/H)$_\star$
4592.049	5.550	4034.483	5.449	4273.326	7.465	4470.472	6.630
4634.070	5.140	4083.628	5.640	4296.570	7.770	4604.982	6.267
4812.337	5.890	4754.042	5.126	4416.830	7.696	5080.528	6.430
5237.329	5.990			4491.405	7.790	5099.927	6.339
5308.440	5.520			4508.288	7.580		
5313.590	5.840			4515.339	7.400		
				4520.224	7.400		
				4522.634	7.459		
				4541.524	7.785		
				4555.890	7.775		
λSr	log(Sr/H)$_\star$	λY	log(Y/H)$_\star$	λZr	log(Zr/H)$_\star$		
4077.709	3.100	4883.684	2.820	4149.217	2.450		
4215.520	2.440	4900.120	2.514	4156.240	2.670		
		5087.416	2.380	4208.980	2.330		

F stars

HD24357

λC	log(C/H)$_\star$	λO	log(O/H)$_\star$	λNa	log(Na/H)$_\star$	λMg	log(Mg/H)$_\star$
		6155-8	8.515	6154.226	6.600	5528.405	7.520
λSi	log(Si/H)$_\star$	λCa	log(Ca/H)$_\star$	λSc	log(Sc/H)$_\star$	λFe	log(Fe/H)$_\star$
				5526.790	3.200	5068.766	7.361
						5072.076	7.363
						5074.748	7.580
						5078.972	7.597
						5506.779	7.330
λNi	log(Ni/H)$_\star$	λY	log(Y/H)$_\star$				
5080.528	6.182						
5084.089	6.209						
5096.854	6.210						

HD25102

λC	log(C/H)$_\star$	λO	log(O/H)$_\star$	λNa	log(Na/H)$_\star$	λMg	log(Mg/H)$_\star$
		6155-8	8.990	6154.226	6.960	5528.405	7.530
				6160.747	6.320		

Table 8. continued.

λSi	log(Si/H)$_\star$	λCa	log(Ca/H)$_\star$	λSc	log(Sc/H)$_\star$	λFe	log(Fe/H)$_\star$
				5526.790	3.005	5068.766	7.270
						5072.076	7.310
						5074.748	7.520
						5078.972	7.340
						5506.779	7.483
λNi	log(Ni/H)$_\star$	λY	log(Y/H)$_\star$				
5080.528	6.290						
5084.089	6.330						

HD26015

λC	log(C/H)$_\star$	λO	log(O/H)$_\star$	λNa	log(Na/H)$_\star$	λMg	log(Mg/H)$_\star$
5052.167	8.710	6155-9	8.780	6154.226	6.400	5528.405	7.428
				6160.747	6.250		
λSi	log(Si/H)$_\star$	λCa	log(Ca/H)$_\star$	λSc	log(Sc/H)$_\star$	λFe	log(Fe/H)$_\star$
5055.984	7.920			5526.790	3.190	5068.766	7.590
						5072.076	7.912
						5074.748	7.560
						5078.972	7.457
						5506.779	7.575
						6136.615	7.680
						6147.835	7.484
						6163.544	7.750
λNi	log(Ni/H)$_\star$	λY	log(Y/H)$_\star$				
5080.528	6.420	5087.416	2.210				
5084.089	6.490						
5096.854	6.430						
5099.927	6.260						

HD26345

λC	log(C/H)$_\star$	λO	log(O/H)$_\star$	λNa	log(Na/H)$_\star$	λMg	log(Mg/H)$_\star$
		6155-8	8.686	6154.226	6.365	5528.405	7.509
				6160.747	6.290		
λSi	log(Si/H)$_\star$	λCa	log(Ca/H)$_\star$	λSc	log(Sc/H)$_\star$	λFe	log(Fe/H)$_\star$
				5526.790	3.120	5068.766	7.499
						5072.076	7.350
						5074.748	7.552
						5078.972	7.570
						5506.779	7.656
λNi	log(Ni/H)$_\star$	λY	log(Y/H)$_\star$				
5080.528	6.270						
5084.089	6.350						

HD26462

λC	log(C/H)$_\star$	λO	log(O/H)$_\star$	λNa	log(Na/H)$_\star$	λMg	log(Mg/H)$_\star$
		6155-8	8.707	6154.226	6.230	5528.405	7.567
				6160.747	6.174		

Table 8. continued.

λSi	log(Si/H)$_\star$	λCa	log(Ca/H)$_\star$	λSc	log(Sc/H)$_\star$	λFe	log(Fe/H)$_\star$
				5526.790	3.145	5068.766	7.400
						5072.076	7.420
						5074.748	7.470
						5078.972	7.596
						5506.779	7.490
						6136.615	7.480
λNi	log(Ni/H)$_\star$	λY	log(Y/H)$_\star$				
5080.528	6.028						
5084.089	6.040						

HD26911

λC	log(C/H)$_\star$	λO	log(O/H)$_\star$	λNa	log(Na/H)$_\star$	λMg	log(Mg/H)$_\star$
5052.167	8.340	6155-8	8.950	6154.226	6.420	5528.405	7.527
				6160.747	6.245		
λSi	log(Si/H)$_\star$	λCa	log(Ca/H)$_\star$	λSc	log(Sc/H)$_\star$	λFe	log(Fe/H)$_\star$
5055.984	7.867	5019.971	6.189	5031.021	3.011	5068.766	7.860
				5526.790	3.151	5072.076	7.408
						5074.748	7.549
						5078.972	7.501
						5506.779	7.580
λNi	log(Ni/H)$_\star$	λY	log(Y/H)$_\star$				
5080.528	6.350	5087.416	2.082				
5084.089	6.270						
5096.854	6.340						
5099.927	6.440						
6163.418	6.590						
6170.567	6.240						
6175.360	6.580						

HD27383

λC	log(C/H)$_\star$	λO	log(O/H)$_\star$	λNa	log(Na/H)$_\star$	λMg	log(Mg/H)$_\star$
		6155-8	8.447	6154.226	6.250	5528.405	7.470
				6160.747	6.301		
λSi	log(Si/H)$_\star$	λCa	log(Ca/H)$_\star$	λSc	log(Sc/H)$_\star$	λFe	log(Fe/H)$_\star$
				5526.790	2.840	5068.766	7.380
						5072.076	7.415
						5074.748	7.537
						5078.972	7.465
						5506.779	7.606
						6136.615	7.850
λNi	log(Ni/H)$_\star$	λY	log(Y/H)$_\star$				
5080.528	6.260						
5084.089	6.600						
5096.854	6.350						

HD27459

λC	log(C/H)$_\star$	λO	log(O/H)$_\star$	λNa	log(Na/H)$_\star$	λMg	log(Mg/H)$_\star$
		6155-8	8.750	6154.226	6.830	5528.405	7.330
				6160.747	6.700		

Table 8. continued.

λSi	log(Si/H)$_\star$	λCa	log(Ca/H)$_\star$	λSc	log(Sc/H)$_\star$	λFe	log(Fe/H)$_\star$
5055.984	7.637			5526.790	3.250	5068.766	7.425
						5072.076	7.740
						5074.748	7.430
						5078.972	7.420
						5506.779	7.510
						6136.615	7.550
						6147.835	7.520
λNi	log(Ni/H)$_\star$	λY	log(Y/H)$_\star$				
5080.528	6.305	5087.416	2.360				
5084.089	6.250						
5096.854	6.090						
5099.927	6.430						
6163.418	6.090						
6170.567	6.420						

HD27524

λC	log(C/H)$_\star$	λO	log(O/H)$_\star$	λNa	log(Na/H)$_\star$	λMg	log(Mg/H)$_\star$
		6155-8	9.030	6154.226	6.740	5528.405	7.460
				6160.747	6.150		
λSi	log(Si/H)$_\star$	λCa	log(Ca/H)$_\star$	λSc	log(Sc/H)$_\star$	λFe	log(Fe/H)$_\star$
				5526.790	3.160	5068.766	7.448
						5072.076	7.512
						5074.748	7.760
						5078.972	7.280
						5506.779	7.570
λNi	log(Ni/H)$_\star$	λY	log(Y/H)$_\star$				
5080.528	6.420						
5084.089	6.240						

HD27534

λC	log(C/H)$_\star$	λO	log(O/H)$_\star$	λNa	log(Na/H)$_\star$	λMg	log(Mg/H)$_\star$
		6155-8	9.070	6154.226	6.320	5528.405	7.670
				6160.747	6.270		
λSi	log(Si/H)$_\star$	λCa	log(Ca/H)$_\star$	λSc	log(Sc/H)$_\star$	λFe	log(Fe/H)$_\star$
				5526.790	3.280	5068.766	7.340
						5072.076	7.400
						5074.748	7.607
						5078.972	7.565
						5506.779	7.530
						6136.615	7.525
λNi	log(Ni/H)$_\star$	λY	log(Y/H)$_\star$				
5080.528	5.960						
5084.089	6.539						

HD27561

λC	log(C/H)$_\star$	λO	log(O/H)$_\star$	λNa	log(Na/H)$_\star$	λMg	log(Mg/H)$_\star$
		6155-8	8.750	6154.226	6.340	5528.405	7.506
				6160.747	6.240		
λSi	log(Si/H)$_\star$	λCa	log(Ca/H)$_\star$	λSc	log(Sc/H)$_\star$	λFe	log(Fe/H)$_\star$
				5526.790	3.030	5068.766	7.410
						5072.076	7.520
						5074.748	7.530
						5078.972	7.570

Table 8. continued.

λNi	log(Ni/H)$_\star$	λY	log(Y/H)$_\star$				
5080.528	6.110						
5084.089	6.450						
5096.854	6.237						

HD27848

λC	log(C/H)$_\star$	λO	log(O/H)$_\star$	λNa	log(Na/H)$_\star$	λMg	log(Mg/H)$_\star$
		6155-8	8.730	6154.226	6.245	5528.405	7.604
				6160.747	6.285		
λSi	log(Si/H)$_\star$	λCa	log(Ca/H)$_\star$	λSc	log(Sc/H)$_\star$	λFe	log(Fe/H)$_\star$
				5526.790	3.092	5068.766	7.470
						5072.076	7.430
						5074.748	7.660
						5078.972	7.609
λNi	log(Ni/H)$_\star$	λY	log(Y/H)$_\star$				
5080.528	6.310						
5084.089	6.390						

HD27991

λC	log(C/H)$_\star$	λO	log(O/H)$_\star$	λNa	log(Na/H)$_\star$	λMg	log(Mg/H)$_\star$
		6155-8	8.388	6154.226	6.400	5528.405	7.453
				6160.747	6.370		
λSi	log(Si/H)$_\star$	λCa	log(Ca/H)$_\star$	λSc	log(Sc/H)$_\star$	λFe	log(Fe/H)$_\star$
				5526.790	3.170	5068.766	7.463
						5072.076	7.460
						5074.748	7.510
						5078.972	7.690
λNi	log(Ni/H)$_\star$	λY	log(Y/H)$_\star$				
5080.528	6.260						
5084.089	6.170						

HD28363

λC	log(C/H)$_\star$	λO	log(O/H)$_\star$	λNa	log(Na/H)$_\star$	λMg	log(Mg/H)$_\star$
		6155-8	8.450	6154.226	6.439		
				6160.747	6.430		
λSi	log(Si/H)$_\star$	λCa	log(Ca/H)$_\star$	λSc	log(Sc/H)$_\star$	λFe	log(Fe/H)$_\star$
						5068.766	7.420
						5072.076	7.360
						5074.748	7.529
						5078.972	7.570
						5506.779	7.470
						6136.615	7.510
λNi	log(Ni/H)$_\star$	λY	log(Y/H)$_\star$				
5080.528	6.027						
5084.089	6.350						

HD28406

λC	log(C/H)$_\star$	λO	log(O/H)$_\star$	λNa	log(Na/H)$_\star$	λMg	log(Mg/H)$_\star$
5052.167	8.310	6155-8	8.570	6154.226	6.330	5528.405	7.527
				6160.747	6.230		

Table 8. continued.

λSi	log(Si/H)$_\star$	λCa	log(Ca/H)$_\star$	λSc	log(Sc/H)$_\star$	λFe	log(Fe/H)$_\star$
5055.984	7.900	5019.971	6.590	5031.021	2.970	5068.766	7.499
		5021.138	6.257	5526.790	3.062	5072.076	7.800
						5074.748	7.390
						5078.972	7.410
						5506.779	7.580
						6136.615	7.700
						6147.835	7.499
						6163.544	7.509
λNi	log(Ni/H)$_\star$	λY	log(Y/H)$_\star$				
5080.528	6.440	5087.416	2.088				
5084.089	6.170						
5096.854	6.420						
5099.927	6.135						
6163.418	6.297						

HD28556

λC	log(C/H)$_\star$	λO	log(O/H)$_\star$	λNa	log(Na/H)$_\star$	λMg	log(Mg/H)$_\star$
		6155-8	8.710			5528.405	7.620
λSi	log(Si/H)$_\star$	λCa	log(Ca/H)$_\star$	λSc	log(Sc/H)$_\star$	λFe	log(Fe/H)$_\star$
				5526.790	3.200	5068.766	7.390
						5072.076	7.400
						5074.748	7.690
						5078.972	7.618
						5506.779	7.502
λNi	log(Ni/H)$_\star$	λY	log(Y/H)$_\star$				
5080.528	6.174						
5084.089	6.380						

HD28568

λC	log(C/H)$_\star$	λO	log(O/H)$_\star$	λNa	log(Na/H)$_\star$	λMg	log(Mg/H)$_\star$
		6155-8	8.970	6154.226	6.800	5528.405	7.583
				6160.747	6.317		
λSi	log(Si/H)$_\star$	λCa	log(Ca/H)$_\star$	λSc	log(Sc/H)$_\star$	λFe	log(Fe/H)$_\star$
				5526.790	3.145	5068.766	7.390
						5072.076	7.449
						5074.748	7.545
						5078.972	7.350
						5506.779	7.490
						6136.615	7.570
λNi	log(Ni/H)$_\star$	λY	log(Y/H)$_\star$				
5080.528	6.490						
5084.089	5.940						
5096.854	6.298						

HD28677

λC	log(C/H)$_\star$	λO	log(O/H)$_\star$	λNa	log(Na/H)$_\star$	λMg	log(Mg/H)$_\star$
		6155-8	8.797			5528.405	7.880

Table 8. continued.

λSi	log(Si/H)$_\star$	λCa	log(Ca/H)$_\star$	λSc	log(Sc/H)$_\star$	λFe	log(Fe/H)$_\star$
				5526.790	3.660	5068.766	7.394
						5072.076	7.350
						5074.748	7.659
						5078.972	7.641
λNi	log(Ni/H)$_\star$	λY	log(Y/H)$_\star$				
5080.528	6.203						
5084.089	6.320						

HD28736

λC	log(C/H)$_\star$	λO	log(O/H)$_\star$	λNa	log(Na/H)$_\star$	λMg	log(Mg/H)$_\star$
		6155-8	9.070	6160.747	6.230	5528.405	7.630
λSi	log(Si/H)$_\star$	λCa	log(Ca/H)$_\star$	λSc	log(Sc/H)$_\star$	λFe	log(Fe/H)$_\star$
				5031.021	3.200	5068.766	7.280
						5072.076	7.435
						5074.748	7.560
						5078.972	7.535
						5506.779	7.536
λNi	log(Ni/H)$_\star$	λY	log(Y/H)$_\star$				
5080.528	6.260						
5084.089	6.330						

HD28911

λC	log(C/H)$_\star$	λO	log(O/H)$_\star$	λNa	log(Na/H)$_\star$	λMg	log(Mg/H)$_\star$
		6155-8	9.050	6154.226	6.750	5528.405	7.583
				6160.747	6.255		
λSi	log(Si/H)$_\star$	λCa	log(Ca/H)$_\star$	λSc	log(Sc/H)$_\star$	λFe	log(Fe/H)$_\star$
				5526.790	3.160	5068.766	7.436
						5072.076	7.398
						5074.748	7.570
						5078.972	7.700
						5506.779	7.460
						6136.615	7.456
λNi	log(Ni/H)$_\star$	λY	log(Y/H)$_\star$				
5080.528	6.219						
5084.089	6.340						
5096.854	6.330						

HD29169

λC	log(C/H)$_\star$	λO	log(O/H)$_\star$	λNa	log(Na/H)$_\star$	λMg	log(Mg/H)$_\star$
		6155-8	8.968	6154.226	6.700	5528.405	7.609
				6160.747	6.800		
λSi	log(Si/H)$_\star$	λCa	log(Ca/H)$_\star$	λSc	log(Sc/H)$_\star$	λFe	log(Fe/H)$_\star$
				5526.790	3.290	5068.766	7.328
						5072.076	7.503
						5074.748	7.620
						5078.972	7.600
						5506.779	7.350
λNi	log(Ni/H)$_\star$	λY	log(Y/H)$_\star$				
5080.528	6.120						
5084.089	6.260						

Table 8. continued.

HD29225

λC	log(C/H)$_\star$	λO	log(O/H)$_\star$	λNa	log(Na/H)$_\star$	λMg	log(Mg/H)$_\star$
5052.167	8.290	6155-8	8.985	6154.226	6.700		
				6160.747	6.216		
λSi	log(Si/H)$_\star$	λCa	log(Ca/H)$_\star$	λSc	log(Sc/H)$_\star$	λFe	log(Fe/H)$_\star$
5055.984	8.010	5019.971	6.313	5526.790	2.920	5068.766	7.462
						5072.076	7.610
						5074.748	7.520
						5078.972	7.630
						5506.779	7.600
λNi	log(Ni/H)$_\star$	λY	log(Y/H)$_\star$				
5080.528	6.460	5087.416	2.110				
5084.089	6.500						
5096.854	6.310						
5099.927	6.440						
6163.418	6.480						

HD30034

λC	log(C/H)$_\star$	λO	log(O/H)$_\star$	λNa	log(Na/H)$_\star$	λMg	log(Mg/H)$_\star$
		6155-8	8.640	6154.226	6.780	5528.405	7.860
				6160.747	6.800		
λSi	log(Si/H)$_\star$	λCa	log(Ca/H)$_\star$	λSc	log(Sc/H)$_\star$	λFe	log(Fe/H)$_\star$
				5526.790	3.541	5068.766	7.380
						5072.076	7.486
						5074.748	7.800
						5078.972	7.600
						5506.779	7.420
λNi	log(Ni/H)$_\star$	λY	log(Y/H)$_\star$				
6154.226	6.780						
6160.747	6.800						

HD30810

λC	log(C/H)$_\star$	λO	log(O/H)$_\star$	λNa	log(Na/H)$_\star$	λMg	log(Mg/H)$_\star$
		6155-8	8.730	6154.226	6.320		
				6160.747	6.340		
λSi	log(Si/H)$_\star$	λCa	log(Ca/H)$_\star$	λSc	log(Sc/H)$_\star$	λFe	log(Fe/H)$_\star$
						5068.766	7.320
						5072.076	7.490
						5074.748	7.520
						5078.972	7.445
λNi	log(Ni/H)$_\star$	λY	log(Y/H)$_\star$				
5080.528	6.164						
5084.089	6.260						

HD30869

λC	log(C/H)$_\star$	λO	log(O/H)$_\star$	λNa	log(Na/H)$_\star$	λMg	log(Mg/H)$_\star$
		6155-8	8.790	6154.226	6.380		
				6160.747	6.190		
λSi	log(Si/H)$_\star$	λCa	log(Ca/H)$_\star$	λSc	log(Sc/H)$_\star$	λFe	log(Fe/H)$_\star$
						5068.766	7.400
						5072.076	7.360
						5074.748	7.600
						5078.972	7.410

Table 8. continued.

λNi	log(Ni/H)$_\star$	λY	log(Y/H)$_\star$				
5080.528	6.040						
5084.089	6.250						

HD31236

λC	log(C/H)$_\star$	λO	log(O/H)$_\star$	λNa	log(Na/H)$_\star$	λMg	log(Mg/H)$_\star$
		6155-8	8.752	6154.226	6.380	5528.405	7.690
				6160.747	6.080		
λSi	log(Si/H)$_\star$	λCa	log(Ca/H)$_\star$	λSc	log(Sc/H)$_\star$	λFe	log(Fe/H)$_\star$
				5526.790	3.300	5068.766	7.132
						5072.076	7.505
						5074.748	7.660
						5078.972	7.437
λNi	log(Ni/H)$_\star$	λY	log(Y/H)$_\star$				
5080.528	6.321						

HD31845

λC	log(C/H)$_\star$	λO	log(O/H)$_\star$	λNa	log(Na/H)$_\star$	λMg	log(Mg/H)$_\star$
		6155-8	8.550	6154.226	6.206	5528.405	7.547
				6160.747	6.250		
λSi	log(Si/H)$_\star$	λCa	log(Ca/H)$_\star$	λSc	log(Sc/H)$_\star$	λFe	log(Fe/H)$_\star$
				5526.790	2.910	5068.766	7.526
						5072.076	7.490
						5074.748	7.540
						5078.972	7.640
						5506.779	7.690
						6136.615	7.640
λNi	log(Ni/H)$_\star$	λY	log(Y/H)$_\star$				
5080.528	6.480						
5084.089	6.320						

HD18404

λC	log(C/H)$_\star$	λO	log(O/H)$_\star$	λNa	log(Na/H)$_\star$	λMg	log(Mg/H)$_\star$
5052.167	8.280	6155-8	8.379	6154.226	6.098	5528.405	7.499
				6160.747	6.330		
λSi	log(Si/H)$_\star$	λCa	log(Ca/H)$_\star$	λSc	log(Sc/H)$_\star$	λFe	log(Fe/H)$_\star$
5055.984	7.487	5019.971	6.840	5031.021	2.860	5068.766	7.690
				5526.790	3.059	5072.076	7.740
						5074.748	7.706
						5078.972	7.585
						5506.779	7.496
						6136.615	7.444
						6147.835	7.490
						6163.544	7.679
						6173.336	7.550
						6187.990	7.703

Table 8. continued.

λNi	log(Ni/H)$_\star$	λY	log(Y/H)$_\star$
5080.528	6.480	5087.416	2.108
5084.089	6.220		
5096.854	5.931		
5099.927	6.270		
6163.418	6.280		
6170.567	6.453		
6175.360	6.295		

Procyon

λC	log(C/H)$_\star$	λO	log(O/H)$_\star$	λNa	log(Na/H)$_\star$	λMg	log(Mg/H)$_\star$
4932.049	8.320	6155.961	8.800	4668.559	6.440	4390.510	7.479
5052.167	8.530	6158.149	8.600	4982.813	6.080	4427.994	7.545
5380.337	8.440					4481.0	7.660
λSi	log(Si/H)$_\star$	λCa	log(Ca/H)$_\star$	λSc	log(Sc/H)$_\star$	λTi	log(Ti/H)$_\star$
5055.984	7.600	4472.050	6.300	4314.083	3.290	4163.644	5.001
5978.930	7.550	5001.479	6.320	4324.996	3.150	4287.873	5.100
6347.110	7.680	5021.138	6.100	5031.021	3.250	4300.042	5.004
						4386.844	5.004
						4394.059	5.200
						4395.051	5.020
						4399.772	5.250
						4443.801	5.100
λCr	log(Cr/H)$_\star$	λMn	log(Mn/H)$_\star$	λFe	log(Fe/H)$_\star$	λNi	log(Ni/H)$_\star$
4592.049	5.500	4033.062	5.450	4273.326	7.370	4470.472	5.720
4616.629	5.492	4034.483	5.440	4416.830	7.460	4604.982	6.200
4634.070	5.600	4055.544	5.510	4491.405	7.480	5080.528	6.180
4812.337	5.690	4083.628	5.400	4508.288	7.500	5099.927	6.110
5237.329	5.500			4515.339	7.500	5476.904	6.240
5308.440	5.570			4520.224	7.520		
5313.590	5.500			4522.634	7.440		
				4541.524	7.480		
				4555.890	7.500		
				4582.835	7.650		
λSr	log(Sr/H)$_\star$	λY	log(Y/H)$_\star$	λZr	log(Zr/H)$_\star$		
4077.709	3.120	4883.684	2.420	4149.217	2.560		
4215.520	3.240	4900.120	2.100	4156.240	2.840		
		5087.416	2.380	4161.210	2.800		
		5200.406	2.300	4208.980	2.600		
				4496.980	2.750		

Annexe B

Les effets de la perte de masse sur l'évolution des abondances chimiques dans les étoiles Fm

Contrib. Astron. Obs. Skalnaté Pleso **35**, 1 – 6, (2005)

The Effects of Mass Loss on the Evolution of Chemical Abundances in Fm Stars

M. Vick[1,2] **and G. Michaud**[1]

[1] *Département de physique – Université de Montréal, Montréal, Québec, Canada, H3C 3J7*

[2] *Université Montpellier II, GRAAL-UMR5024/IPM (CNRS), Place Eugène-Bataillon, 34095 Montpellier, France*

Received: December 1, 2007; Accepted: , 2007

Abstract. Self-consistent stellar models including all effects of atomic diffusion and radiative accelerations as well as mass loss are evolved from the pre main sequence for stars of 1.35-1.5 $M_\odot$ at solar metallicity (Z=0.02). A mass loss rate similar to the solar mass loss rate is sufficient to reproduce observations of the star τUMa. We discuss the effect of mass loss on the iron convection zone that naturally appears beneath the main hydrogen convection zone of these stars. We also find that the effects of mass loss can be distinguished from those caused by turbulence, but are nevertheless able to explain the particularities of the AmFm phenomenon.

Key words: Stars: abundances – Stars: evolution – Stars: atomic diffusion – Stars: mass loss

1. Introduction

Since 1970 it is generally agreed that atomic diffusion driven by radiative accelerations plays a role in creating the anomalous surface abundances of F, A and B stars (Michaud 1970). However, some 40 years later, many questions remain as to the exact behavior of many physical processes within the stable envelopes of these stars. In fact, for Fm stars, two competing scenarios which have each had their share of success are presently being confronted to observations. The "classical" scenario Watson (1971) suggests that separation occurs below the H-He convection zone. In this framework, models which only consider atomic diffusion without extra mixing generate predicted anomalies that are 3-5 times larger than the ones observed (Turcotte et al. 1998), thus implying that there is at least one competing process that slows the effects of separation. This lead to more recent models (Richer et al. 2000, Richard et al. 2001) in which turbulence enforces mixing down to about 200 000 K. In these models, it is implied that separation occurs deeper in the star.

Like turbulence or rotation, mass loss is another macroscopic process that can reduce inhomogeneities on the surface of these stars. However, until now, only static stellar models have included the effects of mass loss (Michaud et al. 1983, Alecian 1996 for Ca and LeBlanc et Alecian 2007 for Sc) with the latter paper showing that the actual depth at which separation occurs is still uncertain.

With self-consistent models of Fm stars ($6500\,\mathrm{K} \leq T_{\mathrm{eff}} \leq 7000\,\mathrm{K}$) we will show that mass loss can reduce predicted abundances to the observed levels. The first aim is to see to what extent observations can constrain the importance of mass loss and if its effects can be deciphered from the ones encountered with turbulence. We will also discuss the implications of our models on the depth of chemical separation.

2. Evolutionary Models

The following is a continuation of the Montreal stellar model development project (Richard et al., 2001 and references therein). The evolutionary calculations take into detailed account the time-dependent variations of 28 chemical species and include all effects of atomic diffusion and radiative accelerations. These are the first fully self-consistent stellar models which include mass loss. Models were calculated for $1.35\,\mathrm{M}_{\odot}$, $1.40\,\mathrm{M}_{\odot}$,$1.45\,\mathrm{M}_{\odot}$ and $1.50\,\mathrm{M}_{\odot}$. All models have evolved from the homogeneous pre-main sequence phase with a solar metallicity (Z=0.02). The mass loss rates considered varied from $1\times10^{-14}\mathrm{M}_{\odot}\mathrm{yr}^{-1}$ to $3\times10^{-13}\mathrm{M}_{\odot}\mathrm{yr}^{-1}$. The mass loss is considered spherical, chemically homogeneous and weak enough not to disturb burning in the core or stellar structure. The net effect is the appearance of an outward flowing wind which is represented as an advection term in the transport equation. Due to numerical instabilities resulting from very large advection velocities in the surface convection zone, some adjustments must be made in order to avoid convergence problems. The method is well described in Charbonneau (1993). The transport equation then becomes:

$$\begin{aligned}\rho\frac{\partial c}{\partial t} &= -\nabla\cdot[-\rho D\nabla\ln c+\rho(\mathbf{U}+\mathbf{U}_w)c]\\ &\quad +\rho(S_{nuc}+S_w)c,\end{aligned} \tag{1}$$

with a Neumann condition (no flux) imposed at the surface and with $\mathbf{U}_w$ and S_w defined as:

$$\mathbf{U}_w=\begin{cases}w_w\hat{\mathbf{e}}_{\mathbf{r}}\text{ under the SCZ},\\ 0\text{ in the SCZ};\end{cases} \tag{2}$$

$$S_w=\begin{cases}0\text{ under the SCZ},\\ \frac{\dot{M}}{M_{ZC}}\text{ in the SCZ}.\end{cases} \tag{3}$$

Here, c is the time and depth dependent concentration, ρ is density, D is the total diffusion coefficient, U is the total velocity field, U_w is wind velocity, M_{CZ} is the mass of the SCZ, $\dot{M}$ is the mass loss rate, S_{nuc} is a source/destruction term linked to nuclear reactions and S_w is a destruction term linked to mass loss.

3. The Effects of Mass Loss on Surface Abundances

One of the effects of mass loss is to drag elements which tend to sink. Because the diffusion velocity must be greater than the wind velocity for separation to occur, the greater

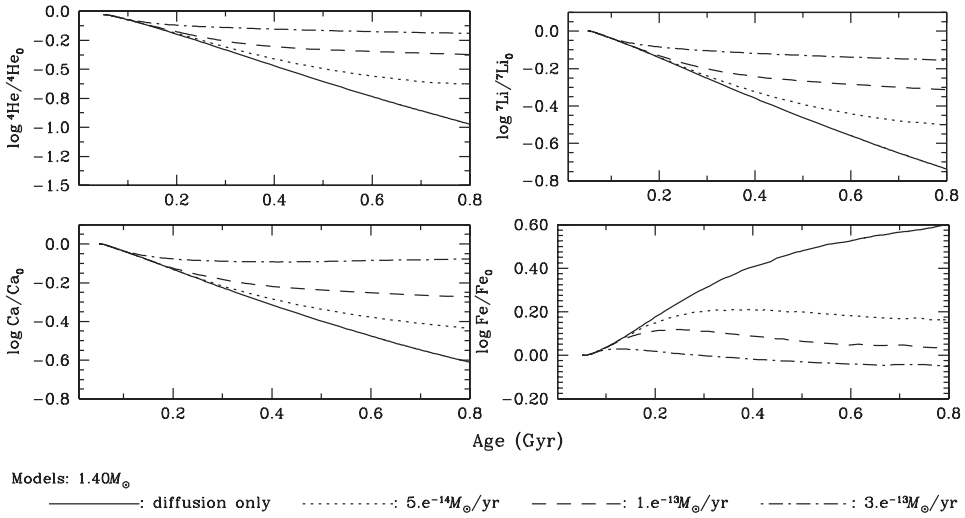

Figure 1. Evolution of surface abundances (^{4}He, Li, Ca and Fe) for 1.4 $M_\odot$ models with different mass loss rates as well as with atomic diffusion only. It is clear that a slight change in the mass loss rate can have an important effect on abundance anomalies.

the mass loss the deeper we have to look to see any effects of separation. On the other hand, elements which are naturally supported by the radiation field will be pushed into the surface convection zone and evacuated through the stellar surface. As seen in Figure 1, models in which only atomic diffusion is included lead to larger surface abundances anomalies than in the presence of mass loss. For instance, after 0.8 Gyr of evolution predicted anomalies (in terms of the original abundance) for the plotted elements are respectively, without mass loss and with a mass loss rate of 5×10^{-14}M$_\odot$yr^{-1}, $\times$0.2 and $\times$0.3 for Li, $\times$0.25 and $\times$0.3 for Ca, $\times$4 and $\times$1.5 for Fe. We also see that for the given stellar mass, a mass loss rate of 5×10^{-14}M$_\odot$yr^{-1} is sufficient to reduce anomalies by a factor of 1.5 to 3, and a mass loss rate of 3×10^{-13}M$_\odot$yr^{-1} practically flattens the surface abundances.

3.1. The 1.5 M$_\odot$ models

The 1.5 M$_\odot$ model is particularly interesting because it corresponds to the minimum mass at which iron accumulation due to the spatial distribution of its radiative acceleration causes the appearance of a convection zone (Figure 3, left panel). As mentioned above, recent evolutionary models (Richer et al. 2000, Richard et al. 2001 and Michaud et al. 2005) have successfully reproduced observations by considering that turbulence homogenizes abundances from the surface down to a temperature that corresponds to the bottom of this iron convection zone ($\log T = 5.3$). Therefore, in this context, sepa-

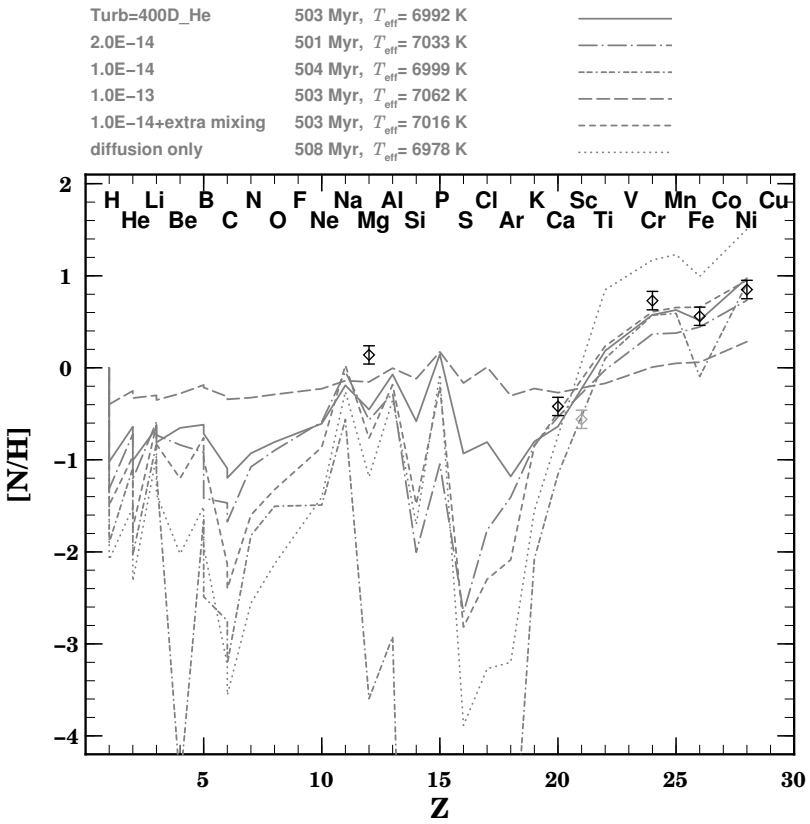

Figure 2. Observed surface abundances of τUMa (diamonds) compared to $1.5\,M_\odot$ models at 500 Myr. Scandium is not include in our calculations. Models with mass loss are designated by their respective rate (e.g 1.0E-14$\rightarrow 1\times10^{-14}M_\odot yr^{-1}$).

ration must take place deeper than the classical model in which separation occurs above this convection zone. Both of these scenarios have been tested with mass loss.

In Figure 2 we have compared 6 different models of $1.5\,M_\odot$ to the observed abundances of the star τUMa (Hui-Bon-Hoa 2000) from the Ursa Major moving group which has an age of approximately 500 Myr (Monier 2005) and $T_{\rm eff}\sim 7000$ K (van't Veer-Menneret et Mégessier 1996). There are 4 models in which separation is allowed immediately below the H-He convection zone (3 mass loss models, and one diffusion only model), as well as 2 models in which mixing was enforced to $\log T = 5.3$ or deeper (which is the case for the turbulence model).

It appears from the plot that the two models which best fit the data are the turbulence model as well as the model with a mass loss rate of $1\times10^{-14}M_\odot yr^{-1}$ with enforced mixing down to the bottom of the Fe convection zone. However the model with a mass loss rate of $2\times10^{-14}M_\odot yr^{-1}$ and without any turbulent mixing does very nearly as well. We also see that the model with the mass loss rate $1\times10^{-14}M_\odot yr^{-1}$ without

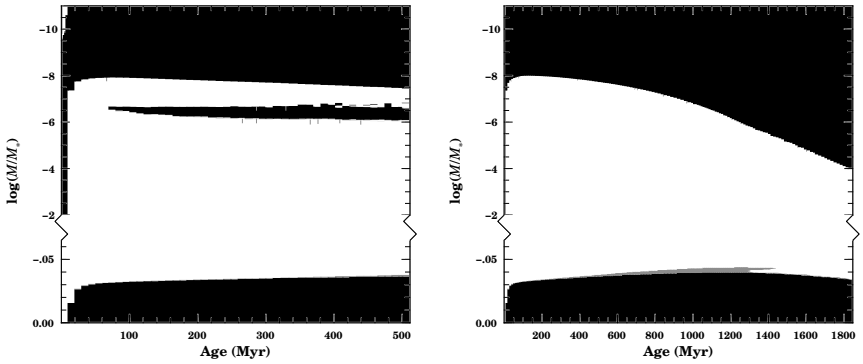

Figure 3. Evolution of convection (black) and semiconvection (gray) zones in two $1.5\,M_\odot$ models ($1\times10^{-14}M_\odot yr^{-1}$ [*right*]; $2\times10^{-14}M_\odot yr^{-1}$ [left]). In the left panel, we see that an Fe convection zone develops under the main H-He convection zone. In the right panel, this convection zone does not appear because the stronger wind flattens the opacity spike due to Fe accumulation which is responsible for the Fe convection zone.

homogenized abundances between convection zones can reproduce quite effectively 3 of the 5 observed abundances. It would therefore be premature to rule out the validity of the classical scenario in the context of mass loss. As we can see in the same plot, observations between Al and Ar would help in identifying if the zone between the H-He and Fe convections zones is mixed. Another important result is that turbulence and mass loss models have noticeable element to element differences which is necessary if we wish to eventually constrain the importance of both these processes. Finally, the models with the mass loss rate of $10^{-13}M_\odot yr^{-1}$ flatten the abundance profiles in such a way that they can no longer reproduce observations (see also Cayrel et al. 1991).

4. Conclusions

Our results seem to suggest that the scenario in which separation is to take place at $T\sim2\times10^5$ K in Fm stars must be favored over the classical scenario. In this framework, a mass loss rate of the order of the solar mass loss rate is able to reduce predicted anomalies to the observed abundances of τUMa. However, it is too early to eliminate the possibility of separation below the H convection zone. Abundance determinations between Al and Ar could help distinguish between these two regimes. It is also shown that turbulence and mass loss affect anomalies differently, though the discrepancy is slight in the models shown. Once again, more observations are required to further constrain these two mechanisms. More massive models in the $T_{\rm eff}$ range where observations are not as scarce are also needed. They are currently being calculated. In any case, it is shown that reasonable mass loss rates can effectively reduce the anomalies predicted by atomic diffusion models to the observed levels.

Acknowledgements. This research was partially supported at the Université de Montréal by the Natural Sciences and Engineering Research Council of Canada. The computational resources were provided by the Réseau Québecois de Calcul de Haute Performance (RQCHP). M.Vick also thanks the Département de physique at l'Université de Montréal as well as the GRAAl at l'Université Montpellier II.

References

Alecian, G.: 1996, *Astron. Astrophys.* **310**, 872
Cayrel, R. and Burkhart, C. and Van't Veer C.: 1991, in *The Fm-Am Stars: Observed Anomalies*, ed.: IAU Symposium 145, G.Michaud and A.Tutukov, Bulgaria, 99
Charbonneau, P. : 1993, *Astrophys. J.* **405**, 720
Hui-Bon-Hoa, A.: 2000, *Astron. Astrophys., Suppl. Ser.* **144**, 203
LeBlanc, F. and Alecian, G.: 2007, *ArXiv e-prints* **711**,
Michaud, G.: 1970, *Astrophys. J.* **160**, 641
Michaud, G. and Tarasick, D. and Charland, Y. and Pelletier, C.: 1983, *Astrophys. J.* **269**, 239
Michaud, G. and Richer, J. and Richard, O.: 2005, *Astrophys. J.* **623**, 442
Monier, R.: 2005, *Astron. Astrophys.* **442**, 563
Richer, J. and Michaud, G. and Turcotte, S.: 2000, *Astrophys. J.* **529**, 338
Turcotte, S. and Michaud, G. and Richer, J.: , *Astrophys. J.* **504**, 559
van't Veer-Menneret, C. and Mégessier, C.: 1996, *Astron. Astrophys.* **309**, 879
Watson, W. D.: 1971, *Astron. Astrophys.* **13**, 263

Annexe C

Modèles évolutifs avec perte de masse et turbulence

Proceedings Title IAU Symposium
Proceedings IAU Symposium No. 238, 2008
A.C. Editor, B.D. Editor & C.E. Editor, eds.

DOI: 00.0000/X000000000000000X

Stellar evolution models with mass loss and turbulence

M. Vick[1,2], G. Michaud[1] and O. Richard[2]

[1]Département de Physique, Université de Montréal, Montréal, PQ, H3C 3J7

[2]GRAAL, Université Montpellier II, CNRS, Place E. Bataillon, 34095 Montpellier Cedex, France

Abstract. Although chemical separation is generally accepted as the main physical process responsible for the anomalous surface abundances of AmFm stars, its exact behavior within the interior of these stars is still uncertain. We will explore two hydrodynamical processes which could compete with atomic diffusion: mass loss and turbulence. We will also discuss the extent to which separation occurs immediately below the H convection zone as well as the extent to which separation occurs below 200,000 K. To do so, self-consistent stellar models with mass loss and turbulence where calculated using the Montreal stellar evolution code and compared to observations of A and F stars. It is shown that to the precision of observations available for F stars, a mass loss rate of $2\times10^{-14}\,M_\odot\cdot\mathrm{yr}^{-1}$ is compatible with observations and that no turbulence is then required.

Keywords. stars: evolution, stars: abundances, stars: mass loss, turbulence

1. Introduction

On the main sequence, most if not all slowly rotating and non magnetic A and early type F stars are believed to have anomalous surface abundances. These chemically peculiar stars are classified as AmFm stars (Preston 1974) and typically have observed underabundances of CNO, Sc and Ca as well as overabundances of iron peak elements and rare earths (see Cayrel, Burkhart, & Van't Veer 1991). In these stars, the surface convection zone is sufficiently shallow for the effects of a relatively slow processes such as atomic diffusion to manifest itself at the the stellar surface. More efficient processes, such as convective, rotational or turbulent mixing as well as large scale processes such as mass loss can slow the effects of atomic diffusion, thereby reducing surface abundance anomalies. In order to quantitatively reproduce observed surface abundances, models with atomic diffusion must consider one of these aforementioned inhibiting processes in order to reduce predicted anomalies which are larger (by a factor of 2-5) than those observed (Turcotte, Michaud, & Richer 1998).

In Richer, Michaud, & Turcotte (2000), diffusion models which include turbulent mixing are able to reproduce the observed surface abundance anomalies for AmFm stars of many open clusters. These same models have also successfully explained observed abundances in Pop II (Richard, Michaud et & Richer 2005, Korn et al. 2006) and horizontal branch stars (Michaud, Richer, & Richard 2007, Michaud, Richer, & Richard 2008). In the AmFm models as well as the Pop II models, mixing is enforced in such a way that chemical separation occurs deeper than 200,000 K. Around this temperature, an iron convection zone naturally appears for models of at least $1.5\,M_\odot$ (this also depends on the amount of mixing which tends to suppress it). In contrast, another explanation for

AmFm stars suggests that chemical separation is to occur below the surface convection zone (SCZ). Both these scenarios will be discussed.

The effects of mass loss on the surface abundances of these stars have also been previously investigated by Michaud et al. (1983), Michaud & Charland (1986) , Alecian (1996) and Leblanc & Alecian (2008). However, a further investigation is warranted since these studies analysed static stellar models which included a limited number of elements.

In the following we will look at the effects of mass loss and turbulence both at the surface and within the stable radiative zone of these stars. We will start by detailing our models as well as our treatment of mass loss. The following sections will look at the effects of mass loss and turbulence on abundances.

2. Stellar Evolution Models

These 1D stellar evolution models were calculated as described in Turcotte et al. (1998b) (see also Richard, Michaud, & Richer 2001 and references therein). Models were evolved from the homogeneous pre-main sequence up to the bottom of the sub giant branch with the abundance mix listed in Table 1 of Turcotte et al. (1998b). Radiative accelerations are calculated at each time step and at each mesh point for 28 chemical species. The atomic data is taken from the OPAL database (Iglesias & Rogers 1996). The Rosseland mean opacity is also continuously updated which means that the treatment of chemical transport is completely self-consistent. The corrections for redistribution of momentum are from Gonzalez et al. (1995) and LeBlanc, Michaud & Richer (2000). The atomic diffusion coefficients are taken from Paquette et al. (1986). Semi-convection is included as described in Richard et al. (2001), following Kato (1966), Langer, El Eid & Frick (1985) and Maeder (1997). The Krishna-Swamy $T-\tau$ relation (Krishna-Swamy 1966) is used as the boundary condition in the atmosphere. The corresponding value of the mixing length parameter, which is calibrated to fit the radius and luminosity of the Sun is $\alpha = 2.096$ (model H of Turcotte et al. (1998b)) with the initial mass fraction of He set to $Y_0 = 0.27769$. Models were calculated from $1.30\,M_\odot$ to $1.55\,M_\odot$, with mass loss rates ranging from 10^{-14} to 10^{-12}.

3. Treatment of Mass Loss

The mass loss is assumed spherical and chemically homogeneous. In the presence of mass loss, mass conservation results in the appearance of an outward flowing wind expressed as:

$$v_w = -\frac{\dot{M}}{4\pi r^2 \rho} \tag{3.1}$$

where $\dot{M} < 0$ since we are dealing with mass loss. In order to avoid numerical instabilities, the wind velocity is included as discussed in Charbonneau (1993). The resulting transport equation is:

$$\begin{aligned}\rho\frac{\partial c}{\partial t} = &-\nabla\cdot[-\rho D\nabla\ln c + \rho(\mathbf{U}+\mathbf{U}_w)c] \\ &+\rho(S_{nuc}+S_w)c,\end{aligned} \tag{3.2}$$

with a Neumann condition imposed at the surface and with $\mathbf{U}_w$ and S_w defined as:

$$\mathbf{U}_w = \begin{cases} v_w\hat{\mathbf{e}}_\mathbf{r} \text{ under the SCZ,} \\ 0 \text{ in the SCZ;} \end{cases} \tag{3.3}$$

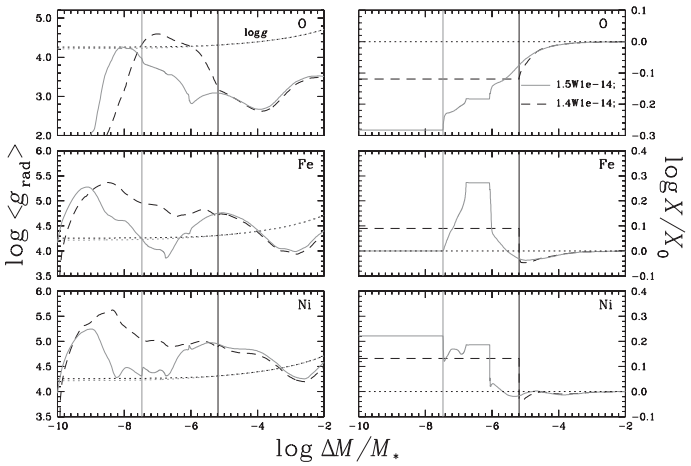

Figure 1. Radiative accelerations of O, Fe and Ni and gravity for two models of different masses at 500 Myr. The number on the right of the left W in the model name indicates the mass and the num,ber on the right is the mass loss rate in $M_\odot \cdot \mathrm{yr}^{-1}$.The vertical lines show the position of the hydrogen-helium surface convection zone for the respective models.

$$S_w = \begin{cases} 0 \text{ under the SCZ,} \\ \frac{\dot{M}}{M_{ZC}} \text{ in the SCZ.} \end{cases} \tag{3.4}$$

Here, c is the time and depth dependent composition, ρ density, D the total diffusion coefficient, $\mathbf{U}$ the total velocity field, $\mathbf{U}_w$ wind velocity, M_{CZ} the mass of the SCZ, $\dot{M}$ the mass loss rate, S_{nuc} a source/destruction term linked to nuclear reactions and S_w a destruction term linked to mass loss. The mass of the star is also continuously updated so that all quantities which depend on stellar mass are correctly calculated.

4. Internal structure

The anomalous surface abundances of AmFm stars are the result of chemical transport below the surface convection zone which is modulated by the competition between gravity and radiative accelerations. In Figure 1 we see how radiative accelerations and gravity varie with the mass coordinate for three models of different masses ($1.40\,M_\odot$, $1.50\,M_\odot$) with a mass loss rate of 10^{-14}. When g is always greater than g_{rad}, the element will tend to sink toward the interior of the star, thus creating an underabundance at the surface, as is the case for oxygen. On the other hand, when an element is supported by the radiative field throughout most of the stellar interior (and more importantly below the surface convection zone), we can expect an overabundance of that element at the surface (as for Ni). In other cases, elements accumulate where $g \sim g_{\mathrm{rad}}$. The abundance at the surface will be determined by the position of this accumulation and the bottom of the surface mixing zone (which in the presence of turbulence is an extension of the SCZ), since the material at its base is the mixed to the surface. For the $1.50\,M_\odot$ model, g_{rad}(Fe) dips below gravity just under the surface convection zone which causes an accumulation of iron in that region. This accumulation triples the local metal content, which leads to an increase of opacity and the appearance of an iron convection zone (which can be seen in the abundance profiles: the plateau between $\log \Delta M/M_* = 6-7$ shows the homogenized abundances due to this convection zone).

In Figure 2, we see the effect of turbulence and mass loss on the abundances pro-

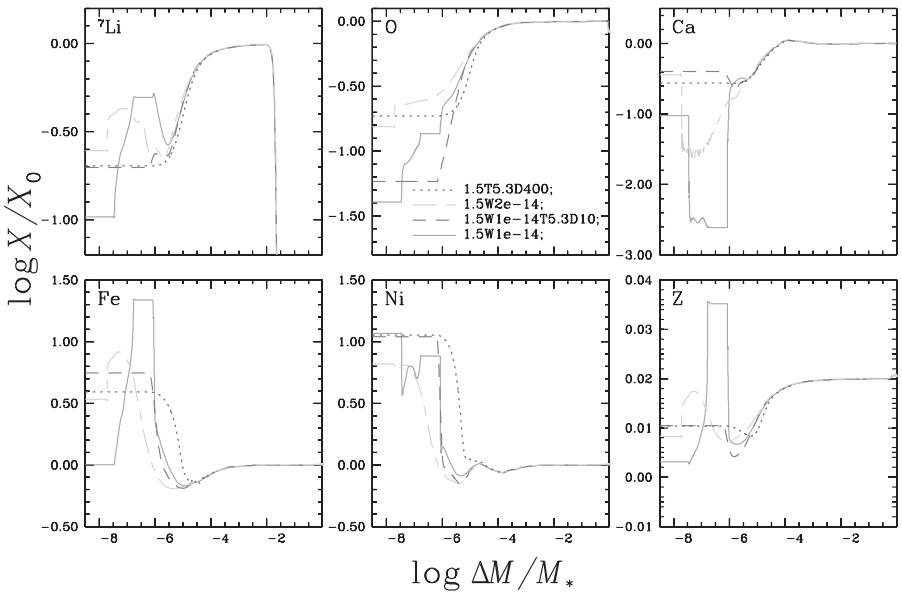

Figure 2. Abundance profiles for 4 models with turbulence and/or mass loss at 500 Myr. In the model name, T is the log of the temperature down to which abundances are completely homogenized by turbulence and D is the coefficient multiplying the turbulent diffusion coefficient (see Richer et al. 2000). The dip in lithium around $\log \Delta M/M_* = -2$ is due to nuclear burning. Some numerical noise appears in the Ca profile for the 1.5W2e14 model.

files. For all models, we see that at 500 Myr, chemical separation implies the outer $10^{-4}\,M_*$. In the models with mass loss only (1.5W1e-14 and 1.5W2e-14), separation is allowed to occur immediately below the surface convection zone. In models with turbulence (1.5W1e-14T5.3D10 and 1.5T5.3D400), abundances are mixed down to $\log T = 5.3$, which corresponds to $\log \Delta M/M_* \sim$-6. The only model which leads to an iron convection zone is the model with a mass loss rate of $10^{-14}\,M_\odot \cdot \mathrm{yr}^{-1}$ with no additional turbulence. This model does not generate an advective current which is strong enough to push the accumulation of iron into the surface convection zone. This also leads to a surface iron abundance which is close to its original value. However, if the wind is twice as strong ($2\times10^{-14}\,M_\odot \cdot \mathrm{yr}^{-1}$, the solar value) the iron spike is weakened and pushed toward the surface.

5. Surface Abundances

In Figure 3, we compare surface abundances for a $1.50\,M_\odot$ model with observed abundances of τUMa (Hui-Bon-Hoa 2000) which has an age of approximately 500 Myr (Monier 2005) and $T_{\rm eff} \sim 7000$ K (van't Veer-Menneret & Mégessier 1996). We tested 2 scenarios: chemical separation below 200,000 K (right panel) and the scenario in which separation occurs immediately below the surface convection zone. At this age, the surface convection zone is composed of both hydrogen and helium since helium has not yet settled gravitationally. We see that both turbulence and mass loss can effectively reduce the surface abundances to the observed levels. The model with the solar mass loss rate (1.5W2e14) leads to a very good agreement with the data. The model with both mass loss and turbulence (1.5W1e-14D5.3D10) leads to the best fit . The mass loss rate of $10^{-13}\,M_\odot \cdot \mathrm{yr}^{-1}$ is too strong to reproduce the observations.

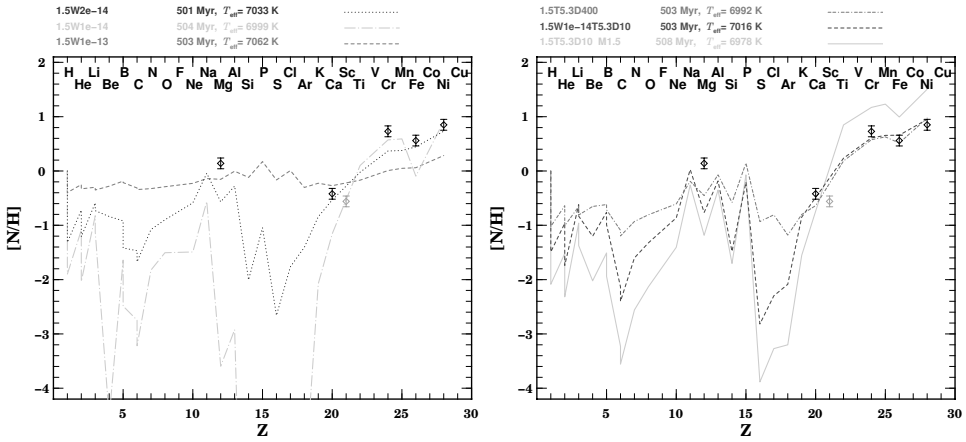

Figure 3. Observed surface abundances of τUma (diamonds) compared to 1.50 $M_{\odot}$ models. The abundance of Sc is shown, but is not calculated in our models. [left panel] Chemical separation occurs immediately below the surface convection zone. The models have mass loss only.[right panel] Chemical separation occurs below 200,000 K.

6. Conclusions

With a mass loss rate of the order of the solar mass loss rate we can successfully reproduce the observed abundance anomalies of τUMa. We also find that with sufficiently weak winds and no turbulence, an iron convection zone naturally appears in 1.50 $M_{\odot}$ models. However, for these models the surface abundance of Fe does not match the observed abundance. It is also shown that mass loss and turbulence affect abundances differently (at the surface and in the interior). It is thus possible that sufficiently precise abundance determinations could constrain the relative importance of each process. This being said, models of greater mass, where abundance determinations are more abundant, would also help in this venture. These are presently being calculated. It is still premature to favor either of the two proposed scenarios as both offer models that are able to adequately reproduce observations within the given errors.

Acknowledgements

This reasearch was partially supported at the Université de Montréal by the Natural Sciences and Engineering Researh Council of Canada. The computational resources were provided by the Réseau Québecois de Calcul de Haute Performance (RQCHP). M.Vick also thanks the Département de physique at l'Université de Montréal as well as the GRAAL at l'Université Montpellier II.

References

Alecian, G. 1996, *A&A*, 310, 872

Cayrel, R., Burkhart, C., & Van't Veer, C. 1991, in IAU Symposium 145, ed. G.Michaud & A.Tutukov

Charbonneau, P. 1993, *ApJ*, 405, 720

Gonzalez, J.-F., LeBlanc, F., Artru, M.-C., & Michaud, G. 1995, *ApJ*, 297, 223

Hui-Bon-Hoa, A. 2000, *A&AS*, 144, 203

Iglesias, C. A. & Rogers, F. 1996, *ApJ*, 464, 943

Kato, S. 1966, *PASP*, 18, 374

Korn, A. J., Grundahl, F., Richard, O., Barklem, P. S., Mashonkina, L., Collet, R., Piskunov, N., & Gustafsson, B. 2006, *Nature*, 442, 657
Krishna-Swamy, K. S. 1966, *ApJ*, 145, 176
Langer, N., El Eid, M. F., & Fricke, K. J. 1985, *A&A*, 145, 179
LeBlanc, F., Michaud, G., & Richer, J. 2000, *ApJ*, 538, 876
Leblanc, F., & Alecian, G. 2008, *A&A*, 477, 243
Maeder, A. 1997, *A&A*, 321, 134
Michaud, G., Tarasick, D., Charland, Y., & Pelletier, C. 1983, *ApJ*, 269, 239
Michaud, G. & Charland, Y. 1986, *ApJ*, 311, 326
Michaud, G., Richer, J., & Richard, O. 2007, *ApJ*, 670, 1178
Michaud, G., Richer, J., & Richard, O. 2008, *ApJ*, 675, 1223
Monier, R. 2005, *A&A*, 442, 563
Paquette, C., Pelletier, C., Fontaine, G., & Michaud, G. 1986,*ApJS*, 61, 177
Preston, G. W. 1974, *ARAA*, 12, 257
Richard, O., Michaud, G., & Richer, J. 2001, *ApJ*, 558, 377
Richard, O., Michaud, G., & Richer, J. 2005, *ApJ*, 619, 538
Richer, J., Michaud, G., Rogers, F., Turcotte, S., & Iglesias, C. A. 1998, *ApJ*, 492, 833
Richer, J., Michaud, G., & Turcotte, S. 2000, *ApJ*, 529, 338
Turcotte, S., Michaud, G., & Richer, J. 1998a, *ApJ*, 504, 559
Turcotte, S., Richer, J., Michaud, G., Iglesias, C. A., & Rogers, F. 1998b, *ApJ*, 504, 539
van't Veer-Menneret, C. & Mégessier, C. 1996, *A&A*, 309, 879

Annexe D

Diffusion atomique, perte de masse et anomalies d'abondances dans les étoiles Fm

Mem. S.A.It. Vol. 79, 762

Memorie della

Atomic diffusion, mass loss and abundance anomalies in Fm stars

M. Vick[1,2] and G. Michaud[1]

[1] Département de physique – Université de Montréal, Montréal, Qubec, Canada, H3C 3J7 [redacted]

[2] Université Montpellier II, GRAAL-UMR5024/IPM (CNRS), Place Eugène-Bataillon, 34095 Montpellier, France

Abstract. Self-consistent stellar models including all effects of atomic diffusion and radiative accelerations as well as mass loss are evolved from the pre main sequence for stars of 1.3-1.5 $M_\odot$ of solar metallicity (Z=0.02). By including homogeneous mass loss in these models we determine that mass loss rates similar to the one measured on the surface of the Sun can effectively reduce the predicted surface abundance anomalies from purely diffusive models of Fm stars. By comparing our models with the star τUMa we find that observations can be reproduced. We also find that the effects of mass loss can be distinguished from those of turbulence, but are nonetheless able to explain the particularities of the AmFm phenomenon.

Key words. Stars: abundances – Stars: evolution – Stars: atomic diffusion – Stars: mass loss

1. Introduction

This is a continuation of the Montreal stellar model development project (Richard, Michaud & Richer 2001 and references therein). Fm stars ($6500\,\mathrm{K} \leq T_{\mathrm{eff}} \leq 7000\,\mathrm{K}$) are at the lower T_{eff} limit of the Ap, Bp and Am star phenomenon for which atomic diffusion leads to surface abundance anomalies. They are Population I stars that are non-magnetic (Landstreet 1982) and slowly rotating ($v \sin i < 100\,\mathrm{kms}^{-1}$, Abt 2000). Prior studies (Turcotte, Michaud & Richer 1998a) have shown that stellar models in which only atomic diffusion is considered predict anomalies that are 3 to 5 times larger than the anomalies observed. This suggests that there is at least one competing hydrodynamical process that reduces the effects of atomic diffusion. These processes include turbulence (Richard et al. 2001, Richer, Michaud & Turcotte 2000), meridional circulation (Charbonneau & Michaud 1991) and mass loss (Michaud et al. 1983, Alecian 1996 for Ca). The aim is to see to what extent observations can constrain the importance of mass loss and if its effects can be deciphered from those encountered with turbulence.

Send offprint requests to: M. Vick

2. Evolutionary models

The evolutionary calculations take into detailed account the time-dependent variations of 28 chemical species and include all effects

of atomic diffusion and radiative accelerations (for further details on the code see Richard et al. (2001). These are the first fully self-consistent stellar models which include mass loss. Models were calculated from $1.30\,M_\odot$ to $1.50\,M_\odot$ in $0.05\,M_\odot$ increments. All models have evolved from the homogeneous pre-main sequence phase with a solar metallicity (Z=0.02). The mass loss rates considered varied from $1\times10^{-14}M_\odot yr^{-1}$ to $3\times10^{-13}M_\odot yr^{-1}$. Mass loss is assumed spherical, chemically homogeneous and weak enough not to disturb burning in the core or stellar structure. The main effect is the appearance of an outward flowing wind which is represented as an advection term in the transport equation. Due to numerical instabilities resulting from very large advection velocities in the surface convection zone, some adjustments must be made in order to avoid convergence problems. The method is well described in Charbonneau (1993). The transport equation then becomes:

$$\rho\frac{\partial c}{\partial t} = -\nabla\cdot[-\rho D\nabla\ln c+\rho(\mathbf{U}+\mathbf{U}_w)c] +\rho(S_{nuc}+S_w)c, \quad (1)$$

with a Neumann condition (no flux) imposed at the surface and with $\mathbf{U}_w$ and S_w defined as:

$$\mathbf{U}_w=\begin{cases} w_w\hat{\mathbf{e}}_\mathbf{r} \text{ under the SCZ,}\\ 0 \text{ in the SCZ;}\end{cases} \quad (2)$$

$$S_w=\begin{cases} 0 \text{ under the SCZ,}\\ \frac{\dot{M}}{M_{ZC}} \text{ in the SCZ.}\end{cases} \quad (3)$$

Here, c is the time and depth dependent concentration, ρ is density, D is the total diffusion coefficient, $\mathbf{U}$ is the total velocity field, $\mathbf{U}_w$ is the wind velocity, M_{CZ} is the mass of the surface convection zone, $\dot{M}$ is the mass loss rate, S_{nuc} is a source/destruction term linked to nuclear reactions and S_w is a destruction term which models mass loss (Charbonneau 1993).

3. Results and discussion

3.1. The $1.5\,M_\odot$ models

In Figure 1 (left panel) we have compared our models of $1.5\,M_\odot$ to the observed abundances of the star τUMa (Hui-Bon-Hoa 2000) from the Ursa Major moving group which has an age of approximately 500 Myr (Monier 2005) and $T_{\rm eff}\sim 7000$ K (Van't Veer-Menneret & Mégessier 1996). The are six models shown: a strong turbulence model (taken from Richard et al. 2001), 3 models with mass loss only, one model with mass loss and *extra mixing* immediately below the surface convection zone as well as one model with atomic diffusion only. As seen in Figure 1 (right panel), a iron convection zone naturally appears below the surface H-He convection zone for models with small mass loss ($1\times10^{-14}M_\odot yr^{-1}$).

We see that the model with a mass loss rate of $2\times10^{-14}M_\odot yr^{-1}$ (the solar mass loss rate) can reproduce quite effectively 3 of the 5 observed abundances. However, if we assume that the abundances are homogenized between the Fe and H-He convection zones (i.e. with *extra mixing*), the model with $1\times10^{-14}M_\odot yr^{-1}$ becomes the best fit, better than the model with strong turbulence. The models with stronger mass loss rates flatten the abundance profiles in such a way that they can no longer reproduce observations. Also, the internal structure of the star changes as the mass loss rate increases due to the fact that the opacity maximum due to Fe and Ni accumulation is practically eliminated by the strong advective current (Figure 1 (right panel)). Finally, it is important to note that turbulence and mass loss models have noticeable element to element differences. Moreover, the $1\times10^{-14}M_\odot yr^{-1}$ models with and without seperation show large differences between Ar and Al.

4. Conclusions

With a mass loss rate of the order of the solar mass loss rate, we can succesfully reproduce the observed abundances of τUMa. It is shown that turbulence and mass loss affect anomalies differently, though the discrepancy is slight in the models shown. Nevertheless, it is possible to constrain the relative importance of the two processes, if accurate enough observations are available. In particular, observations between Ar and Al would help in that regard as they could distinguish between models with

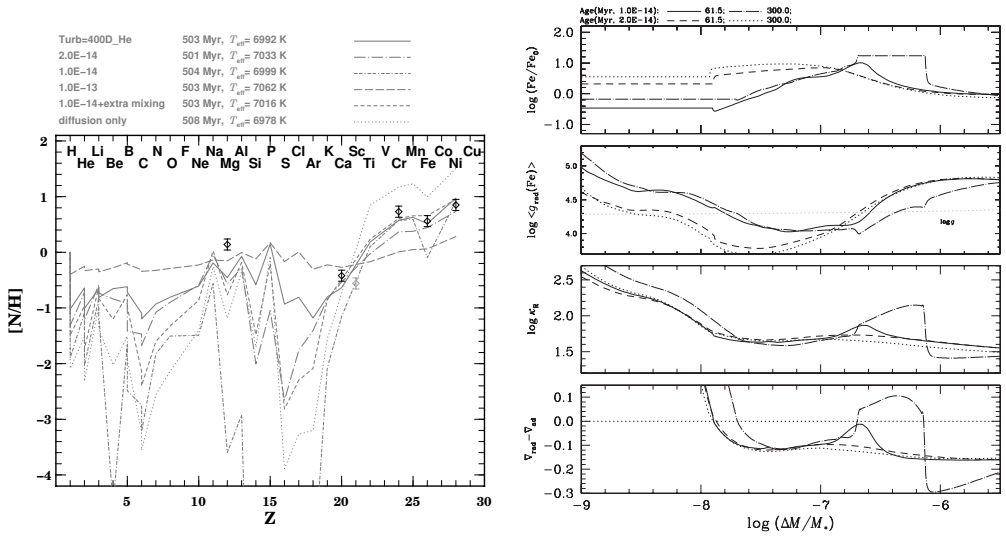

Fig. 1. [left panel] Observed surface abundances of τUMa (diamonds) compared to 1.5 $M_\odot$ models at 500 Myr. Scandium is not include in our calculations. Models with mass loss are designated by their respective rate (e.g 1.0E-14$\rightarrow 1\times10^{-14}M_\odot yr^{-1}$). [right panel] Comparison of internal abundance profiles and radiative accelerations (cm s^{-2}) of Fe, Rosseland opacity ($cm^2\,g^{-1}$) and the difference between the radiative and adiabatic temperature gradients at 61.5 Myr and 300 Myr for two 1.5 $M_\odot$ models having different mass loss rates. The accumulation of Fe caused by the space distribution of its radiative acceleration causes a convection zone only in the smaller mass loss model.

or without separation between the Fe and H-He convection zones. More massive models in the $T_{\rm eff}$ range where observations aren't as scarce are also needed. They are currently being calculated. In any case, it is shown that reasonable mass loss rates can effectively reduce the anomalies predicted by atomic diffusion models to the observed levels.

Acknowledgements. This research was partially supported at the Université de Montréal by the Natural Sciences and Engineering Research Council of Canada. The computational resources were provided by the Réseau Québecois de Calcul de Haute Performance (RQCHP). M.Vick also thanks the Département de physique at l'Université de Montréal as well as the GRAAl at l'Université Montpellier II.

References

Abt, H.A. 2000, ApJ, 544, 933
Alecian, G. 1996, A&A, 310, 872
Charbonneau, P., & Michaud, G. 1991, ApJ, 370, 693
Charbonneau, P. 1993, ApJ, 405, 720
Hui-Bon-Hoa, A. 2000, A&AS, 144, 203
Landstreet, J.D. 1982, ApJ, 258, 639
Michaud, G., Tarasick, D., Charland, Y., & Pelletier, C. 1983, ApJ, 269, 239
Monier, R. 2005, A&A, 442, 563
Richard, O., Michaud, G., & Richer, J. 2001, ApJ, 558, 377
Richer, J., Michaud, G., & Turcotte, S. 2000, ApJ, 529, 338
Turcotte, S., Michaud, G., & Richer, J. 1998a, ApJ, 504, 559
van't Veer-Menneret, C., & Mégessier, C. 1996, A&A, 309, 879